Doctoral Program in

Materials Science and Engineering

EDMX

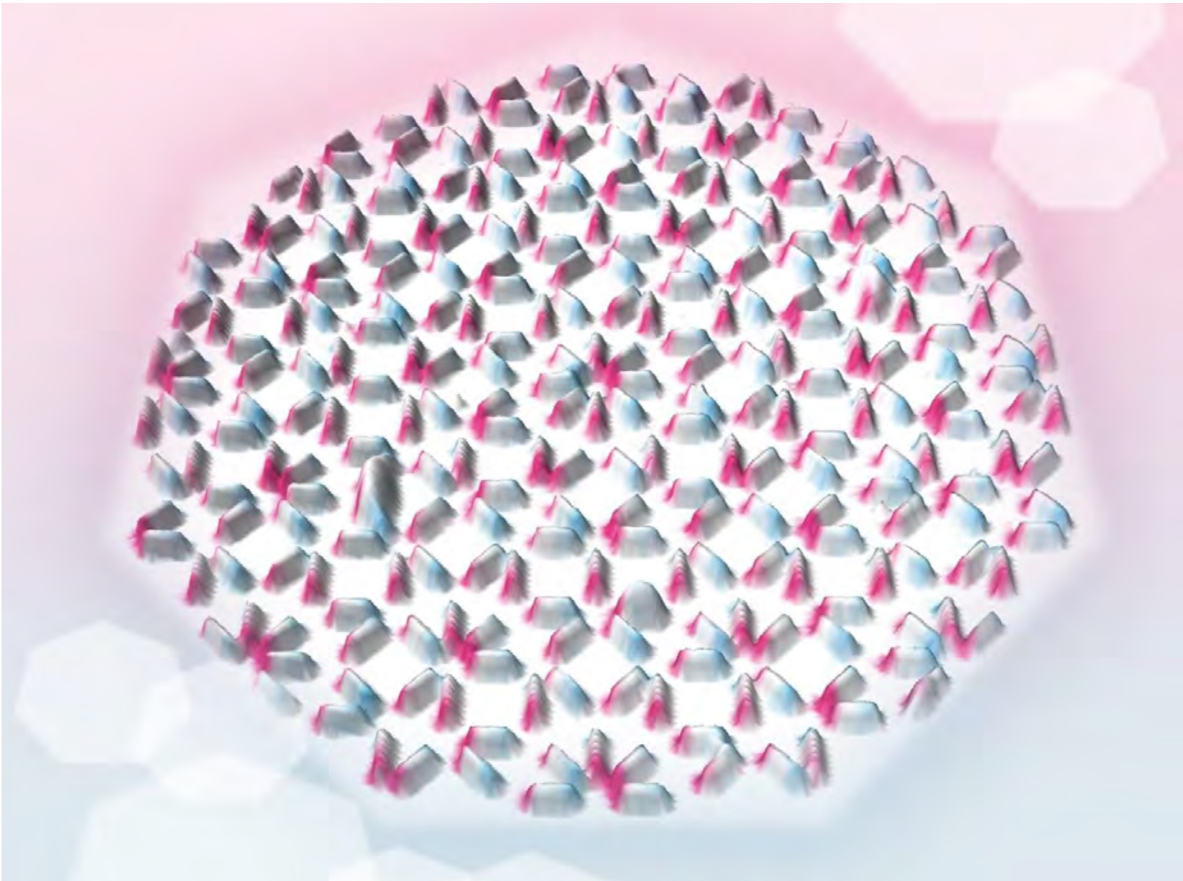

PhD Course

MSE-670

Advanced Microscopy for Magnetic Materials

Chiral magnets were known for decades to host a specific but unclear magnetic phase (A phase) below a critical temperature at which their magnetic ordering occurred. In 2009, neutron scattering in an unconventional configuration, i.e., in a magnetic field applied parallel to the neutron propagation direction, obtained reciprocal space data that suggested an ordered lattice of magnetic skyrmions. Two years later, Lorentz transmission electron microscopy provided real-space imaging of the nanoscale and topologically protected spin whirls.

The sinergia project 171003 “Discovery and Nanoengineering of Novel Skyrmion-hosting Materials” aimed at further exploring the fundamental properties of non-collinear spin structures in chiral magnets and their possible functionalization in modern technologies covering frequencies from DC to several GHz. In the framework of this interdisciplinary project funded by the Swiss National Science Foundation (https://www.epfl.ch/labs/lmgn/skyrmions/) magnetic imaging techniques and microscopy were further developed. The research in the consortium stimulated this PhD course MSE-670 which attracted funding from the doctoral school at EPFL (EDOC).

We are happy that experts from within Switzerland and surrounding European countries contribute lectures to MSE-670. They reflect the latest state of different magnetic characterization and microscopy techniques. We particularly acknowledge Prof. R. Dunin-Borkoswki (FZ Juelich, Germany), Dr. V. Ukleev (Bessy, Berlin, Germany), Dr. P. Che (Thales/Paris Sud, France) and Prof. M. Poggio (U Basel, CH) for coming to EPFL campus and offering in-person lectures together with Prof. F. Carbone (EPFL), Dr. P. Tengdin (EPFL) and the organizers. We thank all the lecturers for their efforts put into this PhD course, the administration at EDMX, and EDOC for financial support which allows lecturers and PhD students to interact closely in the framework of this block course.

Thomas Lagrange and Dirk Grundler, Lausanne, EPFL, November 2022

Front page: Data (colored) obtained by a scanning probe microscopy (magnetic force microscope) on ferromagnetic nanoelements forming an artificial magnetic quasicrystal. The blue and red colors indicate north and south poles, respectively, of the sub-100nm wide nanomagnets.

Course Title:
Advanced Microscopy techniques for characterizing the magnetic properties of materials
MSE-670

Course Description:

Recent advances in X-ray, optical, scanning probe, and electron microscopy techniques allow one to characterize and image the static and dynamic magnetic configurations of nanostructures and non-collinear spin systems down to the nanoscale. These pump-probe techniques can explore spin dynamics with high spatial resolution down to sub-ns timescales. The techniques are based on principles such as transmission electron microscopy, x-ray scattering, x-ray, and electron magnetic dichroism, scanning probe microscopy, and inelastic light scattering. They probe different physical quantities and provide complementary information for fundamental research on magnetic materials and their functional properties, e.g., magnetic storage, spintronics, and magnonics. Swiss research groups have contributed to recent technological advancements, and the magnetism research community is continuously growing. Hence, this course provides an overview and specific insight into advanced optical, x-ray, and electron microscopy techniques for the characterization of magnetic properties of materials. The planned course allows Ph.D. students to acquire theoretical knowledge through lectures and get practical insight via live demonstrations performed in different labs on the EPFL campus.

Plan: **3-day block course for Ph.D. students held on Nov. 16th-18th, 2022**

(A) 2.5 days – 90 min (including examples and Q&A sessions) lectures from 8 experts (4 external and 5 internal). Online recordings will be provided and accessible in a Moodle, as well as slide handouts and literature references. The lectures are numbered as follows.

(B) 0.5-day demonstrations- LTEM (CIME Titan Facility, EPFL), BLS (LMGN, EPFL), and MOKE (LUMES, EPFL)

Agenda

Day 1: (Lecture are of 2x45 min plus a 15 min break) **in MXF-312**

9h30-10h15
Welcome coffee

10h15-12h

1) Dirk Grundler, Professor, EPFL "Introduction-Materials science of magnetic materials."

12h15-13h15

Lunch served in the meeting room

13h30-15h15

2) Victor Ukleev, Staff Scientist, BESSYII, Berlin, Germany "Static and dynamic magnetic imaging using x-ray based techniques."

15h30-17h15

3) Thomas La Grange, Senior Scientist, EPFL “Lorentz Transmission Electron Microscopy: Theory, Practice, Simulations, and Quantitative Phase reconstruction.”

Day 2: in MXF-312

8h30-10h15

4) Fabrizio Carbone, Professor, EPFL “In-situ and Ultrafast Lorentz Transmission Electron Microscopy (LTEM)”

10h30-12h15h

5) Martino Poggio, Professor Department of Physics, University of Basel “Nanomagnetic studies using scanning probe microscopy techniques”

12h30-13h30
Lunch served in the meeting room

13h45h-15h30

6) Rafal Dunin-Borkowski: Director of Ernst Ruska-Centre for Microscopy and Spectroscopy with Electrons, Juelich, Germany, “Electron Holography: Theory, Practical Examples from Medium to Atomic resolution.”

15h45-18h LTEM demonstration and free discussion
Students are separated into 3 groups for LTEM Demonstration (45 min) at CIME Titan Facility, EPFL (MXC 014). Groups of 7-8 people are formed due to limited space in the microscope room. The remaining time is for free discussion/preparation for test.

Day 3: in MED2 1124

10h15-12h

7) Ping Che, Scientist, Université Paris-Saclay (UMR-137), France “Characterizing magnetic materials using inelastic Brillouin light scattering (BLS) technique”

12h15-13h15
Free Lunch

13h30-15h15

8) Phoebe Tengdin, Scientist, EPFL “Ultrafast Optical Spectroscopy and Imaging Techniques: Magnetic Optical Kerr Effect (MOKE)

15h30-17h30
Demonstrations 45 min each on BLS (LMGN, EPFL), and on MOKE (LUMES, CH H0 604 EPFL)

17h45 – 18h15 Written Test for PhD students aiming at credits

EPFL

MSE-670
Advanced magnetic microscopy

Fall 2022

Lecture 1:
Introduction
-
Materials science of magnetic materials

Lecturer: Prof. Dirk Grundler

Laboratory of Nanoscale Magnetic Materials and Magnonics
lmgn.epfl.ch

dirk.grundler@epfl.ch
BM3141

Institute of Materials

LABORATORY OF NANOSCALE MAGNETIC MATERIALS AND MAGNONICS LMGN

Research Teaching People Publications Collaborations

Share:

Welcome to LMGN

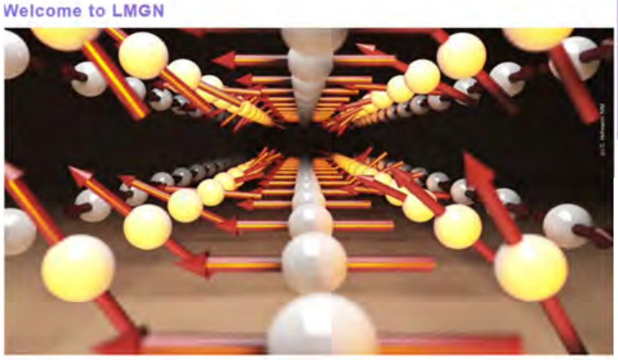

Competences and Objectives

- Magnetic properties of nanostructured materials
- Nanofabrication and cleanroom processing
- Microwave properties of magnetic nanomaterials
- GHz spectroscopy
- Magnonics
- Spintronics
- Skyrmionics

The **Laboratory of Nanoscale Magnetic Materials and Magnonics (LMGN)** aims at the exploitation of magnetic nanomaterials for information technology (data processing, transmission, logic), sensing and multifunctional devices. In our experiments and simulations, we prepare and explore individual ferromagnetic nanostructures such as **nanotubes**, periodic and aperiodic nanomagnet arrangements such as **magnonic crystals**, artificial spin ice and quasicrystals as well as Skyrmion lattices. We study their fundamental properties and aim at novel functionalities.

The focus is devoted to the microwave properties of magnetic materials in the few GHz to 100 GHz frequency regime. Here, electromagnetic waves that, in free space, exhibit a wavelength of several

Introduction to magnetic materials

Synopsis: Magnetic materials offer a rich versatility in modern technologies (information technology, daily appliances, renewable energy production, …)
Their functionality depends on the materials science and engineering of compounds

Bibliography: Textbooks about technologically relevant magnetic materials
Available at library, eg.
B.D. Cullity, C.D. Graham, Introduction to Magnetic Materials, (2009);
J.D. Coey, Magnetism and Magnetic Materials (2010).
R.C. O'Handley, Modern magnetic materials: principles and applications (2000);
the library provides several copies of the book by
K. Krishnan, Fundamentals and Applications of Magnetic Materials

Ressources en bibliothèque
- Introduction to Magnetic Materials / Cullity
- Fundamentals and Applications of Magnetic Materials / Krishnan
- Magnetism and Magnetic Materials / Coey
- Modern magnetic materials: principles and applications / O'Handley

Contents

1. Magnetic materials: Review of properties, concepts and magnetic parameters (focussing on hard magnets):
   magnetic ordering, critical temperature, elements vs compounds, magnetic hysteresis, figure of merit, demagnetization effect, domain formation
2. Materials science and engineering of a functional magnetic material (hard magnet Nd-Fe-B):

   relevant energy terms, magnetic anisotropy,

   microstructure, characterization/imaging (microscopy)

EPFL

1. Magnetic materials: properties and concepts

EPFL

Types of "magnetic materials"

The following four categories (a) to (d) originate from microscopic magnetic moments existing in the material already at zero magnetic field: (a) field is needed to align moments, (b) to (d) moments undergo ordering due to (symmetric) exchange interaction even at zero magnetic field. (c) and (d) can provide a net magnetization M even at zero field

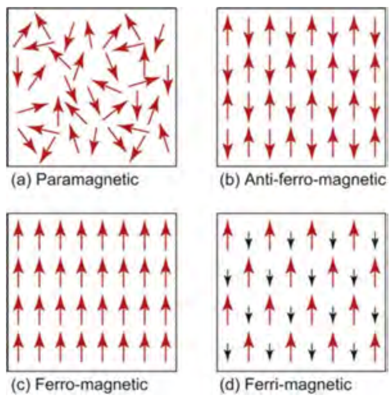

(e) Diamagnetic:
resulting from the orbital motion of electrons in atomic orbitals. The motion is modified by the presence of a magnetic field => the applied magnetic field is partly repelled from the material (diamagnetism)

EPFL

Periodic table of elements

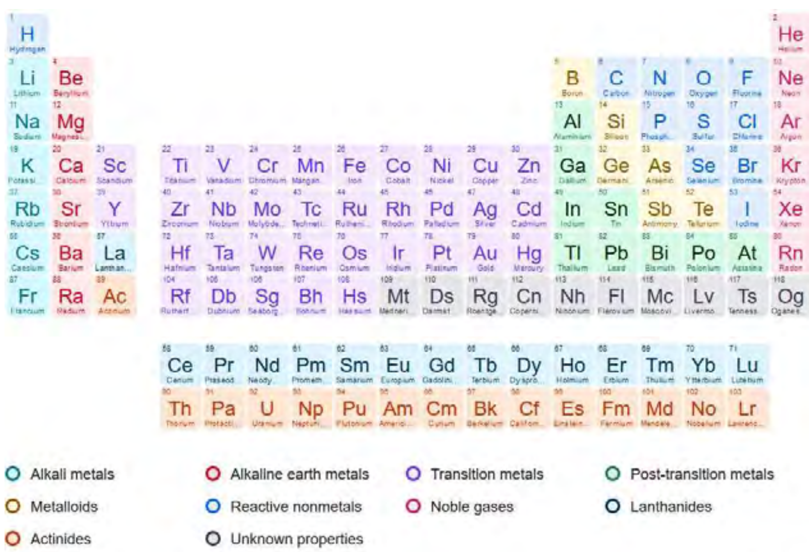

https://www.google.com/search?client=firefox-b-d&q=periodic+table+of+elements

EPFL

Table A The magnetic periodic table. Diamagnetic elements are uncoloured, paramagnets are pale grey, ferromagnets are dark grey antiferromagnets are mid grey, and the Curie or Néel temperatures are marked. Common paramagnetic ions are indicated. Elements which bear a magnetic moment as isolated atoms are marked in bold type.

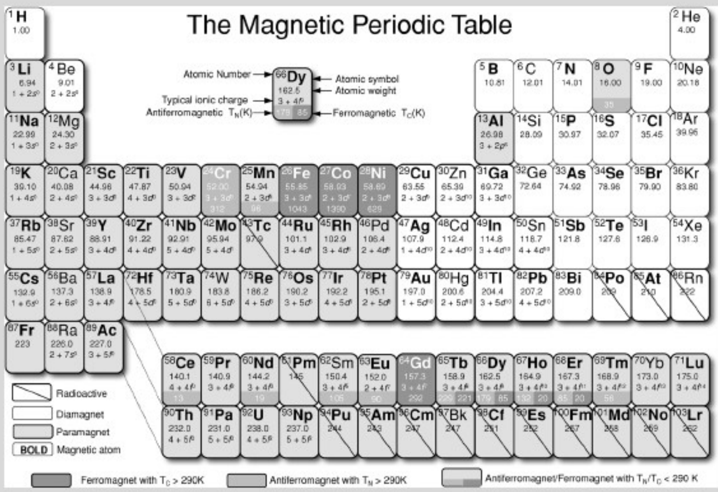

At room temperature **only Fe, Co and Ni** are known to form a ferromagnet starting from a single element.
Nowadays many alloys and compounds are known to be ferromagnetic at room temperature as well. (Graph taken from J.M.D. Coey)

TABLE 7.1
Magnetic Properties of Iron, Cobalt, and Nickel

	Fe	Co	Ni
Magnetic moment per atom [6] at 0 K (in Bohr magnetons)	2.22	1.72	0.62
Saturation magnetization (in 10^6 A m^{-1})			
(at 0 K)	1.74	1.43	0.52
(at 300 K)	1.71	1.40	0.48
Exchange energy *J* [3,7]			
(in J)	2.5×10^{-21}	4.5×10^{-21}	2×10^{-21}
(in meV)	0.015	0.03	0.020
Curie temperature [6]			
(in °C)	770	1131	358
(in K)	1043	1404	631
Anisotropy energy K_1 [8,9,10,11] (in J m^{-3})			
(at 0 K)	5.7×10^4	68×10^4	-5.7×10^4
(at 300 K)	4.8×10^4	45×10^4	-0.5×10^4
Lattice spacing [12] (in nm)			
A	0.29	0.25	0.35
C		0.41	
Domain-wall thickness [3,4]			
(in nm)	40	15	100
(in lattice parameters)	138	36	285
Domain-wall energy [6,11] (in J m^{-2})	3×10^{-3}	8×10^{-3}	1×10^{-3}

Source: For further details consult the paper by Lilley, B.A., *Phil. Magn.*, 41, 792, 1950.
Note: Domain-wall thicknesses and energies are approximate values only, since they will depend on the crystallographic direction of the moments in the domains on either side of the wall.

11

Magnetic ordering (critical) temperature

A magnetically ordered state is found below a critical temperature (Curie/Néel temperature):

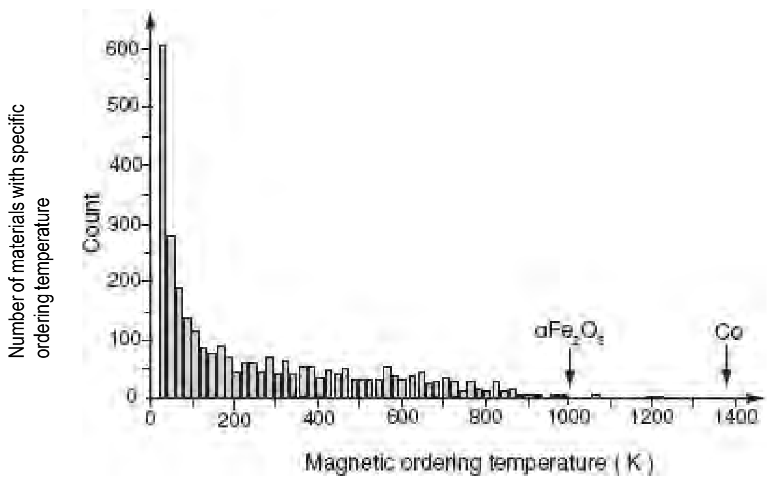

EPFL

Temperature dependent magnetization/magnetic susceptibility

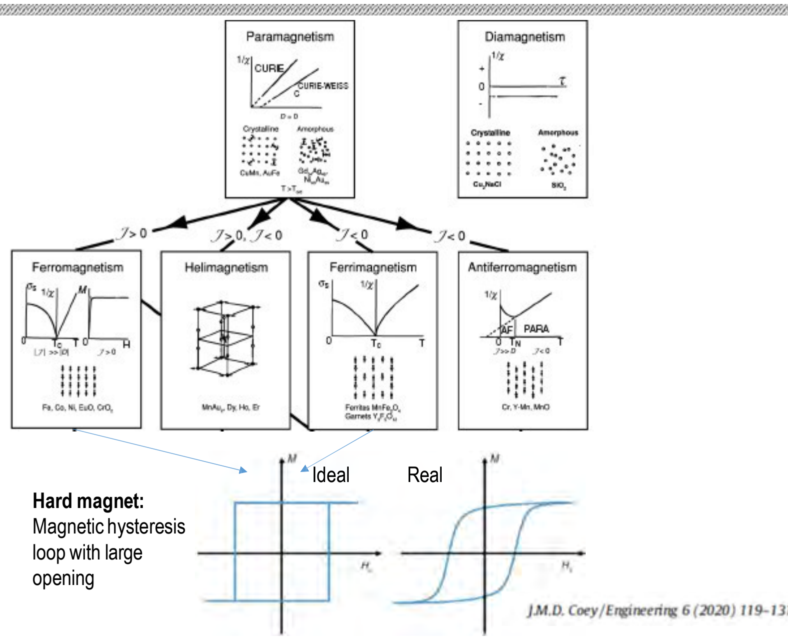

EPFL

From Fe to Iron Oxides

Bulk Fe is a ferromagnet.
In air, Fe oxidizes. The most common forms are α-Fe_2O_3 (hematite is the mineral) and Fe_3O_4 (magnetite is the mineral). The latter contains iron in oxidization states 2^+ and 3^+.
Magnetite **(lodestone)** is a so-called **ferrimagnet**, which means that microscopic magnetic moments of the Fe ions are aligned antiparallel, thereby reducing the saturation magnetization $\mu_0 M_s$ of the bulk material below the value of iron (which is about 2.15 T at room temperature).

Iron crystal:
$\mu_0 M_s$ = 2.15 T
ferromagnetic

Hematite:
canted antiferromagnetic
phase

Magnetite (lodestone):
$\mu_0 M_s$ = 0.56 T
ferrimagnetic

None of these single or poly-crystals are used in high-end technical applications based on hard magnets. Why?

EPFL

Permanent (hard) magnets: Optimization of coercive field and energy product

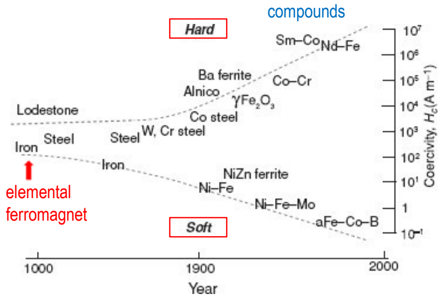

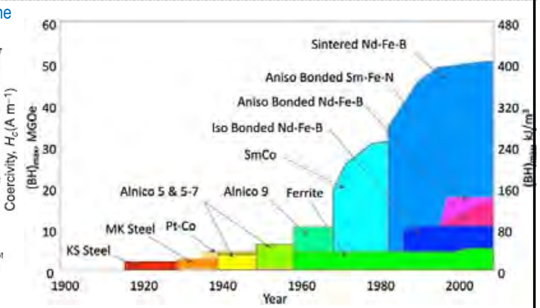

Figure of merit:
max. energy product (BH),
via large coercive
field and remanent
magnetization

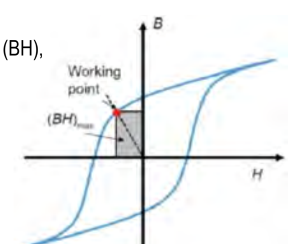

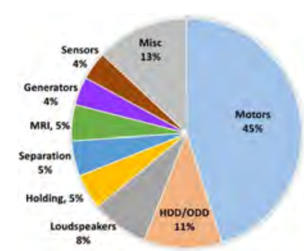

Applications of permanent magnets
by market ($) share in 2019.
https://link.springer.com/article/10.1007/s11837-022-05156-9

EPFL

Queen Elizabeth Prize for Engineering honours magnet pioneer (01. Feb. 2022)

Permanent magnet technology: NdFeB

Dr Masato Sagawa

https://qeprize.org/

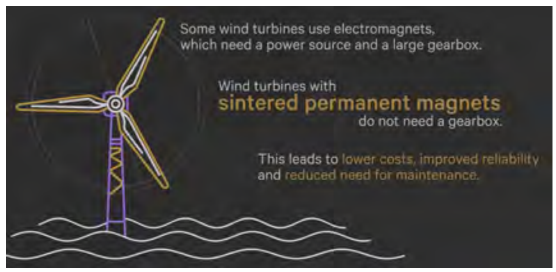

EPFL

Permanent magnets provide large magnetic fields

The Flux Detector makes magnetic fields visible.

It's accomplished by a foil filled with nickel particles in a gelatinous suspension.

The Flux Detector turns

- dark in color

when the magnetic field is perpendicular to the foil (for example, near the poles) and

- lighter

when the magnetic field runs parallel to the foil.

EPFL

Magnetic field B

The lines of the magnetic field:

- Never intersect
- Have neither sources or sinks, unlike electrical and gravitational fields. Therefore, a magnetic field always froms a closed loop.
  $\vec{\nabla} \cdot \vec{B} = 0$

One distinguishes two magnetic fields *B* and *H.* For

$$\vec{B} = \mu_r \mu_0 \vec{H} = \mu_0(\vec{H} + \vec{M}),$$

the field lines are closed

The density of the magnetic field lines is proportional to the magnitude of the field.

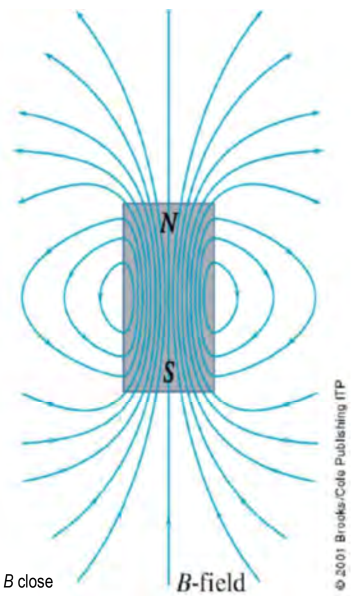

Field lines of field *B* close as required by **Maxwell's equations**. Field lines of field *H* do not follow this restriction.

Energy densities stored in different permanent magnets

Permanent magnet: energy stored ~ B^2

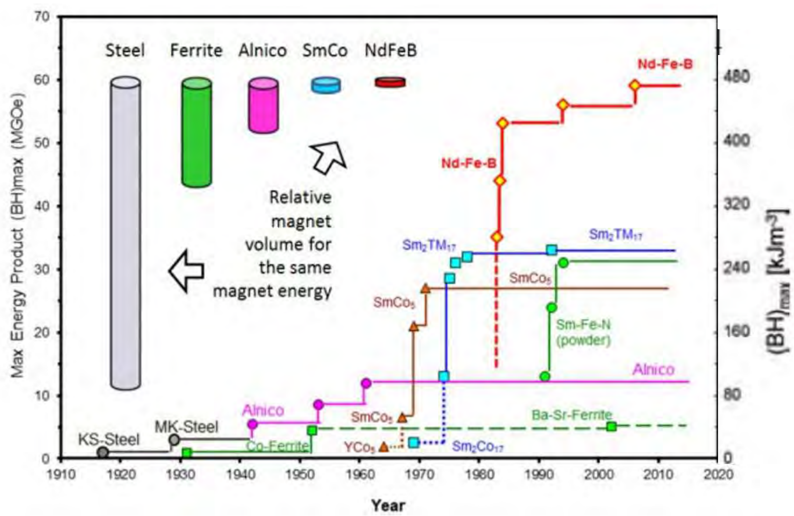

EPFL

Field lines of *H*-field

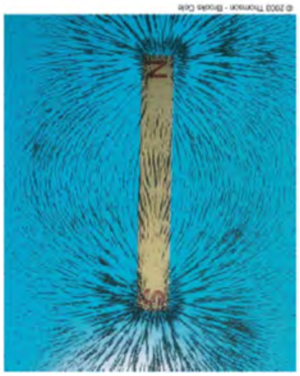

H-field:

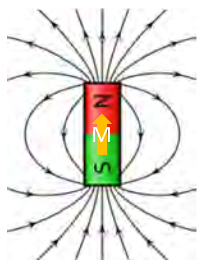

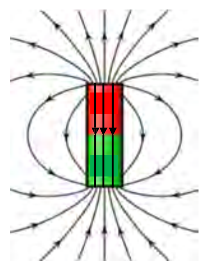

One distinguishes two magnetic fields *B* and *H.*
For

$\vec{B} = \mu_r\mu_0\vec{H} = \mu_0(\vec{H} + \vec{M})$,

the field lines are closed

Here we sketch the **field lines of *H***
They do not form closed loops:

$\vec{\nabla} \cdot \vec{B} = 0$

$\Rightarrow \vec{\nabla} \cdot (\vec{H} + \vec{M}) = 0$

$\Rightarrow \vec{\nabla} \cdot \vec{H} = - \vec{\nabla} \cdot \vec{M}$ The field ***H*** is **not divergence-free.**

EPFL

In magnetism two main unit systems coexist: CGS and SI. In the lecture we will use mainly the SI system.

Table 1.6.1 *Key relationships and conversions between SI and CGS units in magnetism.*

	CGS	SI	Conversions
Magnetic field [H]	[Oersted]	[A/m]	1 A/m = $4\pi.10^{-3}$ Oe
Magnetic inductance [B]	[Gauss]	[Tesla] = [Weber/m^2] = [V s m^{-2}]	1 T = 10^4 Gauss
Pole strength [p]	[dynes/Oe]	[A m]	
Magnetic moment [m]	[ergs/Oe] = emu	[A m^2]	1 emu = 10^{-3} A m^2
Magnetization [M]	emu/cm^3	[A/m]	1 emu cm^{-3} = 10^3 A/m
Permeability of free space	1	$\mu_0 = 4\pi \times 10^{-7}$ [Wb A^{-1}m^{-1}] = [H m^{-1}].	
Field of a straight wire carrying current i [A] at a distance, r	$H = \frac{2i}{10r}$(Oe)	$H = \frac{i}{2\pi r}$[A/m]	
Relationship between M, H, and B	$\mathbf{B} = \mathbf{H} + 4\pi\mathbf{M}$	$\mathbf{B} = \mu_0(\mathbf{H} + \mathbf{M})$	
Torque on a moment, m	$\tau = \mathbf{m} \otimes \mathbf{H}$	$\tau = \mathbf{m} \otimes \mathbf{B}$	
Potential energy of m	$E_{pot} = -\mathbf{m} \cdot \mathbf{H}$ [erg]	$E_{pot} = -\mathbf{m} \cdot \mathbf{B}$ [J]	1 J = 10^7 ergs

Taken from Kannan Krishnan
(Fundamentals and Applications
of Magnetic Materials)

Demagnetization field inside magnet

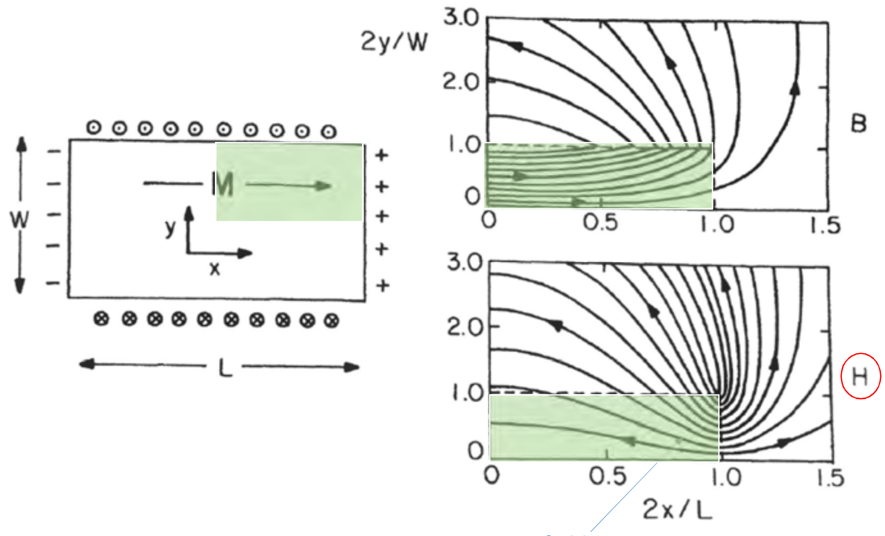

Demagnetization field,
pointing against magnetization vector

EPFL

Field strengths inside ferromagnets

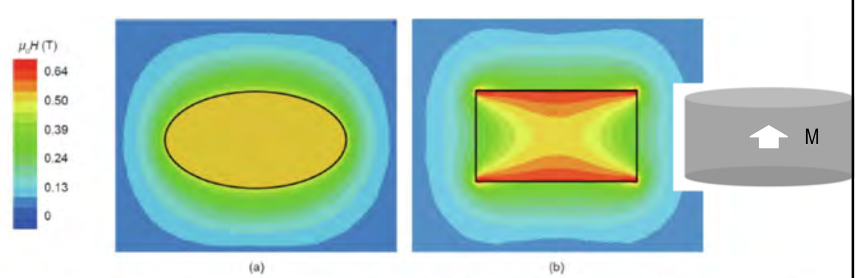

Fig. 2. Illustration of the magnitude of H (a) for an ellipsoid and (b) for an ideal, uniformly magnetized cylinder, both with $N = 1/2$ and $\mu_0 M = 1$ T. The demagnetizing field is uniform in the ellipse, but highly non-uniform in the cylinder, where it is stronger than −0.6 T at the flat surfaces and edges.

Large demagnetization fields destabilize the magnetization and without specific materials optimization leads to the formation of magnetic domains. Such domains reduce significantly the remanent magnetization.

EPFL

Examples of different kinds of domains depending on magnetic anisotropies

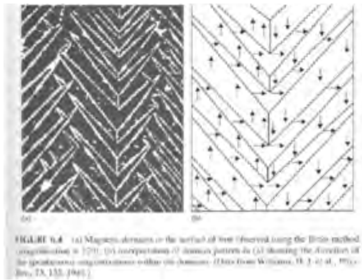

Examples of domains depending on sample thickness and type of anisotropy:

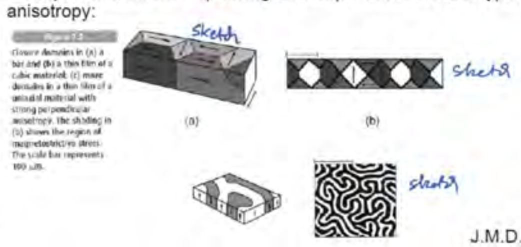

J.M.D. Coey

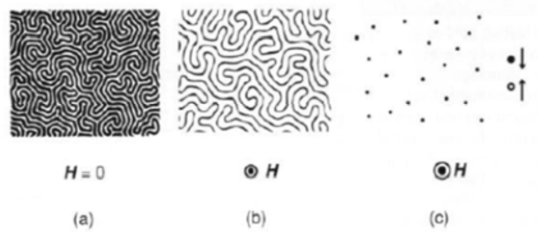

Figure 7.17

Magnetization and domain structure of a thin film with perpendicular anisotropy. Maze domains give way to bubble domains on increasing magnetic field.

How to avoid domain formation after saturation?

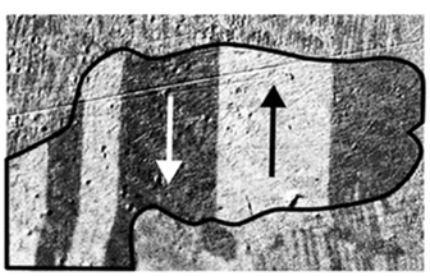

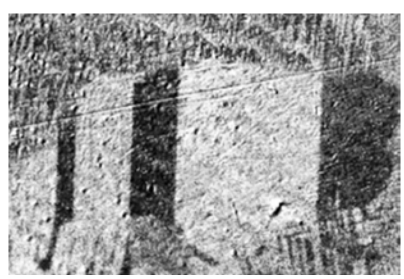

http://mriquestions.com/uploads/3/4/5/7/34572113/2618271_orig.gif

Here domains are detected
by magnetooptical Kerr effect.
See lecture by Dr. Phoebe Tengdin

EPFL

2. Materials optimization and characterization

In the following we discuss aspects of the optimization of a functional magnetic material by considering the hard (permanent) magnet.

EPFL

Landau-Lifshitz-Gilbert equation

$$\vec{H}_{\text{eff}} = -\frac{1}{V}\frac{dE_{\text{tot}}}{d\vec{M}}$$

$$\frac{d\mathbf{M}}{dt} = -\gamma(\mathbf{M} \times \mu_0 \mathbf{H}) + \frac{\alpha}{|M_0|}(\mathbf{M} \times \frac{d\mathbf{M}}{dt})$$

Equilibrium condition:

$$\vec{M} \times \vec{H}_{\text{eff}} = 0$$

If there is a misalignment angle, a torque exists:
=> precession of magnetization vector,
and relaxation (second term) towards the effective field

Contributions in total energy, e.g.:

Zeeman energy $E_Z = -\mu_0 \int_V \mathbf{H}_{\text{ext}} \mathbf{M} dV$

Demagnetization field energy $E_d = -\frac{\mu_0}{2} \int_V \mathbf{H}_d \mathbf{M} dV$

Magnetic anisotropy energy (MAE) $\epsilon_a = K_u \sin^2\theta$

Exchange energy $E_{\text{exch}} = \int A_{\text{exch}} (\nabla \mathbf{e}_M)^2 dV$ where $\mathbf{e}_M = \mathbf{M}(r)/M_s$

Helices, magnetic skyrmions result from e.g. antisymmetric exchange interaction (Dzyaloshinskii-Moriya interaction; here, bulk inversion asymmetry assumed):

$$E_{DM,\alpha} = \int [\alpha \vec{M} \times (\vec{\nabla} \times \vec{M})] d\alpha$$

EPFL

Origin of magnetocrystalline anisotropy

Effect of spin-orbit coupling: change of orbital functions when rotating M

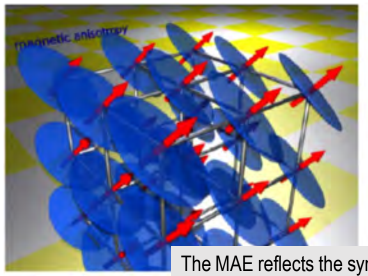

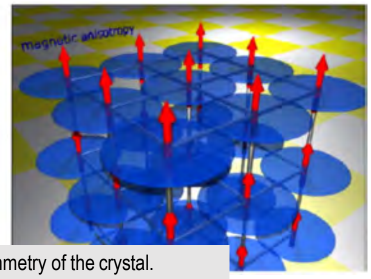

The MAE reflects the symmetry of the crystal.
A tetragonal crystal experiences a uniaxial anisotropy.

Figure 6.6.1 *Absolute values of the anisotropy constants, K (ergs/cm^3), at room temperature. (Note, 1 J/m^3 = 10 ergs/cm^3) Courtesy, Dr. R.F.C. Farrow.*

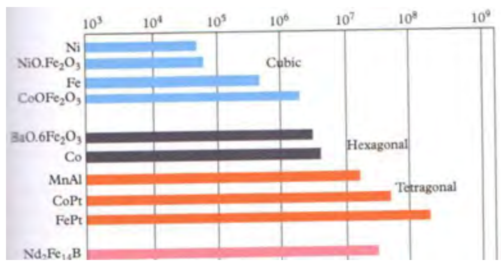

EPFL

How to test effective fields? Resonant spin precession

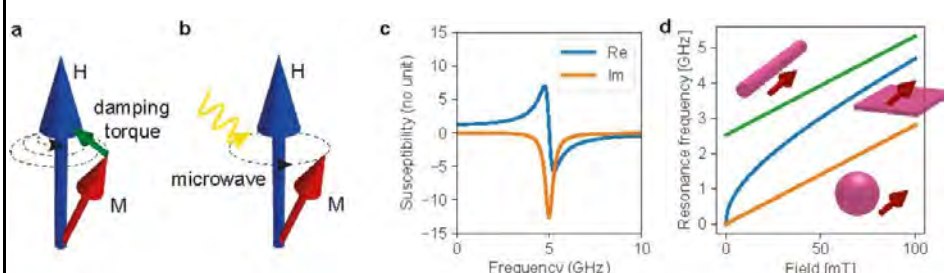

See lecture by Dr. Ping Che

EPFL S. Watanabe, 2021 (PhD thesis)

Optimization of energy product via large MAE

Anisotropy Demagnetization

Ideal coercive field in a finite sample: $H_c \geq \left(\frac{2K_1}{\mu_0 M_s}\right) - \mathcal{N} M_s$

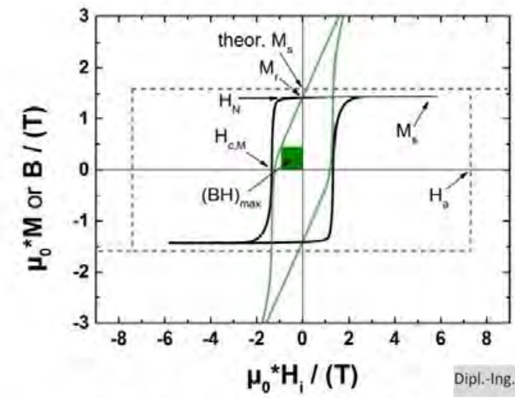

Dipl.-Ing. Konrad Löwe aus Stralsund

Figure 2-2: Comparison of an experimental hysteresis loop μ_0*M(H_i) (full black line) of an sintered Nd-Fe-B magnet with the theoretical hysteresis loop (blacked dashed line) after equation 2-7. Also shown is B(H_i) (full green line). The values for the theoretical M_s and H_a can be found in Table 2-1. H_a ... anisotropy field, M_r ... remanence, M_s ... saturation magnetization, H_N ... nucleation field, $H_{c,M}$ ... coercivity of the M(H) curve, $(BH)_{max}$ ... maximum energy product.

How to explain the maximum coercive field?

$$E_{tot} = E_{ani}(\theta,\varphi) + E_{Zeeman} = E_{ani}(\theta,\varphi) - \mu_0 \vec{M} \cdot \vec{H}_{ext}$$

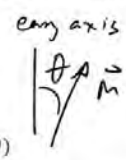

For uniaxial anisotropy assume: $E_{ani}(\theta,\varphi) = K_1^u \sin(\theta)$

The anisotropy comes with an anisotropy field (see previous chapter): $H_{ani} = \frac{2K_1^u}{\mu_0 M_s}$

Using $K_1^u = 8.2\ 10^5\ \frac{\mathrm{J}}{\mathrm{m}^3}$ for Co, one gets $\mu_0 H_{ani} = 0.58$ T

When the external field reaches 0.58 T and is applied either exactly parallel to the easy axis or exactly perpendicular to the hard axis, the anisotropy field is balanced. For any larger field the magnetization vector then follows the field direction.

EPFL

Intrinsic magnetic properties

J.M.D. Coey / Engineering 6 (2020) 119–131 127

Table 2
Intrinsic magnetic properties of some permanent magnet phases.

Compound	T_C (K)	$\mu_0 M_s$ (T)	K_1 (MJ·m^{-3})	κ	$(BH)_{MAX}$ (kJ·m^{-3})
$Nd_2Fe_{14}B$	588	1.61	4.3	1.54	516

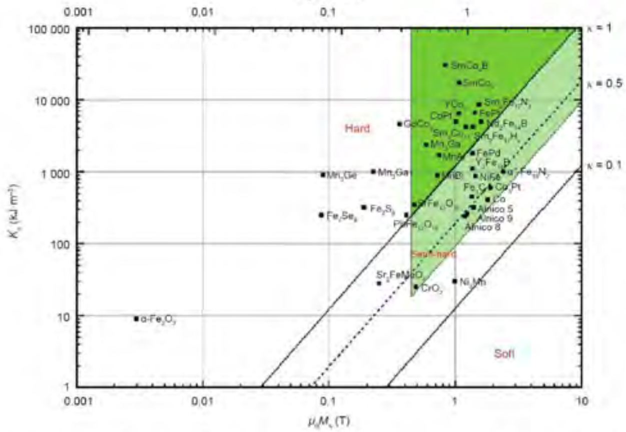

Fig. 7. Plots of anisotropy K_u as a function of polarization $\mu_0 M_s$ for many magnetic materials with uniaxial anisotropy. The anisotropy of the Alnicos is intrinsic shape anisotropy. Solid and dotted lines correspond to κ = 1, 0.5, and 0.1. Hard materials in the bright green area can be used to make efficient magnets of any shape. Semi-hard materials in the pale green area can be used to make oriented magnets with a shape-limited energy product. Reproduced from Ref. [2] with permission of Elsevier B.V., © 2015.

Solution to domain formation

Functional magnetic materials originate from materials science and engineering with materials having optimized composition and microstructure

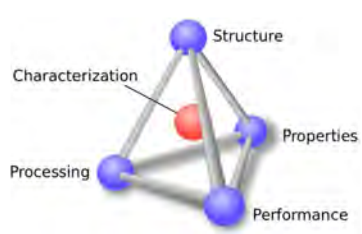

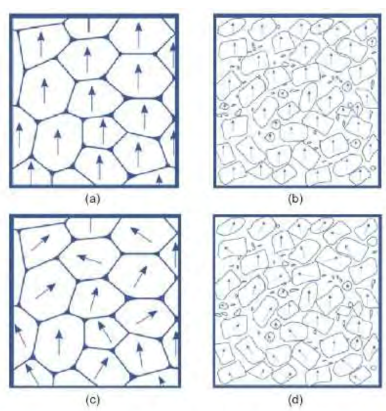

Fig. 3. Possible forms of rare earth permanent magnets. (a) Oriented, sintered magnet; (b) oriented, bonded magnet; (c) random, sintered magnet; (d) random, bonded magnet.

EPFL

Production of rare earth permanent magnets

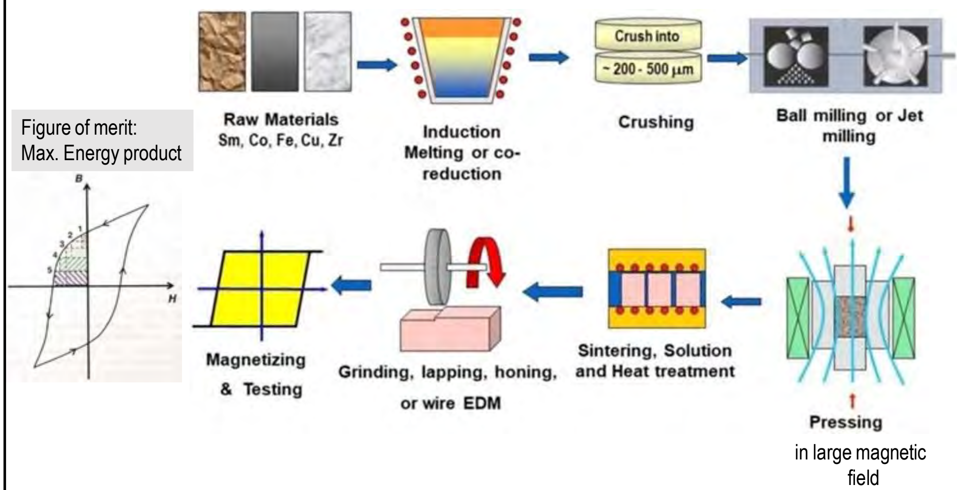

EPFL

Relevant temperatures while processing

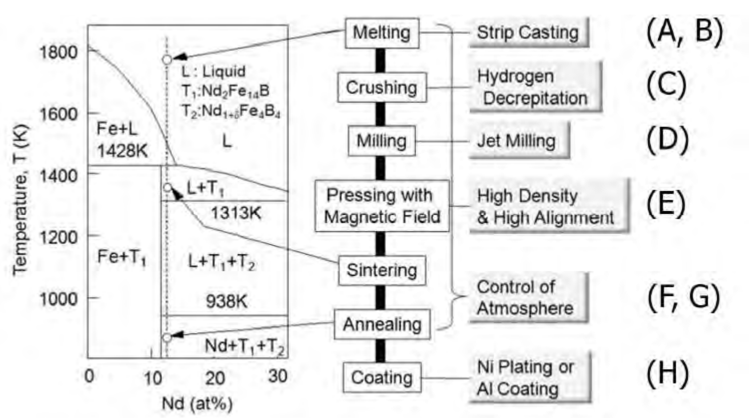

Figure 2-4: Production route of NdFeB sintered permanent magnets [Sugimoto2011]

PhD thesis, TU Darmstadt

Dipl.-Ing. Konrad Löwe aus Stralsund

EPFL

Tetragonal phase of $Nd_2Fe_{14}B$ in the grains

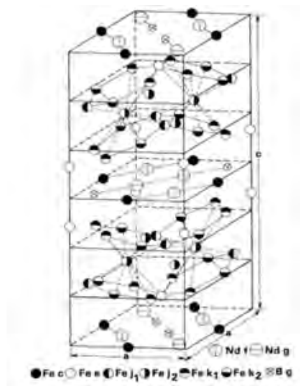

Figure 2-1: Crystal structure of $Nd_2Fe_{14}B$ [Herbst1991].

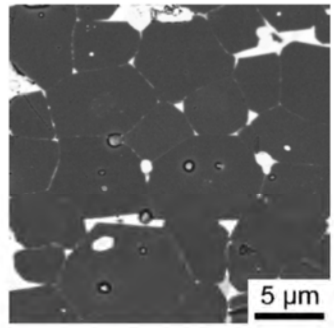

Figure 1. Backscattered electron image showing the typical microstructure of a Nd–Fe–B sintered magnet. Brighter regions correspond to Nd-rich phases and the large, darker grains are $Nd_2Fe_{14}B$.

The large content of Fe ensures a large saturation/ remanent magnetization.

tetragonal /

PhD thesis, TU Darmstadt

Dipl.-Ing. Konrad Löwe aus Stralsund

EPFL

Table 13.3. Properties of commercial oriented magnets

	$\mu_0 M_r$ (T)	J_s (T)	${}_iH_c$ (kA m^{-1})	${}_BH_c$ (kA m^{-1})	$(BH)_{max}$ (kJ m^{-3})	$\mu_0 M_r^2/4$ (kJ m^{-3})
$SrFe_{12}O_{19}$	0.42	0.47	275	265	34	35
Alnico 5	1.25	1.40	54	52	43	310
$SmCo_5$	0.88	0.95	1700	700	150	154
Sm_2Co_{17} [a]	1.08	1.15	1100	800	220	232
$Nd_2Fe_{14}B$	1.28	1.54	1000	900	350	326

[a] Intergrown with 1:5 phase

Fig. 5 Neodymium-iron-boron applications

Computers and office automation
disk drives and voice coil motors
printer and fax stepper motors
printer hammer
copy machine rollers
CD drive spindle and pickup motors

Appliances
portable power tool motors
household appliance motors
scales

Automotive
permanent magnet starter moors
sensors
electric fuel pumps
instrumentation gauges
brushless dc motors
actuators

Factory automation and industrial
robot motors
robot arms
magnetic couplings
pumps
servo motors
bearings
generators (especially portable)

Consumer electronics/communications
VCRs and camcorders
DVD
cameras
watches
speakers
headsets
microphones
pagers
mobile phones

Medical/health
MRI
surgical tools
water purifiers

Security/safety
sensors
illumination

Relevant length scales for magnetic materials optimization

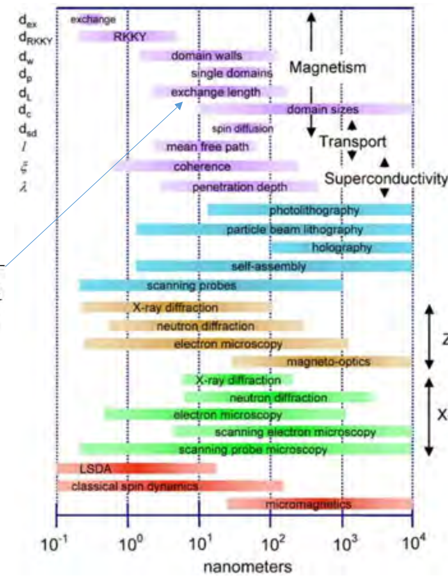

$$l_{\mathrm{exch}} = \sqrt{\frac{2A_{\mathrm{exch}}}{\mu_0 M_s^2}}$$

M.R. Fitzsimmons et al.,
JMMM **271**, 103 (2004).

Domain imaging on NdFeB versus grain imaging

Table 2-2: Micromagnetic parameters and characteristic length scales for $Nd_2Fe_{14}B$ [Coey2010]. exchange stiffness A, anisotropy constant K_1, exchange length l_{ex}, domain wall width δ_W, domain wall energy γ_W.

A [pJ/m]	K_1 [MJ/m^3]	l_{ex} [nm]	δ_W [nm]	γ_W [mJ/m^2]
8.0	4.9	1.9	3.9	25

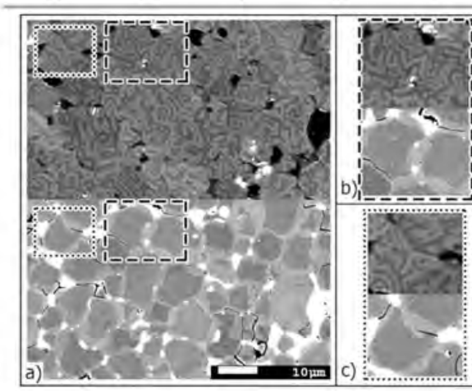

Figure 4-7: Microstructure of a Dy coated magnet after annealing at 900 °C for 6 h. a) Correlation between magneto-optical Kerr (top) and SEM BSE (below) contrast. The respective images show the exact same region of the sample. The easy axis of the material is pointing out - of - plane and the Kerr image is showing polar contrast. b) and c) show magnified views from a).

EPFL

Dipl.-Ing. Konrad Löwe aus Stralsund

Internal spin structures of domain walls

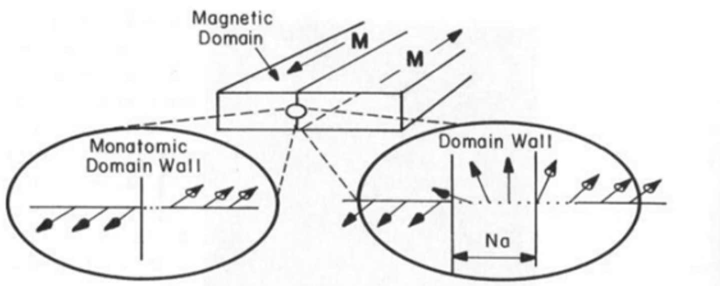

Bulk material

Thin film

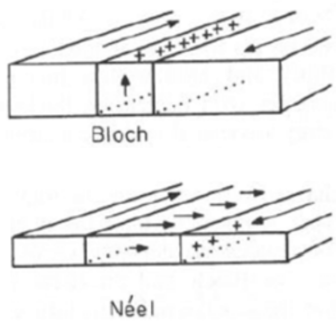

EPFL

Imaging techniques

Table 1. Comparison of magnetic imaging techniques, presenting some of the key specifications and attributes. The quoted values are in general typical achievable values.* Proof of concept recently demonstrated [42, 43, 121]

Technique	Probed Quantity	Spatial Resolution	Temporal Resolution	Info. Depth	Comments
Lorentz Microscopy	stray field + sample induction	10 nm	1 ns	sample average	Thin samples, Quantitative info. with differential phase contrast microscopy.
Electron Holography	stray field + sample induction	5 nm	10 ms	sample average	Quantitative info. through mathematical image reconstruction.
SEMPA	magnetization	20 nm	700 ps*	1 nm	Quantitative info., Long acquisitions, UHV required.
SP-STM	magnetization	atomic	120 ps*	surface	UHV required, Usually low temperature, Long acquisitions.
MFM	stray field	10-100 nm	low	1000 nm	Potentially invasive, Long acquisitions, Few sample requirements.
TXM	magnetization	25 nm	50 ps	sample average	Synchrotron technique, Quick overview images.
STXM	magnetization	25 nm	50 ps	sample average	Synchrotron technique, High repetition rates.
PEEM	magnetization	25 nm	50 ps	5 nm	Synchrotron technique, Discharges possible due to high potential.
CDI	magnetization	40 nm	fs-ps	sample average	Zero drift, Synchrotron technique Complex sample fabrication & image reconstruction.
MRI	proton density & environment	1-2 mm	100 ms-several sec	3D imaging	Low risk, Very versatile.
MEG	stray field	5 mm	<1 ms	3D imaging via modelling	No unique solution, Risk free.

Photoemission electron microscopy

Coherent diffractive imaging

Magnetic resonance imaging

Magnetoencephalography

https://arxiv.org/abs/1806.07767

EPFL

Summary

Functional magnetic materials originate from materials science and engineering with materials having optimized composition and microstructure

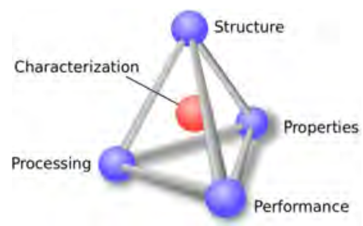

The optimization is a multiscale problem involving scales ranging from the **atomic scale (exchange interaction)** and **nm scale (domain wall widths)** via the **micronscale (magnetic domains, grains)** to the **mm scale (demagnetization effect, shape, processing/machining)**.

Advanced magnetic imaging (microscopy) is key to optimize the functionality of magnetic materials and unravel the fundamentals of spin structure formation
("intended ones like magnetic skyrmions and unintended ones, i.e., domain walls in permanent magnets").

EPFL

HZB Helmholtz Zentrum Berlin

STATIC AND DYNAMIC MAGNETIC IMAGING USING X-RAY BASED TECHNIQUES

Victor Ukleev
Spin and Topology in Quantum Materials
Helmholtz-Zentrum Berlin für Materialen und Energie, Germany

Advanced Microscopy techniques for characterizing the magnetic properties of materials

EPFL
Switzerland
16.11.2022

OVERVIEW

- Introduction:
  - x-ray absorption and x-ray magnetic dichroism
  - resonant x-ray absorption and scattering
  - polarized x-ray sources and beamline optics
- Classic x-ray magnetic imaging techniques
  - Photoemission electron microscopy (PEEM)
  - Transmission x-ray microscopy
- State-of-the-art techniques
  - Coherent x-ray diffraction imaging and holography
  - Three-dimensional x-ray imaging
  - Time-resolved magnetic x-ray imaging with synchrotrons and free-electron lasers
- Summary

INTRODUCTION

Polarization-dependent x-ray absorption

- *L*-edges of transition metals: probes valence states and magnetism
- Peak corresponds to transition from core level to valence band
- Soft x-rays: ~100 eV ... ~2 keV
- Due to the symmetry of the transition operator we obtain the dipole selection rules: Δs=0 Δl=±1 -> orbital and spin moment selectivity

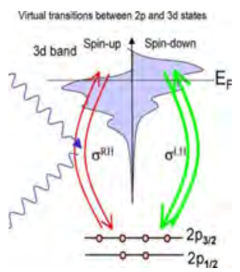

Sensitivity to magnetism

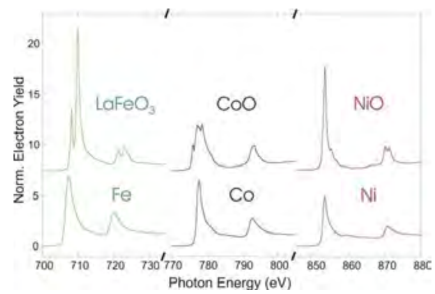

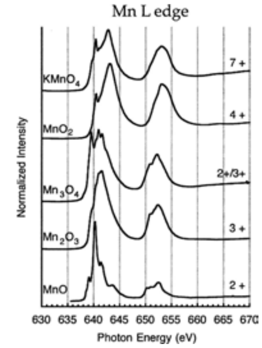

IEEE Trans. on Magn. 2015, 51, 2 https://www-ssrl.slac.stanford.edu/stohr/ J. Phys. Chem. A 2003, 107, 16, 2839–2847

INTRODUCTION

X-ray Circular Magnetic Dichroism (XMCD)

Theoretical prediction -> 1975

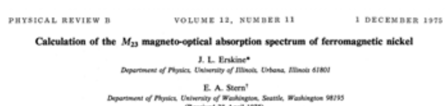
PHYSICAL REVIEW B VOLUME 12, NUMBER 11 1 DECEMBER 1975

Calculation of the M_{23} magneto-optical absorption spectrum of ferromagnetic nickel

J. L. Erskine*
Department of Physics, University of Illinois, Urbana, Illinois 61801

E. A. Stern†
Department of Physics, University of Washington, Seattle, Washington 98195
(Received 28 April 1975)

Experimental observation -> 1987


VOLUME 58, NUMBER 7 PHYSICAL REVIEW LETTERS 16 FEBRUARY 1987

Absorption of Circularly Polarized X Rays in Iron

G. Schütz, W. Wagner, W. Wilhelm, and P. Kienle[(a)]
Physik Department, Technische Universität München, D-8046 Garching, West Germany

R. Zeller
Institut für Festkörperforschung der Kernforschungsanlage Jülich, D-5175 Jülich, West Germany

and

R. Frahm and G. Materlik
Hamburger Synchrotronstrahlungslabor am Deutschen Elektronen-Synchrotron DESY, D-2000 Hamburg 52, West Germany
(Received 22 September 1986)

Polarization-dependent absorption of circularly polarized x-rays by magnetic materials (magnetic atoms)

- **Element-specific magnetic contrast**
- **Spin and orbital moment selectivity**
- **Very high sensitivity**

- X-ray techniques can be transferred into it's magnetic counterpart, by tuning the x-ray energy to a corresponding XMCD sensitive edge: microscopy, spectroscopy, diffraction, reflectometry, small-angle scattering, etc.

INTRODUCTION

X-ray magnetic circular dichroism (XMCD)

Circular dichroism - a tool to study ferro(ferri)magnets

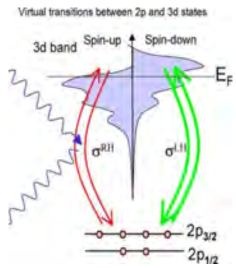

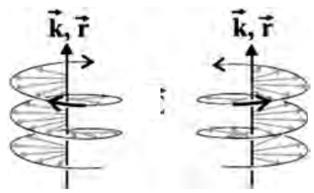

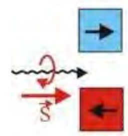

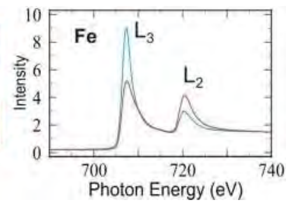

$$I(z) = I_0\, e^{-\mu_x z}$$

where μ is material-specific coefficient dependent on photon energy

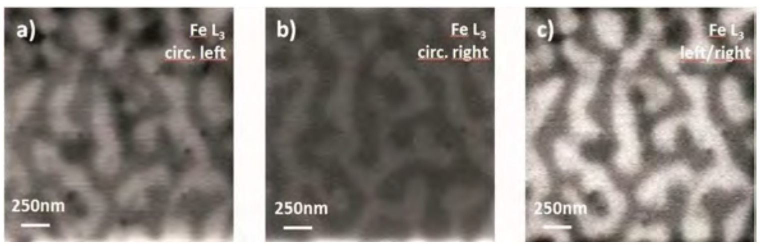

XMCD microscopy and scattering

IEEE Trans. on Magn. 2015, 51, 2 https://www-ssrl.slac.stanford.edu/stohr/

INTRODUCTION

X-ray magnetic linear dichroism (XMLD)

Linear dichroism - a tool to study antiferromagnets

- XMLD is sensitive to the antiferromagnetic order: spin orbit coupling breaks spherical symmetry of the charge density
- XMLD is quadratic to magnetization
- Similarly to XMCD allows to employ magnetic and element-selective imaging

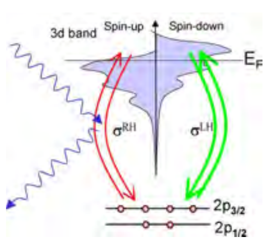

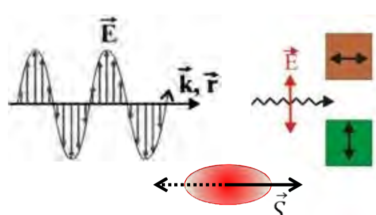

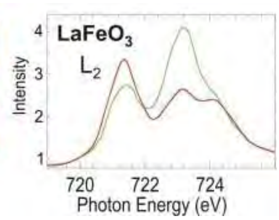

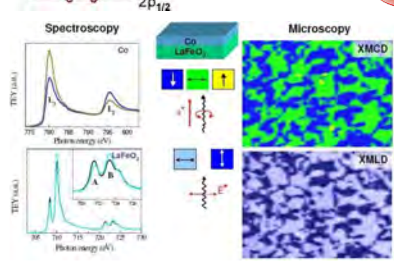

$$I(z) = I_0\, e^{-\mu_x z}$$

XMLD microscopy and scattering on AFM

https://www-ssrl.slac.stanford.edu/stohr/
http://xraysweb.lbl.gov/peem2

INTRODUCTION

X-ray resonant magnetic scattering (XRMS)

- Same transition is used to observe resonant scattering and diffraction: $L_{2,3}$ edges of TM correspond to soft x-rays in the energy range of 480 – 950 eV, λ ~ 15-20 Å
- Resonant x-rays allow both reciprocal (scattering) and real-space (imaging)

Thickness: transmission vs magnetic scattering intensity

$I_{mag} \sim M^2 = (\mu A z)^2$

$I_{trans} = I_0 exp(-l_{att} z)$

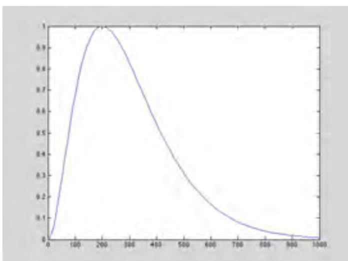

charge magnetic

$$f^n = (\hat{e}_n \cdot \hat{e}'_n) f_c^n + (\hat{e}_n \times \hat{e}'_n) \cdot M^n f_{m1}^n + (\hat{e}_n \cdot M^n)(\hat{e}'_n \cdot M^n) f_{m2}^n$$

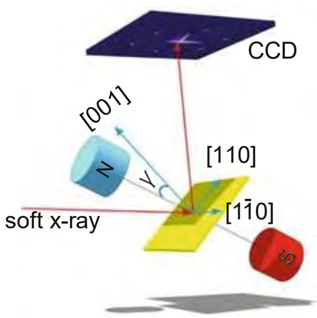

Zhang, S. L., Nat Comm. 8.1 (2017)

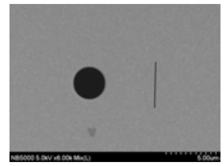

$\frac{\sigma_m}{\sigma_c} \sim 10^{-2}$

charge magnetic

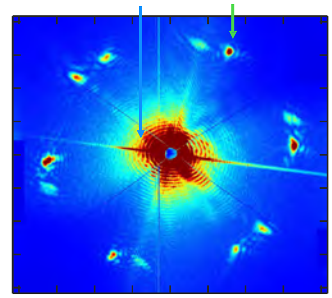

V.U., unpublished

INTRODUCTION

Polarized synchrotron x-rays

Polarised synchrotron radiation by bending magnets and insertion devices (IDs)

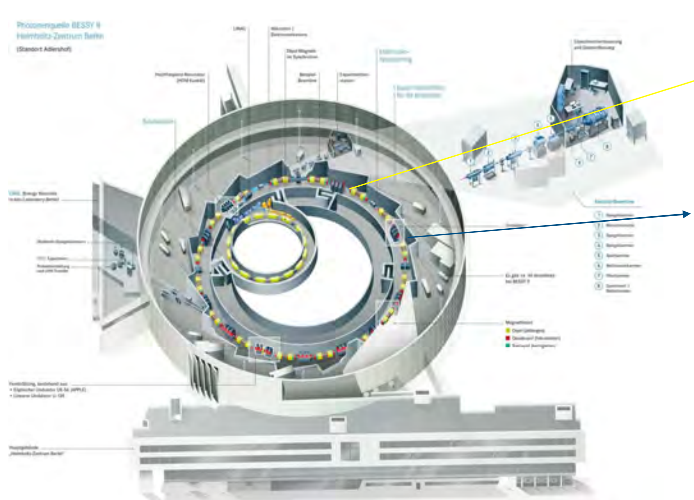

https://www.helmholtz-berlin.de

bending magnet

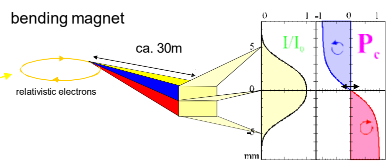

Circular +

Linear horizontal

Circular -

Controlled by the beamline optics

undulator

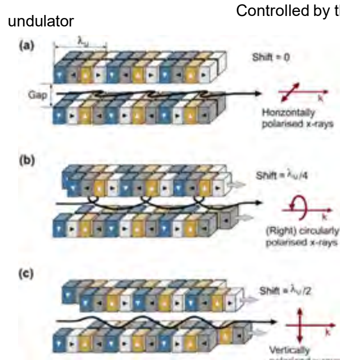

Circular, elliptic any linear angle, in principle controlled by the undulator

~1000 higher brilliance

C.Schmitz-Antoniak,Rep.Prog.Phys.78(2015)06250

INTRODUCTION

X-ray optics

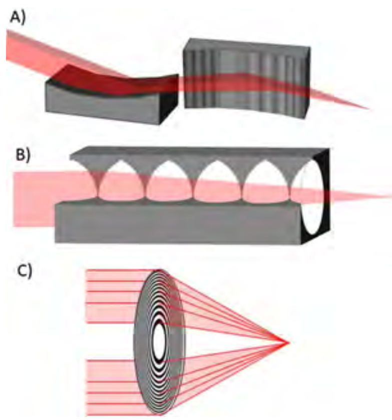

(A) Kirkpatrick–Baez (KB) mirror system

Diffraction, spectroscopy, etc.

(B) compound refractive lenses (CRL)

High energy x-rays

(C) Fresnel zone-plates (FZP)

Microscopy, nano-spectroscopy

X-ray Optics	CRLs	Fresnel ZP	KB Mirrors
ZP-equivalent Numerical Aperture (based on outermost zone, smaller is better)	30 nm	30 nm	16 nm
Achievable Focus Resolution (Typical Value | Best Possible)	Very High (1 µm | <30 nm)	Very High (200 nm | 10 nm)	Very High (1 µm | 20 nm)
Handling/Ease of Alignment (Compact)	✓	✓	✗
Achromatic	✗	✗	✓
Working Distance Range Selection	5 mm – 10's m	1 mm – 30 mm	10 cm – 10's m
Efficiency	~50%	~10%	~75%
In-line with Beam	✓	✓	✗
Price (including beamline costs & motion control systems)	Depends	High	Mid to High (long beamline & stability needs)

Cotte, M., et al., Comptes Rendus Physique 19.7 (2018): 575-588

https://www.sigray.com/

INTRODUCTION

X-ray optics

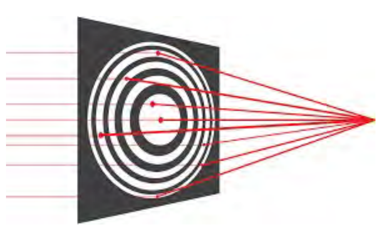

Alternate 'zones' modify phase/amplitude of incident wavefront:
for material of thickness (t), wavelength (λ), refractive index (1-δ-iβ), the phase shift Δφ, is: $\Delta\varphi = 2\pi\delta t/\lambda$

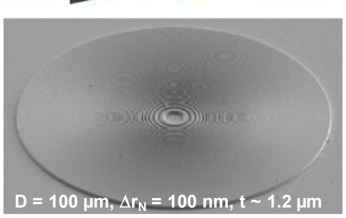

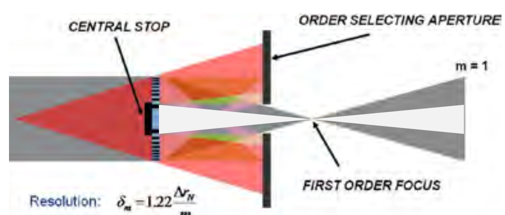

Resolution: $\delta_m = 1.22\frac{\Delta r_N}{m}$

Focal length: $f_m = \frac{D\,\Delta r_N}{m\,\lambda}$

Working distance is 0.5 - 1.5 mm depending on the ZP and the x-ray wavelength

λ (nm)	Material	δ	β	Thick[†] (nm)	Transmission
13.5	Ru	0.113	0.017	59.7	0.38
13.5	Mo	0.076	0.0064	88.8	0.59
0.155 (8 keV)	Si	7.67e-6	1.77e-7	10000	0.86
0.155 (8 keV)	Au	4.77e-5	4.96e-6	1600	0.52

http://zoneplate.lbl.gov/theory

Barrett, R., X-ray Optics for Synchrotron Radiation Beamlines (ESRF)

INTRODUCTION

X-ray detection

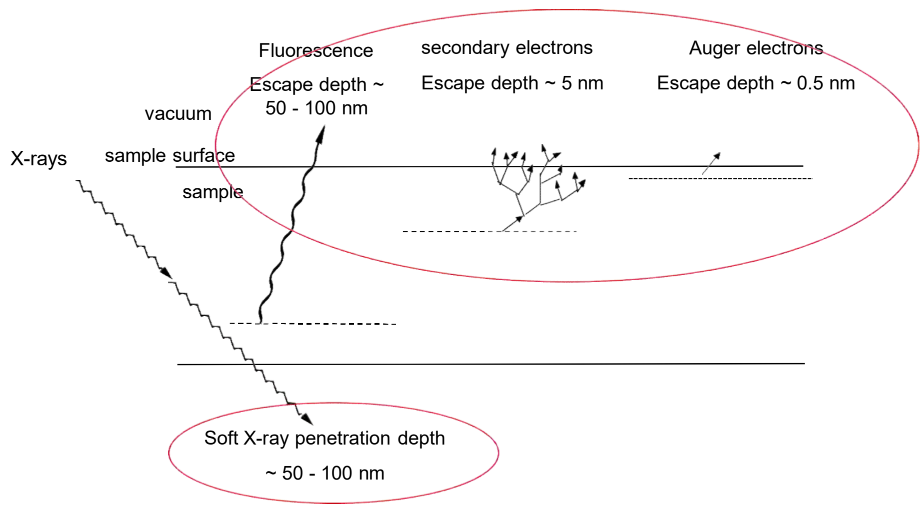

Transmission x-ray microscopy (TXM), scanning TXM, holography, coherent diffraction imaging, ptychography, etc.

TECHNIQUES

X-ray photoemission electron microscopy (PEEM)

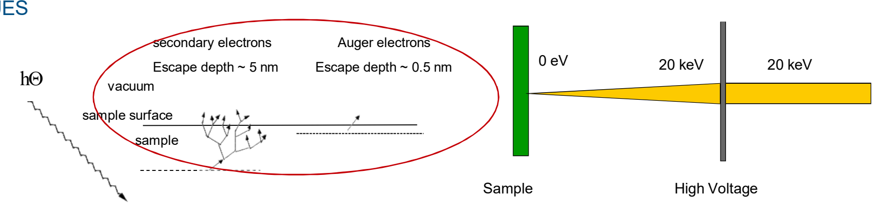

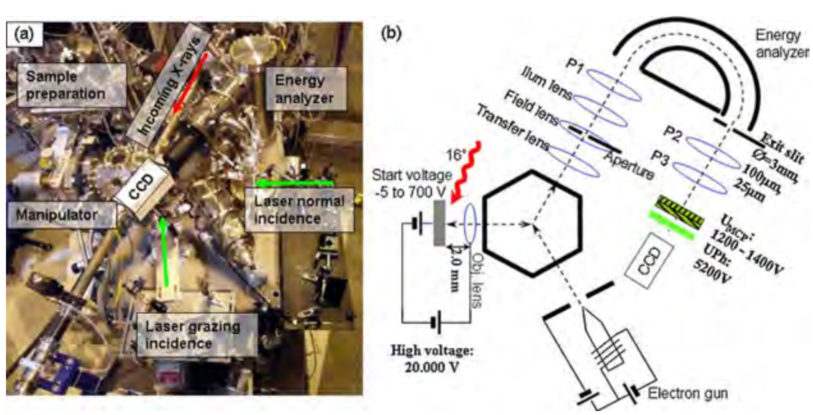

L. Le Guyader et al., Journal of Electron Spectroscopy and Related Phenomena 185 (2012)

TECHNIQUES

X-ray photoemission electron microscopy (PEEM)

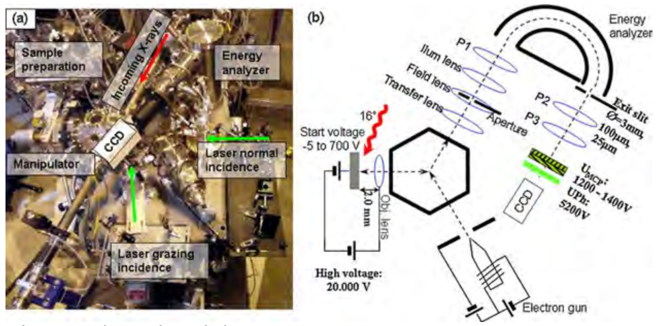

Aperture size and resolution

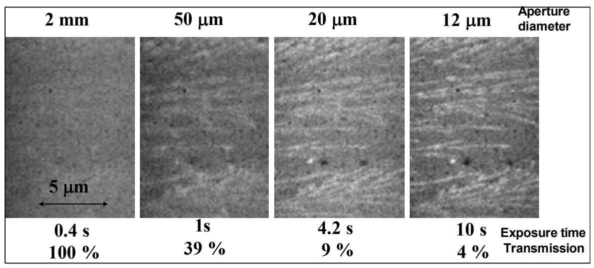

Aberration correction allows to push the resolution down to a few nm

L. Le Guyader et al., Journal of Electron Spectroscopy and Related Phenomena 185 (2012)

TECHNIQUES

X-ray photoemission electron microscopy (PEEM)

Magnetic domains

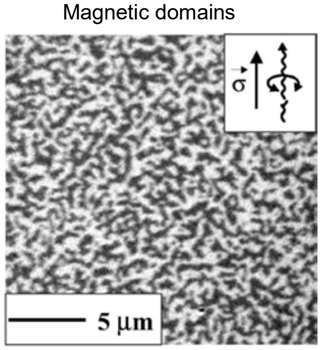

FM (0.7 nm Co) AFM ($LaFeO_3$)

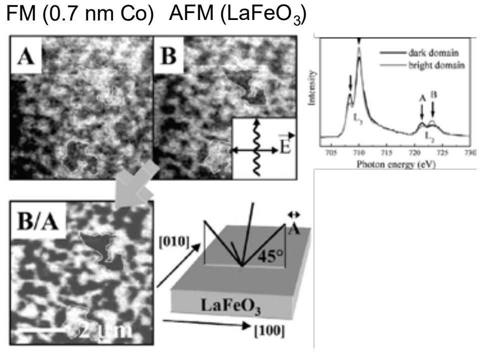

A. Scholl / Current Opinion in Solid State and Materials Science 7 (2003) 59–66

Artificial spin ice

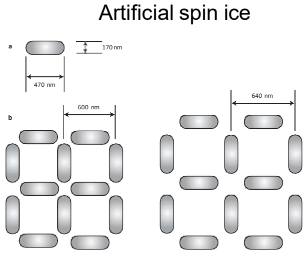

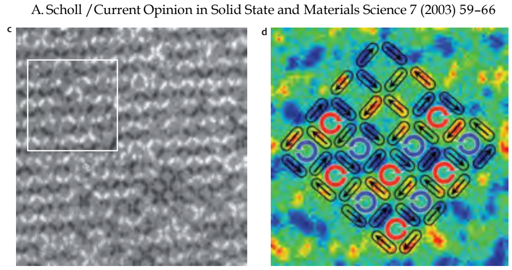

Kapaklis, V., et al. Nature nanotechnology 9.7 (2014): 514.

TECHNIQUES

X-ray photoemission electron microscopy (PEEM)

Vector mapping of magnetization

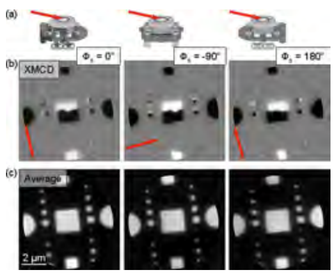

$I_{XMCD} = (I_{0^+} - I_{0^-})/(I_{0^+} + I_{0^-}) = \mathbf{M} \cdot \mathbf{K} = |\mathbf{M}| \cos(\,)$

Patterned FiM GdFeCo nanostructure

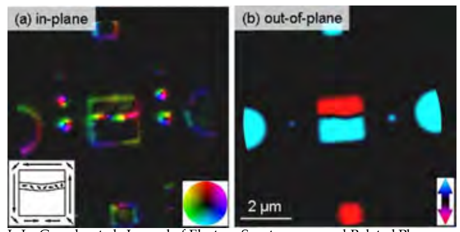

L. Le Guyader et al., Journal of Electron Spectroscopy and Related Phenomena 185 (2012)

Topological AFM vortices in a-Fe2O3/Co

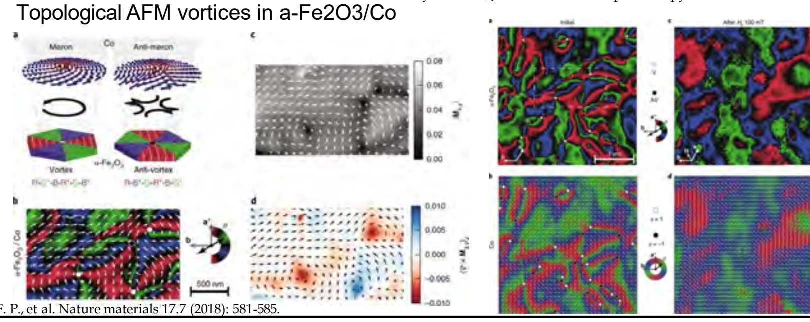

Chmiel, F. P., et al. Nature materials 17.7 (2018): 581-585.

TECHNIQUES

Transmission x-ray microscopy

Beamline layout (MISTRAL, ALBA, Spain)

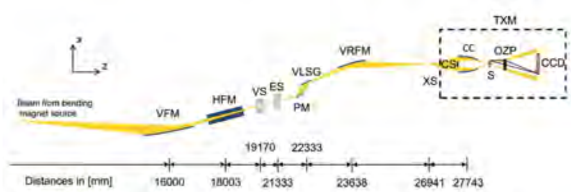

Full-field image measured by a 2D detector

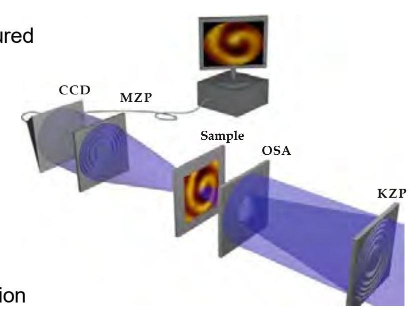

~10 nm spatial resolution

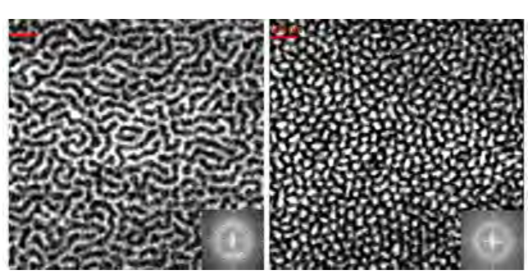

XMCD contrast in transmission

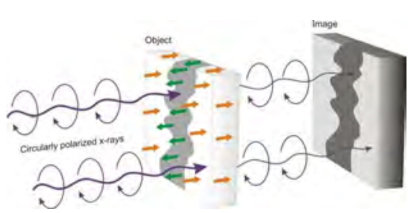

Sorrentino, A, et al., J. Synchrotron Rad. (2015). 22, 1112-1117

TECHNIQUES

Scanning transmission x-ray microscopy

Beamline layout (PolLux, Swiss Light Source, PSI)

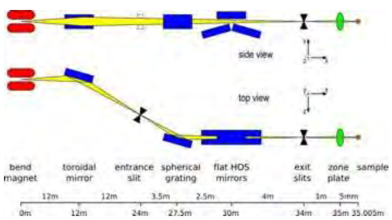

STXM scheme

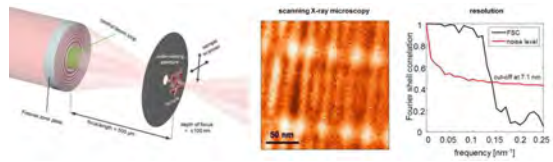

Roesner, B, et al., Optica 7, 11, 1602 (2020)

7 nm is the highest resolution achieved

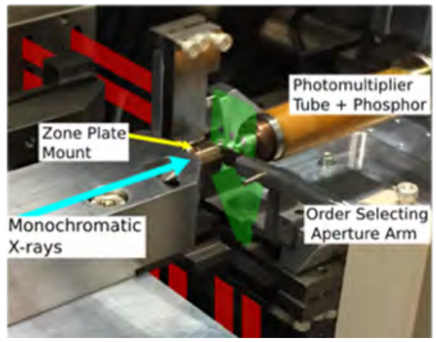

XMCD contrast in transmission

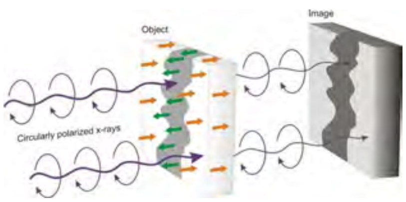

TECHNIQUES

Scanning transmission x-ray microscopy

XMCD contrast in transmission

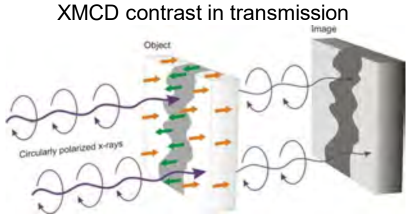

Need thin samples!

https://henke.lbl.gov/optical_constants/

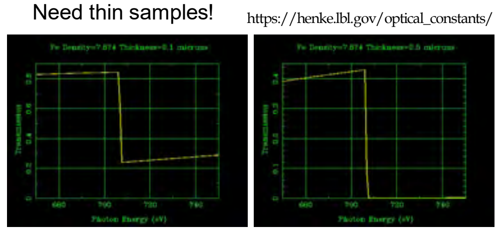

Transparent Si_3N_4 membranes

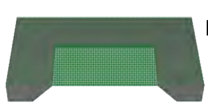

FeGd multilayer grown on Si_3N_4

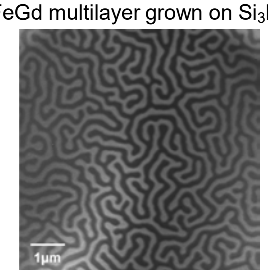

Film deposition

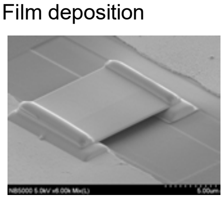

Single crystal plate

IEEE Trans. on Magn. 2015, 51, 2

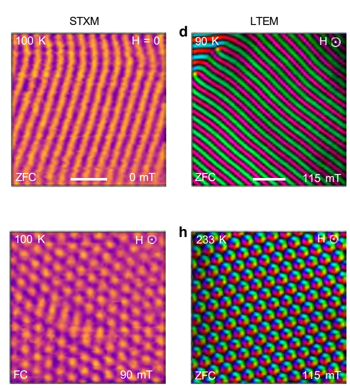

Cryogenic imaging →

Birch, M., et al., Nat Comm. 11(1), 1 (2020).

TECHNIQUES

Phase problem

- X-ray scattering factor: $f^n = f^c - i f_1^m$ is **complex**
- Scattering is a Fourier transform of the real-space density, but the measured intensity $I = |F(f^n)|^2$ is **real**

charge *magnetic*

f^n ¼ ðe_n · $e_n^{\prime}$Þf_c^n þ ðe_n X $e_n^{\prime}$Þ · $M^n f_{ml}^n$
þ ðe_n · M^nÞð$e_n^{\prime}$ · M^nÞf_{m2}^n:

- Coherence-based methods allow to solve the phase problem and reconstruct the real-space image
- Coherent diffraction imaging, holography, ptychography, interferometry, etc.

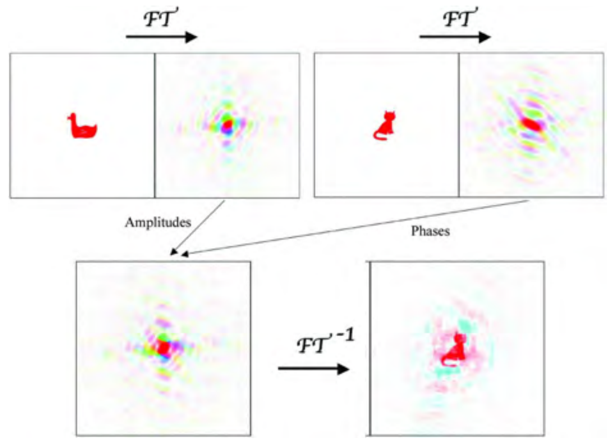

Taylor, G. (2003). Acta Cryst. D59, 1881-1890.

TECHNIQUES

Coherent x-ray scattering / imaging

- X-ray scattering factor: $f^{res} = f^c - i f_1^m$ is **complex**
- Measured intensity $I = |F(f^{res})|^2$ is **real**

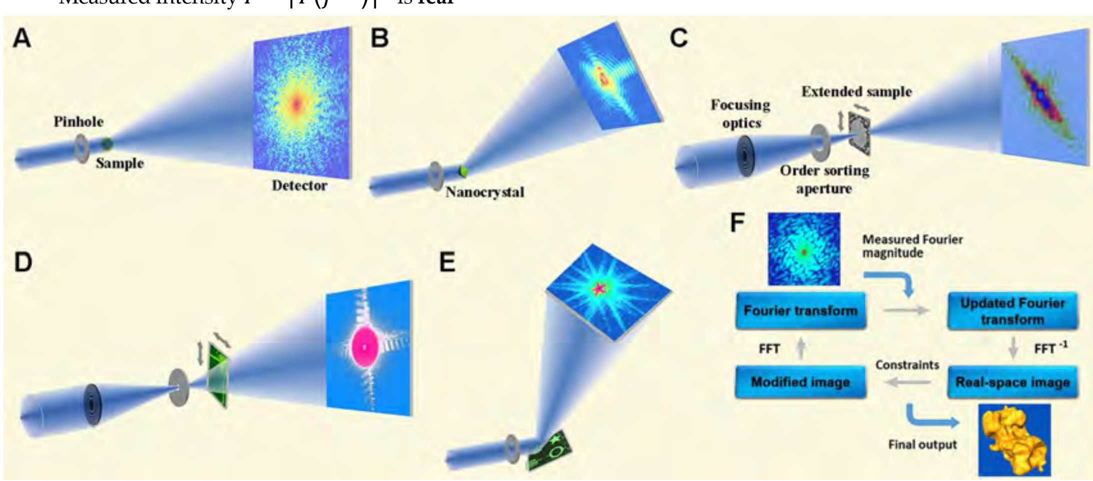

- Coherence-based methods allow to solve the phase problem and reconstruct the real-space image
- Coherent diffraction imaging, holography, ptychography, etc.

http://www.physics.ucla.edu/research/imaging/research_CDI.html

TECHNIQUES

Coherent x-ray scattering / imaging

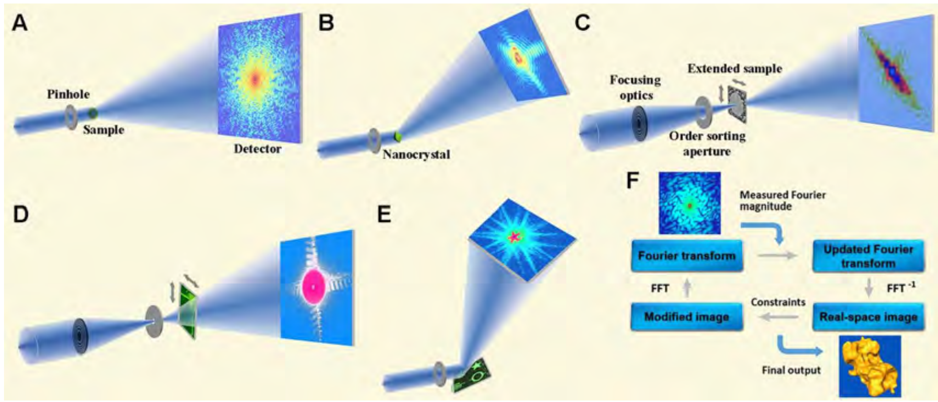

More detailed lectures on coherence-based technique are available at LINXS CoWork channel:

1) Introduction to CDI by Prof. Pablo Villanueva-Perez, https://www.youtube.com/watch?v=RnBnwaYpgk8

2) CDI principles and algorithms by Dr. Tomas Ekeberg, https://www.youtube.com/watch?v=N3bbGsEApzE

3) Bragg CDI by Dmitry Dzhigaev, https://www.youtube.com/watch?v=jiY9e4pl2t0

4) Ptychography by Virginie Chamard, https://www.youtube.com/watch?v=LEfmq1afQo8

5) Algorithms in Bragg CDI by Prof. Ian Robinson, https://www.youtube.com/watch?v=MabspCO3yUs

TECHNIQUES

Coherent x-ray scattering / imaging

- Measured intensity $I = |F(f^{res})|^2$
- Iterative phase retrieval can be used is the sample size is smaller than the coherent size of the beam (oversampling ratio σ>2)

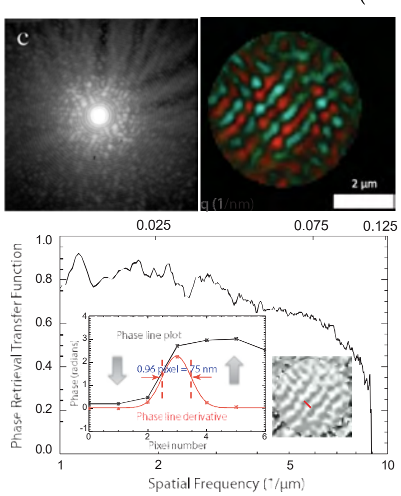

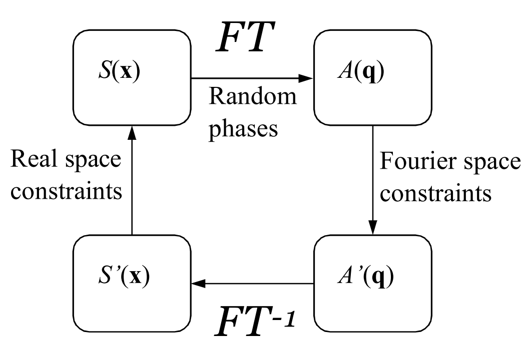

$$\mathrm{PRTF}(\mathbf{u}) = \frac{|F_{\mathbf{u}}\gamma_M|}{\sqrt{I(\mathbf{u})}} = \frac{|\langle f_M(\mathbf{u})\exp(i\varphi_0)\rangle|}{\sqrt{I(\mathbf{u})}}$$

Real-space resolution estimated from PRTF d<50 nm (~ 30-40 nm) without focusing optics

Turner, J., et al., PRL 107.3 (2011): 033904.

Marchesini, S., et al., Physical Review B 68.14 (2003): 140101.

TECHNIQUES

Coherent x-ray scattering / imaging

- Measured intensity $I = |F(f^{res})|^2$
- Iterative phase retrieval can be used is the sample size is smaller than the coherent size of the beam (oversampling ratio σ>2)

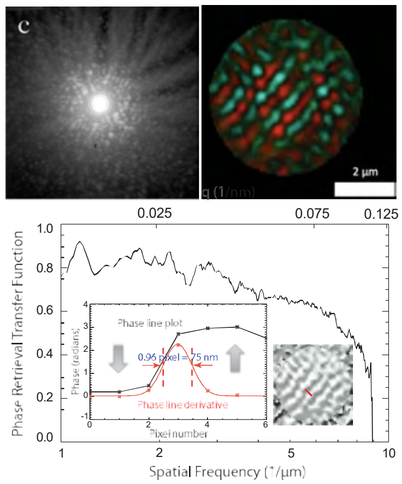

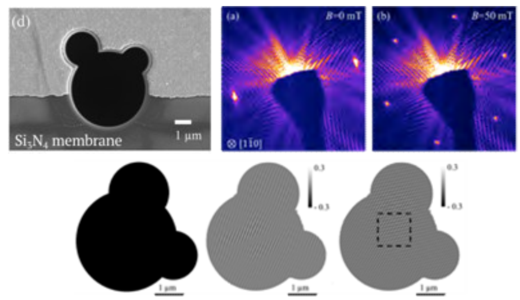

Estimate of the resolution is given by the frequency at which the PRTF reaches a value of 0.5.

Ukleev, V., et al., Quant. Beam. Sci. 2 (2018)

$$\mathrm{PRTF}(\mathbf{u}) = \frac{|\langle F_{\mathbf{u}} \rangle_M|}{\sqrt{I(\mathbf{u})}} = \frac{|\langle \rho_M(\mathbf{u}) \exp(i\phi_0) \rangle|}{\sqrt{I(\mathbf{u})}}$$

Real-space resolution estimated from PRTF d<50 nm (~ 30-40 nm) without focusing optics

Turner, J., et al., PRL 107.3 (2011): 033904.

Marchesini, S., et al., Physical Review B 68.14 (2003): 140101.

TECHNIQUES

Fourier transform holography

- Phase problem can be solved with the amplitude modulation by a reference wave:

$$\mathcal{F}^{-1}\left[|F(u,v)|^2\right] = f \otimes f = o \otimes o + r \otimes r + o \otimes r + r \otimes o,$$

Real-space reconstruction via single Fourier transform

Charge and magnetic contrast separation:

! = |$%|& + |$(|& +)$%$(! = |$%|& + |$(|& −)$%$(! = 2)$%$(

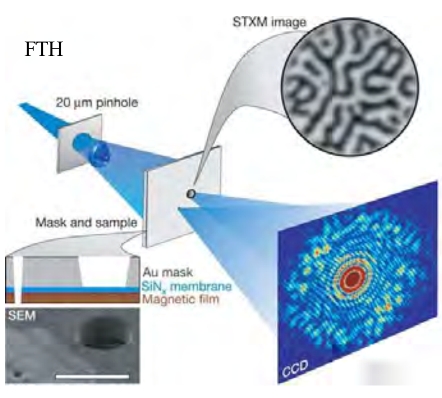

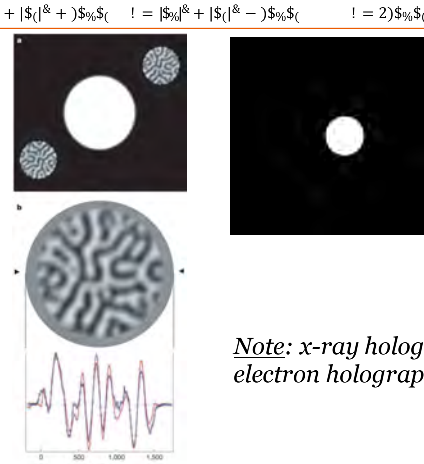

Note: x-ray holography ≠ electron holography

Fourier transform holography (FTH) with a reference hole is limited by the intensity/resolution ratio

TECHNIQUES

Fourier transform holography and HERALDO

- Phase problem can be solved with the amplitude modulation by a reference wave:

The phase is encoded in the interference pattern (object and reference)

$$\mathcal{F}^{-1}\left[|F(u,v)|^2\right] = f\otimes f = o\otimes o + r\otimes r + o\otimes r + r\otimes o,$$

Derivative of the step function is two delta functions

$$L^{(n)}\{f\otimes f\} = \frac{1}{2}(-1)^n\left[A^* r(x+x_0, y+y_0) + r\otimes g\right] + \frac{1}{2}\left[Ar^*(x_0-x, y_0-y) + g\otimes r\right] + L^{(n)}\{o\otimes o\} + (-1)^n o\otimes g + g\otimes o + (-1)^n A^* o(x+x_0, y+y_0) + Ao^*(x_0-x, y_0-y)$$

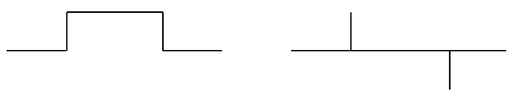

Reference slit can improve the contrast compared to reference hole without loosing the resolution

Guizar-Sicairos, M. and Fienup, J.R., 2007. Holography with extended reference by autocorrelation linear differential operation. Optics express, 15(26), pp.17592-17612.

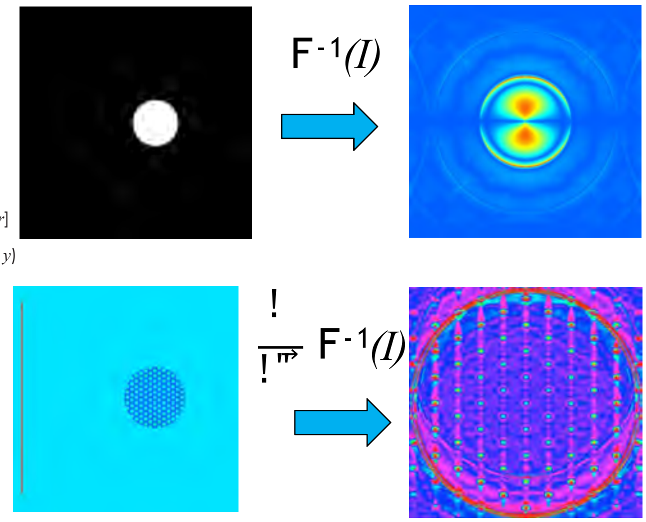

Fourier transform holography (FTH) with a reference hole is limited by the intensity resolution ratio

TECHNIQUES

Holography with extended reference (HERALDO)

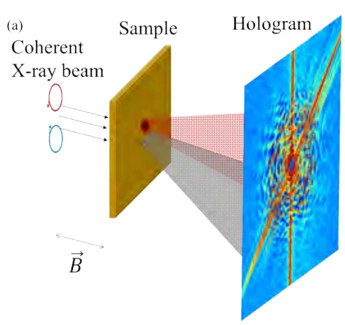

HERALDO slit separation conditions simulation

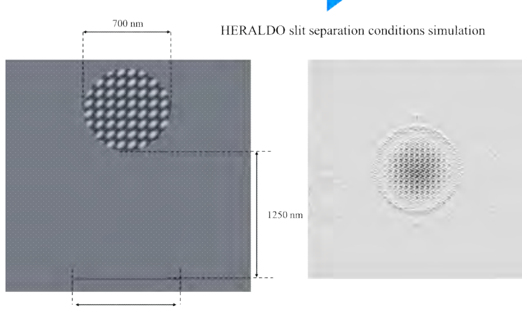

HERALDO example: skyrmion host $Co_8Zn_8Mn_4$

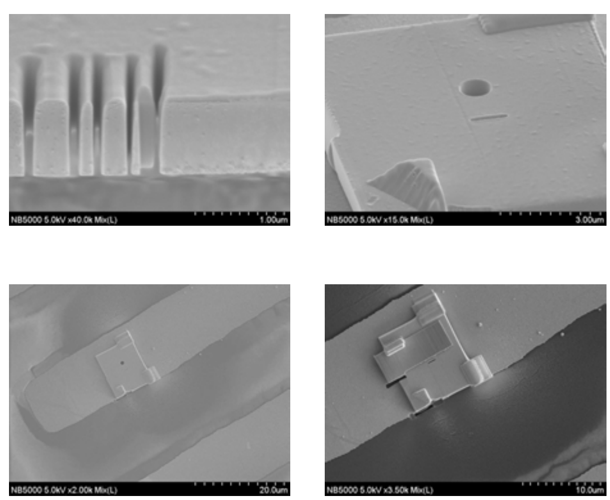

Aperture size: d=700 nm
Slit size:
w=0.04 µm, l=1 µm

Ukleev, V., et al. PRB, 99.14 144408 (2019)

TECHNIQUES

Holography with extended reference (HERALDO)

- Phase problem can be solved with the amplitude modulation by a reference wave:

$$\mathcal{F}^{-1}\left[|F(u,v)|^2\right] = f\otimes f = o\otimes o + r\otimes r + o\otimes r + r\otimes o,$$

Real-space reconstruction via Fourier transform an linear differential operator (HERALDO)

No compromise between the contrast and resolution

HERALDO example: $Co_8Zn_8Mn_4$

! = |$%|& + |$(|& +)$%$(! = |$%|& + |$(|& −)$%$(! = 2)$%$(

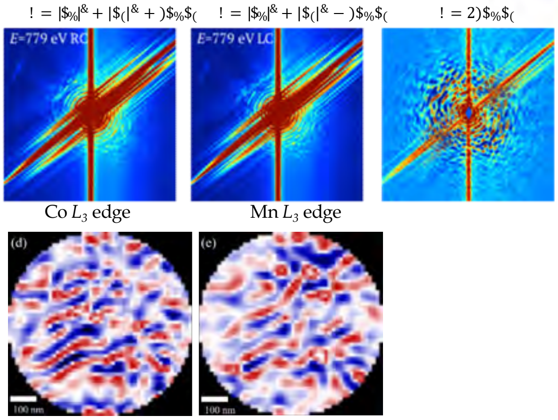

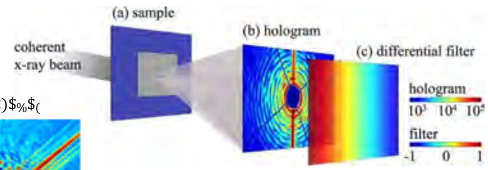

$$\frac{d}{dX}\{t\otimes t\} = C + \frac{d}{dX}\{o\otimes r\} + \frac{d}{dX}\{r\otimes o\} = C + (-o)\otimes\frac{d}{dX}\{r\} + \frac{d}{dX}\{r\}\otimes o$$

$$\rightarrow \frac{d}{dX}\{t\otimes t\} = C - o_{(X+a)} + o_{(X+b)} + cc$$

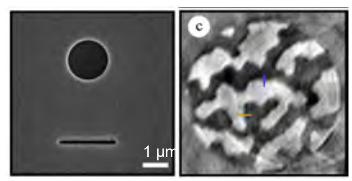

Ukleev, V., et al. PRB, 99.14 144408 (2019)

Duckworth, T. A., (2011). Optics express, 19(17), 16223-16228.

TECHNIQUES

X-ray ptychography

Taking coherent scattering patterns from overlapping regions using FZP

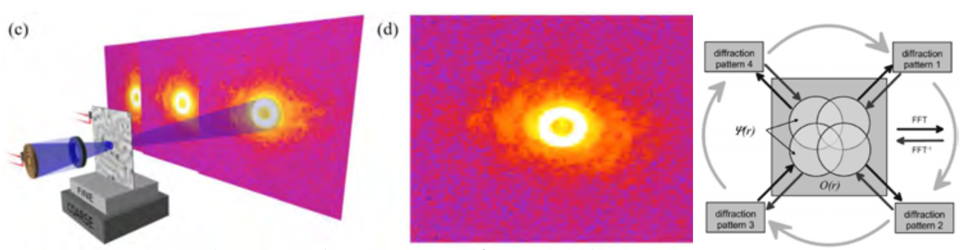

15 nm real-space resolution imaging of magnetic domains in $SmCo_5$

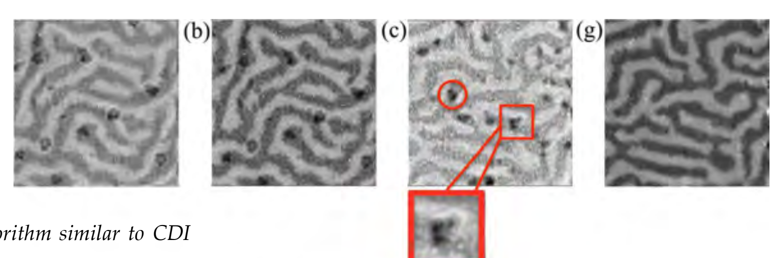

- *Reconstruction algorithm similar to CDI*
- *Ptychography can be used to study* ***extended objects***

Shi et al. Appl. Phys. Lett. 108, 094103 (2016)

TECHNIQUES

X-ray holography in reflection

Holographic mask is placed after reflected beam

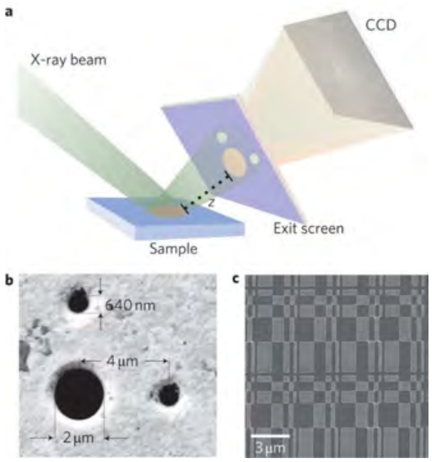

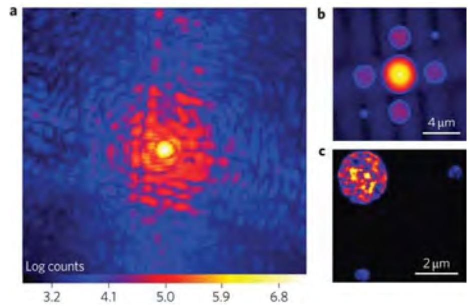

SEM reconstruction

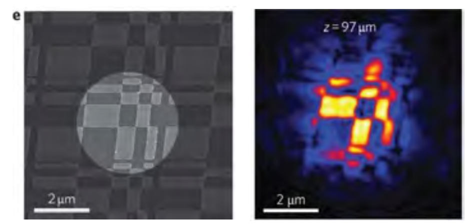

- *So far only demonstrated only for charge patterns…*
- *Ptychography is also possible*
- *~60 nm resolution*

S. Roy et al. Nature Photonics 5, 243–245(2011)

TECHNIQUES

X-ray imaging in three dimensions

Hard x-ray resonant tomography (Gd L_3 edge)

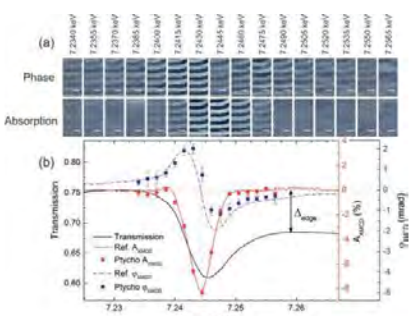

Magnetic contrast variation across the edge

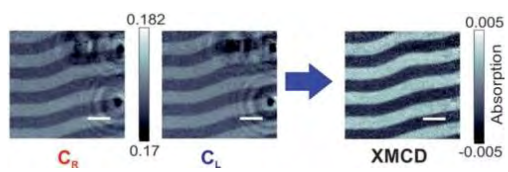

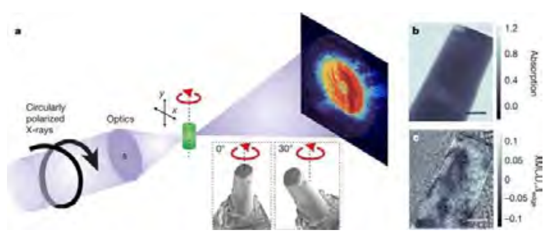

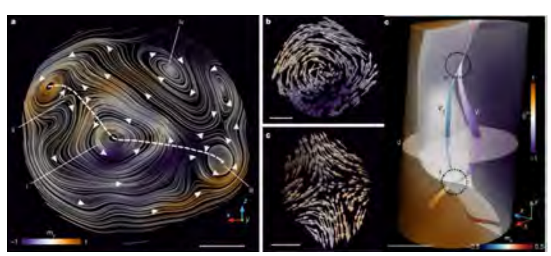

- *High energy allows transmission of a few tens µm*
- *Ptychographic scans are measured for multiple projections to reconstruct 3D magnetization vector distribution*

Donnelly, C., et al., Phys. Rev. B 94, 064421 (2016)

Donnelly, C., et al., Nature 547, 328–331(2017)

TECHNIQUES

X-ray imaging in three dimensions

Soft x-ray resonant laminography (TM L_3 edge or RE M-edge)

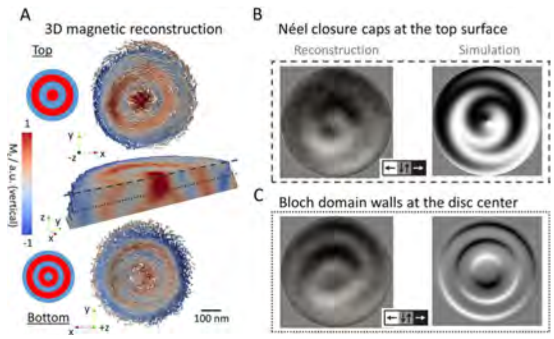

Reconstruction of the magnetic structure of a permalloy nanodisc

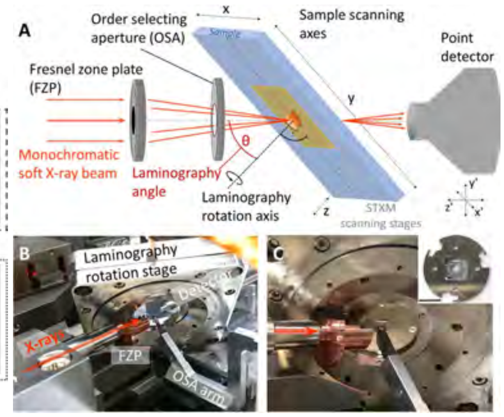

- *Naturally thin or nanofabricated samples*
- *Multiple projections to reconstruct 3D magnetization vector distribution measured with single rotation axis*
- *Challenging to introduce complex sample environment*

Witte, K., et al., Nano Lett., 20, 1305−1314 (2020)
Hierro-Rodriguez, A., et al., Nat. Comm., 11, 6382 (2020)

Great talk by Claire Donnely on 3D imaging (LINXS seminar)
https://www.youtube.com/watch?v=K4jQlE0HaHs

TECHNIQUES

Time-resolved imaging

Stroboscopic pump-probe imaging: synchronized x-ray and excitation pulses (magnetic field, laser pulses, etc.)

Sub-100 ps imaging of *periodic* phenomena
PEEM, STXM, holography, 3D methods, etc.

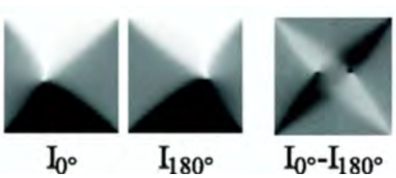

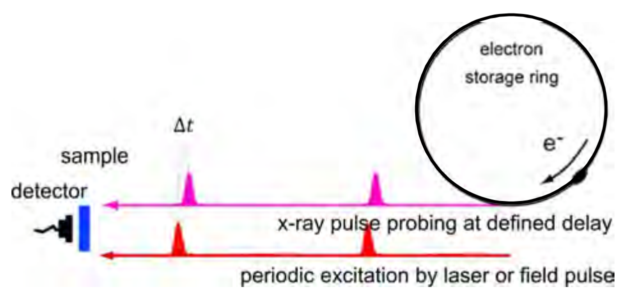

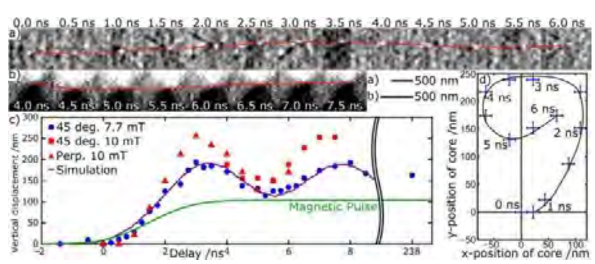

Stevenson, S. E., et al., PRB 87.5: 054423.(2013)
Bukin, N., et al.., Sci. Rep.: 6, 36307 (2016)

TECHNIQUES

Time-resolved imaging

Time resolution is limited by the pulse duration
Need high-flux x-ray source with fs pulses to study spin dynamics at atomic scales:
x-ray free-electron laser

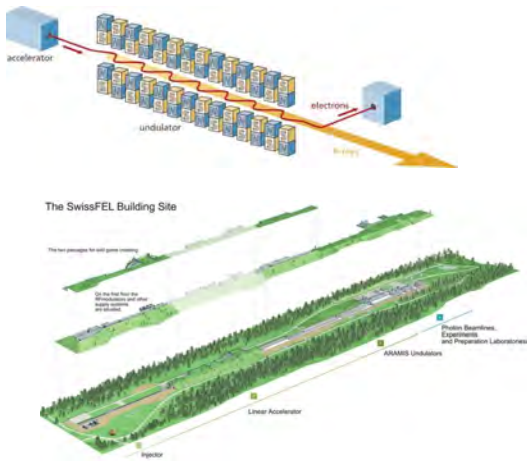

https://www.psi.ch/en/swissfel

Please, watch this (5min) movie about SwissFEL
https://www.youtube.com/watch?v=P2CG69hRYR8

TECHNIQUES

Time-resolved imaging

Time resolution is limited by the pulse duration
Need high-flux x-ray source with fs pulses to study spin dynamics at atomic scales:
x-ray free-electron laser

XFEL experiment@LCLS: single-shot imaging

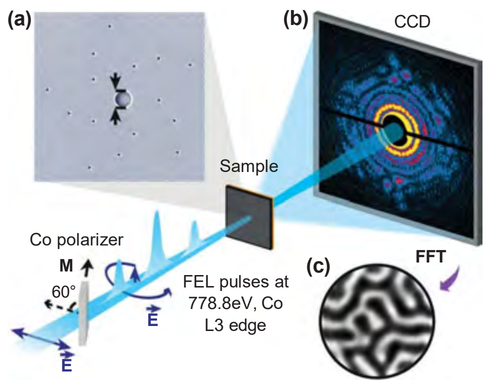

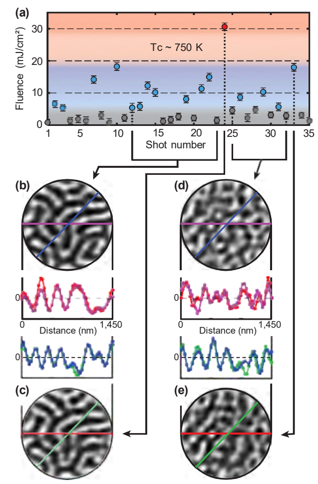

Damage of the spin structure by the pulses longer than 80 ps! -> non-linear interaction of x-rays with electronic order

Wang, T., et al., PRL 108, 267403 (2012)

TECHNIQUES

Time-resolved imaging

Time resolution is limited by the pulse duration
Need high-flux x-ray source with fs pulses to study spin dynamics at atomic scales:
x-ray free-electron laser

Synchrotron-based FTH imaging:

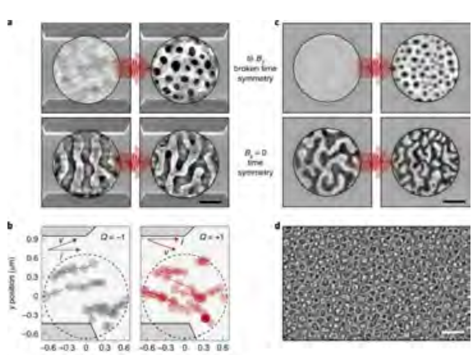

XFEL SAXS experiment

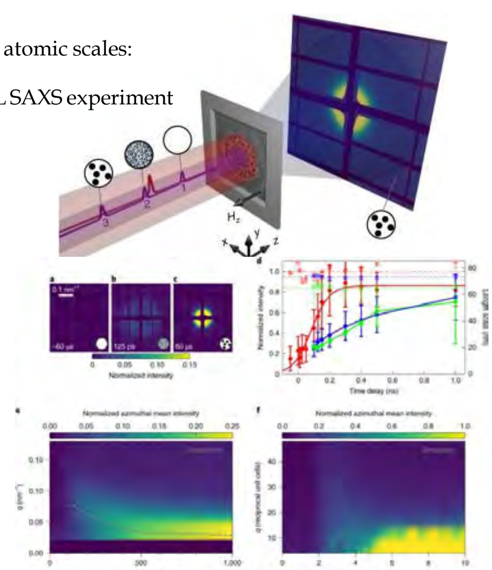

Nucleation of magnetic skyrmions by optical laser pulses: time scale >10 ps

Büttner, F., et al. Nature Materials 20, 30–37 (2021)

SUMMARY

Comparison to other magnetic imaging techniques

Method	Probe	Spatial resolution	Temporal resolution	Magnetization direction	Sample type	Instrument type
Kerr microscopy	Optical photons	Fair (>300 nm)	Very good (fs)	Any	Surface (Kerr) Thin film (Faraday)	Lab.
Lorentz TEM (+DPC, holography, etc.)	Electrons	Very good (<10 nm)	Good (ps)	In-plane	Thin film	Lab.
MFM	Cantilever	Good (10-100 nm)	Bad (min)	Out-of-plane	Surface	Lab.
Neutron imaging	Neutrons	Bad (μm)	Bad (min)	Any	Bulk	Neutron source
PEEM	**X-rays + Electrons**	**Good (10-100 nm)**	**Good (ps)**	**Out-of-plane (NI) In-plane (GI)**	**Surface**	**Synchrotron**
STXM (+ holography, ptychography, etc.)	**X-rays**	**Good (10-100 nm)**	**Good (ps)**	**Out-of-plane**	**Thin film 'thinned bulk' <1 μm**	**Synchrotron**

SUMMARY

Where?

Lightsources of the World

SUMMARY

Where?

…and of Europe

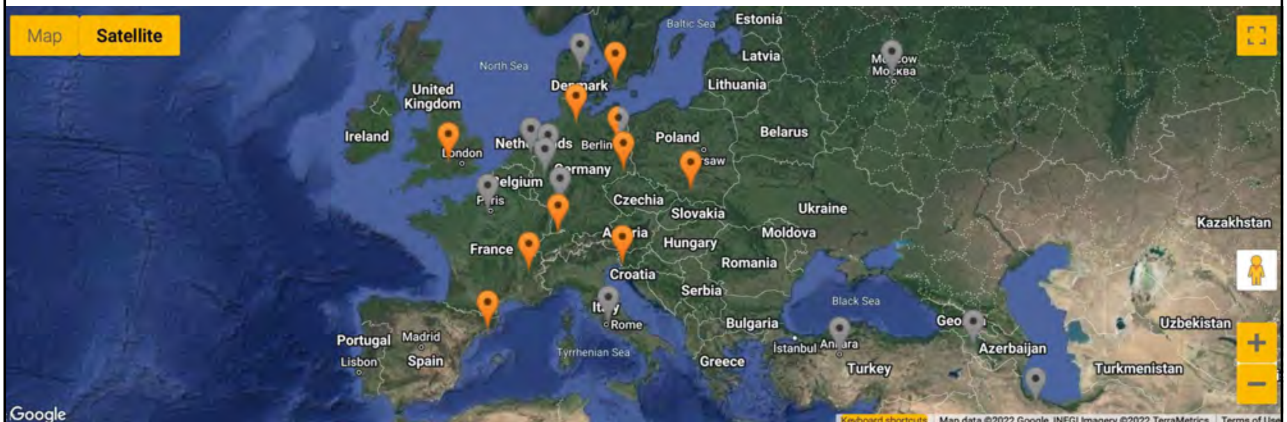

https://www.wayforlight.eu/

SUMMARY

When?

Facility	Deadline
CHESS (USA)	2022/12/20
Pohang XFEL (Korea Rep.)	2022/12/31
Canadian Light Source (Canada)	2022/12/31
European XFEL (Germany)	2022/12/29
MAX IV (Sweden)	2023/02/28
ESRF (France)	2023/03/01
PETRA-III (Germany)	2023/03/01
BESSY-II (Germany)	2023/03/01
APS (USA)	2023/04/17
SwissFEL (Switzerland)	2023/06/30
ALS (USA)	2023/07/31
SLS (Switzerland)	to be announced (SLS 2.0 upgrade is upcoming)

Committee decision ~2-3 months after the proposal submission deadline
Beamtime ~4-12 months after the proposal submission deadline

https://lightsources.org/for-users/proposal-deadlines/

SUMMARY

Beamlines (example)

Method	Beamline	Facility	Energy range	Magnetic field	Temperature range
PEEM	SIM SPEEM@UE49-PGM I06 CIRCE HERMES	SLS PSI, Switzerland BESSY II, Germany Diamond, UK ALBA, Spain SOLEIL. France	90-2000 eV 100-1800 eV 100-1300 eV 100-2000 eV 70-2500 eV	~100 mT ~100 mT available available available	120-800 K 45-600 K 100-1900 K 100-1500 K 150-2000 K
TXM	MISTRAL SPEEM@UE41-PGM	ALBA, Spain BESSY II, Germany	270-1200 eV 180-2800 eV	2 mT no	105-300 K 100-300 K
STXM	POLLUX HERMES MAXYMUS	SLS PSI, Switzerland SOLEIL. France BESSY II, Germany	250-1600 eV 70-2500 eV 200-1900 eV	200 mT 20 mT 250 mT	280-400 K 150-600 K 30-350 K
Holography / coherent diffraction imaging in transmission	ALICE-2 COMET@SEXTANTS MaReS@BOREAS	BESSY II, Germany SOLEIL, France ALBA, Spain	depends on beamline 50-1700 eV 50-4000 eV	700 mT 1000 mT 2000 mT	10-350 K 30-800 K 20-400 K

https://www.wayforlight.eu/

SUMMARY

Summary

- Real-space imaging of magnetization down to (sub)10 nm is possible using resonant x-rays
- Element selectivity is naturally provided
- Complex sample environment (high vacuum, cryogenic temperatures, magnetic fields, optics, etc.)
- Naturally thin or nanofabricated samples or surfaces
- Coherent imaging has great potential to push the resolution to ~1 nm limit
- Three-dimensional imaging is possible
- Time-resolved imaging (sub-100 ps routinely, fs time scale at FELs) is possible

SUMMARY

Further reading/watching

- Fundamentals of magnetic dichroism, sum rules, etc.
  Stöhr, J. "X-ray magnetic circular dichroism spectroscopy of transition metal thin films." Journal of Electron Spectroscopy and Related Phenomena 75 (1995): 253-272.
  van der Laan, G., and Figueroa, A. I.. "X-ray magnetic circular dichroism—A versatile tool to study magnetism." Coordination Chemistry Reviews 277 (2014): 95-129.
- Resonant x-ray scattering
  Fink, J., et al. "Resonant elastic soft x-ray scattering." Reports on Progress in Physics 76.5 (2013): 056502.
  Paolasini, L., and de Bergevin F. "Magnetic and resonant X-ray scattering investigations of strongly correlated electron systems." Comptes Rendus Physique 9.5-6 (2008): 550-569.
- X-ray magnetic imaging
  Fischer, P.. "Magnetic imaging with polarized soft x-rays." Journal of Physics D: Applied Physics 50.31 (2017): 313002.
  Reeve, R. M., et al. "Magnetic imaging and microscopy." Handbook of Magnetism and Magnetic Materials (2020): 1-52.
- Coherence
  Nugent, K. A. "Coherent methods in the X-ray sciences." Advances in Physics 59.1 (2010): 1-99.
  Munro, P. "Coherent x-ray imaging across length scales." Contemporary Physics 58.2 (2017): 140-159.
  LINXS Webinar CoWork series on YouTube https://www.youtube.com/playlist?list=PLoa4trwK2Db7kaHauxrN9KhPYgS44Oo8Y
- Dynamics
  Raftrey, D., and Fischer, P. "Advanced magnetic X-ray spectro-microscopies to characterize mesoscopic magnetic materials." Journal of Magnetism and Magnetic Materials 545 (2022): 168734.

  Huang, N., et al. "Features and futures of X-ray free-electron lasers." The Innovation 2.2 (2021): 100097.

SUMMARY

HZB photon school (with practicals!)

HZB Helmholtz Zentrum Berlin

EPFL

Lorentz Transmission Electron Microscopy: Theory, Practice, Simulations, and Quantitative Phase reconstruction

Thomas LaGrange
Senior Staff Scientist

LUMES

Doctoral Course MSE-670

November 16th, 2022

thomas.lagrange@epfl.ch • www.epfl.ch• cime.epfl.ch• +41 (0)21 6934430

Outline:

Lorentz microscopy has been used extensively for the past 40 years to study magnetic domain structure and magnetization reversal mechanisms in magnetic thin films and elements. Here, a brief introduction to standard image modes in TEM and the theory involved is presented. The second half of lectures is devoted to discussing how the sample's phase shift and magnetic properties can be quantified from the LTEM observations.

1) Lorentz Transmission Electron Microscopy (LTEM)
   - A. Lorentz Force
   - B. LTEM Imaging modes
   - C. Examples
2) Simulation and quantitative analysis
   - A. Modeling magnetic images in a real microscope
   - B. Transport of Intensity Equations (TIE)
   - C. Examples

 thomas.lagrange@epfl.ch • www.epfl.ch• lumes.epfl.ch• +41 (0)21 6935861

Lorentz TEM (LTEM): Lorentz force

Electrons, which pass a region having electrostatic and/or magnetic fields, are deflected by Lorentz force $\boldsymbol{F_L}$.

$$F_L = -e(E + \nu \times \vec{B})$$

Suppose $E \approx 0, and\ F_L$ acts normal and deflects the electron beam. Only the in-plane magnetic induction, $B_\perp$, deflects the beam.

$$\vec{B} = \vec{B}_\perp + B_z\vec{n}$$

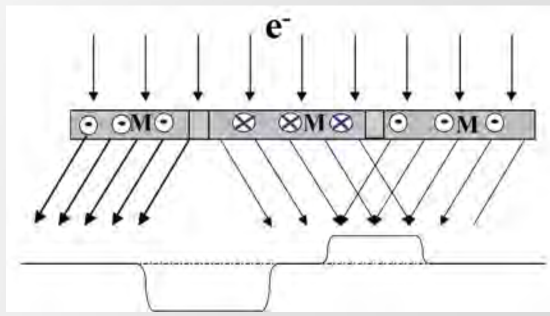

LTEM: Lorentz Transmission Electron Microscopy
Different imaging modes for observing magnetic features

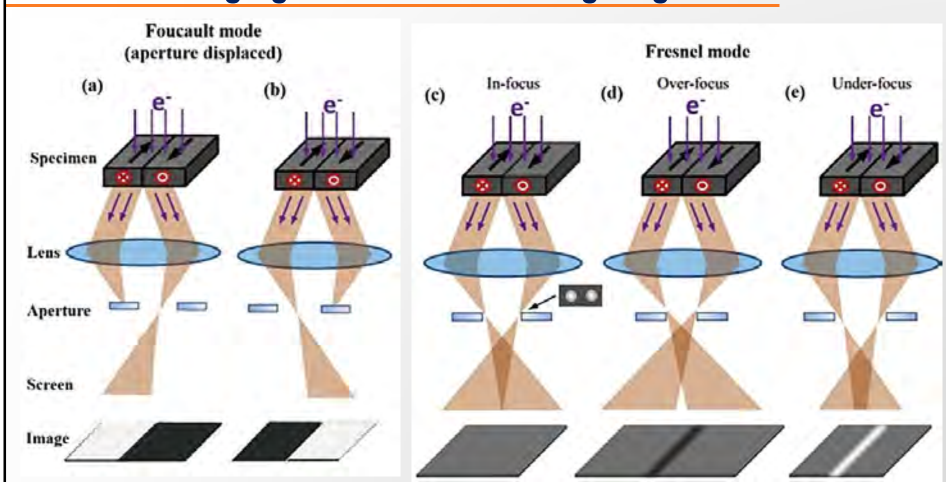

In-focus observation
Scattering contrast that distinguishes domains

Out-of-focus observation
Interference contrast that distinguishes the intersection between domains or changing spin states

Diffraction due to sample magnetization

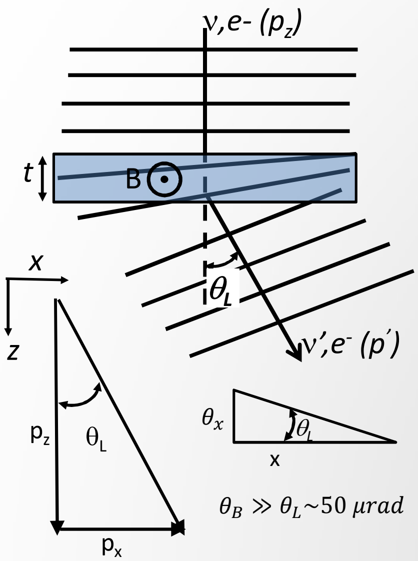

$\theta_B \gg \theta_L \sim 50\ \mu rad$

$$p_x = \int_0^\tau \overrightarrow{F_L} d\tau = e\int_o^t B_\perp \,dz = eB_\perp t$$

$$p_z = mv$$

Lorentz deflection gives small angles

$$\theta_L \approx \frac{p_x}{p_z} = \frac{eB_\perp t}{h\vec{k}} = \frac{eB_\perp t}{mv} = C_E B_\perp t$$

$$\varphi(x) = -2\pi\vec{k}\theta_x = -\frac{2\pi e B_\perp t\, x}{h}$$

For a varying $\vec{B}$, we arrive at the general solution for the phase shift due to a magnetic induction within the sample

$$\varphi\,(x,y) = -\frac{2\pi e}{h}\int \vec{B}\, ds$$

thomas.lagrange@epfl.ch • www.epfl.ch• lumes.epfl.ch• +41 (0)21 6935861

Measuring the Lorentz diffraction angle θ_L with small angle diffraction experiments

PHYSICAL REVIEW B 94, 024407 (2016)

Lorentz microscopy and small-angle electron diffraction study of magnetic textures in $La_{1-x}Sr_xMnO_3$ (0.15 < x < 0.30): The role of magnetic anisotropy

A. Kotani,[1] H. Nakajima,[1] K. Harada,[1,2] Y. Ishii,[1] and S. Mori[1,*]
[1]*Department of Materials Science, Osaka Prefecture University, Sakai, Osaka 599-8531, Japan*
[2]*Center for Emergent Material Science, the Institute of Physical and Chemical Research (RIKEN), Hatoyama, Saitama 350-0395, Japan*
(Received 21 December 2015; revised manuscript received 15 June 2016; published 6 July 2016)

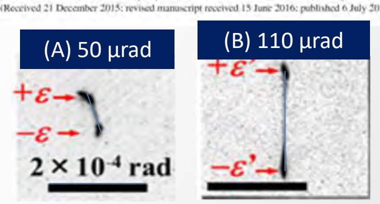

$$\theta_L = \frac{eB_\perp t}{mv} = C_E B_\perp t$$

$$C_E = \frac{9.37783}{\sqrt{E_o + 0.97485\times10^{-3} E_o{}^2}} \xRightarrow{200\ kV} 0.607\ \mu rad/T/nm$$

For a TEM foil thickness of 150 nm

(A) $B_\perp$ = 550mT (B) $B_\perp$ =1.2 T

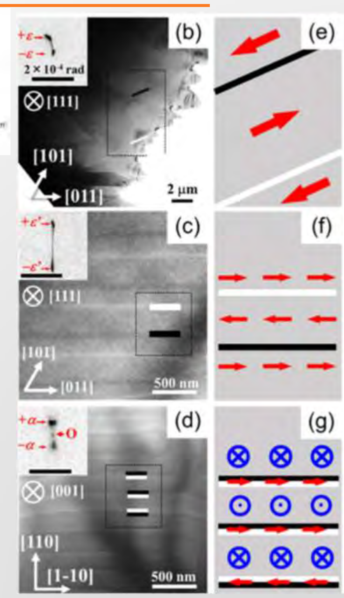

thomas.lagrange@epfl.ch • www.epfl.ch• lumes.epfl.ch• +41 (0)21 6935861

Lorentz TEM (LTEM): Lorentz force

The components of the magnetic induction in the sample can be determined by tilting the specimen.

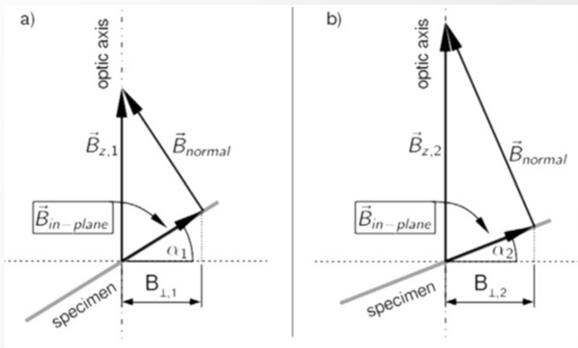

$$\vec{B}_{in-plane} = \vec{B}_{\perp} + B_z \sin\alpha$$

$$\frac{B_{\perp,1}}{B_{\perp,2}} = \frac{\sin\alpha_1}{\sin\alpha_2}$$

Determining the 3 components of the magnetic induction vector in the sample

A Sample of thickness (t) having internal magnetic fields with magnetic inductive vector ($\vec{B}_{\perp}$) in two direction, B_x and B_y

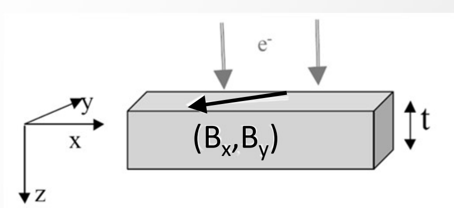

Gauss's Law

$$Div\,\vec{B} = 0 \Longrightarrow \frac{\partial B_x}{\partial x} = -\frac{\partial B_y}{\partial y}$$

$$\frac{\partial^2 \Delta\varphi}{\partial x \partial y} = -\frac{2\pi e t}{h}\frac{\partial B_y(x,y)}{\partial y}$$

$$B_x = -\int \frac{\partial B_y}{\partial y}dx = \frac{h}{2\pi e t}\frac{\partial^2 \Delta\varphi}{\partial x \partial y}dx$$

$$\boxed{B_x = \frac{h}{2\pi e t}\frac{\partial \Delta\varphi}{\partial y}} \quad and \quad \boxed{B_y = -\frac{h}{2\pi e t}\frac{\partial \Delta\varphi}{\partial x}}$$

LTEM: Fresnel imaging mode

Underfocus

Skyrmions in FeGe

Magnetic domains in Co Nanomagnets

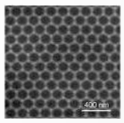

Overfocus

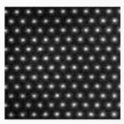

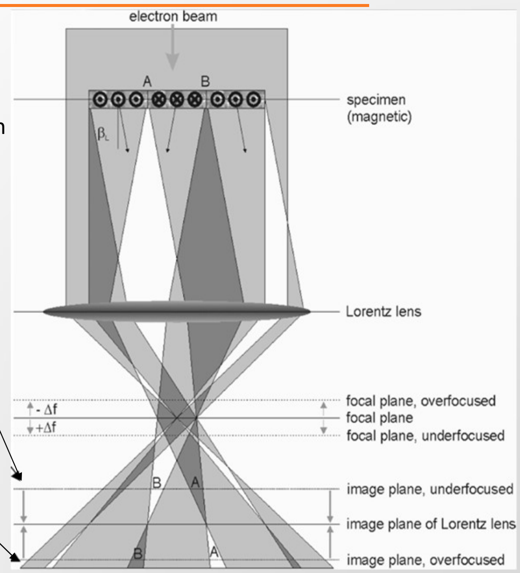

A. Kovacs et al., Lorentz microscopy and off-axis electron holography of magnetic skyrmions in FeGe. Resolution and Discovery 1, 2 (2016)

Example: Magnetic domain structure in ferromagnetic SMA


ScienceDirect

Acta MATERIALIA

In situ lorentz TEM magnetization study of a Ni–Mn–Ga ferromagnetic shape memory alloy

A. Budruk, C. Phatak, A.K. Petford-Long, M. De Graef

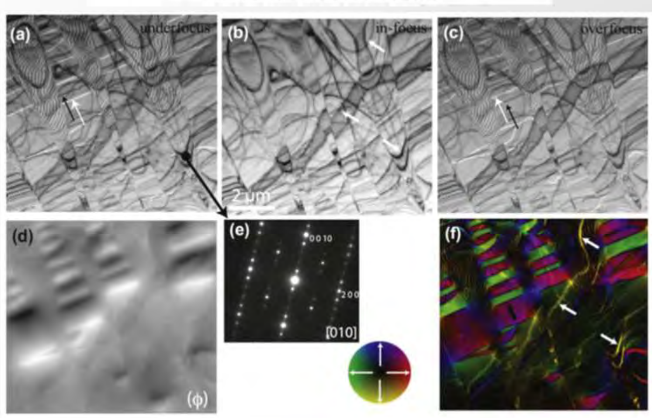

Example: In-situ LTEM observations of Nèel type Skyrmions (Pt-Co multilayers) under an applied field (~100 mT)

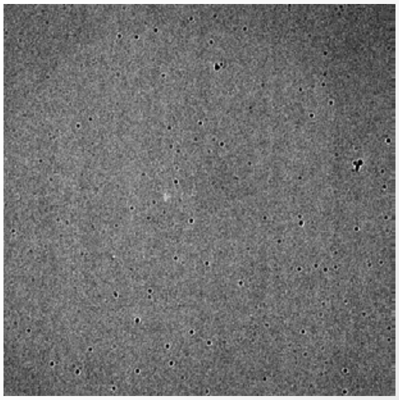

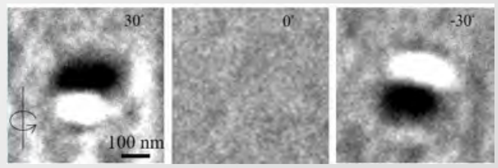

I. Madan, G. Berruto and T. LaGrange Unpublished data

Complementary study in a similar system
Zhang, S., et al. (2018). "Creation of a thermally assisted skyrmion lattice in Pt/Co/Ta multilayer films." Applied Physics Letters **113**(19): 192403.

 thomas.lagrange@epfl.ch • www.epfl.ch• lumes.epfl.ch• +41 (0)21 6935861

Example: Imaging Skyrmions in CoZnMn alloys

Transformation between meron and skyrmion topological spin textures in a chiral magnet

X. Z. Yu[1*] W. Koshibae[1] Y. Tokunaga[2] K. Shibata[1] Y. Taguchi[1] N. Nagaosa[1,3] & Y. Tokura[1,3]

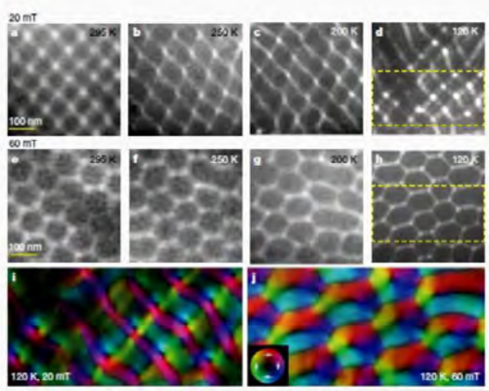

The equilibrium period of the helical phase

$$L_D = 4\pi \frac{A}{D}$$

where A is the micromagnetic exchange constant and D is the DMI constant

Critical field corresponding to the saturation field of the system

$$H_D = \frac{D^2}{2M_s A}$$

where M_s is the magnetization

Fig. 3 | Stability of the square (anti)meron and hexagonal skyrmion lattices in the (001) plate of $Co_8Zn_9Mn_3$. a–h, Over-focused Lorentz TEM images of the square (anti)meron (**a–d**) and hexagonal skyrmion (**e–h**) lattices observed with decreasing temperature at a magnetic field of 20 mT and 60 mT, respectively (experimental procedures are denoted by red dashed arrows in the phase diagram in Extended Data Fig. 3b). **i, j,** Magnetization textures for the boxed regions in **d** and **h**, respectively, deduced by analysing Lorentz TEM images with the transport-of-intensity equation. The colour wheel in the inset of **j** indicates the in-plane magnetization direction.

 thomas.lagrange@epfl.ch • www.epfl.ch• lumes.epfl.ch• +41 (0)21 6935861

LTEM: Foucault imaging

Aperture displaced $2\theta_L$

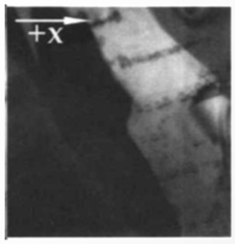

Aperture displaced $-2\theta_L$

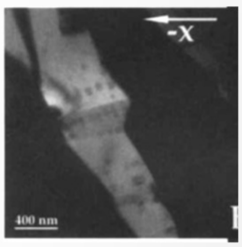

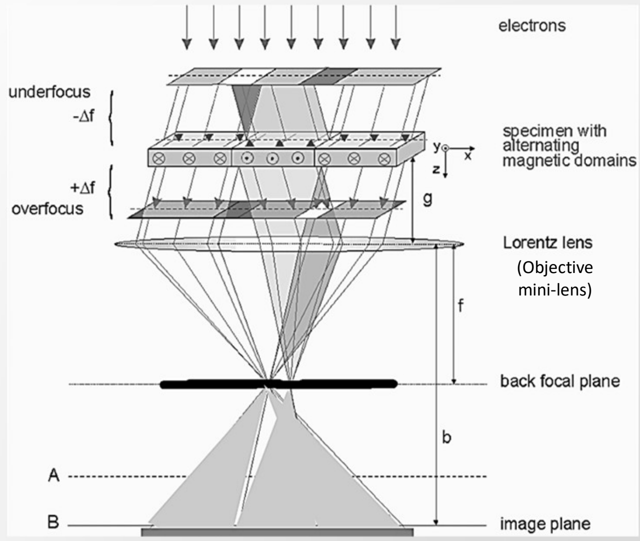

thomas.lagrange@epfl.ch • www.epfl.ch• lumes.epfl.ch• +41 (0)21 6935861

Foucualt imaging is darkfield image formed using the magnetically deflected spots

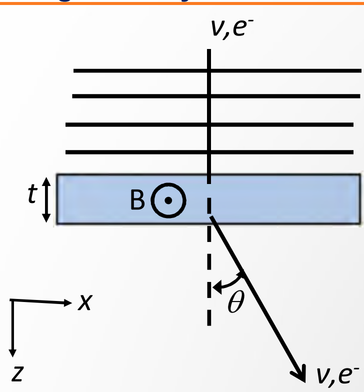

The Foucault image is a darkfield image formed by the magnetically scattered beams

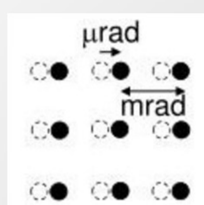

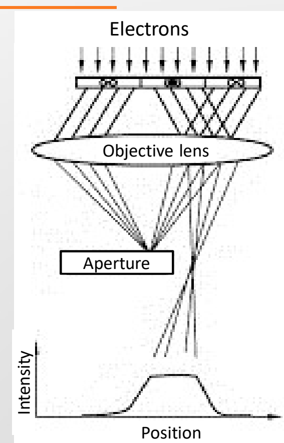

Remember the angle at which electrons are deflected by a magnetic field or potential is more than the order of magnitude smaller than the Bragg angles

$$\theta_L = \frac{\lambda e B_\perp t}{h} \approx 50\mu\text{rad for} \sim 500\text{mT and } 200\text{kV electrons}$$

thomas.lagrange@epfl.ch • www.epfl.ch• lumes.epfl.ch• +41 (0)21 6935861

Experimental setup for Foucault Imaging

Take the example of a magnetic sample having domains of opposing $\overrightarrow{B}$ vectors; the diffraction pattern contains slip spots separated by $2\theta_L$

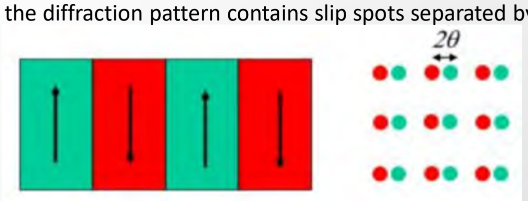

A Foucault image is generated by selecting one of the split spots and using those electrons to form the image intensity (contrast). The dark field or Foucault image exhibits bright intensity having a magnetic induction that allows electrons to pass through the aperture.

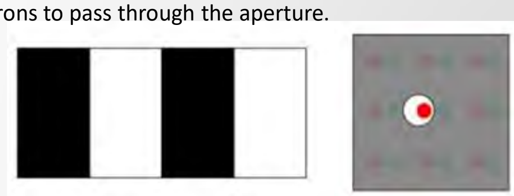

thomas.lagrange@epfl.ch • www.epfl.ch• lumes.epfl.ch• +41 (0)21 6935861

Combining a carbon film phase-plate with Foucault imaging

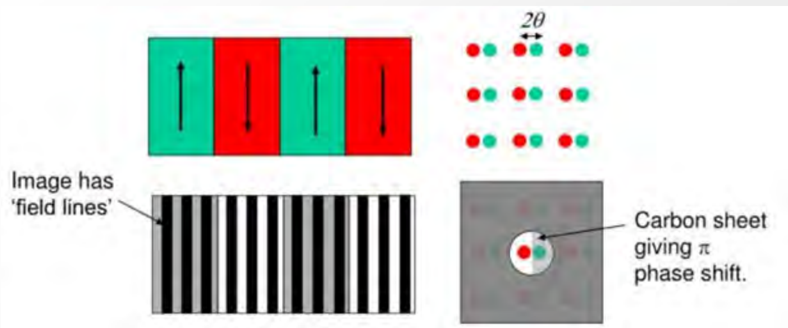

Instead of selecting one of the split spots to generate a Foucault image, both diffracted spots pass through an aperture partially covered by a carbon film. The thickness of the carbon film is designed to give a π phase shift of the electron beam at a given accelerating voltage, and only one of the spots passes through the film. Under this setup, the Foucault image will contain *Field Lines* within the domains with a 2π phase shift between them.

thomas.lagrange@epfl.ch • www.epfl.ch• lumes.epfl.ch• +41 (0)21 6935861

Combining a carbon film phase-plate with Foucault imaging

Circular Permalloy dots on SiN | Phase calculation using TIE

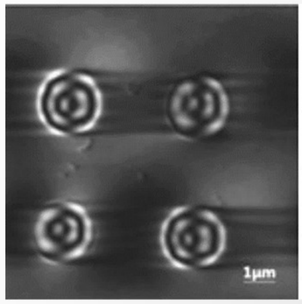

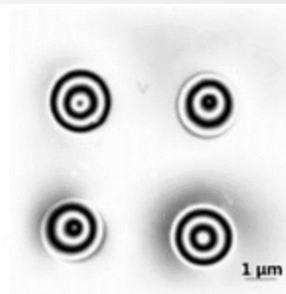

Instead of selecting one of the split spots to generate a Foucault image, both diffracted spots pass through an aperture partially covered by a carbon film. The thickness of the carbon film is designed to give a π phase shift of the electron beam at a given accelerating voltage, and only one of the spots passes through the film. Under this setup, the Foucault image will contain *Field Lines* within the domains with a 2π phase shift between them.

thomas.lagrange@epfl.ch • www.epfl.ch• lumes.epfl.ch• +41 (0)21 6935861

Small Angle Electron Diffraction (SmAED)

SmAED for LTEM studies typically requires camera lengths of 50-1000m

$$\theta_L = \frac{\lambda e B_{\perp} t}{h} \sim 1 - 100\mu\text{rad}$$

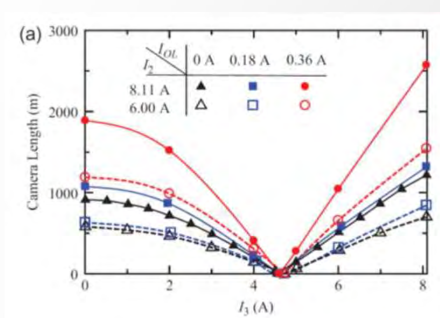

SmAED | Foucault

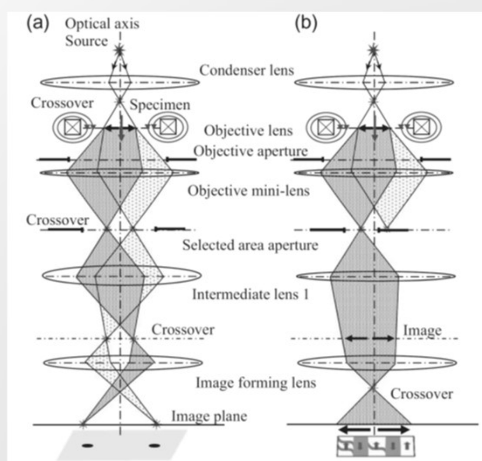

thomas.lagrange@epfl.ch • www.epfl.ch• lumes.epfl.ch• +41 (0)21 6935861

Small Angle Electron Diffraction (SmAED) examples

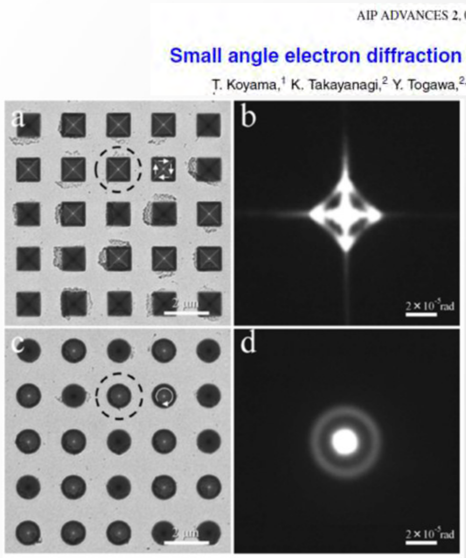

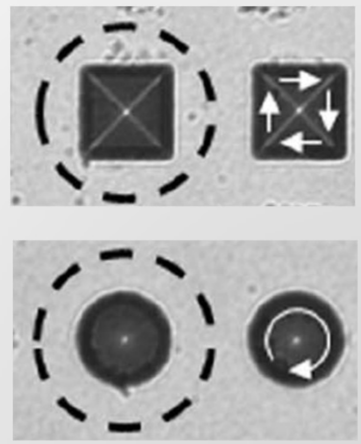

19

thomas.lagrange@epfl.ch • www.epfl.ch• lumes.epfl.ch• +41 (0)21 6935861

Example: Skyrmion lattice

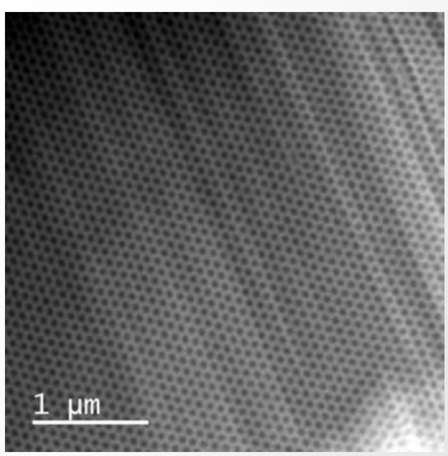

Small angle electron diffraction of Skyrmion Lattice (SKL)

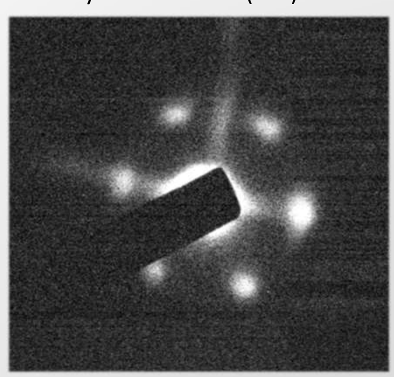

20

thomas.lagrange@epfl.ch • www.epfl.ch• lumes.epfl.ch• +41 (0)21 6935861

QUESTIONS?

21

thomas.lagrange@epfl.ch • www.epfl.ch• lumes.epfl.ch• +41 (0)21 6935861

Outline:

Lorentz microscopy has been used extensively for the past 40 years to study magnetic domain structure and magnetization reversal mechanisms in magnetic thin films and elements. Here, a brief introduction to standard image modes in TEM and the theory involved is presented. The second half of lectures is devoted to discussing how the sample's phase shift and magnetic properties can be quantified from the LTEM observations.

1) Lorentz Transmission Electron Microscopy (LTEM)
   A. Lorentz Force and LTEM Imaging modes
   B. Fresnel Mode
   C. Foucault Mode
   D. Examples
2) Simulations and quantitative analysis
   A. Modeling magnetic images in a real microscope
   B. Transport of Intensity Equations (TIE)
   C. Examples

22

thomas.lagrange@epfl.ch • www.epfl.ch• lumes.epfl.ch• +41 (0)21 6935861

Lorentz image simulation: modeling the TEM image formation

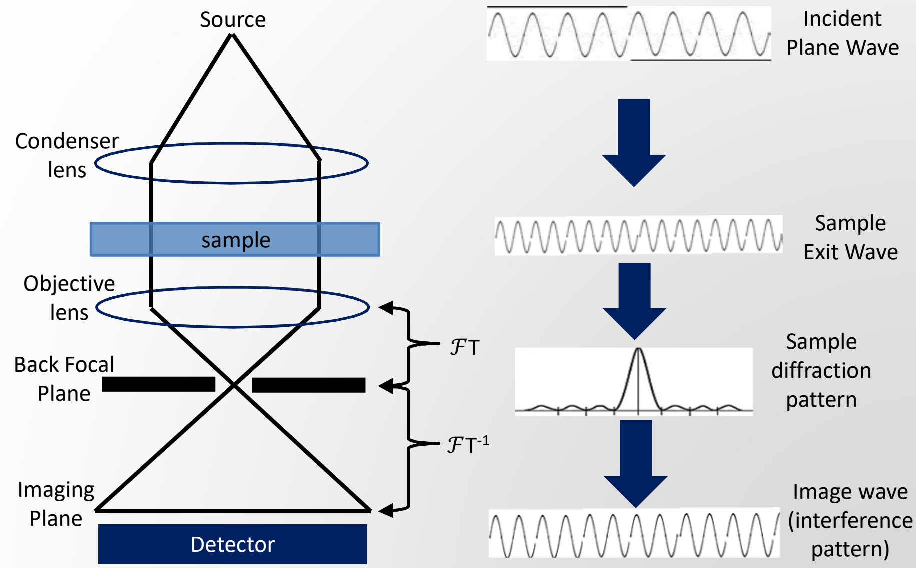

thomas.lagrange@epfl.ch • www.epfl.ch• lumes.epfl.ch• +41 (0)21 6935861

Lorentz image simulation: modeling the TEM image formation

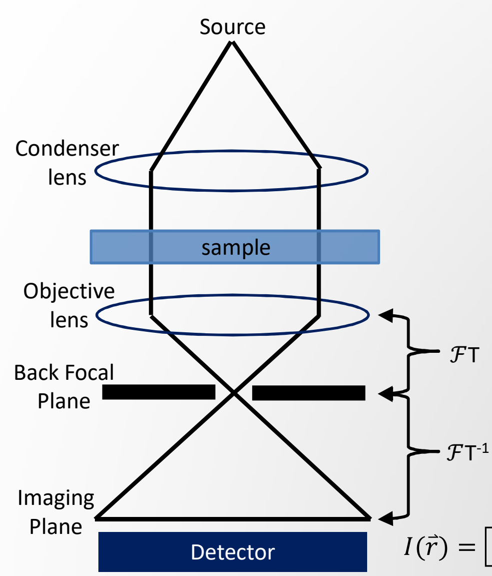

Incident Plane Wave

$$\Psi_i = \Psi_o \exp(2\pi i \vec{\boldsymbol{r}})$$

Sample Exit Wave

$$\Psi_s(\vec{r}) = a(\vec{r})e^{i\varphi_s \vec{r}}$$

Sample diffraction pattern

$$\Psi(\vec{q}) = \mathcal{F}\mathrm{T}[\Psi_s(\vec{r})]\ T(\vec{q})$$

$$T(\vec{q}) = A(|\vec{q}|)e^{-i\chi(\vec{q})}e^{-iD(\vec{q})}$$

Image formation and Transfer Function

$$I(\vec{r}) = \boxed{|\mathcal{F}\mathrm{T}^{-1}[\Psi(\vec{q})]|^2 = |\Psi_s(\vec{r}) \otimes T_L(\vec{r})|^2}$$

thomas.lagrange@epfl.ch • www.epfl.ch• lumes.epfl.ch• +41 (0)21 6935861

Lorentz image simulation: Transfer function

$$\Psi_s(\vec{r}) = a(\vec{r})e^{i\varphi_s \vec{r}}$$

The exit wave of the sample, which has the phase shifts associated with both the sample's electrostatic and magnetic potentials

$$\Psi(\vec{q}) = \mathcal{FT}[\Psi_s(\vec{r})]\; T\,(\vec{q})$$

$$T_L(\vec{q}) = A[|\vec{q}|]e^{-i\chi(\vec{q})}e^{-iD(\vec{q})}$$

Abbe's equation can be used to approximate imaging (Fourier transform) that is convolved with the microscope transfer function.

$A[|\vec{q}|]$ is the aperture function (1 inside and 0 outside). Radius and position are varied for Foucault images simulations

$$\chi(\vec{q}) = \pi\lambda\Delta f\,|\vec{q}|^2 + 1/2\pi C_s\lambda^3|\vec{q}|^4$$

$$D(\vec{q}) \approx \frac{(\pi\theta_D\Delta f)^2}{ln2}|\vec{q}|^2$$

$$T_L(\vec{q}) = A[|\vec{q}|]e^{-i\,\pi\lambda\Delta f|\vec{q}|^2}e^{-\frac{i(\pi\theta_D\Delta f)^2}{ln2}|\vec{q}|^2}$$

$\chi(\vec{q})$ is the phase function corresponding to the defocus and spherical aberration of the objective lens.

$D(\vec{q})$ is the damping envelope of the wave function due to the beam divergence and the finite stability of the lenses and accelerator electronics.

thomas.lagrange@epfl.ch • www.epfl.ch• lumes.epfl.ch• +41 (0)21 6935861

Example: modeling the LTEM Fresnel mode contrast developed by embedded magnetic particles of differing sizes

$$\Delta\varphi_m = \frac{-2\pi e}{h}\oint_l \vec{A}dl = \frac{-2\pi e}{h}\int_S \vec{B}dS$$

$$\Delta\varphi_{m,x} = \frac{2\pi et}{h}B_y\Delta x$$

$$\Delta\varphi_{m,y} = \frac{2\pi et}{h}B_x\Delta y$$

Example: J. Dooley and M. De Graef, Micron 28, (1997) p.371

as a function of np size | as a function of HT

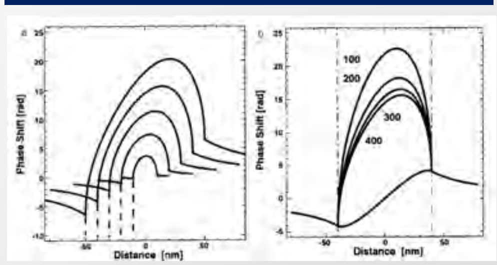

For spherical magnetic particles with radius (a), $\vec{A}(r) = \frac{4\pi a^3}{3(r^3 > a^3)}M_o[y(\hat{x}\sin\theta + \hat{z}\cos\theta) - z\hat{y}]$

Assuming that normalized coordinates (e.g., $\bar{r} = \frac{r}{a}, \bar{y} = \frac{y}{a}$), using $M_o = \frac{3}{8\pi B}$, and $\beta(r,q) = [1-(r^2>1)]^q$

Magnetic phase shift = $\frac{\overline{\varphi_m}\,(r_\perp)}{B_\perp a^2} = \boxed{\frac{2\pi e\bar{y}}{h\bar{r}^2}\left\{1-\beta\left(\bar{r},\frac{3}{2}\right)\right\}}$

Electrostatic phase shift = $\frac{\overline{\varphi_e}(r_\perp)}{\sigma_E eU_i a} = \boxed{2\left\{\frac{V_m}{V_i}\bar{t} - \beta\left(\bar{r},\frac{1}{2}\right)\right\}}$

thomas.lagrange@epfl.ch • www.epfl.ch• lumes.epfl.ch• +41 (0)21 6935861

Example: modeling the LTEM Fresnel mode contrast developed by embedded magnetic particles of differing sizes

For embedded magnetic nanoparticles that are strong phase objects, the exit wave follows,

$$\Psi_s(\vec{r}) = a(\vec{r})e^{i[B_\perp a^2\overline{\varphi_m}(r_\perp)+\sigma_E eU_i a\overline{\varphi_e}(r_\perp)]}$$

Imaging of sample information by the microscope lens system can be modeled as,

$$\Psi(\vec{q}) = \mathcal{FT}[\Psi_s(\vec{r})]\,T(\vec{q})$$

The transfer function associated with LTEM mode can modeled as,

$$T_L(\vec{q}) = A[|\vec{q}|]e^{-i\pi\lambda\Delta f|\vec{q}|^2}e^{-\frac{(\pi\theta_D\Delta f)^2}{ln2}|\vec{q}|^2}$$

The intensity on the detector plane is the convolution of sample exit wave function and the microscope transfer function

$$I(\vec{r}) = \boxed{|\mathcal{F}\mathrm{T}^{-1}[\Psi(\vec{q})]|^2 = |\Psi_s(\vec{r}) \otimes T_L(\vec{r})|^2}$$

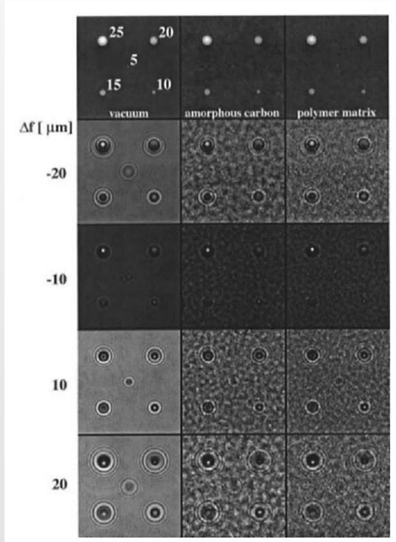

De Graef, M. (1999). Lorentz microscopy and electron holography of nanocrystalline magnetic materials. Advanced Hard and Soft Magnetic Materials. M. Coey, L. H. Lewis, B. M. Ma et al. Warrendale, Materials Research Society. **577:** 519-530.

MALTS: Micromagnetic Analysis to Lorentz TEM Simulation

IEEE TRANSACTIONS ON MAGNETICS, VOL. 49, NO. 8, AUGUST 2013 4795

MALTS: A Tool to Simulate Lorentz Transmission Electron Microscopy From Micromagnetic Simulations

Stephanie K. Walton[1], Katharina Zeissler[1], Will R. Branford[1,2], and Solveig Felton[2,3]

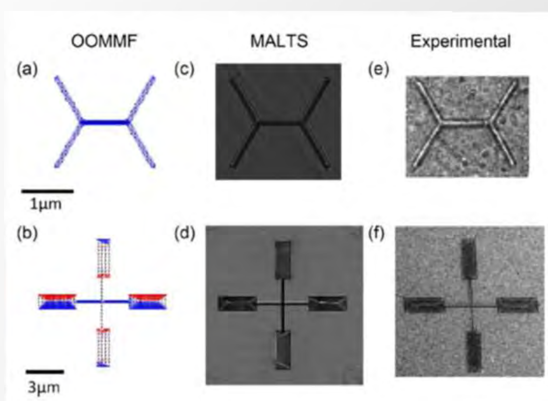

How do we model LTEM contrast and be more quantitative about the magnetic phase shifts due to in-plane B

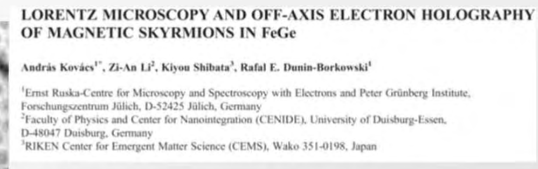
LORENTZ MICROSCOPY AND OFF-AXIS ELECTRON HOLOGRAPHY OF MAGNETIC SKYRMIONS IN FeGe

András Kovács[1*], Zi-An Li[2], Kiyou Shibata[3], Rafal E. Dunin-Borkowski[1]

[1]Ernst Ruska-Centre for Microscopy and Spectroscopy with Electrons and Peter Grünberg Institute, Forschungszentrum Jülich, D-52425 Jülich, Germany
[2]Faculty of Physics and Center for Nanointegration (CENIDE), University of Duisburg-Essen, D-48047 Duisburg, Germany
[3]RIKEN Center for Emergent Matter Science (CEMS), Wako 351-0198, Japan

Overfocus

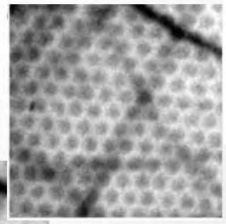

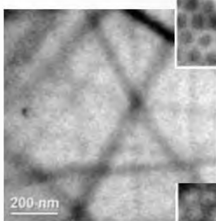

In focus

Underfocus

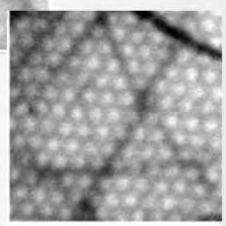

Phase Reconstructed Image

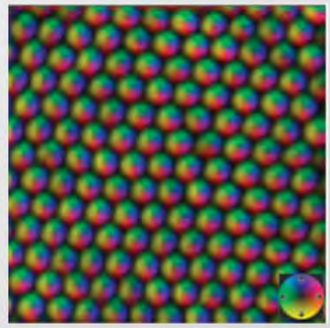

Transport of Intensity Equations (TIE)

For LTEM mode with small deflection angles (i.e.,$|\overrightarrow{q_\perp}|$) and small defocus ($\Delta f$), the phase function ($\chi(\vec{q})$)and damping envelope ($D(\vec{q})$) can be written in terms of z and Taylor series expansion of the transfer function (truncating at the quadratic term)

$$\Psi_q(\overrightarrow{q_\perp}) = \mathcal{F}\mathrm{T}[\,\Psi(\overrightarrow{r_\perp})](1 - z|\vec{q}_\perp|^2)$$

$$z = iz_i + z_r, \quad z_i = \pi\lambda\Delta f \quad \text{and} \quad z_r = \frac{(\pi\theta_D\Delta f)^2}{ln2}$$

The wave function on the image plane (inverse $\mathcal{F}\mathrm{T}$) can be written in this general form,

$$\Psi = ae^{i\varphi} - z\mathcal{F}\mathrm{T}^{-1}\left[\mathcal{F}\mathrm{T}\left(ae^{i\varphi}\right)q^2\right] \;\; and \;\; \mathcal{F}\mathrm{T}\left(ae^{i\varphi}\right) = f(\overrightarrow{q_\perp})$$

$$\mathcal{F}\mathrm{T}^{-1}\left[\mathcal{F}\mathrm{T}(ae^{i\varphi})q^2\right] = \frac{-1}{4\pi^2}\iint f(\overrightarrow{q_\perp})\nabla^2 e^{i2\pi\vec{q}_\perp\overrightarrow{r_\perp}}\, d\overrightarrow{q_\perp} = \frac{-1}{4\pi^2}\nabla^2\left[ae^{i\varphi}\right]$$

$$\Psi = ae^{i\varphi} + \frac{z}{4\pi^2}\nabla^2\left[ae^{i\varphi}\right]$$

The intensity on the detector plane is the convolution of the sample exit wave function and the microscope transfer function. For uniform illumination ($\nabla^2 a = 0$)

$$I = \boxed{a^2 - \frac{\lambda\Delta f}{2\pi}\nabla\cdot(a^2\nabla\varphi) + \frac{(\theta_D\Delta f)^2}{ln2}\left[a\nabla^2 a - a^2(\nabla\varphi)^2\right]}$$

Transport of Intensity Equations (TIE)

Let's consider 3 cases, infocus (i.e, $I(\vec{r}_\perp, 0) = a^2$), overfocus and underfocus with the same magnitude $|\Delta f|$

Underfocus $I(\vec{r}_\perp, -|\Delta f|)$

$$= I(\vec{r}_\perp, 0) - \frac{\lambda|\Delta f|}{2\pi}\nabla\cdot(I(\vec{r}_\perp, 0)\nabla\varphi) + \frac{(\theta_D|\Delta f|)^2}{ln2}\left[\sqrt{I(\vec{r}_\perp, 0)}\nabla^2\sqrt{I(\vec{r}_\perp, 0)} - I(\vec{r}_\perp, 0)(\nabla\varphi)^2\right]$$

and for overfocus $I(\vec{r}_\perp, +|\Delta f|)$

$$= I(\vec{r}_\perp, 0) + \frac{\lambda|\Delta f|}{2\pi}\nabla\cdot(I(\vec{r}_\perp, 0)\nabla\varphi) + \frac{(\theta_D|\Delta f|)^2}{ln2}\left[\sqrt{I(\vec{r}_\perp, 0)}\nabla^2\sqrt{I(\vec{r}_\perp, 0)} - I(\vec{r}_\perp, 0)(\nabla\varphi)^2\right]$$

Subtracting the second equation from the first and rearranging the terms,

$$-\frac{2\pi}{\lambda}\frac{\left(I(\vec{r}_\perp, |\Delta f|) - I(\vec{r}_\perp, -|\Delta f|)\right)}{2|\Delta f|} = \nabla\cdot[I(\vec{r}_\perp, 0)\nabla\varphi]$$

If we take the limit in a vanishingly small defocus, we arrive at the so-called generalized form of the Transport of Intensity Equation (TIE)

$$\nabla\cdot[I(\vec{r}_\perp, 0)\nabla\varphi] = \nabla^2\Psi = \boxed{-\frac{2\pi}{\lambda}\frac{\partial I(\vec{r}_\perp, 0)}{\partial z}}$$

thomas.lagrange@epfl.ch • www.epfl.ch• lumes.epfl.ch• +41 (0)21 6935861

Simplification of the TIE equation

The Transport of Intensity Equation (TIE)

$$\nabla(I(\vec{r}_\perp, 0)\nabla\varphi) = -\frac{2\pi}{\lambda}\frac{\partial I}{\partial z}$$

If the in-focus intensity is constant (I_o) associated with the sample, then,

$$I_o\nabla^2\varphi = -\frac{2\pi}{\lambda}\frac{\partial I}{\partial z}$$

Implementing a 2-D Fourier transform of the images,

$$-4\pi^2q^2\varphi = -\frac{2\pi}{\lambda I_o}\mathcal{F}T\left[\frac{\partial I}{\partial z}\right]$$

rewriting the equation

$$\varphi \approx \frac{1}{2\pi q^2\lambda I_o}\mathcal{F}T\left[\frac{I(\Delta f) - I(-\Delta f)}{2\Delta f}\right]$$

thomas.lagrange@epfl.ch • www.epfl.ch• lumes.epfl.ch• +41 (0)21 6935861

Experimental approach for calculating the phase

$$\varphi \approx \frac{1}{2\pi q^2 \lambda I_o} \mathcal{F}T\left[\frac{I(\Delta f) - I(-\Delta f)}{2\Delta f}\right]$$

$$\nabla\Psi = I(\vec{r}_\perp, 0)\nabla\varphi$$

$$\nabla\cdot\nabla\Psi = \nabla^2\Psi = -\frac{2\pi}{\lambda}\frac{\partial I}{\partial z}$$

$$\nabla\varphi = \frac{\nabla\Psi}{I(\vec{r}_\perp, 0)} = -\frac{2\pi e}{h}\left[\vec{B}(r_\perp)\times\hat{n}\right]t(r_\perp)$$

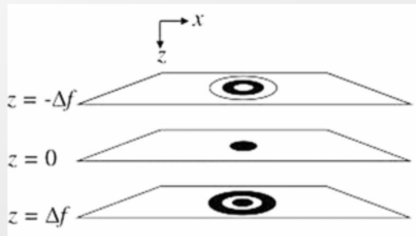

To calculate the phase, images of the same region are taken at overfocus (Δf), in-focus ($\Delta f = 0$), and underfocus ($-\Delta f$). Subtract the overfocus and underfocus, take the Fourier transform, and then divide reciprocal q^2 and constants (in-focus image I_o). The phase is obtained by the inverse $\mathcal{F}T^{-1}$ of this quantify.

Example: permalloy disks deposited on SiN membrane

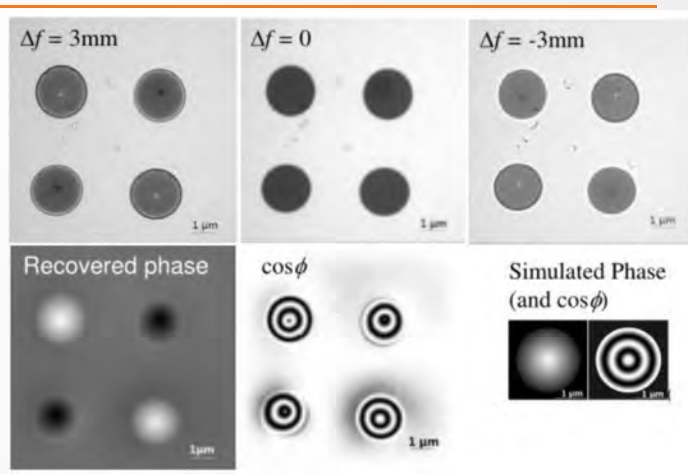

It is convenient to display the calculated phase images as "cosine of the phase" contour map in which there is a phase shift of 2π between the dark lines that resembles the magnetic field lines.

Example: TIE of Skyrmions in FeGe (unpublished results)

In-focus

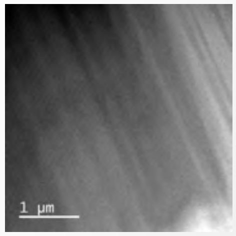

Over-focus

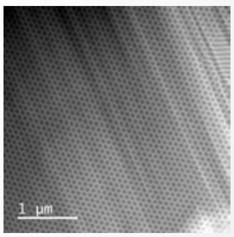

Under-focus

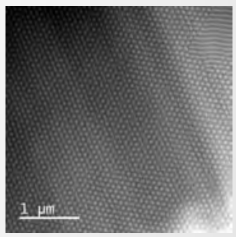

TIE Phase image

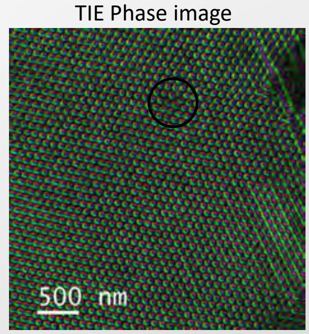

Defect in Crystal

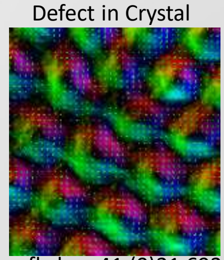

thomas.lagrange@epfl.ch • www.epfl.ch• lumes.epfl.ch• +41 (0)21 6935861

Comparison with electron holography

Simulation | TIE Calc. from LTEM | Electron Holography

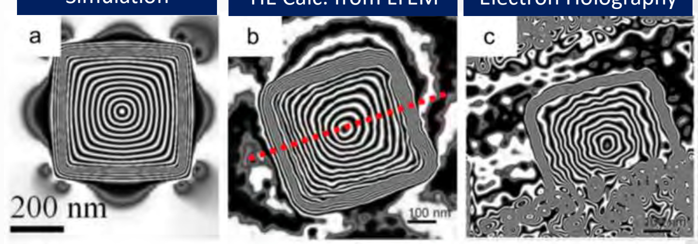

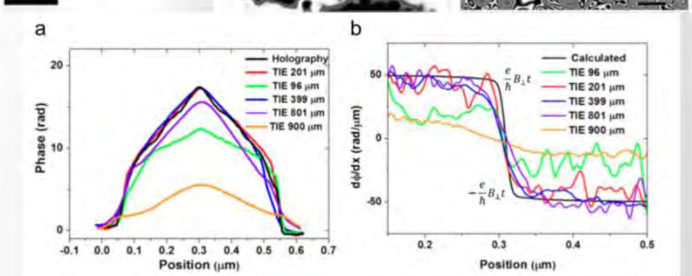

A. Kohn, A. Habibi, M. Mayo, Ultramicroscopy160(2016)44–56

thomas.lagrange@epfl.ch • www.epfl.ch• lumes.epfl.ch• +41 (0)21 6935861

Resolution, optimal defocus, and accuracy of calculated phase using TIE

Phase Measurement in Electron Microscopy Using the Transport of Intensity Equation

Kazuo Ishizuka, and Brendan Allman*

*HREM Research Inc, *IATIA Ltd*

$$\frac{(\pi\lambda\Delta f\, q_{max}^2)}{3!} \leq c \ll 1, c \sim 0.25$$

Table 1. Upper limits of defocus for the three-image case

d_{min} (nm)	πλ(2Δf)	100 kV	200 kV	400 kV
0.14	4.90 x10^{-2}	4.2 nm	6.2 nm	9.5 nm
0.2	9.80x 10^{-2}	8.4 nm	19.0 nm	19.0 nm
1	2.45	211 nm	311 nm	474 nm
10	2.45 x10^{2}	21.1 µm	31.1 µm	47.4 µm
100	2.45 x10^{4}	2.11 mm	3.11 mm	4.74 mm

QUESTIONS?

Bibliography

1. Budruk, A., et al., *In situ lorentz TEM magnetization study of a Ni–Mn–Ga ferromagnetic shape memory alloy.* Acta Materialia, 2011. **59**(12): p. 4895-4906.
2. Chapman, J.N., A.B. Johnston, and L.J. Heyderman, *Coherent Foucault imaging: A method for imaging magnetic domain structures in thin films.* Journal of Applied Physics, 1994. **76**(9): p. 5349-5355.
3. De Graef, M., *Lorentz microscopy and electron holography of nanocrystalline magnetic materials*, in *Advanced Hard and Soft Magnetic Materials*, M. Coey, et al., Editors. 1999, Materials Research Society: Warrendale. p. 519-530.
4. De Graef, M., *2. Lorentz microscopy: Theoretical basis and image simulations*, in *Experimental Methods in the Physical Sciences*, M. De Graef and Y. Zhu, Editors. 2001, Academic Press. p. 27-67.
5. De Graef, M. and Y. Zhu, *Magnetic Imaging and Its Applications to Materials*. Experimental methods in the Physic Sciences, ed. R. Celotta and T. Lucatorto. Vol. 36. 2000, London, UK: Elsevier Science.
6. Dooley, J. and M. De Graef, *Energy filtered magnetic induction mapping.* Micron, 1997. **28**(5): p. 371-380.
7. Gureyev, T.E. and K.A. Nugent, *Phase retrieval with the transport-of-intensity equation .2. Orthogonal series solution for nonuniform illumination.* Journal of the Optical Society of America a-Optics Image Science and Vision, 1996. **13**(8): p. 1670-1682.
8. Gureyev, T.E., A. Roberts, and K.A. Nugent, *PHASE RETRIEVAL WITH THE TRANSPORT-OF-INTENSITY EQUATION - MATRIX SOLUTION WITH USE OF ZERNIKE POLYNOMIALS.* Journal of the Optical Society of America a-Optics Image Science and Vision, 1995. **12**(9): p. 1932-1941.
9. Gureyev, T.E., A. Roberts, and K.A. Nugent, *PARTIALLY COHERENT FIELDS, THE TRANSPORT-OF-INTENSITY EQUATION, AND PHASE UNIQUENESS.* Journal of the Optical Society of America a-Optics Image Science and Vision, 1995. **12**(9): p. 1942-1946.
10. Kohn, A., A. Habibi, and M. Mayo, *Experimental evaluation of the 'transport-of-intensity' equation for magnetic phase reconstruction in Lorentz transmission electron microscopy.* Ultramicroscopy, 2016. **160**: p. 44-56.

thomas.lagrange@epfl.ch • www.epfl.ch• lumes.epfl.ch• +41 (0)21 6935861

Bibliography

11. Kotani, A., et al., *Lorentz microscopy and small-angle electron diffraction study of magnetic textures in La1-xSrxMnO3 (0.15 < x < 0.30): The role of magnetic anisotropy.* Physical Review B, 2016. **94**(2): p. 7.
12. Koyama, T., et al., *Small angle electron diffraction and deflection.* AIP Advances, 2012. **2**.
13. McVitie, S. and M. Cushley, *Quantitative Fresnel Lorentz microscopy and the transport of intensity equation.* Ultramicroscopy, 2006. **106**(4-5): p. 423-431.
14. Nakajima, H., et al., *Foucault imaging and small-angle electron diffraction in controlled external magnetic fields.* Microscopy, 2016. **65**(6): p. 473-478.
15. Nakajima, H., et al., *Foucault optical system by using a nondedicated conventional TEM.* Surface and Interface Analysis, 2016. **48**(11): p. 1166-1168.
16. Paganin, D. and K.A. Nugent, *Noninterferometric phase imaging with partially coherent light.* Physical Review Letters, 1998. **80**(12): p. 2586-2589.
17. Phatak, C., A.K. Petford-Long, and M. De Graef, *Recent advances in Lorentz microscopy.* Current Opinion in Solid State and Materials Science, 2016. **20**(2): p. 107-114.
18. Portier, X., et al., *Lorentz transmission electron microscopy on NiFe/Cu/Co/NiFe/MnNi active spin valve elements.* Applied Physics Letters, 1997. **71**(14): p. 2032-2034.
19. Taniguchi, Y., H. Matsumoto, and K. Harada, *Foucault imaging by using non-dedicated transmission electron microscope.* Applied Physics Letters, 2012. **101**(9): p. 4.
20. Volkov, V.V. and Y. Zhu, *Magnetic structure and microstructure of die-upset hard magnets RE13.75Fe80.25B6 (RE = Nd, Pr): A possible origin of high coercivity.* Journal of Applied Physics, 1999. **85**(6): p. 3254-3263.
21. Zhang, S., et al., *Creation of a thermally assisted skyrmion lattice in Pt/Co/Ta multilayer films.* Applied Physics Letters, 2018. **113**(19): p. 192403.

thomas.lagrange@epfl.ch • www.epfl.ch• lumes.epfl.ch• +41 (0)21 6935861

Practical considerations for doing TIE analysis

thomas.lagrange@epfl.ch • www.epfl.ch• lumes.epfl.ch• +41 (0)21 6935861

Difficulties and Errors with TIE phase retrieval: Noise

To understand noise effects on the phase recovery, consider a wave with no intensity modulation but has a phase distribution

$$k\frac{\partial \rho}{\partial z} = -\nabla^2 \varphi$$

Implementing Fourier theory then gives,

$$\frac{2\pi}{\lambda}\mathcal{FT}\left[\frac{\partial \rho}{\partial z}\right] = |q_\perp|^2$$

Where $q_\perp$ is the spatial frequency, the solution phase follows,

$$\varphi = \frac{2\pi}{\lambda}\mathcal{FT}^{-1}\left[\frac{1}{|q_\perp|^2}\mathcal{FT}\left[\frac{\partial \rho}{\partial z}\right]\right]$$

Thus, the phase recover from input data involves the numerical differentiation of experimental data, noise sensitive operation. However, phase recovery with TIE is relatively insensitive to noise even at levels around 10%

Thus, to reduce noise effects, a larger defocus can be used at the expense of reduced spatial resolution

thomas.lagrange@epfl.ch • www.epfl.ch• lumes.epfl.ch• +41 (0)21 6935861

Difficulties and Errors with TIE phase retrieval: Systematic errors, e.g., magnification, image shifts, image rotation

- Image shifts
  - Suppose an electron plane wave traveling at an angle, θ, can be described by the phase gradient, $\varphi' = \frac{2\pi}{\lambda}\sin\theta$
  - If an image (sample) shifts by Δ causing defocus error of δz, then $\varphi' = \frac{2\pi}{\lambda}\frac{\Delta}{\delta z}$
  - The acceptable misalignment depends on the extent of phase excursion (size) required to observe a feature.
- Magnification errors
  - A difference of 1% in magnification can cause significant errors in the recovered phases.
  - In an astigmatic system, the magnification can differ with transverse direction, and defocus error-induced magnification changes result in an additional cylindrical phase across the image
- Image rotation
  - For phase distribution of $\phi = n\theta$, where θ is the azimuthal angle on intensity distribution, the phase distribution undergoes a differential rotation separated by differential distance.
  - A small amount of rotation can create local phase gradients and distortion artifacts.
- Image Normalization
  - Incorrect image normalization on the order of <1% can even cause dramatic effects on the recovered phase and image artifacts

Other techniques and examples for imaging magnetic structures in the TEM

Lorentz Scanning TEM and Differential Phase Contrast (DPC)

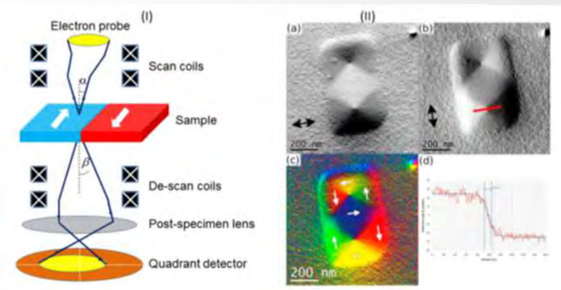

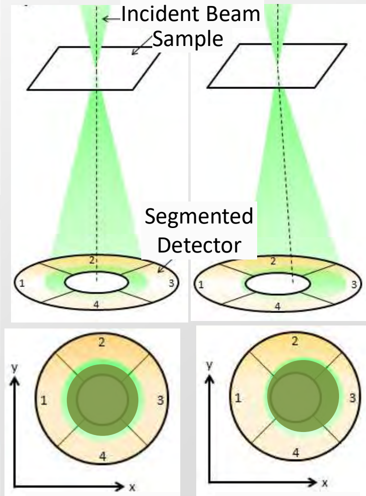

$I_{det1}-I_{det3}=0$
$I_{det2}-I_{det4}=0$

$I_{det1}-I_{det3}>0$
$I_{det2}-I_{det4}=0$

Examples: Hollow Cone Foucault imaging

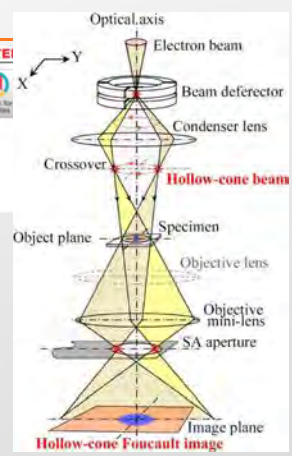

Conventional Foucault imaging

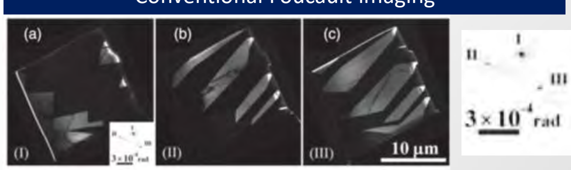

Darkfield image 72 μrad angle	HCF Brightfield 16 μrad angle	HCF Darkfield 50 μrad angle

Precessing the beam (azimuthal angle) about small tilt angles ($2\theta_L$) allows imaging all domains and their boundaries with high spatial resolution(~1nm)

Foucault mode example: in-situ measurements in spintronics

Lorentz transmission electron microscopy on NiFe/Cu/Co/NiFe/MnNi active spin valve elements

X. Portier,[a] A. K. Petford-Long, and R. C. Doole
Department of Materials, University of Oxford, Oxford OX1 3PH, United Kingdom
T. C. Anthony and J. A. Brug
Hewlett-Packard Laboratories, Palo Alto, California, 94304

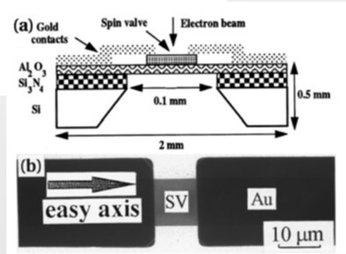

They observed the magnetic domain structure and made simultaneous magnetoresistance measurements under an applied, controlled field and current in which they correlated changes in the domains to GMR (giant magnetoresitance).

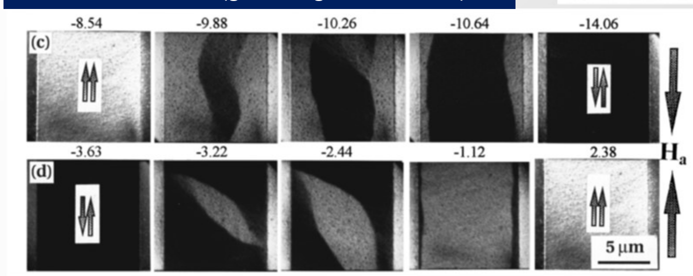

Applied magnetic field in Oersted
1Oe= 0.1 mT

Current density
1.5×10^6 A cm^{-2}

Example: Combining LTEM imaging modes

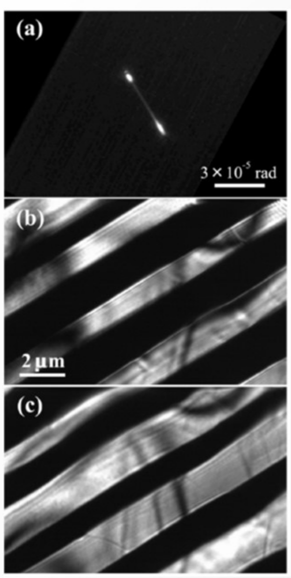

APPLIED PHYSICS LETTERS 101, 093101 (2012)

Foucault imaging by using non-dedicated transmission electron microscope

Yoshifumi Taniguchi (谷口佳史),[1] Hiroaki Matsumoto (松本弘昭),[2] and Ken Harada (原田研)[3,a)]
[1]*Science and Medical Systems Business Group, Hitachi High-Technologies Corp., Ichige, Hitachinaka, Ibaraki 312-8504, Japan*
[2]*Corporate Manufacturing Strategy Group, Hitachi High-Technologies Corp., Ishikawa-cho, Hitachinaka, Ibaraki 312-1991, Japan*
[3]*Central Research Laboratory, Hitachi Ltd., Hatoyama, Saitama 350-0395, Japan*

Combining Small Angle Electron Diffraction (SmAED) with Foucault and Fresnels mode LTEM imaging provides high spatial resolution (1-10nm) and quantification of the magnetic induction vector components.

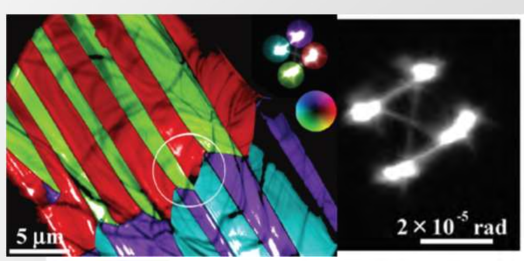

Quantum mechanical description of Lorentz TEM and Heisenberg uncertainty principle

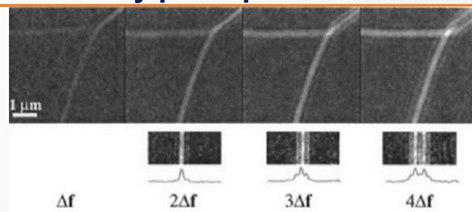

The classical description of Lorentz deflected beam does not explain the observed fringes in the convergent "bright" domain walls

$$\varphi(y) = \frac{2\pi e B_\perp t y}{h}, \qquad \nabla\varphi = \frac{2\pi e}{\lambda}\theta_L, \qquad \Delta p_y = et\Delta B_\perp$$

The magnetic phase shift relates to the magnetic flux quantum as,

$$\Delta\varphi_m(r_\perp) = \frac{2\pi e}{h}\Phi_m(r_\perp) = \pi\frac{\Phi_m(r_\perp)}{\Phi_o}, where\ \Phi_o = \frac{h}{2e} \text{ is the flux quantum}$$

Uncertainty principle states $\Delta p_y \Delta y \geq h$

$$\boxed{\frac{\Delta y \Delta B_\perp t}{2} = \frac{\Delta\Phi}{2} \geq \frac{h}{2e} = \Phi_o}$$

thomas.lagrange@epfl.ch • www.epfl.ch• lumes.epfl.ch• +41 (0)21 6935861

Quantum mechanical description of Lorentz TEM and fringe spacings in LTEM images

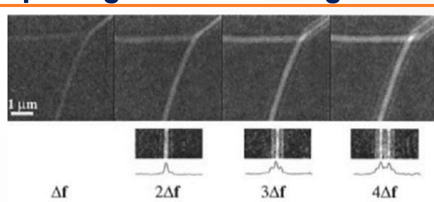

The angle (γ) between 2 sources on the image plane is,

$$\gamma = 2s\theta_L/(s + \Delta f)$$

The fringe width can be described as,

$$\delta_i = \frac{\lambda}{\gamma} = \frac{h(s+\Delta f)}{2etsB_\perp}$$

The spatial region of the fringe at the sample plane is,

$$\delta_s = \delta_i \frac{s}{s+\Delta f} = -\frac{h}{2eB_\perp t} = \frac{\Phi_o}{tB_\perp}$$

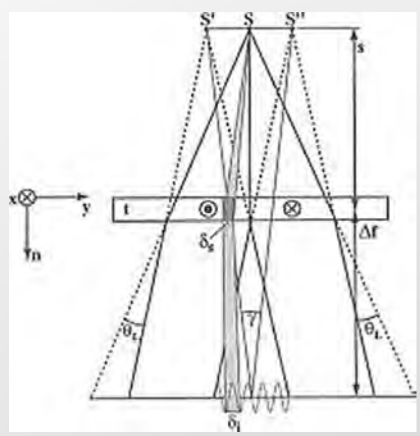

$$\boxed{\Phi_o = \delta_s\, tB_\perp}$$

thomas.lagrange@epfl.ch • www.epfl.ch• lumes.epfl.ch• +41 (0)21 6935861

thomas.lagrange@epfl.ch • www.epfl.ch• lumes.epfl.ch• +41 (0)21 6935861

thomas.lagrange@epfl.ch • www.epfl.ch• lumes.epfl.ch• +41 (0)21 6935861

53

54

Coherent control of skyrmions

Prof. Fabrizio Carbone

Collaboration:

- Henrik Ronnow, Dirk Grundler, P. Huang, A. J. Kruchkov, T. Schonenberger, M. Cantoni, A. Magrez, B. Truc, I. Madan, G. Berruto, Y. Murooka and Tom Lagrange, EPFL CH
- Damien McGrouther, R. Lamb, Glasgow UK
- Thierry Giamarchi, University of Geneva
- Achim Rosch, University of Koln

Swiss National Science Foundation

Introduction

- Dynamic imaging of magnetization in modern microscopy
- Magnetic skyrmions:
  - Properties
  - Control
- Coherent control of skyrmions

Modern Electron Microscopy

Observing atoms

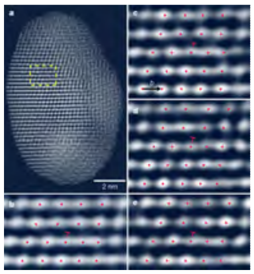

Nature 496 74 (2013)

Observing charges/orbitals

Tokunga et al., Nat. Mater. 5 (2006)

Observing spins

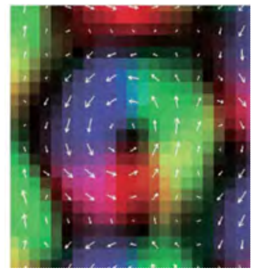

Seki et al, Science 336 (2012)

Textured ground states rule the physics of novel materials

Reciprocal-space probes average over the illuminated area

dynamical imaging

Why time-resolved experiments?

Given a distribution of
Ions
Spins or
Charges
Their dynamical evolution reveals
Their properties across phase-transitions

Blake R (1993) Cats perceive biological motion. Psychological Science 4, 54-57
http://www.psy.vanderbilt.edu/faculty/blake/BM/BioMot.html

The stroboscopic method

Stroboscopic pump-probe concept

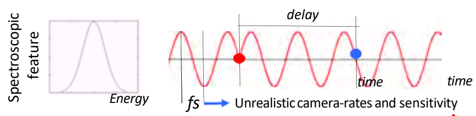

pump or clock
probe

Need for clocking (pump) and reversible processes

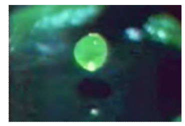

Pump is the hose ejecting a drop at periodic times (reversible-like process)

Probe is the light flash

https://www.youtube.com/watch?v=YTj4Hi1HdJQ

Lattice dynamics

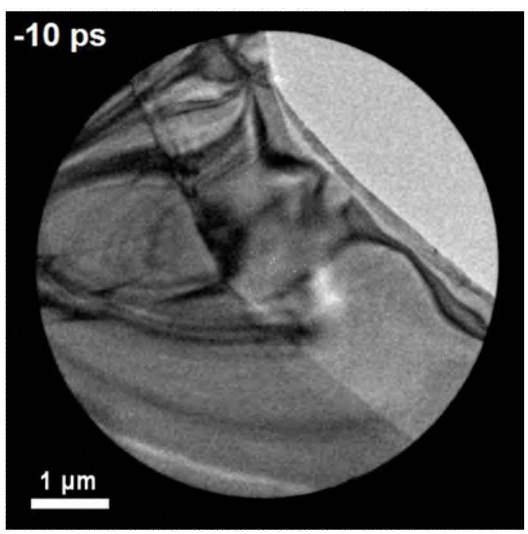

Cremons et al, Nat. Comm. 7, 11230 (2016)

Charge dynamics

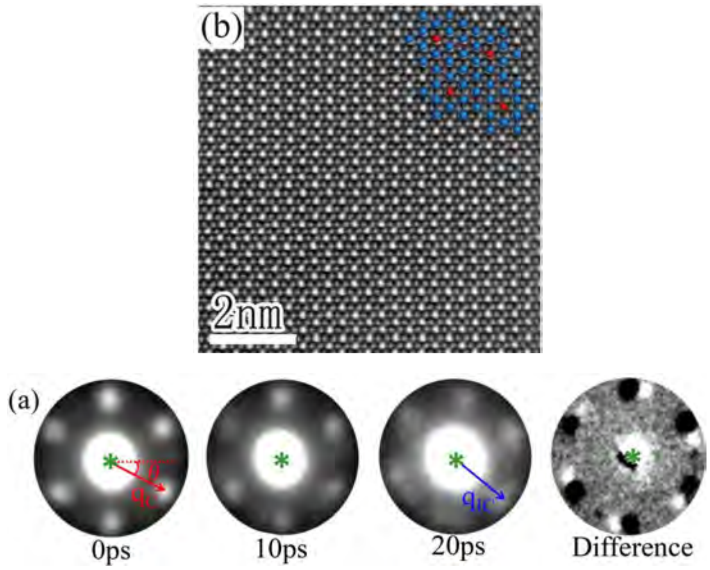

Sun et al., Phys. Rev. B 92 224303 (2015)

Spin dynamics

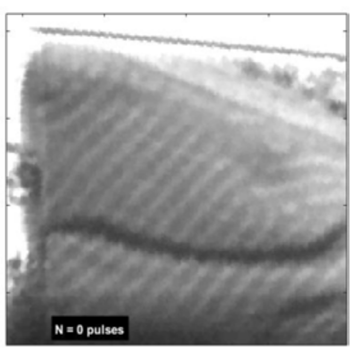

Berruto et al., Phys. Rev. Lett. 120 117201 (2018)

Magnetic skyrmions

Dzyaloshinskii-Moriya Interaction: favors canting of antiparallel spins. Promotes weak frerromagnetism in antiferro background

$$\mathcal{H}_{DM} = \sum_{i,j} \mathbf{D}_{ij} \cdot (\mathbf{S}_i \times \mathbf{S}_j),$$

$$\mathcal{H}_{DM}^{\mathrm{Bloch}} = -D \sum_i \left(\mathbf{S}_i \times \mathbf{S}_{i+\hat{x}} \cdot \hat{x} + \mathbf{S}_i \times \mathbf{S}_{i+\hat{y}} \cdot \hat{y} \right),$$

$$\mathcal{H}_{DM}^{\mathrm{N\acute{e}el}} = -D \sum_i \left(\mathbf{S}_i \times \mathbf{S}_{i+\hat{x}} \cdot \hat{y} - \mathbf{S}_i \times \mathbf{S}_{i+\hat{y}} \cdot \hat{x} \right),$$

Topological charge of a skyrmion:

$$Q = \frac{1}{4\pi} \int dx\, dy \; \mathbf{m} \cdot \left(\frac{\partial \mathbf{m}}{\partial x} \times \frac{\partial \mathbf{m}}{\partial y} \right),$$

$$\mathbf{m}(x, y) = \mathbf{M}(x, y)/|\mathbf{M}|$$

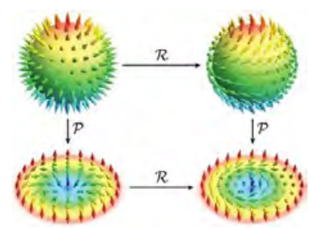

Néel skyrmion Bloch skyrmion

Roszler, Bodganov, Pfleiderer **Nature** 442 797 (2006)

Magnetic phase diagram

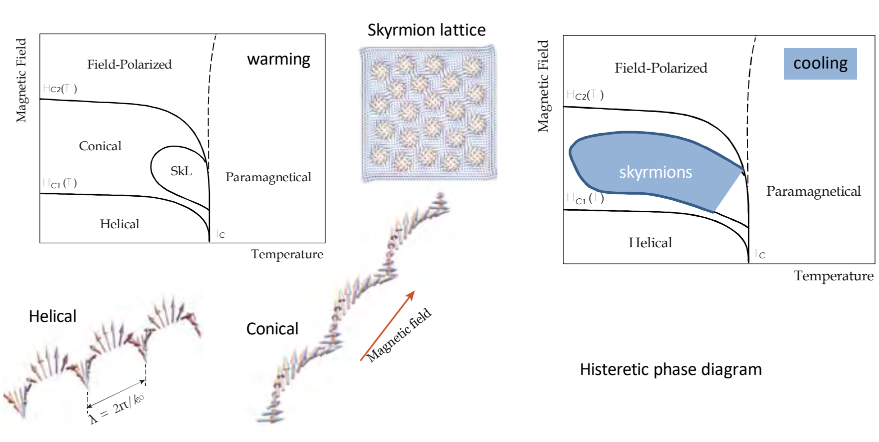

Histeretic phase diagram

A. Krutchkov PhD thesis, EPFL 2017

Topological protection vs thermodynamical fluctuations

Topological magnetization patterns determined by dynamical interplay between
- Topological protection
- Thermodynamical fluctuations

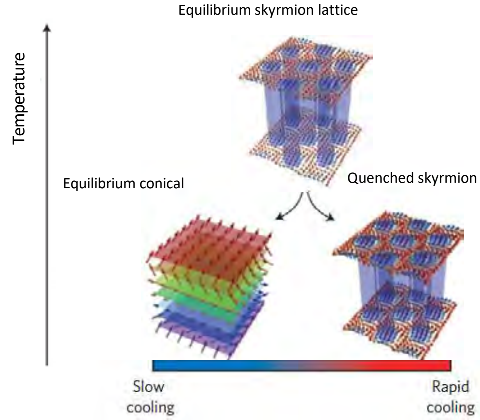

Nat. Phys. 12, 62 (2015)

How to look at skyrmions

Reciprocal space: neutron scattering

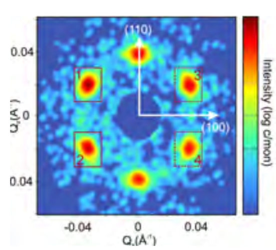

Real space: Lorentz TEM

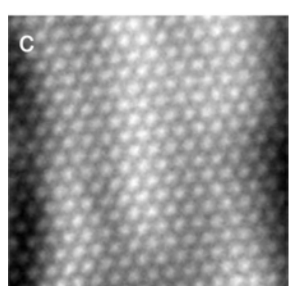

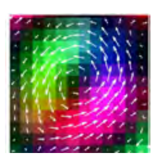

Fs Lorentz microscopy

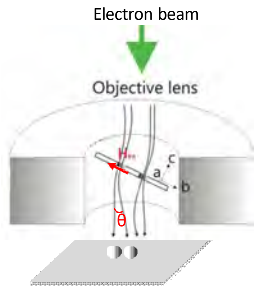

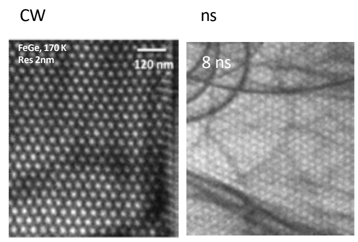

- Static images
- Camera-rate resolved movies
- Ns to fs-resolved stroboscopic movies

- θ≈ μrad
- defocus = nm – cm
- parallel illumination: beam diameter >sample
- pulsed beam: very few e^-

The Ultrafast TEM

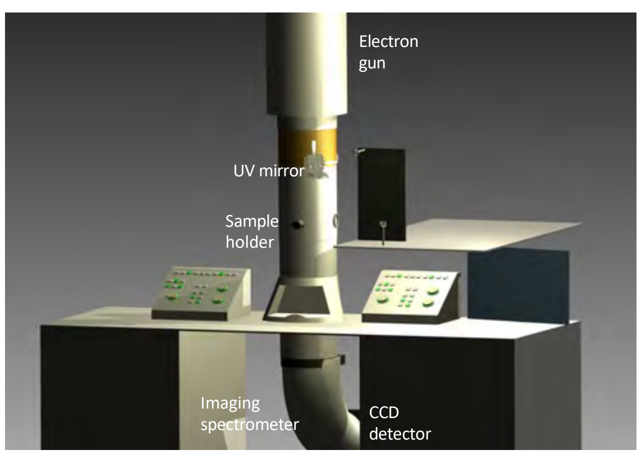

The Ultrafast TEM

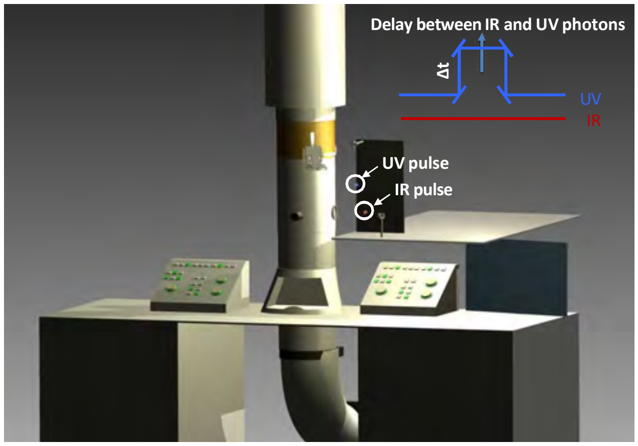

The Ultrafast TEM

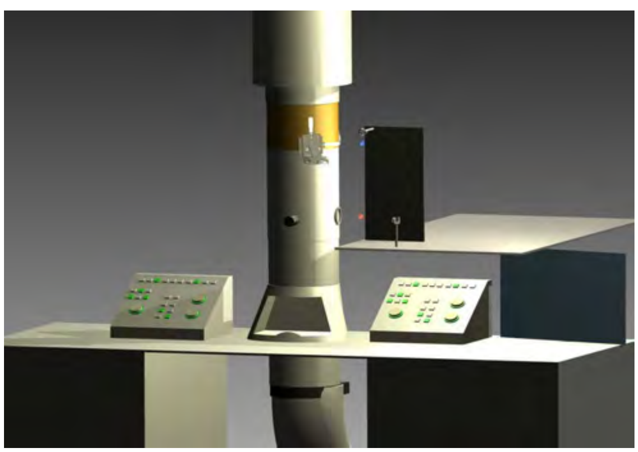

The Ultrafast TEM

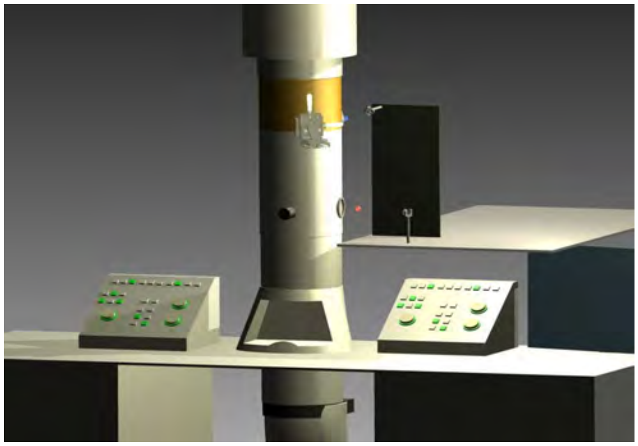

The Ultrafast TEM

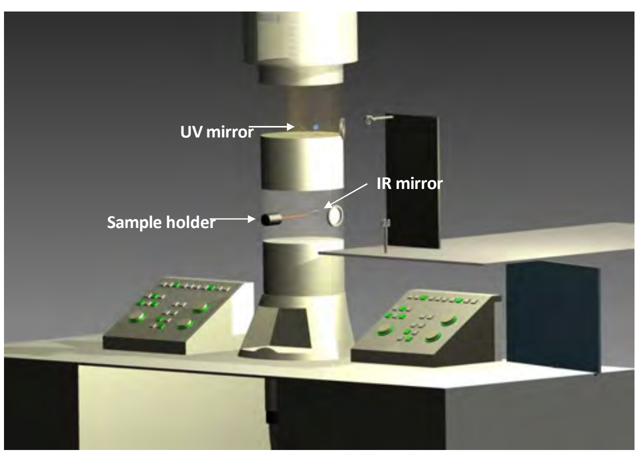

The Ultrafast TEM

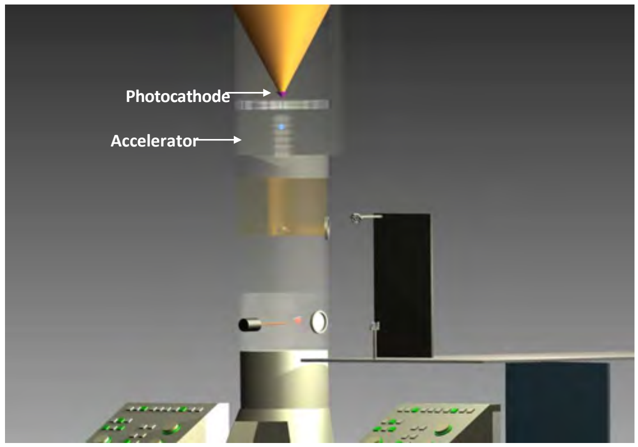

The Ultrafast TEM

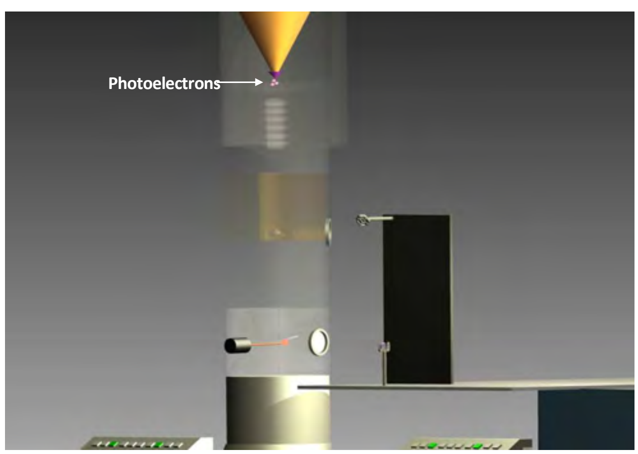

The Ultrafast TEM

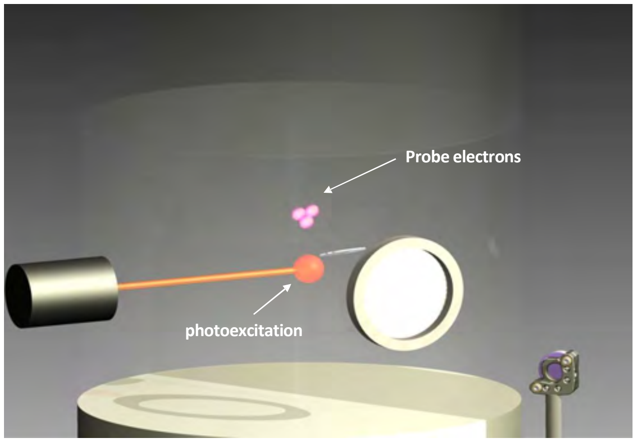

Light-control of magnetic bubbles in Co films

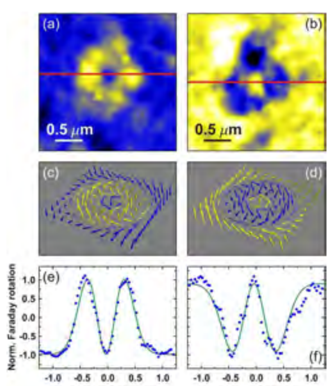

Stabilization mechanism for bubbles:
- anysotropic exchange + dipole/dipole interaction
- Chiral bubble size proportional to beam diameter

The laser beam demagnetize the core of the bubble and a whirling spin distribution forms around it

Finazzi et al., **Phys. Rev. Lett.** 110, 177205 (2013)

Dynamics of skyrmions in a metallic background

Controlling skyrmions: light-induced writing/erasing in a metal

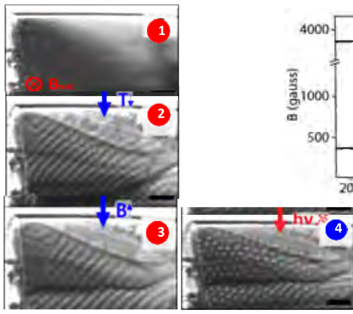

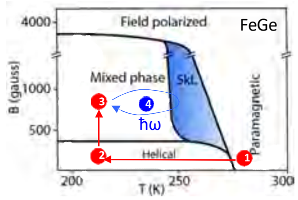

- T = 170 K, 25 ns and 2 nm resolution
- Light injects topological charge
- Skyrmion lattice melts without disordering
- Energy consumption fJ/skyrmion

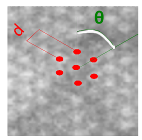

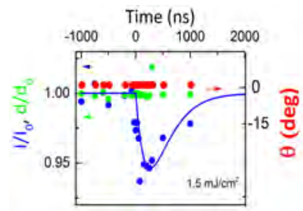

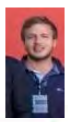

Berruto et al., Phys. Rev. Lett. 120 117201 (2018). Editor's suggestion

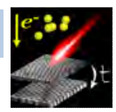

Skyrmions in Cu_2OSeO_3

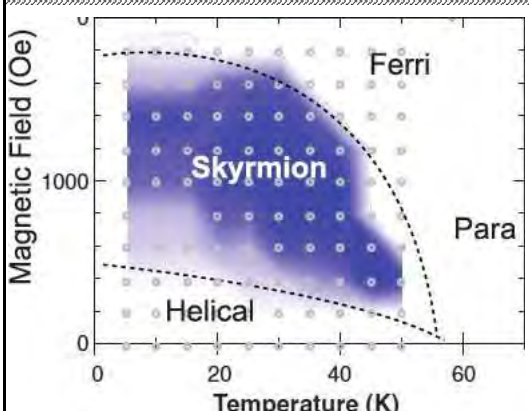

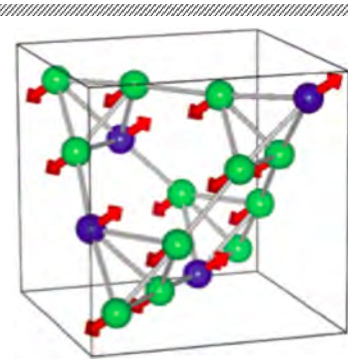

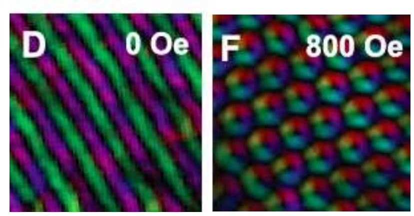

Observation of Skyrmions in a Multiferroic Material
S. Seki *et al.*
Science **336**, 198 (2012);

Skyrmions lattice ordering properties (camera-rate)

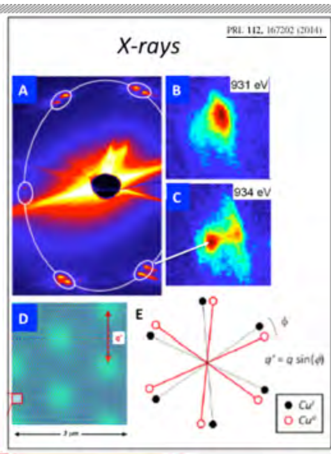

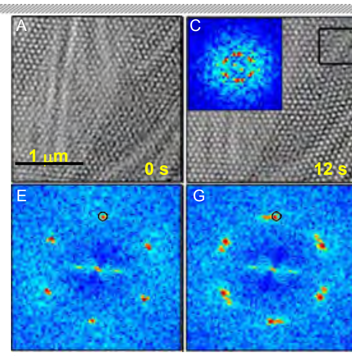

No overlapped skyrmion lattices,
time-space fluctuating domains with
different orientations (switching)

Rajeswary et al. PNAS 112 14212 (2015)

Skyrmions flowing in different background

Skyrmions motion in a ferromagnetic background (MnSi)

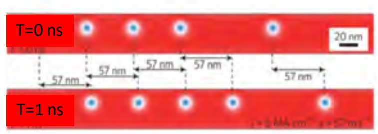

Fert et al., **Nature Nanotechnology** 8, 152–156 (2013)

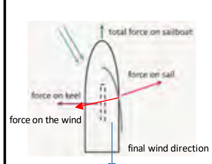

In ferromagnets:
$V_{skyrmions} = V_{current}$

In helimagnet:
$V_{skyrmions} = V_{current}/a$
a = Gilbert damping<1
Helical background = keel

Skyrmions/antiskyrmions and skyrmions clusters in the helical background Cu_2OSeO_3

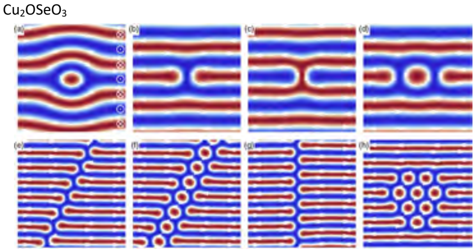

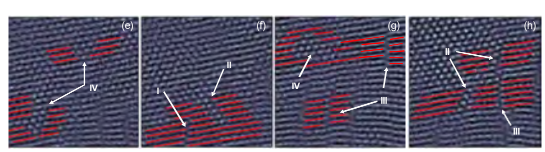

Muller et al., **Phys. Rev. Lett.** 119, 137201 (2017)

Electric field control of skyrmions

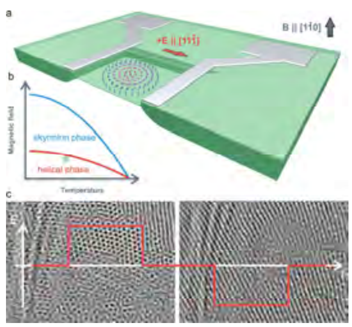

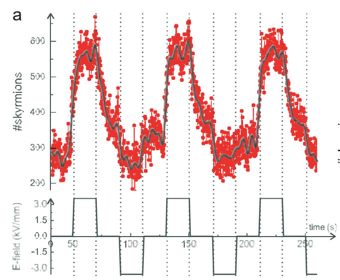

Currently limited to ms E-field pulse. Energy consumption: fJ/skyrmion

Huang et al., **Nanoletters** under review: arXiv:1710.09200

Discovery of the hexatic phase of the SkL

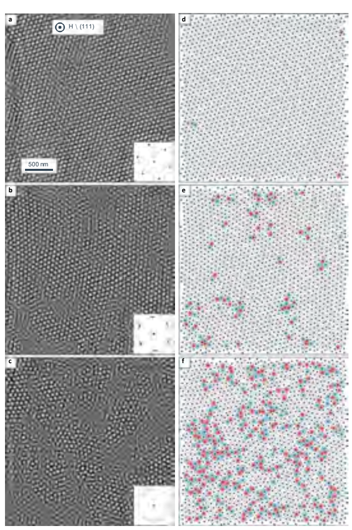

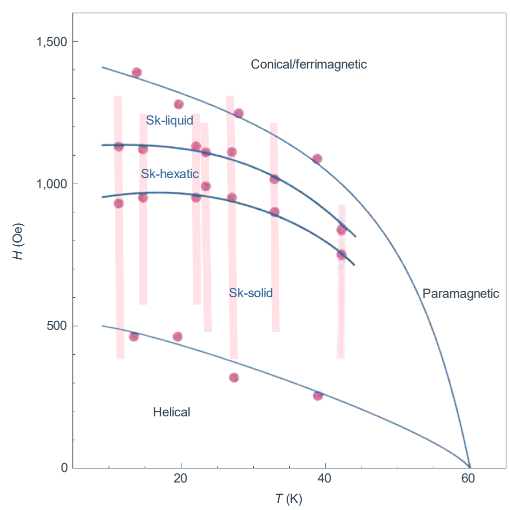

Huang et al, Nat. Nano 15 761 (2020)
News & Views Klaui Nat. Nano

Skyrmion lattice melting

Translational order parameter

$$\Psi_{q_l}(\mathbf{r}) = e^{-i\mathbf{q}_l \cdot \mathbf{r}}$$

Translational correlation function

$$G_k(r) = \frac{1}{6}\sum_{l=1}^{6}\frac{1}{N_r}\sum_{\langle i,j\rangle}\Psi_{q_l}(\mathbf{r}_i)\Psi^*_{q_l}(\mathbf{r}_j)$$

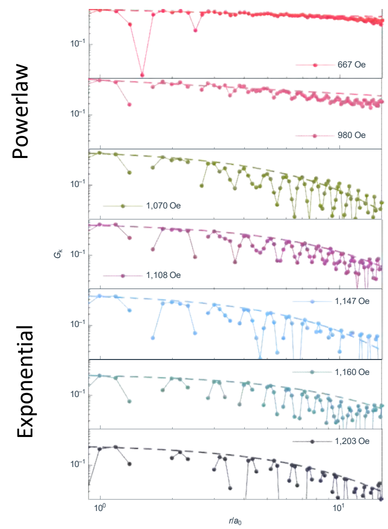

Coherent control of skyrmions

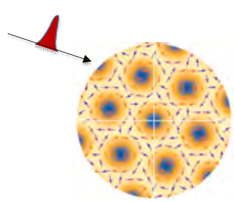

1 fs circularly polarized IR (>1!") laser pulse induces a rotation

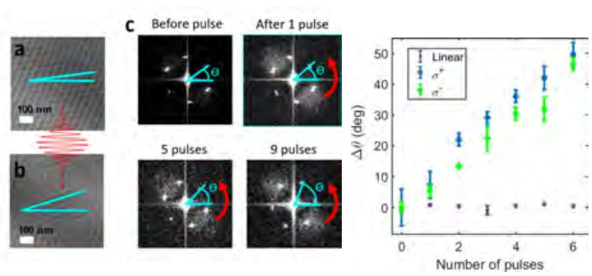

How fast does it rotate? What causes it?

- First hint: rotation has a threshold 2mJ/cm²

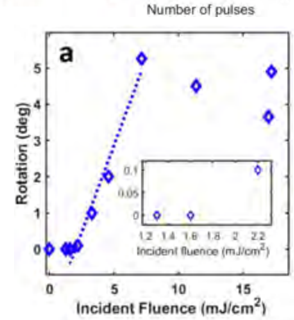

Coherent control of skyrmions

- Is it a thermal effect? Above a certain temperature jump the lattice rotates?
  - Happens on a slow time-scale (ns to !s) ?
  - Should not depend on polarization (CuOSeO is optically isotropic)
  - Threshold fluence should be higher for wavelengths corresponding to lower absorption coefficient

Rotation is an **IRREVERSIBLE** effect, no stroboscopic method possible

Two pump pulses, CW imaging with LTEM

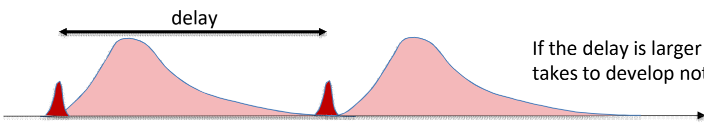

If the delay is larger than the time heat takes to develop nothing happens

Each pulse is **half** what is needed to induce rotation

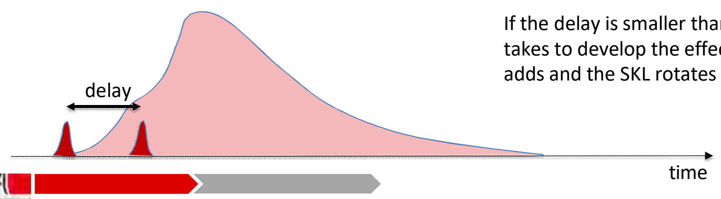

If the delay is smaller than the time heat takes to develop the effect of the two pulses adds and the SKL rotates

Coherent control of skyrmions

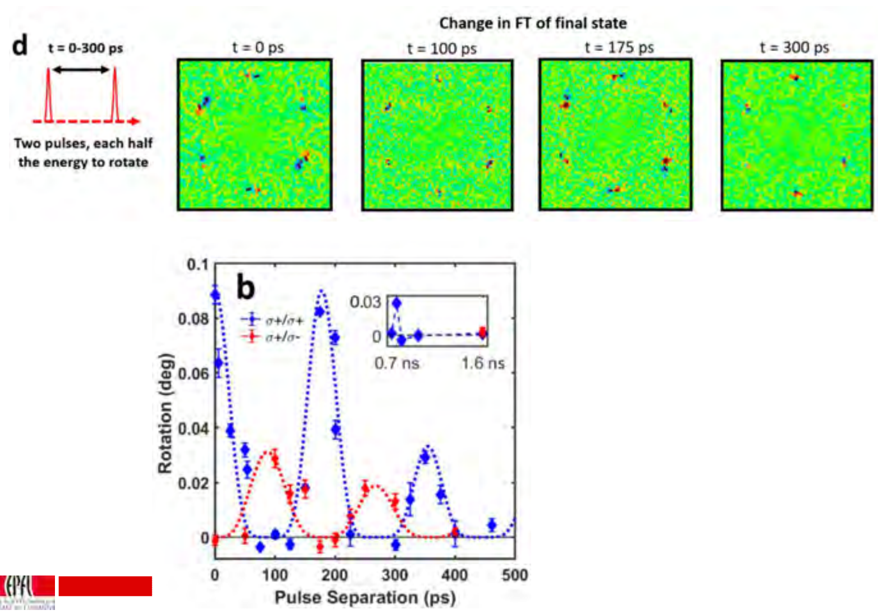

Inverse-Farady induced coherent magnons

IR pump, induces coherent oscillations of the magnetization via inverse Faraday effect. Oscillations are vibration modes of the SKL

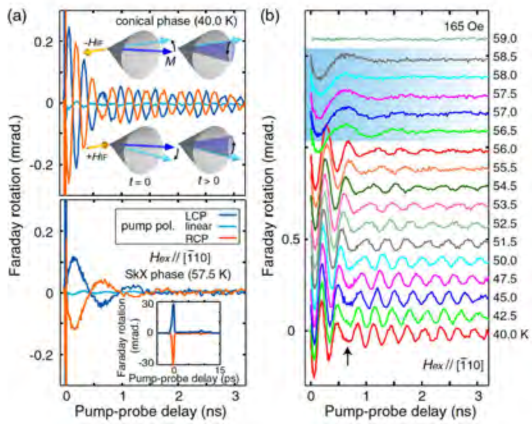

Ultrafast MOKE on CuOSeO

Ogawa, Seki, Tokura,
Sci. Rep. (2015)

Coherent control of skyrmions

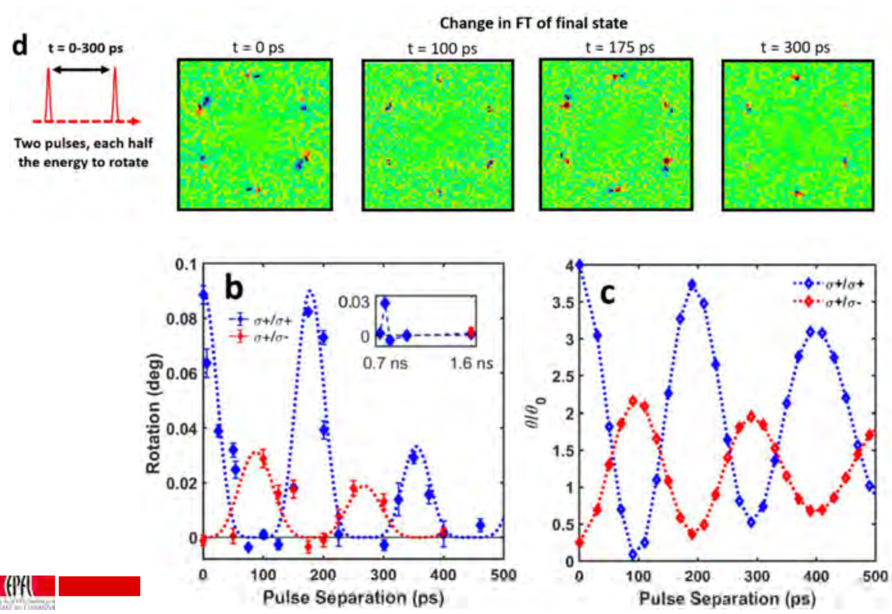

Coherent control of skyrmions

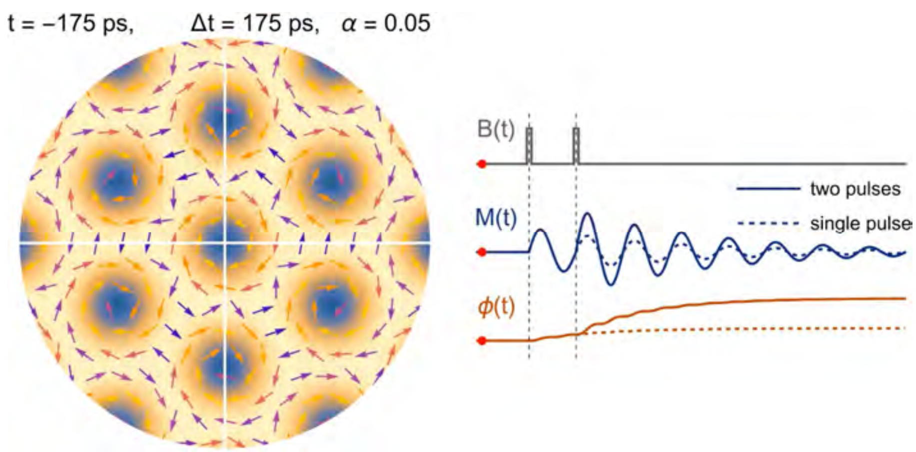

Take home messages

- Magnetic background influences skyrmions motion
- Laser light can write/erase skyrmions via super-cooling effects
- Electric fields can move/create skyrmions efficiently
- Inverse Faraday effect provides the possibility to coherently control the skyrmions

Imparting topological charge to electrons

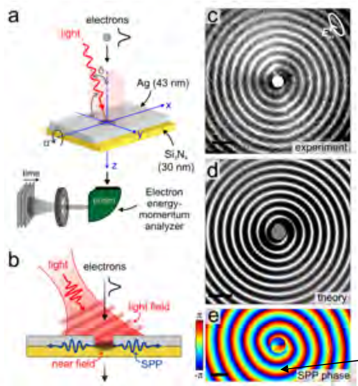

- Chiral SPP launched by elliptically polarized light
- Simulated Chiral SPP
- A chiral plasmonic field can impart a phase singularity onto the transverse component of an e^- wavefunction

Vanacore et al., arXiv:1806.00366

Electron vortex beam, m = 1

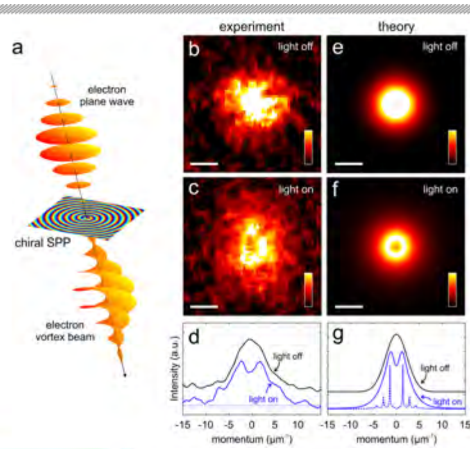

Electron wavefunction microscopy in momentum space

Vanacore et al., arXiv:1806.00366

Light-control of skyrmions in FeGe (metallic)

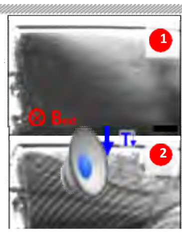

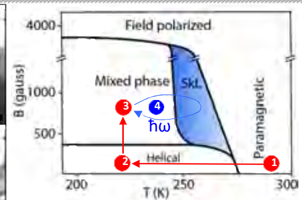

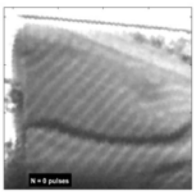

- Supercooling stabilizes skyrmions
- Light injects topological charge
- Energy consumption fJ/bit
- Histeretic PD shape depends on cooling rate

Berruto et al., **Phys. Rev. Lett.** 120, 117201 (2018)

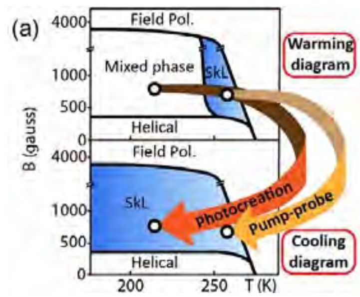

Skyrmion writing mechanism

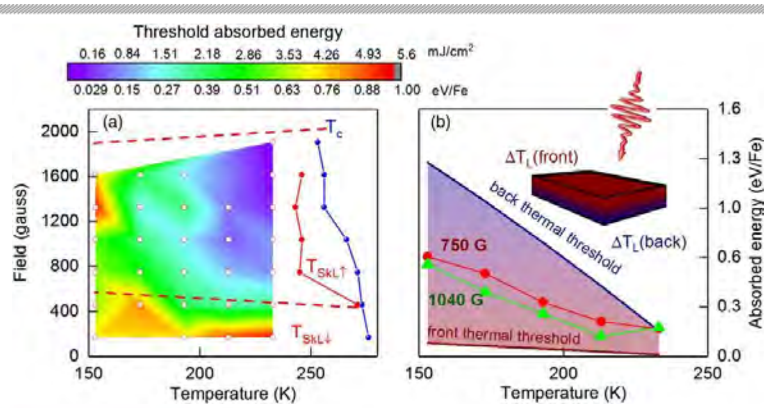

Transient lattice temperature must exceed $T_{Sk\uparrow}$

Berruto et al., **Phys. Rev. Lett.** 120, 117201 (2018)

Skyrmion writing mechanism

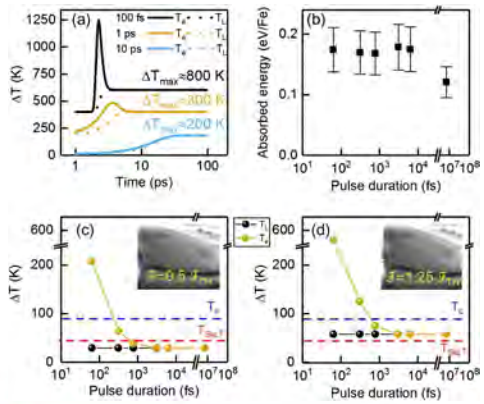

- No effect of the electronic temperature (slow response of the magnetic system)

Berruto et al., **Phys. Rev. Lett.** 120, 117201 (2018)

Skyrmions erasing mechanism (ns pump-probe)

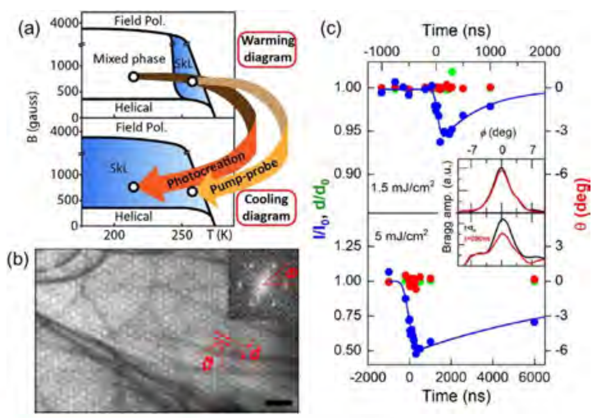

- Skyrmion lattice quenched without distorting it
- Melting the SkL with B does go through positional and orientational disorder (paper in prep.)

Berruto et al., **Phys. Rev. Lett.** 120, 117201 (2018)

POGGIO LAB

Nanomagnetic Imaging using Scanning Probe Microscopy Techniques

PhD Course:
"Advanced microscopy techniques for characterizing magnetic properties of materials"
17.11.2022
Prof. Martino Poggio

Based on *Nat. Rev. Phys.* **4**, 49 (2022).

Faraday's iron filings

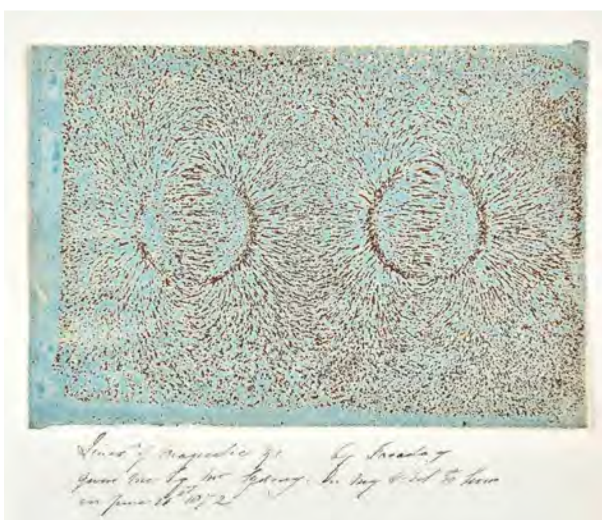

M. Faraday, ca. 1830s

2

Scanning tunnelling spectroscopy on atomic-scale

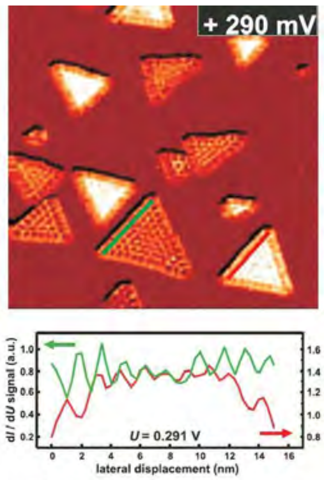

FIG. 44. (Color) SP-STS data (60×60 nm²) revealing the spin dependence of the 2D electronic confinement states in nano-scale Co islands which manifests itself by a spin-dependent oscillation amplitude of the confinement states for differently magnetized Co nanoislands. From Pietzsch *et al.*, 2006.

Magneto-optical imaging of local spin-polarization

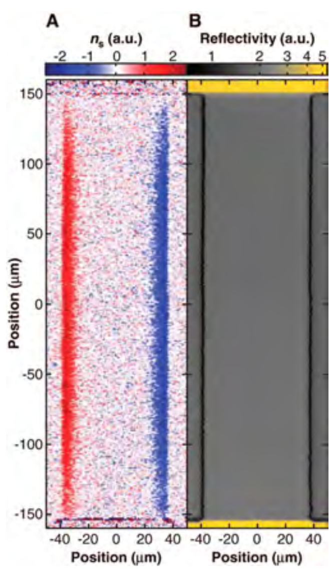

Kato et al., *Science* **306**, 5703 (2004).

Lorentz microscopy of skyrmion crystals

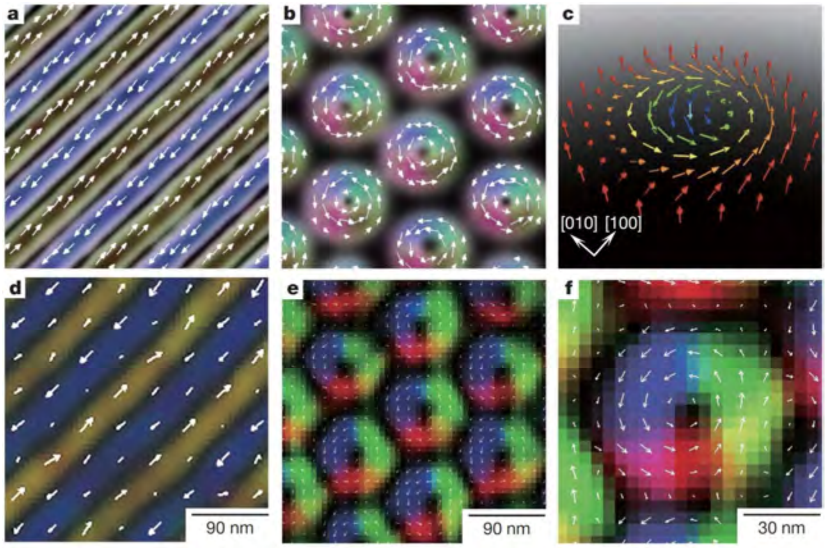

Yu et al., *Nature* **465**, 901 (2010).

5

SQUID microscopy of edge currents

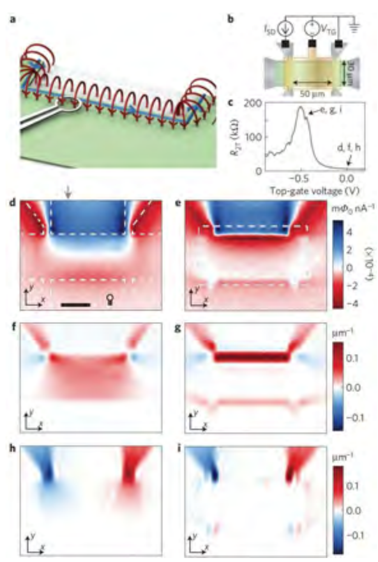

Nowack et al., *Nat. Phys.* **12**, 787 (2013).

6

Energence of 2D materials and vdW heterostructures

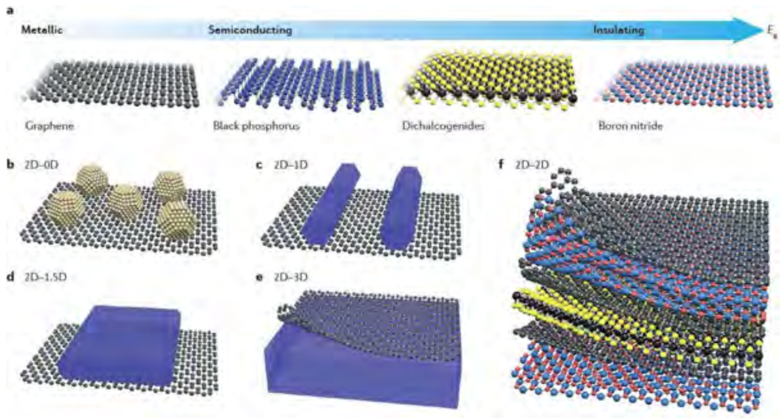

Figure 1 | **Two-dimensional layered materials and van der Waals heterostructures. a** | A broad library of two-dimensional layered materials (2DLMs) with varying chemical composition, atomic structures and electronic properties, with an increasing bandgap from left to right. **b–f** | Van der Waals heterostructures formed by integrating the dangling-bond-free 2DLMs with 0D nanoparticles or quantum dots (panel **b**), 1D nanowires (panel **c**), 1.5D nanoribbons (panel **d**), 3D bulk materials (panel **e**) and 2D nanosheets (panel **f**).

Liu et al., *Nat. Rev. Mater.* **1**, 1 (2016)

7

Energence of 2D materials and vdW heterostructures

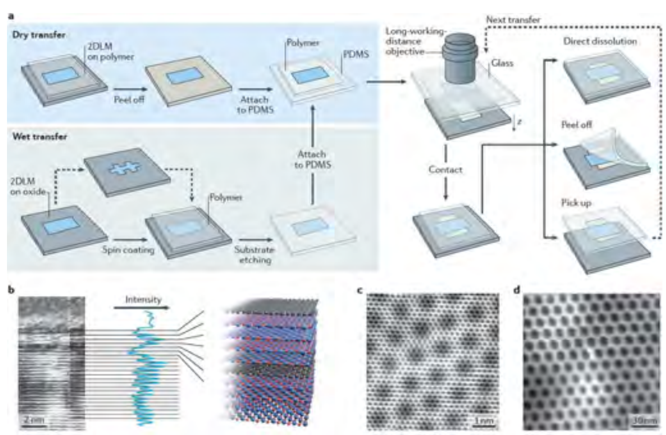

Figure 2 | **Assembly and characterization of 2D–2D vdWHs. a** | Schematic illustration of state-of-the-art alignment transfer processes for van der Waals heterostructure (vdWH) integration. Wet and dry transfer techniques are used to attach the target sheet to the stamp material. The stamp is then attached to a glass slide and placed in a transfer microscope. Micromanipulators allow for the precise alignment of sheets using a long-working-distance objective lens. The polymer transfer stamp can either be chemically dissolved away, mechanically peeled off or used to pick up the entire stack for further transfer steps. **b** | False-coloured high-resolution cross-sectional scanning tunnelling electron microscopy image of the BN–graphene–BN–graphene stack (left) and a corresponding schematic representation (right). **c,d** | Moiré pattern of graphene on BN (panel **c**) and a much larger moiré pattern of the commensurate–incommensurate transition of graphene on BN (panel **d**). 2DLM, two-dimensional layered material; BN, boron nitride; PDMS, poly(dimethyl siloxane). Panel **b** is from REF. 71, Nature Publishing Group. Panel **c** is courtesy of Brian LeRoy, University of Arizona, USA. Panel **d** is from REF. 75, Nature Publishing Group.

Liu et al., *Nat. Rev. Mater.* **1**, 1 (2016)

8

Correlated states in atomically layered materials

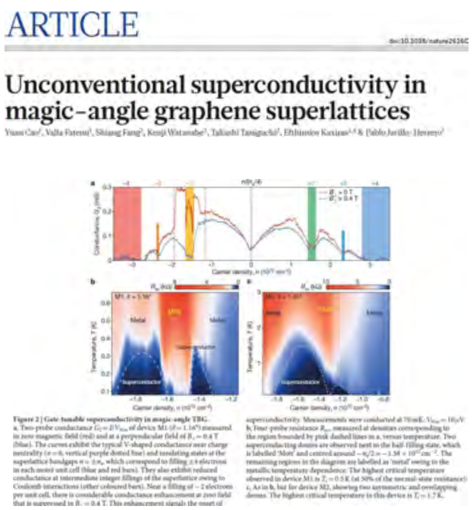

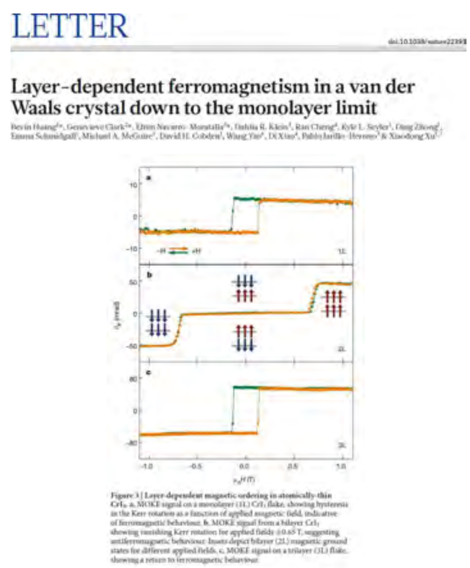

9

How to decipher the mechanism behind these phenomena?

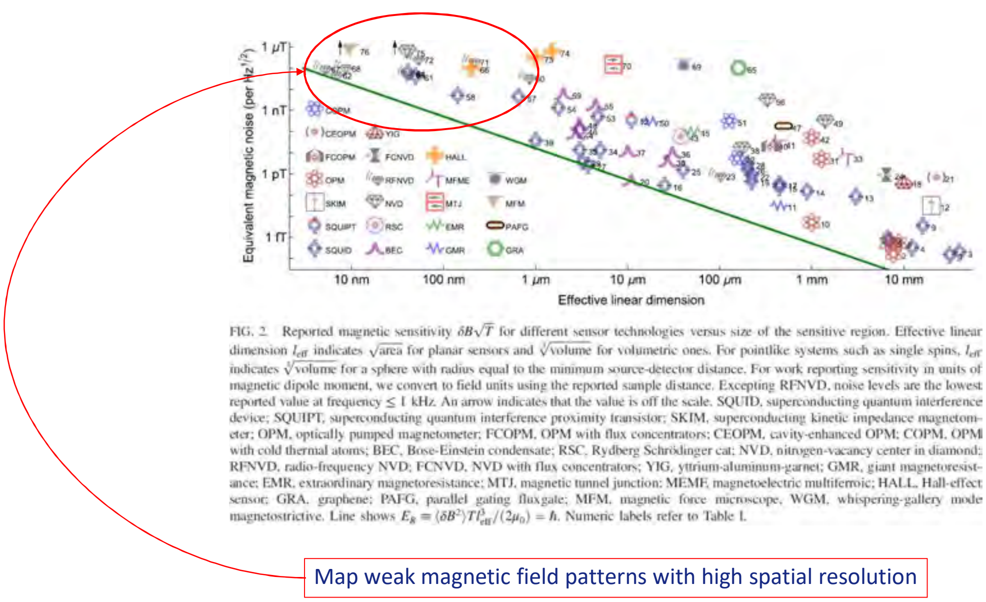

FIG. 2. Reported magnetic sensitivity $\delta B\sqrt{T}$ for different sensor technologies versus size of the sensitive region. Effective linear dimension L_{eff} indicates $\sqrt{\text{area}}$ for planar sensors and $\sqrt[3]{\text{volume}}$ for volumetric ones. For pointlike systems such as single spins, L_{eff} indicates $\sqrt[3]{\text{volume}}$ for a sphere with radius equal to the minimum source-detector distance. For work reporting sensitivity in units of magnetic dipole moment, we convert to field units using the reported sample distance. Excepting RFNVD, noise levels are the lowest reported value at frequency ≤ 1 kHz. An arrow indicates that the value is off the scale. SQUID, superconducting quantum interference device; SQUIPT, superconducting quantum interference proximity transistor; SKIM, superconducting kinetic impedance magnetometer; OPM, optically pumped magnetometer; FCOPM, OPM with flux concentrators; CEOPM, cavity-enhanced OPM; COPM, OPM with cold thermal atoms; BEC, Bose-Einstein condensate; RSC, Rydberg Schrödinger cat; NVD, nitrogen-vacancy center in diamond; RFNVD, radio-frequency NVD; FCNVD, NVD with flux concentrators; YIG, yttrium-aluminum-garnet; GMR, giant magnetoresistance; EMR, extraordinary magnetoresistance; MTJ, magnetic tunnel junction; MEMF, magnetoelectric multiferroic; HALL, Hall-effect sensor; GRA, graphene; PAFG, parallel gating fluxgate; MFM, magnetic force microscope, WGM, whispering-gallery mode magnetostrictive. Line shows $E_R = \langle\delta B^2\rangle T l_{eff}^3/(2\mu_0) = \hbar$. Numeric labels refer to Table I.

Map weak magnetic field patterns with high spatial resolution

Mitchell & Palacios Alvarez, *Rev. Mod. Phys.* **92**, 021001 (2020)

10


b Scanning SQUID microscopy
Zoom-in
c Scanning NV microscopy
Zoom-in

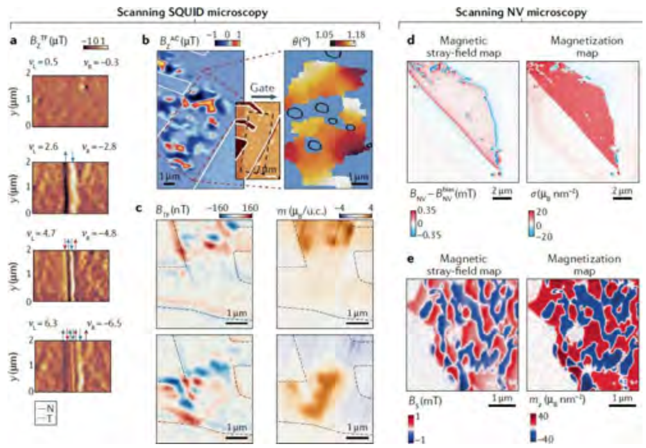
Scanning SQUID microscopy
Scanning NV microscopy
Gate
Magnetic stray-field map
Magnetization map
1 μm
2 μm

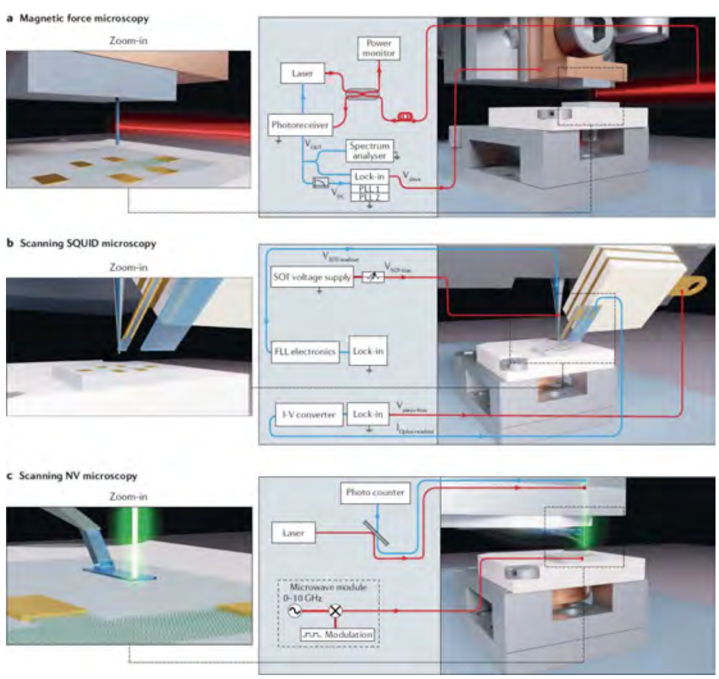
a Magnetic force microscopy
Zoom-in
Power monitor
Laser
Photoreceiver
Spectrum analyser
Lock-in
b Scanning SQUID microscopy
Zoom-in
SOT voltage supply
FLL electronics
Lock-in
I-V converter
Lock-in
c Scanning NV microscopy
Zoom-in
Photo counter
Laser
Microwave module
0–10 GHz
Modulation

Idealized signal sources

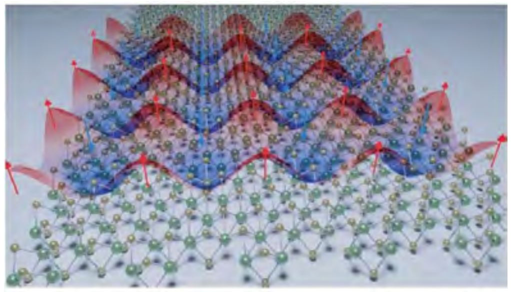

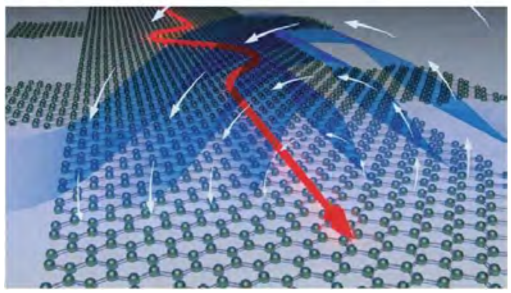

Magnetic imaging by "force microscopy" with 1000 Å resolution

Y. Martin and H. K. Wickramasinghe
IBM T. J. Watson Research Center, P. O. Box 218, Yorktown Heights, New York 10598

(Received 19 December 1986; accepted for publication 19 March 1987)

We describe a new method for imaging magnetic fields with 1000 Å resolution. The technique is based on using a force microscope to measure the magnetic force between a magnetized tip and the scanned surface. The method shows promise for the high-resolution mapping of both static and dynamic magnetic fields.

Appl. Phys. Lett. **50** (20), 18 May 1987

Magnetic force microscopy: General principles and application to longitudinal recording media

D. Rugar, H. J. Mamin, P. Guethner,[a] S. E. Lambert,[b] J. E. Stern,[c] I. McFadyen,[b] and T. Yogi[b]
IBM Research Division, Almaden Research Center, 650 Harry Road, San Jose, California 95120-6099

(Received 15 January 1990; accepted for publication 13 April 1990)

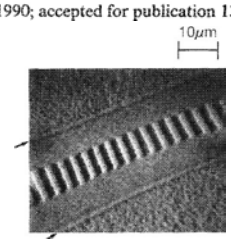

J. Appl. Phys. **68** (3), 1 August 1990

MFM achieves down to 10 nm resolution

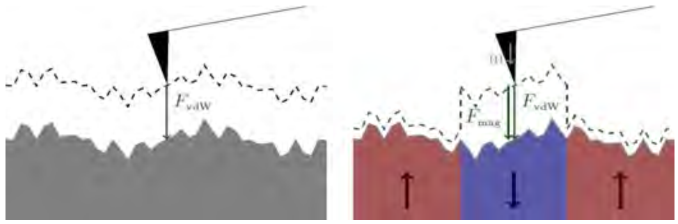

Schwenk, *Ph.D. Thesis in Physics,* University of Basel (2016).

Schmid et al., *Phys. Rev. Lett.* **105**, 197201 (2010).

15

NWs with magnetic tips

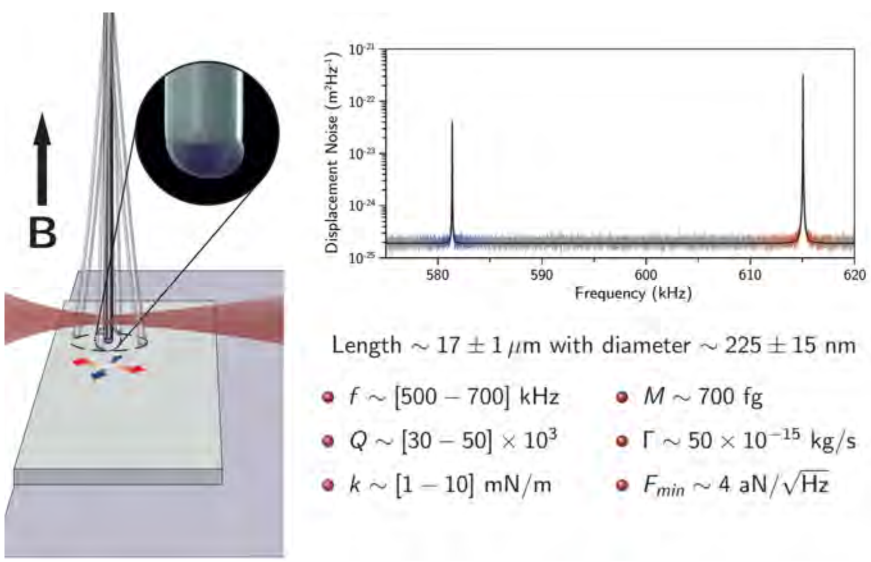

Rossi et al., *Nano Lett.* **19**, 930 (2019).

16

MFM

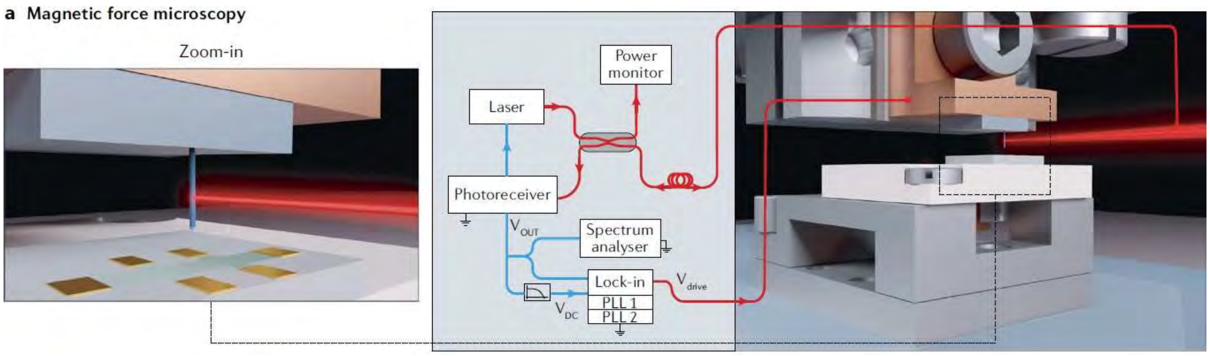
a Magnetic force microscopy
Zoom-in
Power monitor
Laser
Photoreceiver
Spectrum analyser
Lock-in
PLL 1
PLL 2
V_{OUT}
V_{DC}
V_{drive}

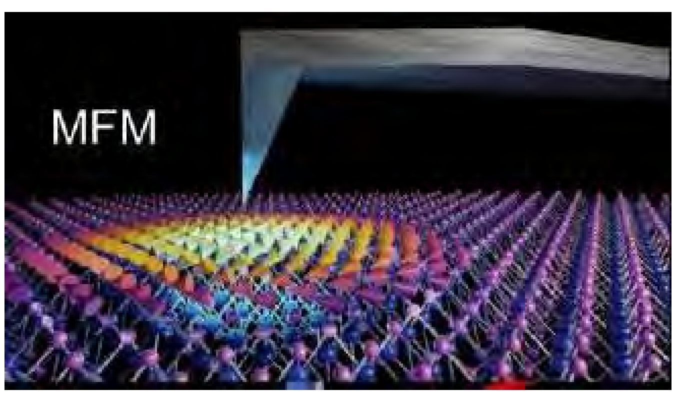
MFM

SCANNING SQUID MICROSCOPY

John R. Kirtley
IBM T. J. Watson Research Center, Yorktown Heights, New York 10598; e-mail: kirtley@watson.ibm.com

John P. Wikswo, Jr.
Department of Physics and Astronomy, Vanderbilt University, Nashville, Tennessee 37235; e-mail: wikswojp@ctrvax.vanderbilt.edu

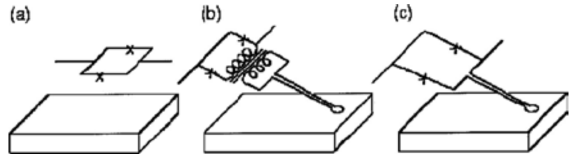

Annu. Rev. Mater. Sci. 1999. 29:117–48

Pick-up loop scanning SQUIDs

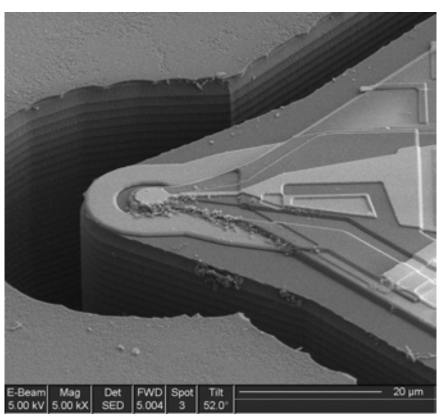

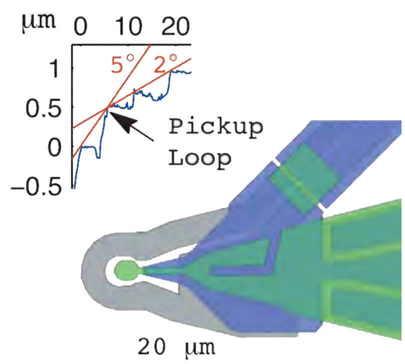

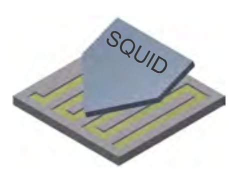

- Spatial resolution ~ 1 µm
- Field sensitivity ~ 130 nT $Hz^{-1/2}$
- ~ 400 nm to the sample

Koshnick et al., APL **93**, 243101 (2008)
Kirtley et al., RSI **87**, 093702 (2016)

Self-Aligned Nanoscale SQUID on a Tip

Amit Finkler,*,† Yehonathan Segev,† Yuri Myasoedov,† Michael L. Rappaport,† Lior Ne'eman,† Denis Vasyukov,† Eli Zeldov,† Martin E. Huber,‡ Jens Martin,§ and Amir Yacoby§

†Department of Condensed Matter Physics, Weizmann Institute of Science, Rehovot 76100, Israel, ‡Departments of Physics and Electrical Engineering, University of Colorado, Denver, Colorado 80217, and §Department of Physics, Harvard University, Cambridge, Massachusetts 02138

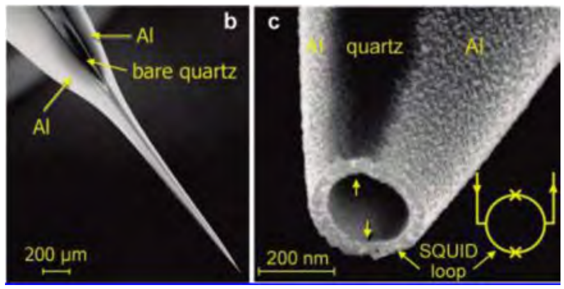

Nano Lett. **2010,** *10,* 1046–1049

Intial results show great potential

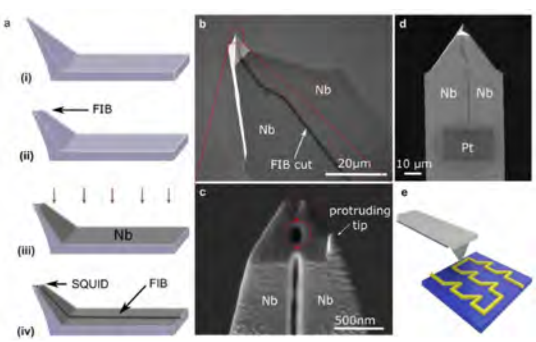

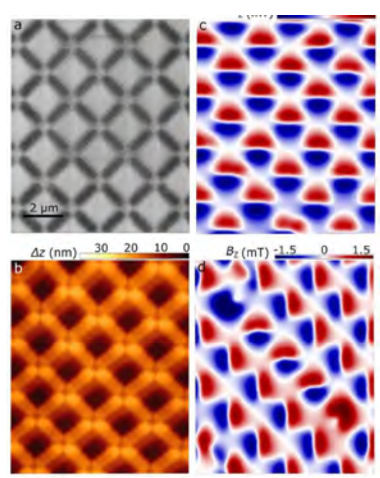

Scanning SQUID Microscopy

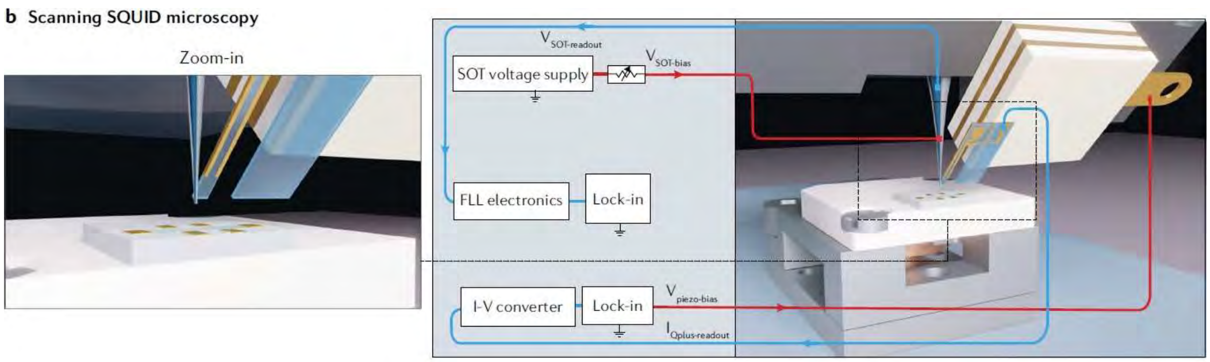

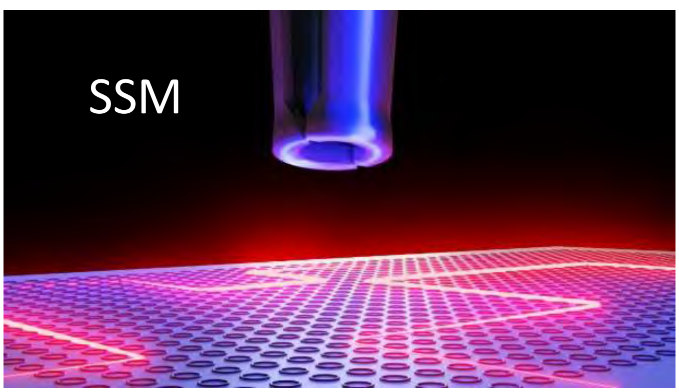

Scanning Nitrogen-vacancy Center Microscopy (SNVM)

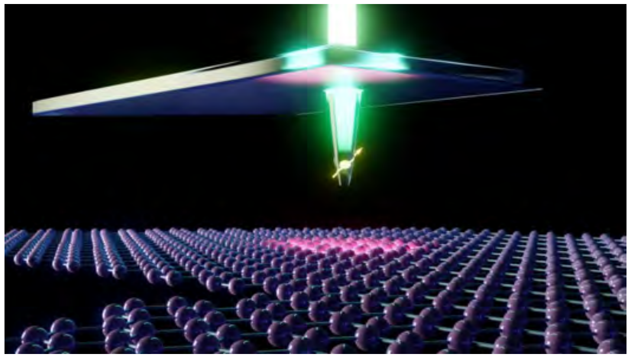

Sensitivity down to 100 nT/(Hz)$^{1/2}$

Spatial resolution down to 10 nm

Imaging current with SNVM

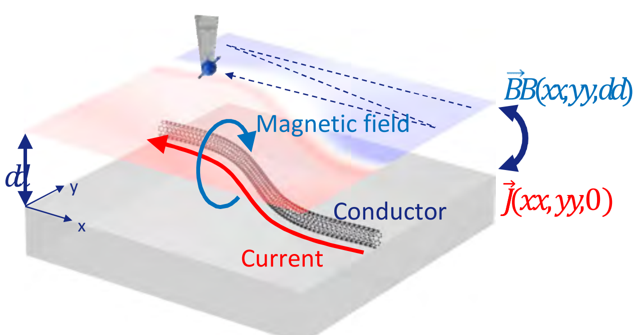

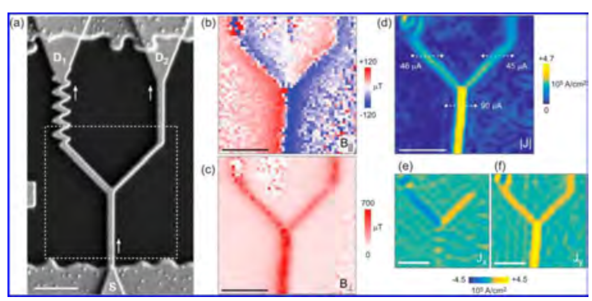

Chang et al., *Nano Lett.* **17**, 2367 (2017).

Scanning NV microscopy of 2D magnets

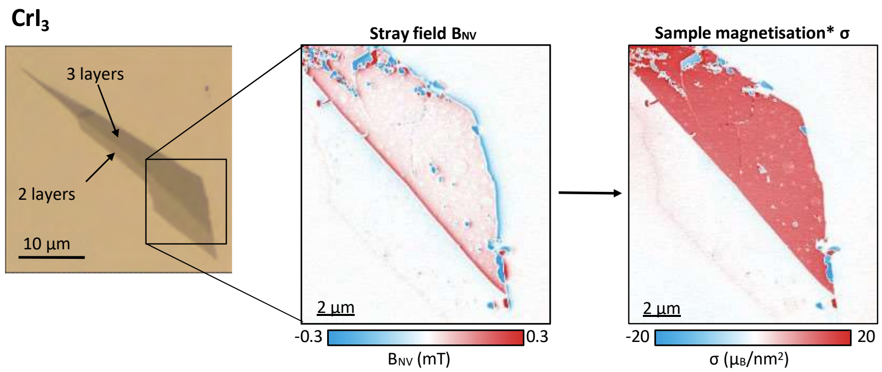

Thiel et al., *Science* **364**, 973 (2019).

27

Scanning NV Microscopy

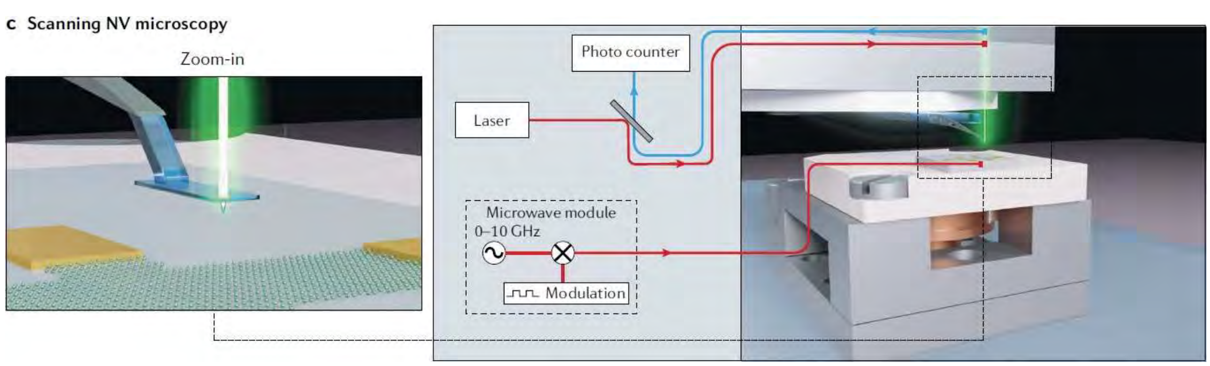

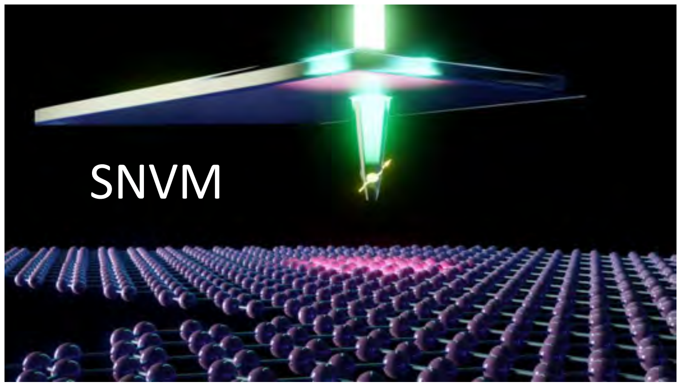

Contrast & Techniques

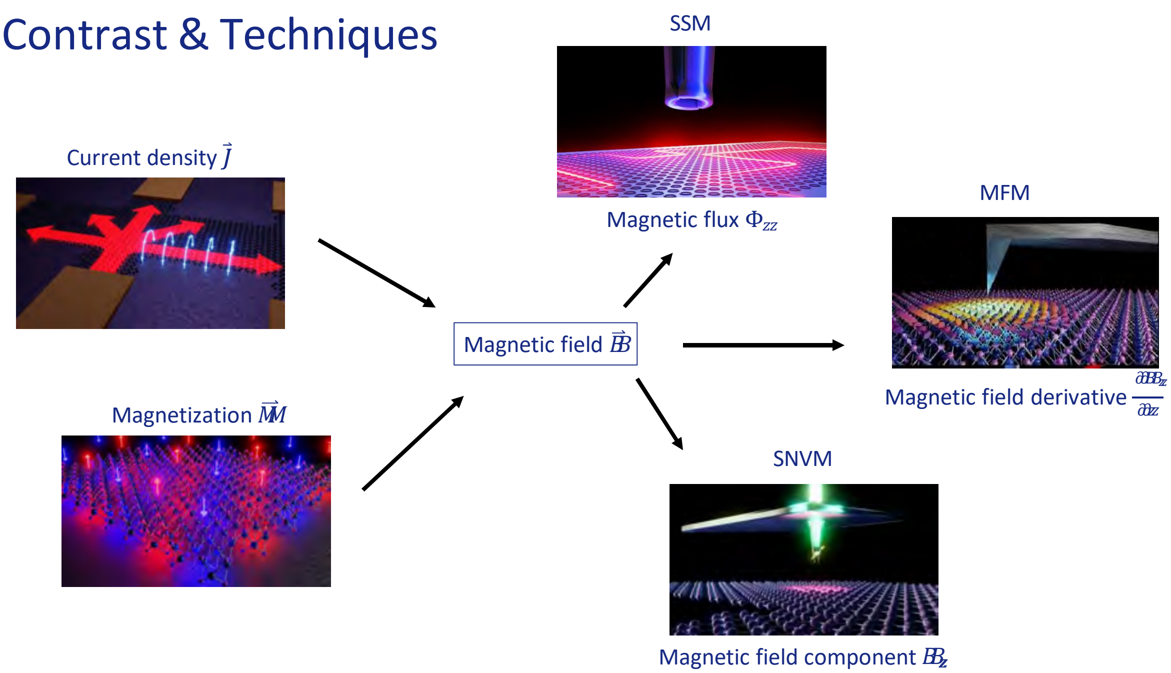

30

Probe-sample Spacing

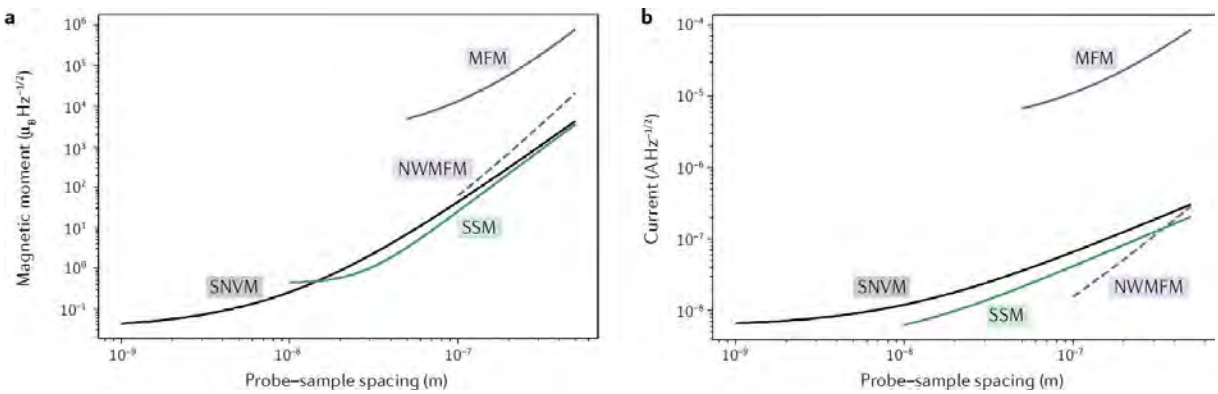

31

Sensor Size

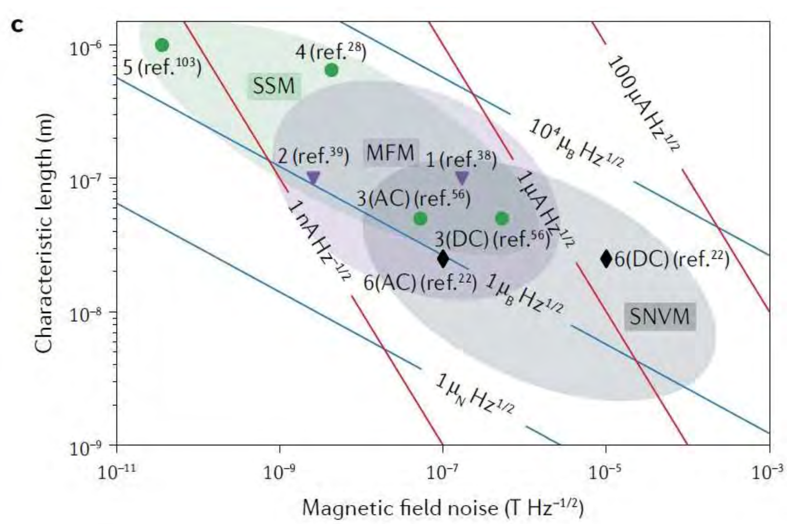

32

Properties

Table 1 | **Parameters for state-of-the-art magnetic scanning probe microscopies combining the highest sensitivity with the highest resolution**

	MFM (conventional)[31,32,38,102–104]	MFM (nanowire)[39]	SSM (susceptometer)[53]	SSM (SQUID-on-tip)[56]	SNVM[22,74,82,83]
Sensor size	10–100 nm	100 nm	0.5 μm	50 nm	<1 nm
Sensor stand-off	10–100 nm	50 nm	330 nm	25 nm	50 nm
Spatial resolution	10–100 nm	100 nm[a]	0.5 μm	100 nm	15–25 nm
DC sensitivity	10–100 $\mu T Hz^{-1/2}$	3 $nT Hz^{-1/2}$[a]	660 $nT Hz^{-1/2}$	50 $nT Hz^{-1/2}$	4 $\mu T Hz^{-1/2}$
AC sensitivity	170 $nT Hz^{-1/2}$	3 $nT Hz^{-1/2}$	130 $nT Hz^{-1/2}$	5 $nT Hz^{-1/2}$	100 $nT Hz^{-1/2}$
Operating field	<20 T	<10 T	<30 mT	<1.2 T	<hundreds of mT
Operating temperature	<500 K	<300 K	<9 K	<7 K	<600 K

MFM, magnetic force microscopy; SNVM, scanning nitrogen-vacancy microscopy; SQUID, superconducting quantum interference device; SSM, scanning SQUID microscopy. [a]Represents estimates based on the properties of the sensors, which have not yet been experimentally confirmed.

Sensitivity as a function of feature size

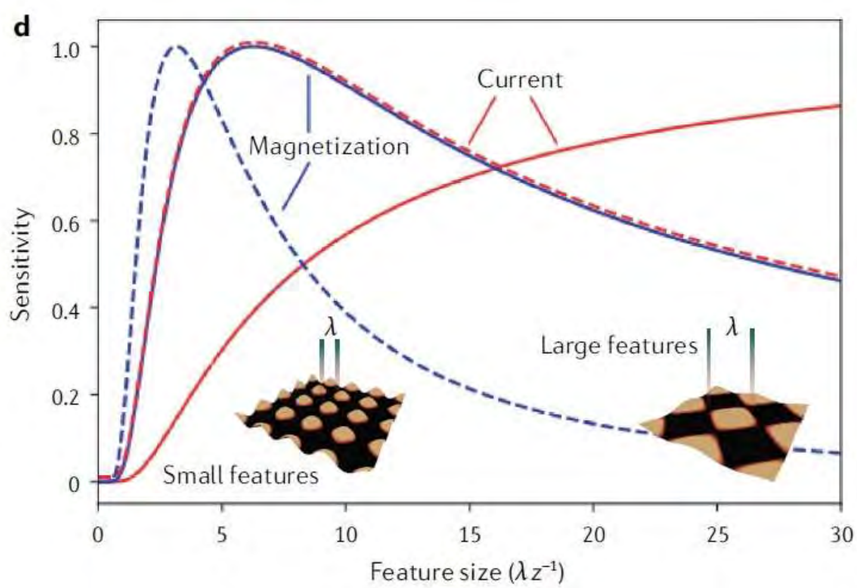

References

- Reviews on scanning magnetic field probes
  - *Nat. Rev. Phys.* **4**, 49 (2022).
  - *Rep. Prog. Phys.* **73**, 126501 (2010)
  - *Rev. Mod. Phys.* **92**, 021001 (2020)
- Current and magnetization reconstruction
  - *Nano Lett.* **17**, 2367 (2017)
  - *J. Geophys. Res.* **114**, B06102 (2009)
  - *J. Appl. Phys.* **65**, 361 (1989)

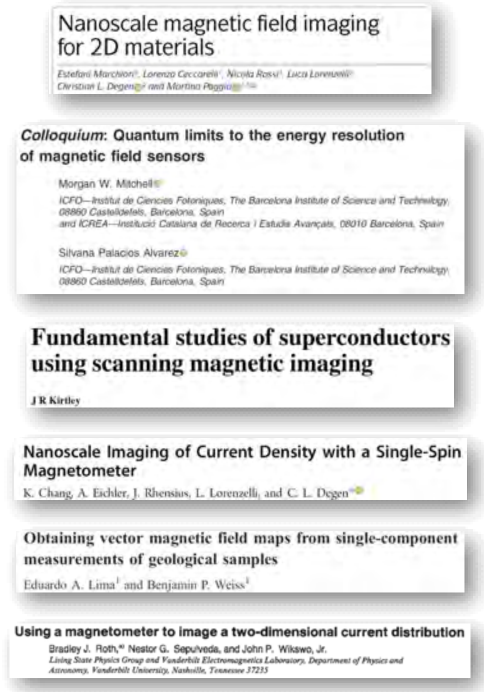

Nanoscale magnetic field imaging for 2D materials

Estefani Marchiori, Lorenzo Ceccarelli, Nicola Rossi, Luca Lorenzelli, Christian L. Degen and Martino Poggio

Colloquium: Quantum limits to the energy resolution of magnetic field sensors

Morgan W. Mitchell

ICFO—Institut de Ciencies Fotoniques, The Barcelona Institute of Science and Technology, 08860 Castelldefels, Barcelona, Spain and ICREA—Institució Catalana de Recerca i Estudis Avançats, 08010 Barcelona, Spain

Silvana Palacios Alvarez

ICFO—Institut de Ciencies Fotoniques, The Barcelona Institute of Science and Technology, 08860 Castelldefels, Barcelona, Spain

Fundamental studies of superconductors using scanning magnetic imaging

J R Kirtley

Nanoscale Imaging of Current Density with a Single-Spin Magnetometer

K. Chang, A. Eichler, J. Rhensius, L. Lorenzelli, and C. L. Degen

Obtaining vector magnetic field maps from single-component measurements of geological samples

Eduardo A. Lima[1] and Benjamin P. Weiss[1]

Using a magnetometer to image a two-dimensional current distribution

Bradley J. Roth, Nestor G. Sepulveda, and John P. Wikswo, Jr.

Living State Physics Group and Vanderbilt Electromagnetics Laboratory, Department of Physics and Astronomy, Vanderbilt University, Nashville, Tennessee 37235

Nanomagnetic Imaging using Scanning Probe Microscopy Techniques

PhD Course, EPFL, 2022

Sensitivity

To evaluate sensitivity : Signal - to - noise

Let's take two idealized signals :

- a line of current $\vec{I}$
- a magnetic moment $\vec{m}$

- Current :

$$\vec{B}_I = \frac{\mu_0 \, \vec{I} \times \vec{r}}{2\pi r^2}$$

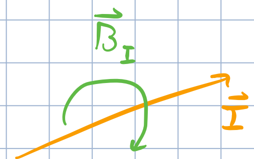

- moment :

$$\vec{B}_m = \frac{\mu_0}{4\pi r^3}\left(\frac{3(\vec{m}\cdot\vec{r})\,\vec{r}}{r^2} - \vec{m}\right)$$

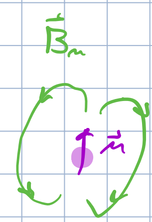

MFM

- Signal

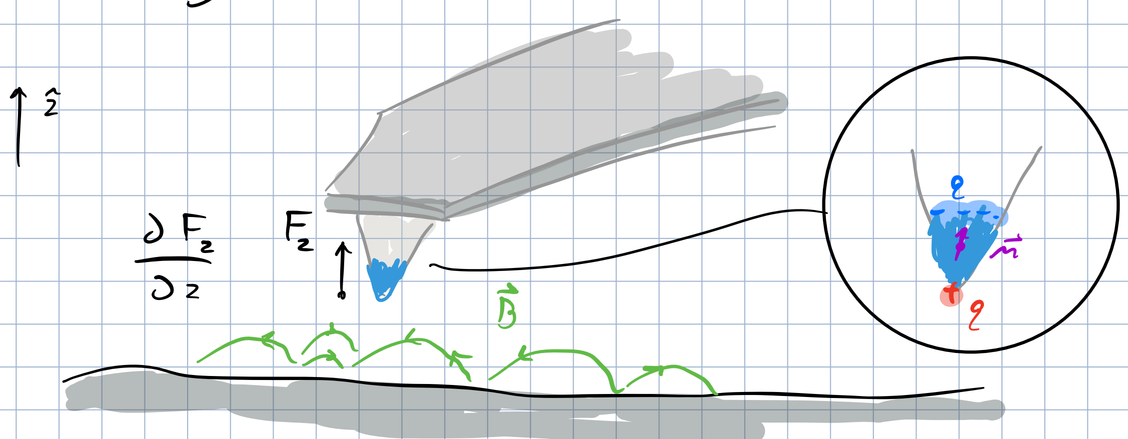

$$F_z = q\vec{B}\cdot\hat{z} + \vec{\nabla}(\vec{m}\cdot\vec{B})\cdot\hat{z}$$

(q → monopole; $\vec{\nabla}(\vec{m}\cdot\vec{B})$ → dipole)

If we assume a mono-pole tip and a measurement of force gradients (Δf):

$$\frac{\partial F_z}{\partial z} = q\frac{\partial B_z}{\partial z} \quad \therefore \quad \boxed{\frac{\partial B_z}{\partial z} = \frac{1}{q}\frac{\partial F_z}{\partial z}}$$

The maximum signal at a given height z that we can measure for a line of current:

$$\frac{\partial}{\partial x}\left(\frac{\partial B_{Iz}}{\partial z}\right) = 0$$

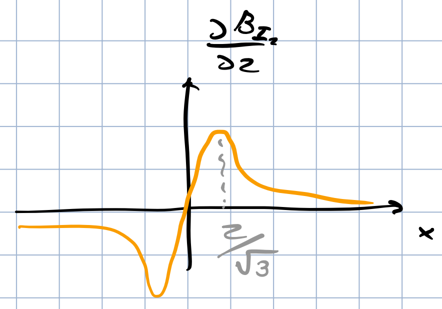

$$x = -\frac{z}{\sqrt{3}},\ \frac{z}{\sqrt{3}}$$

$$\boxed{\left(\frac{\partial B_{Iz}}{\partial z}\right)_{max} = \frac{3\sqrt{3}\,\mu_0 I}{16\pi z^2}} \qquad [T/m]$$

Similarly for a μ_B of magnetic moment:

$$\frac{\partial}{\partial x}\left(\frac{\partial B_{\mu_B z}}{\partial z}\right) = 0$$

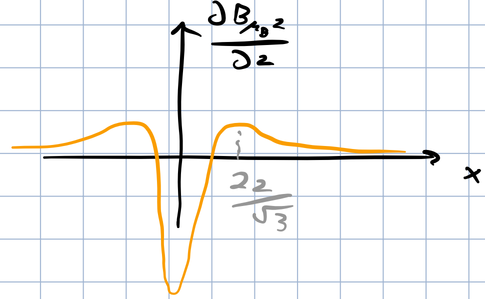

$$x = -\frac{2z}{\sqrt{3}},\ 0,\ \frac{2z}{\sqrt{3}}$$

$$\boxed{\left(\frac{\partial B_{\mu_B z}}{\partial z}\right)_{max} = \frac{3\mu_0\mu_B}{2\pi z^4}} \qquad [T/m]$$

- Noise

The ultimate noise limit is from the thermal motion of the cantilever :

$$S_F = 4 k_B T \Gamma$$ ← Fluctuation - Dissipation Theorem

This implies a thermal force noise amplitude that sets a minimum measurable force :

$$F_{min} = \sqrt{4 k_B T \Gamma}$$

For measurements of force gradients done by oscillating the cantilever by z_{rms} and monitoring its resonant frequency , we have :

$$\left(\frac{\partial F}{\partial z}\right)_{min} = \frac{1}{z_{rms}} \sqrt{4 k_B T \Gamma}$$

$$\therefore \left(\frac{\partial B_z}{\partial z}\right)_{min} = \frac{1}{q\, z_{rms}} \sqrt{4 k_B T \Gamma}$$

→ 30 $\frac{T}{m\sqrt{Hz}}$ @ 4K

$\left[\frac{T}{m\sqrt{Hz}}\right]$

We can then see the sensitivity to I or μ_B by writing :

Current Sens.

$$\frac{\left(\frac{\partial B_z}{\partial z}\right)_{min}}{\left(\frac{\partial B_{I_z}}{\partial z}\right)_{max}} \cdot I \propto z^2 \quad \left[A/\sqrt{Hz} \right] \rightarrow \mu A/\sqrt{Hz} \text{ @ } 50\,nm$$

Moment Sens.

$$\frac{\left(\frac{\partial B_z}{\partial z}\right)_{min}}{\left(\frac{\partial B_{\mu_B z}}{\partial z}\right)_{max}} \cdot \mu_B \propto z^4 \quad \left[\mu_B/\sqrt{Hz} \right] \rightarrow 10^3\,\mu_B/\sqrt{Hz} \text{ @ } 50\,nm$$

SSM

- Signal

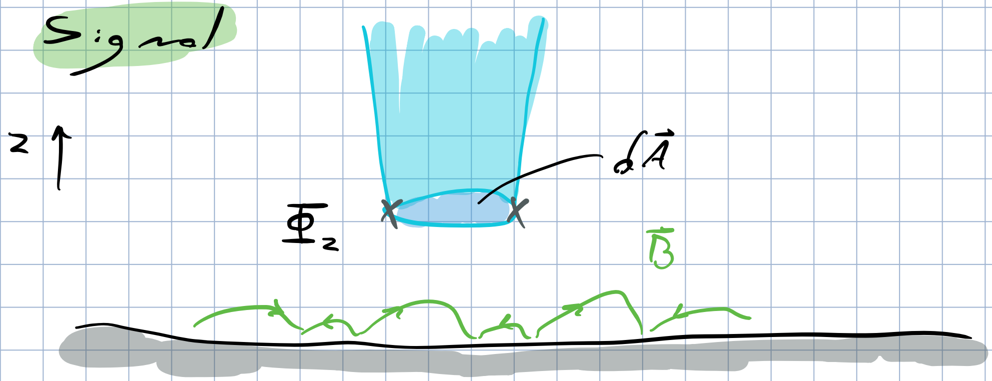

$$\Phi_z = \int \vec{B} \cdot \delta\vec{A}$$

If we now calculate the flux directly above a μ_B of moment:

$$\left(\Phi_{\mu_B z}\right)_{max} = \frac{\mu_0 \mu_B R^2}{2(z^2+R^2)^{3/2}}$$

loop radius

$[T \cdot m^2 = Wb]$

- **Noise**

There are several sources of noise:

- Johnson noise
- shot noise
- 1/f noise ← at low freq
- quantum noise → $\Phi_Q = \sqrt{\hbar L}$ (Loop inductance)

state of the art are ~ 4x this limit

$$\therefore \left(\Phi_z\right)_{min} = \Phi_{noise}$$

→ $50 \sim \Phi_0/\sqrt{Hz}$

Sensitivity:

Current Sens.

$$\frac{\left(\Phi_z\right)_{min}}{\left(\Phi_{Iz}\right)_{max}} \cdot I \quad \left[A/\sqrt{Hz}\right]$$

→ $10\ nA/\sqrt{Hz}$ @ 50nm

Moment Sens.

$$\frac{\left(\Phi_z\right)_{min}}{\left(\Phi_{\mu z_B}\right)_{max}} \cdot \mu_B \propto z^3 \quad \left[\mu_B/\sqrt{Hz}\right]$$

→ $\mu_B/\sqrt{Hz}$ @ 50nm

SNVM

- Signal

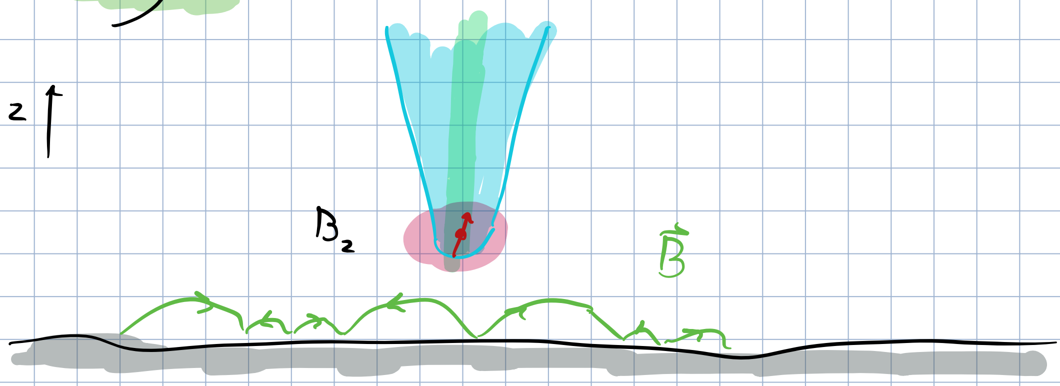

By measuring the NV splitting, we measure the magnetic field along the NV axis:

$$B_z = \vec{B} \cdot \hat{z}$$

$$(B_{Iz})_{max} = \frac{\mu_0 I}{4\pi z} \quad [T]$$

$$(B_{\mu_B z})_{max} = \frac{\mu_0 \mu_B}{2\pi z^3} \quad [T]$$

- **Noise**

SNVM is typically limited by photon shot noise from the optical read-out. Minimum measurable field can be written as:

$$(B_z)_{min} = \frac{1}{\gamma \, \varepsilon \sqrt{I_0 \, t_{acq} \, T_2^*}} \rightarrow 100 \, nT/\sqrt{Hz}$$

(γ: gyromagnetic ratio; ε: optical contrast; I_0: count rate; t_{acq}: integration; T_2^*: decoherence)

Sensitivity:

Current Sens. $\frac{(B_z)_{min}}{(B_{I_z})_{max}} \cdot I \propto z$ $\left[A/\sqrt{Hz} \right]$ → $10 \, nA/\sqrt{Hz}$ @ 25 nm

Moment Sens. $\frac{(B_z)_{min}}{(B_{\mu_0 z})_{max}} \cdot \mu_B \propto z^3$ $\left[\mu_B/\sqrt{Hz} \right]$ → $\mu_B/\sqrt{Hz}$ @ 25 nm

Reconstruction of $\vec{I}$ + $\vec{m}$ from $\vec{B}$

Biot - Savart :

$$\vec{B} = \frac{\mu_0}{4\pi} \int \frac{\vec{J}(\vec{r}\,') \times (\vec{r} - \vec{r}\,')}{|\vec{r} - \vec{r}\,'|^3} d^3\vec{r}\,'$$

For current density $\vec{J} = J_x \hat{x} + J_y \hat{y}$

or magnetization $\vec{m} = m_z \hat{z}$ in 2D

we can write this in k-space :

$$\tilde{B}_z(k_x, k_y, z) = \underbrace{i \frac{1}{2} \mu_0 d\, e^{-kz}}_{g(k,z)} \left[\frac{k_y}{k} \tilde{J}_x(k_x, k_y) - \frac{k_x}{k} \tilde{J}_y(k_x, k_y) \right]$$

w/ $k = \sqrt{k_x^2 + k_y^2}$

and $d \ll z$

↑ film thickness

Continuity equation : $\vec{\nabla} \cdot \vec{J} = 0$

$$\longrightarrow \quad k_x \tilde{J}_x + k_y \tilde{J}_y = 0$$

$$\tilde{J}_y = - \frac{k_x}{k_y} \tilde{J}_x$$

Together :

$$\tilde{B}_z = i g \frac{\tilde{J}_x}{k} \left(k_y + \frac{k_x^2}{k_y} \right) = i g \frac{\tilde{J}_x}{k_y} k$$

$$\tilde{J}_x = -\frac{i k_y \tilde{B}_z}{k g}$$

$$\tilde{J}_y = \frac{i k_x \tilde{B}_z}{k g}$$

Magnetization :

$$\vec{J} = \vec{\nabla} \times \vec{m}$$

$$\therefore \quad J_x = \frac{\partial m_z}{\partial y}, \quad J_y = -\frac{\partial m_z}{\partial x}$$

$$\tilde{J}_x = -i k_y \tilde{m}_z, \quad \tilde{J}_y = i k_x \tilde{m}_z$$

$$\therefore \quad \tilde{m}_z = \frac{\tilde{B}_z}{k g}$$

Current density

Magnetization

$$\tilde{B}_z = -i \frac{1}{2} \mu_0 d e^{-kz} \frac{k}{k_x} \tilde{J}_y \qquad \tilde{B}_z = \frac{1}{2} \mu_0 d e^{-kz} k \tilde{m}_z$$

Derivative along z :

$$\frac{\partial \tilde{B}_z}{\partial z} \propto e^{-kz} \frac{k^2}{k_x} \qquad \frac{\partial \tilde{B}_z}{\partial z} \propto e^{-kz} k^2$$

$$k \propto k_x \propto \frac{1}{\lambda}$$ → Feature size

Normalized to distance : $\frac{\lambda}{z}$

$$\tilde{B}_z \propto e^{-\frac{z}{\lambda}}$$

$$\tilde{B}_z \propto \frac{1}{z}\left(\frac{z}{\lambda}\right) e^{-\frac{z}{\lambda}}$$

$$\frac{\partial \tilde{B}_z}{\partial z} \propto \frac{1}{z}\left(\frac{z}{\lambda}\right) e^{-\frac{z}{\lambda}}$$

$$\frac{\partial \tilde{B}_z}{\partial z} \propto \frac{1}{z^2}\left(\frac{z}{\lambda}\right)^2 e^{-\frac{z}{\lambda}}$$

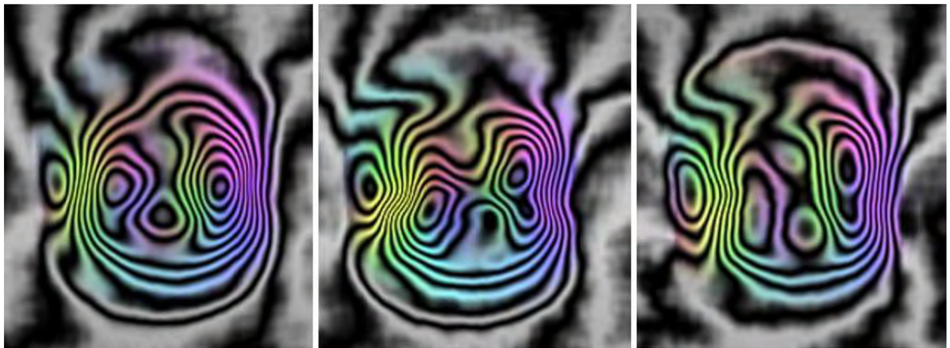

ELECTRON HOLOGRAPHY: THEORY & PRACTICAL EXAMPLES FROM MEDIUM TO ATOMIC RESOLUTION

R. E. DUNIN-BORKOWSKI

JÜLICH Forschungszentrum
ERNST RUSKA CENTRE FOR MICROSCOPY AND SPECTROSCOPY WITH ELECTRONS

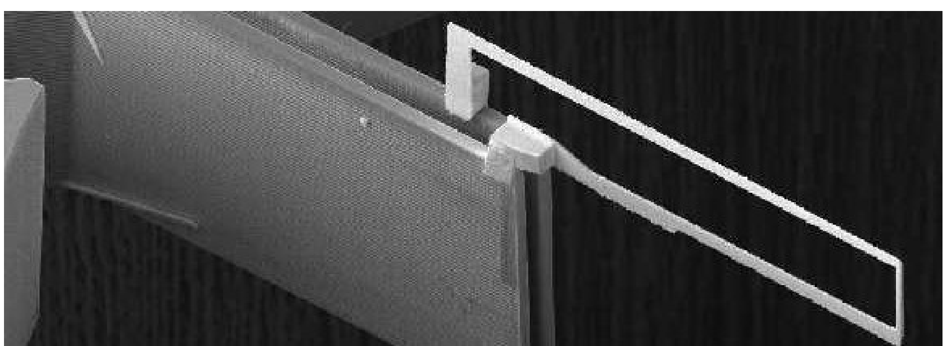

ELECTRON HOLOGRAPHY: THEORY & PRACTICAL EXAMPLES FROM MEDIUM TO ATOMIC RESOLUTION

R. E. DUNIN-BORKOWSKI

Member of the Helmholtz Association

JÜLICH Forschungszentrum
ERNST RUSKA CENTRE FOR MICROSCOPY AND SPECTROSCOPY WITH ELECTRONS

Outline

1. Introduction to off-axis electron holography

2. Historical aspects

3. Off-axis electron holography of magnetic fields

4. Other forms of electron holography

What is off-axis electron holography?

Off-axis electron holography

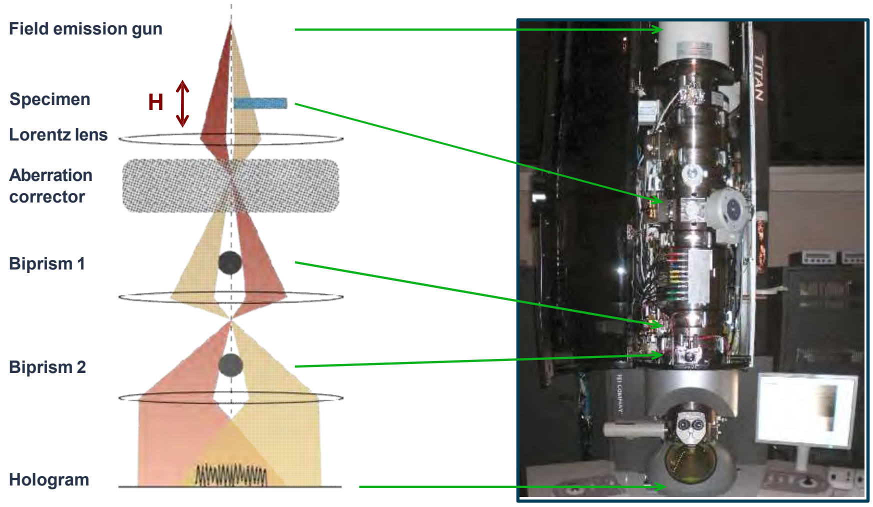

Electron holography provides access to the phase shift of the electron wave that passes through a specimen in the TEM. The phase shift can be related to the in-plane magnetic induction and to the electrostatic potential within and around the specimen, projected in the electron beam direction.

Phase shift

Phase shift:

$$\varphi(x,y) = C_E \int_{z=-\infty}^{z=+\infty} V(x,y,z)\,dz - \left(\frac{e}{\hbar}\right) \int_{z=-\infty}^{z=+\infty} \int_{x=-\infty}^{x=x} B_x(x,y,z)\,dz\,dx$$

Sensitive to:

magnetic fields

composition
density
bonding/ ionicity
electrostatic fields at depletion layers
electrostatic fringing fields outside materials

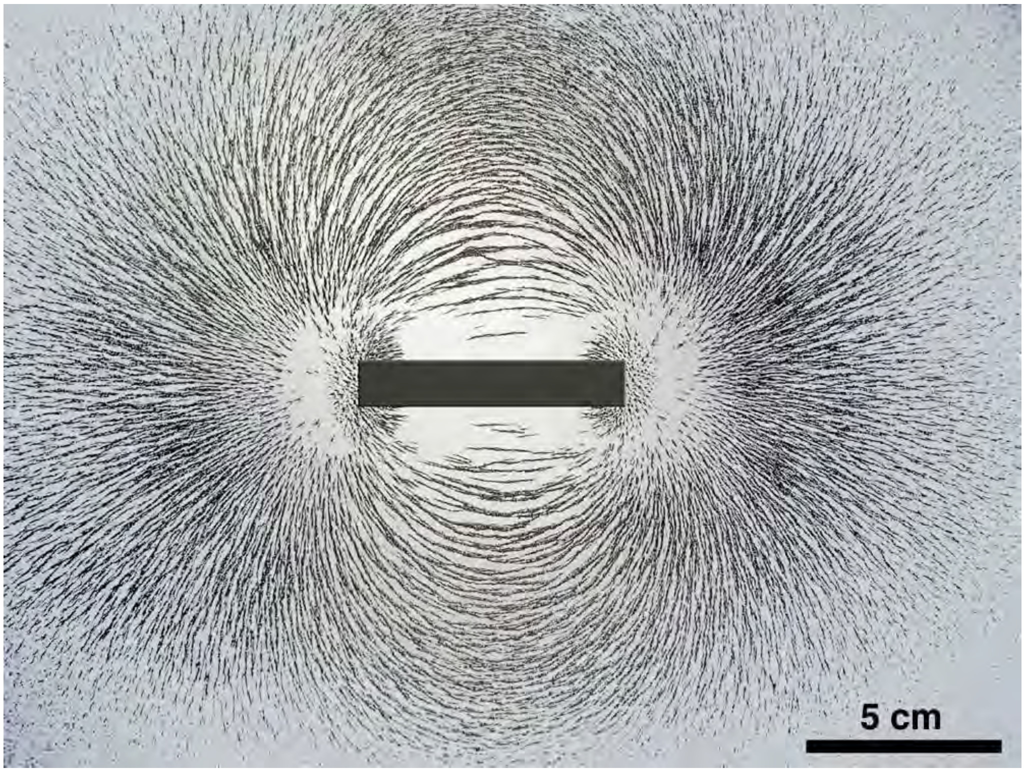

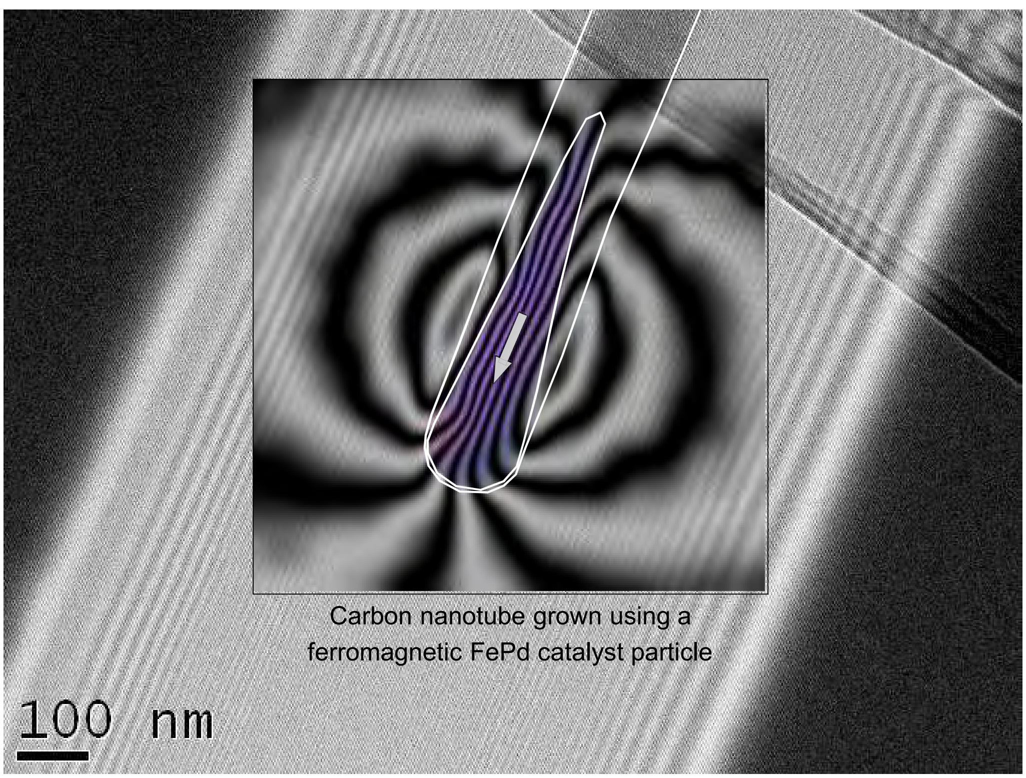

Carbon nanotube grown using a ferromagnetic FePd catalyst particle

Historical background of electron holography

Electron holography: historical background

1947 Denis Gabor proposes holography ("whole writing") as a means to correct for electron microscope aberrations - Nobel prize 1971.

1936 First commercial TEM - Metropolitan Vickers EM1.

1932 E. Ruska and M. Knoll proposed the idea of an electron microscope - Nobel prize 1986.

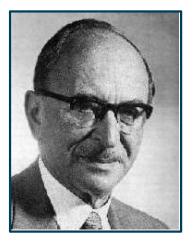

Denis Gabor

Electron microscope built by Ruska and Knoll in Berlin in the 1930s.

1927 G.P. Thomson and A. Reid with C.J. Davisson and L.H. Germer showed the electron was a wave - first electron diffraction experiments - Nobel prize 1937.

1897 J.J. Thomson discovers the electron (particle with a certain charge-to-mass ratio) - Nobel prize 1906.

Off-axis electron holography

Gottfried Möllenstedt
(1913-1997)
Tübingen, Germany

Invention of electron biprism in 1954

Off-axis electron holography

Akira Tonomura
Hitachi, Japan

Hannes Lichte
Triebenberg, Germany

Giulio Pozzi
Bologna, Italy

Basis of electron holography

Basis of off-axis electron holography

Schematic illustration of set-up for generating off-axis electron holograms.

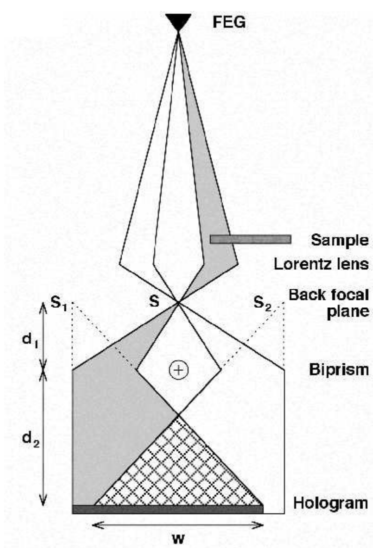

- If α is the deflection angle introduced by a biprism of radius **R** and A is the wavelength of the illumination then:
- the overlap width

$$w = 2\left(\frac{d_1 + d_2}{d_1}\right)\left(\alpha \frac{d_1 d_2}{d_1 + d_2} - R\right)$$

- the interference fringe spacing

$$s = \lambda\left(\frac{d_1 + d_2}{2\alpha d_1}\right)$$

- the total number of interference fringes is proportional to the square of the biprism voltage.

Off-axis electron holography

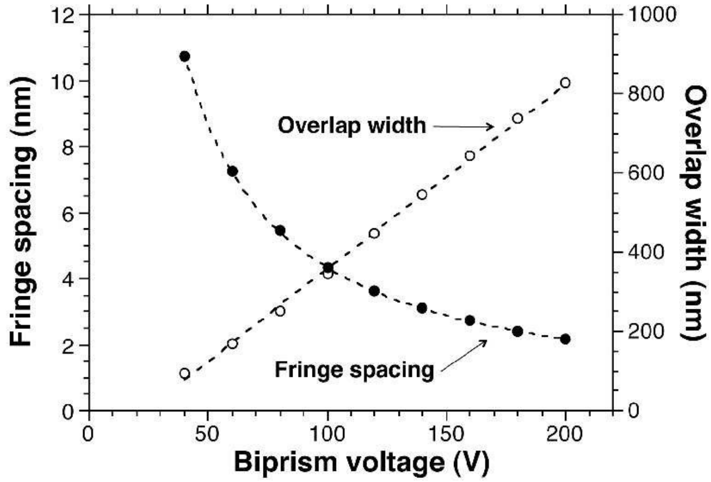

Off-axis electron holography

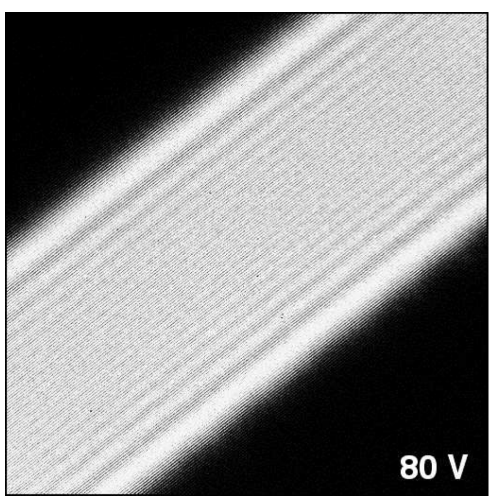

Acknowledgment: M. R. McCartney

Basis of off-axis electron holography

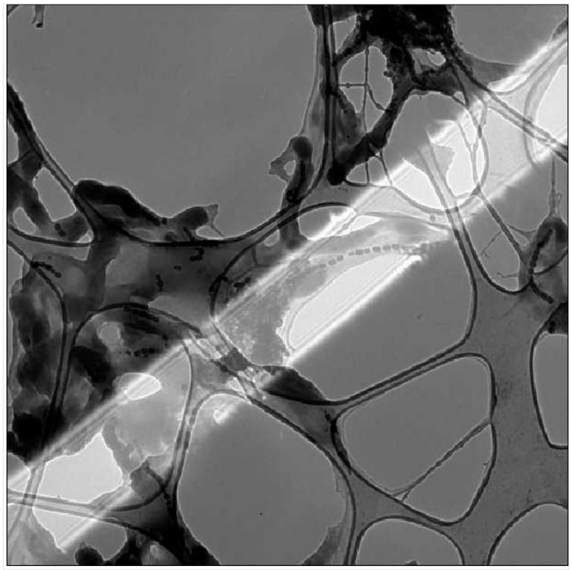

Off-axis electron hologram of magnetic nanocrystals

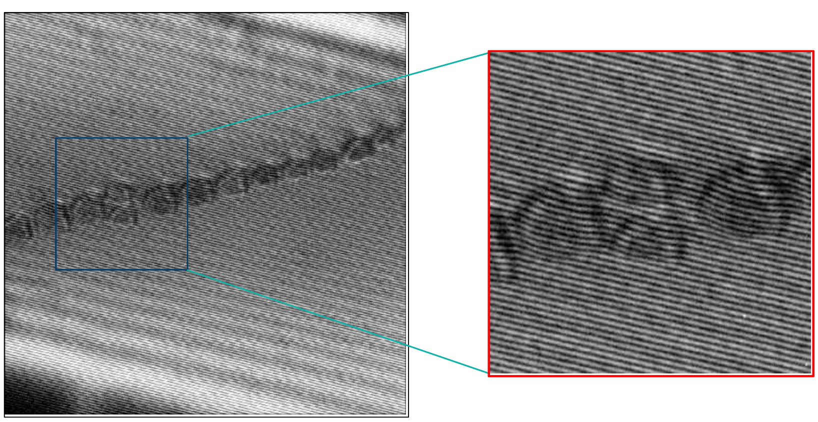

Electron hologram acquired in magnetic-field-free conditions
3.9 nm interference fringe spacing

Off-axis electron holography: digital reconstruction

Off-axis electron hologram from thin crystal showing interference fringes within sample

Phase image obtained from inverse Fourier transform of one 'sideband' selected from Fourier transform of hologram

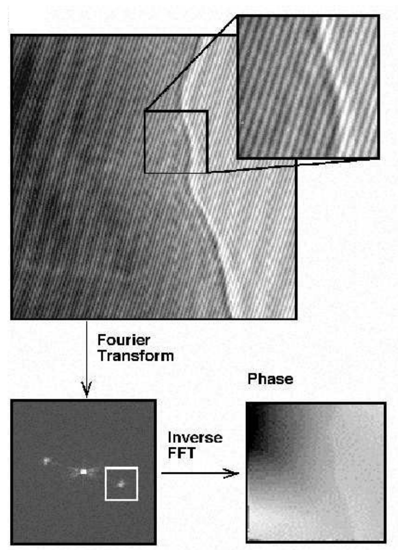

Acknowledgment: M. R. McCartney

Off-axis electron holography

Conventional bright-field TEM:

$$\psi_i(\mathbf{r}) = A_i(\mathbf{r})\exp[i\varphi_i(\mathbf{r})]$$

$$I(\mathbf{r}) = |A_i(\mathbf{r})|^2$$

Off-axis electron holography:

$$I_{hol}(\mathbf{r}) = |\psi_i(\mathbf{r}) + \exp[2\pi i\mathbf{q_c} \bullet \mathbf{r}]|^2$$

$$I_{hol}(\mathbf{r}) = 1 + A_i^2(\mathbf{r}) + 2A_i(\mathbf{r})\cos[2\pi i\mathbf{q_c} \bullet \mathbf{r} + \varphi_i(\mathbf{r})]$$

$$FT[I_{hol}(\mathbf{r})] = \delta(\mathbf{q}) + FT[A_i^2(\mathbf{r})] + \delta(\mathbf{q}+\mathbf{q_c}) \otimes FT[A_i(\mathbf{r})\exp[i\varphi_i(\mathbf{r})]] + \delta(\mathbf{q}-\mathbf{q_c}) \otimes FT[A_i(\mathbf{r})\exp[-i\varphi_i(\mathbf{r})]]$$

$$A = \sqrt{\mathrm{Re}^2 + \mathrm{Im}^2} \qquad \varphi = \tan^{-1}\left(\frac{\mathrm{Im}}{\mathrm{Re}}\right)$$

Basis of off-axis electron holography

Each electron travels as a wave but interacts with the detector as a particle

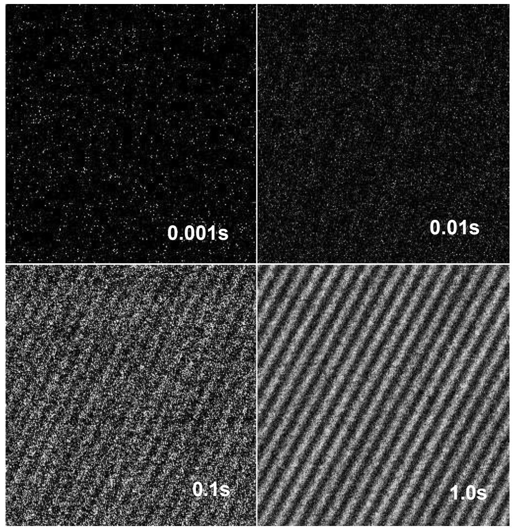

Acknowledgment: M. R. McCartney

The most beautiful experiment in physics

Off-axis electron holography of magnetic fields

Off-axis electron holography of magnetic materials

1965 **Akira Tonomura works on field emission electron sources and pioneers the characterization of magnetic materials using electron holography.**

Hitachi Advanced Research Laboratory

Off-axis electron holography of magnetic materials

'Optical' reconstruction of electron holograms

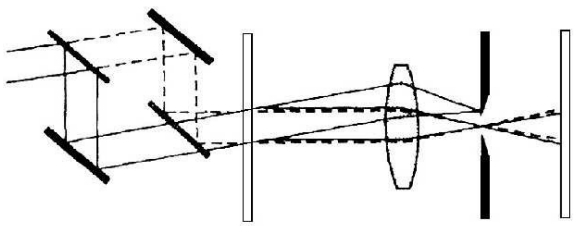

Acknowledgment: A. Tonomura

Off-axis electron holography of magnetic materials

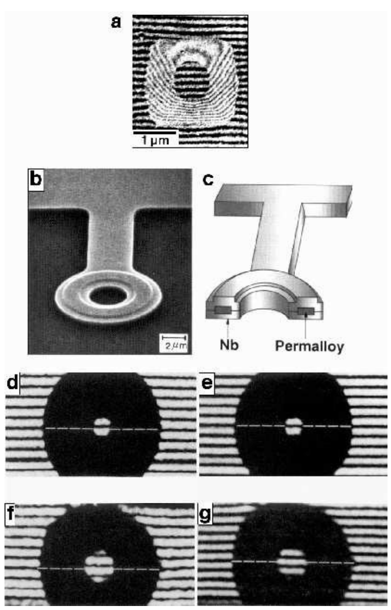

Interferogram of a toroidal 40 nm thick film of permalloy.

SEM image and schematic diagram of permalloy toroid covered with superconducting Nb.

Interferograms: (d) and (e) are for a toroid in which the magnetic flux is quantized below T_c in units of *n(h/2e)*, where *n* is even. For (f) and (g), *n* is odd. For (d) and (f), *T* = 15 K, whereas for (e) and (g) *T* = 5 K (phase amplification x 1).

Phys. Rev. Lett. 48, 1443 (1982).

Phys. Rev. A 34, 815 (1986).

Acknowledgment: A. Tonomura

Off-axis electron holography of magnetic materials

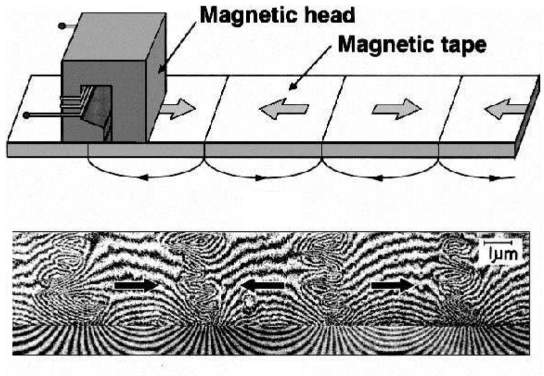

45-nm-thick recorded Co film with 5 μm bit length

Appl. Phys. Lett. 42, 746 (1983)

Acknowledgment: A. Tonomura

Digital recording and analysis of holograms

Off-axis electron holography of magnetic materials

COBALT NANOPARTICLE RINGS

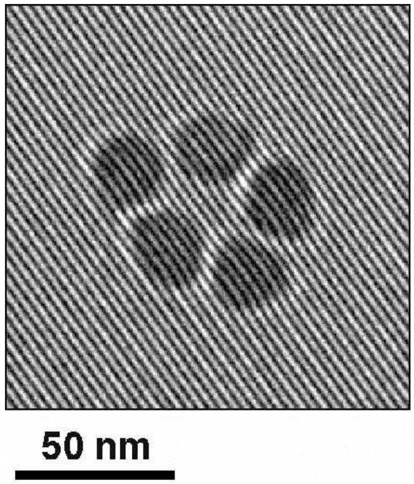

Acknowledgment: Alexander Wei

Off-axis electron holography of magnetic materials

COBALT NANOPARTICLE RINGS

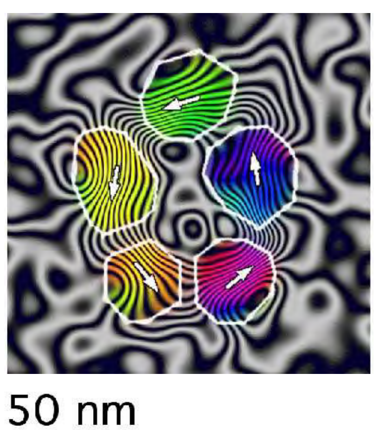

Acknowledgment: Alexander Wei

Separation of magnetic contribution to phase

Off-axis electron holography of magnetic materials

- Magnetic and electrostatic contributions can be separated by recording holograms:
    - With opposite magnetization configurations in the sample
    - Before before and after turning the sample over
    - Below and above a magnetic transition
    - In different applied magnetic fields
    - At two microscope accelerating voltages

Off-axis electron holography of magnetic materials

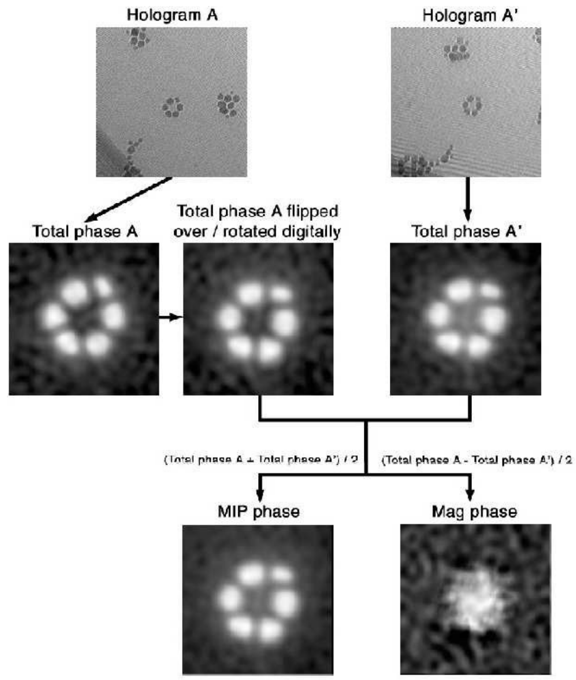

Off-axis electron holography of magnetic materials

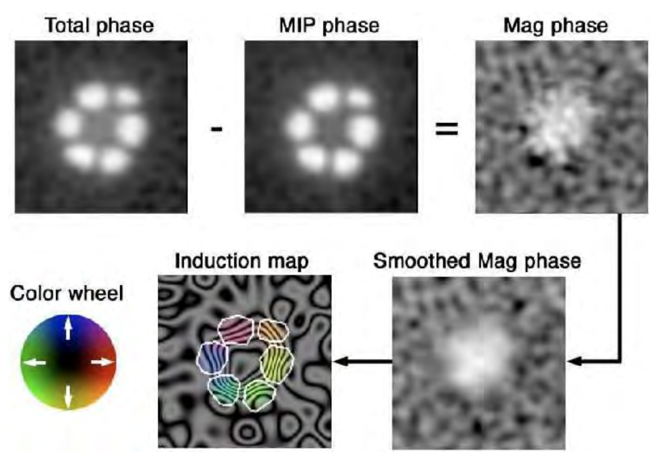

Off-axis electron holography of magnetic materials

Ring of 20 nm Co nanoparticles

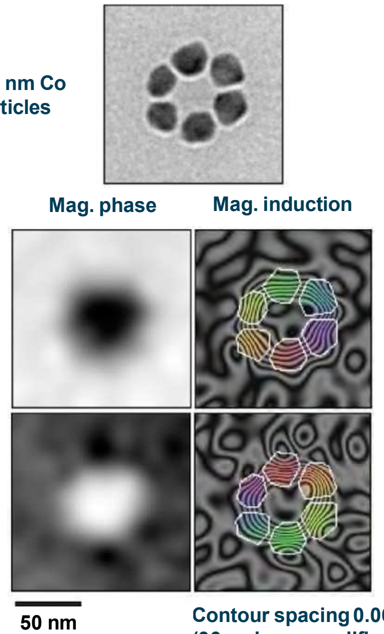

Contour spacing 0.065 rad (96 × phase amplification)

Acknowledgment:
Alexander Wei

In situ magnetization reversal

Off-axis electron holography of magnetic materials

APPLICATION OF VERTICAL MAGNETIC FIELD TO TILTED SAMPLE
USING FIELD OF CONVENTIONAL OBJECTIVE LENS

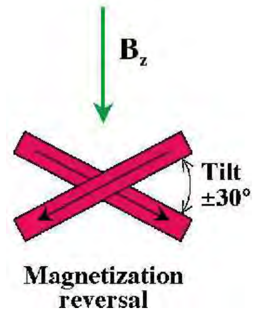

Determination of coercivity of remananence by applying successive increasing OOP fields.

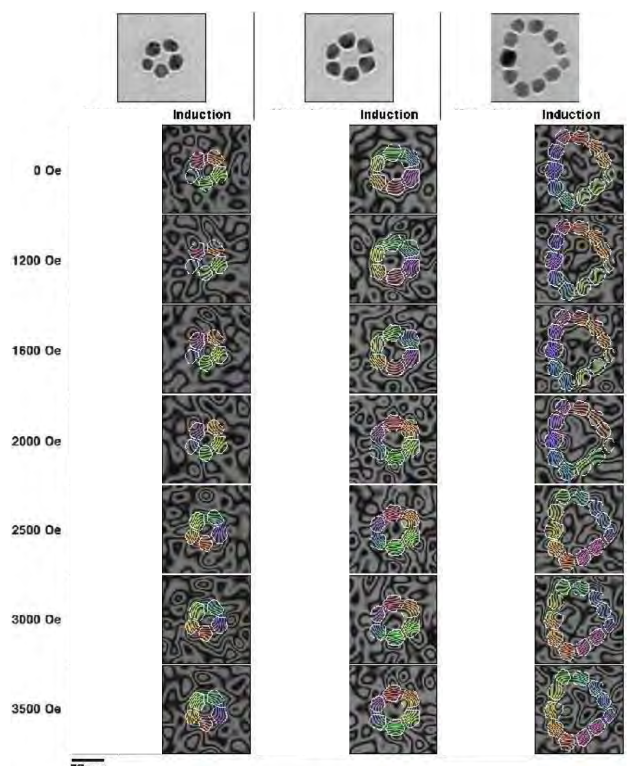

Turning specimen holder

Turning specimen holder

(a) Cartridge, on-axis tomography specimen holder and inclinometer. The inset shows the retractable mounting arm. (b) Position of the cartridge during an experiment. The cartridge is retracted during sample insertion.

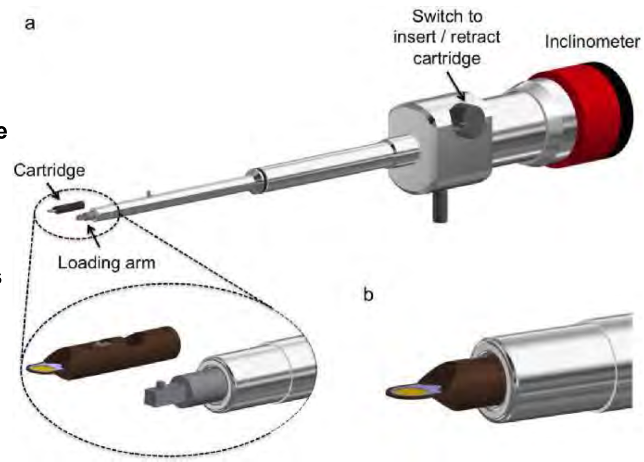

A cartridge-based turning specimen holder with wireless tilt angle measurement for magnetic induction mapping in the transmission electron microscope
P Diehle et al., Ultramicroscopy 220 (2021), 113098.

Turning specimen holder

Cartridge designs for on-axis tomography specimen holder. Scale bars: 2 mm. (a) Cartridge for 3 mm grids and SiN chips with ±70° tilt range; (b) Cartridge with clamping mechanism for full tilt without shadowing; (c) Cartridge for needle-shaped samples with a diameter of 0.25 mm.

A cartridge-based turning specimen holder with wireless tilt angle measurement for magnetic induction mapping in the transmission electron microscope
***P Diehle et al.*, Ultramicroscopy 220 (2021), 113098.**

Turning specimen holder

On-axis tomography holder inserted into the microscope stage with the inclinometer unit attached to its end with wireless recording of the holder tilt angle.

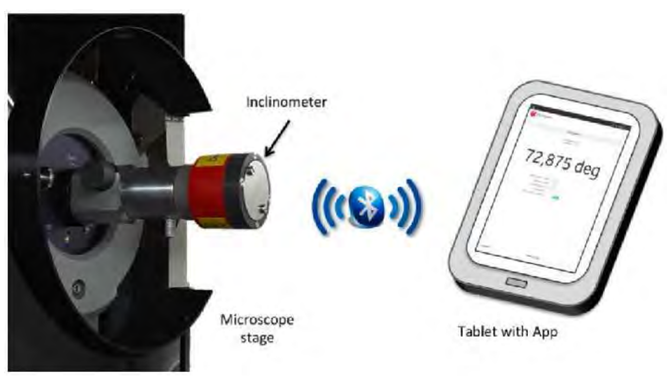

A cartridge-based turning specimen holder with wireless tilt angle measurement for magnetic induction mapping in the transmission electron microscope
***P Diehle et al.*, Ultramicroscopy 220 (2021), 113098.**

Specimen holders for *in situ* magnetic studies

TEM specimen holders

Examples of commercial magnetizing specimen holders

HUMMINGBIRD SCIENTIFIC

Tilt Range	Up to ±45° depencing on objective pole
Sample Size	1x2mm
In-plane applied magnetic flux density	Up to 900 Gauss, depending on microscope and pole piece
Electron imaging	From -300 Oe to +300 Oe applied field depending on microscope and pole piece
Beam Deflection	Integrated passive magnetic compensation

Mel-Build

Kind of TEM:	ARM HR PP Thermo fisher Observation in Lorenz mode is required
App. max:	197mT (Ex situ) 50mT (in situ) Defferent cartridge between in-situ mode and highpower mode
Sample:	φ3 mm

Specimen holders for *in situ* magnetizing experiments

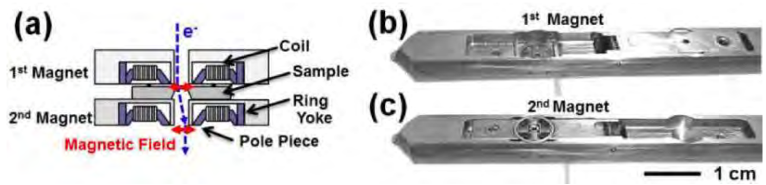

Holder with 2 four-pole electromagnets to compensate for beam deflection. The maximum field is 214 Oe at 500 mA and is homogeneous (100 x 100 µm).

(a) Two superposed images with ±9 Oe.
(b) Images recorded with beam deflection compensation system.

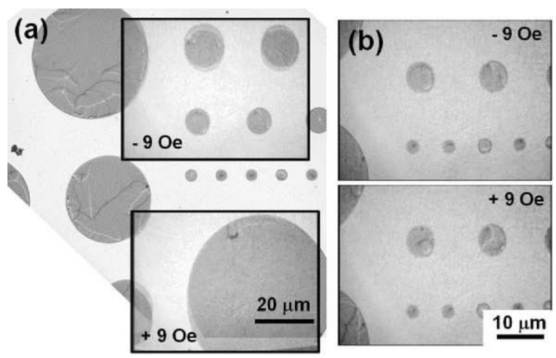

M Arita et al.
Mater. Trans. 55 (2014), MD201310.

Heating & gas reaction studies of Fe_3O_4 crystals

Electron holography at elevated temperature

Fe_3O_4 grain heated to 550 °C and cooled to room temperature

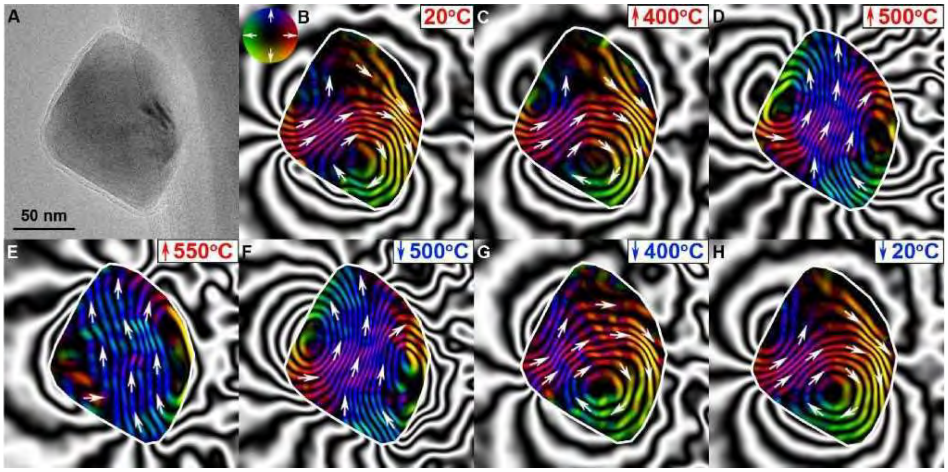

Acknowledgment: Trevor Almeida

In situ heating in oxygen

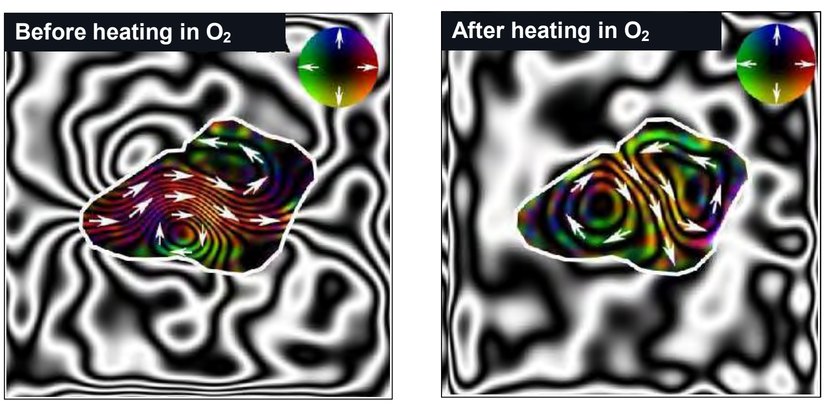

Bright-field TEM images and magnetic induction maps of an elongated 250 nm Fe_3O_4 particle acquired before and after *in situ* heating to 700 °C in 9 mbar of O_2 in the TEM.

Acknowledgment: Trevor Almeida

What is really being measured?

Off-axis electron holography of magnetic materials

The difference between the magnetic contribution to the phase shift at any two points is:

$$\Delta\varphi_m = \varphi_m(x_1,y_1) - \varphi_m(x_2,y_2) = -\frac{e}{\hbar}\int_{-\infty}^{+\infty} A_z(x_1,y_1,z)\,dz + \frac{e}{\hbar}\int_{-\infty}^{+\infty} A_z(x_2,y_2,z)\,dz$$

For a rectangular loop formed by two parallel electron trajectories crossing the sample at these points and joined, at infinity, by segments perpendicular to the trajectories:

$$\Delta\varphi_m = -\frac{e}{\hbar}\oint \mathbf{A}\cdot d\mathbf{l}$$

Using Stokes' theorem:

$$\Delta\varphi_m = \frac{e}{\hbar}\iint \mathbf{B}\cdot\hat{\mathbf{n}}\,dS = \frac{\pi}{\varphi_0}\Phi(S)$$

where $\varphi_0 = h/2e = 2.07\times10^{15}$ Tm^2 is a flux quantum.

Off-axis electron holography of magnetic materials

The relationship between the magnetic contribution to the phase shift and the magnetic induction can be established from the gradient of φ_m

$$\vec{\nabla}\varphi_m(x,y) = \frac{e}{\hbar}\left(B_y^p(x,y)\,,\,-B_x^p(x,y)\right)$$

where $B_j^p(x,y) = \int_{-\infty}^{+\infty} B_j(x,y,z)\,dz$ are the components of the magnetic induction perpendicular to the electron beam direction projected in the beam direction

In the special case when (i) stray fields surrounding the sample can be neglected, (ii) the sample has a constant thickness and (iii) the magnetic induction does not vary with z within the specimen:

$$\vec{\nabla}\varphi_m(x,y) = \frac{et}{\hbar}\left(B_y(x,y)\,,\,-B_x(x,y)\right)$$

The separation of electrostatic and magnetic contributions to the phase shift is almost always mandatory in order to obtain quantitative magnetic information from a phase image. The few instances when this extra step may be avoided include the special case of magnetic domains in a thin film of constant thickness.

Low temperature studies of skyrmions

Magnetic skyrmions

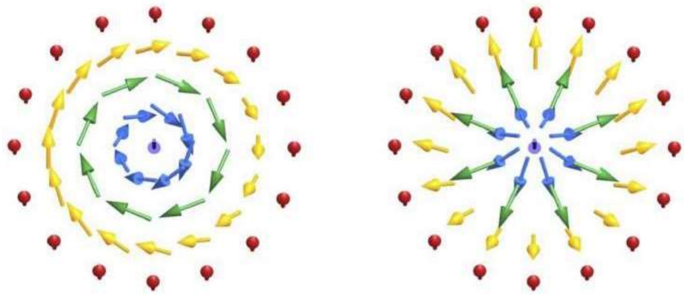

Spin configuration of a Bloch-type skyrmion.

Spin configuration of a Néel-type skyrmion.

The 2020 Skyrmionics Roadmap

C. Back *et al.* J. Phys. D: Appl. Phys. 53 (2020) 363001

Magnetic skyrmions

Schematic B-T phase diagram for magnetic skyrmions in B20 FeGe

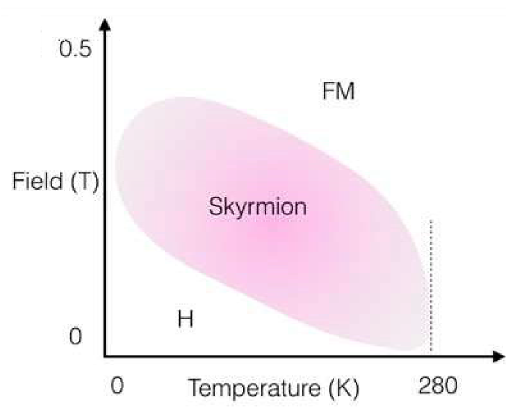

Regions "H", "Skyrmion" and "FM" denote a helical structure, a skyrmion lattice and a saturated ferromagnetic state, respectively. The critical temperature is 278.3 K.

Skyrmions in FeGe

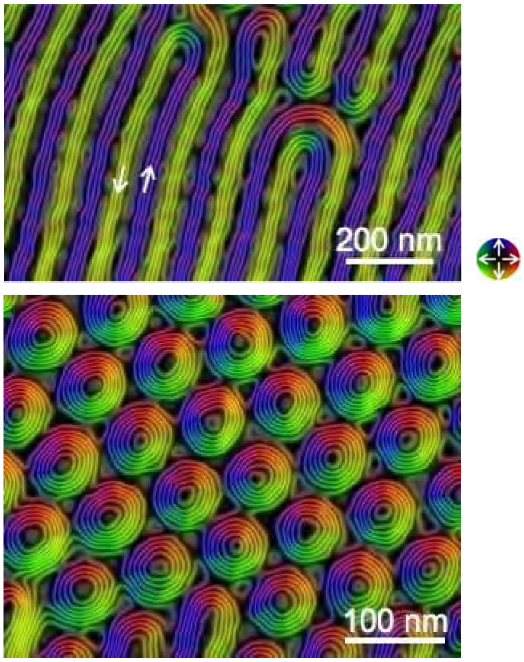

Magnetic induction maps of helical structures and a skyrmion lattice recorded in out-of-plane magnetic fields of 0 and 100 mT at 200 K. The contour spacing is 0.098 rad.

Kiyou Shibata,
Yoshinori Tokura

Magnetic skyrmions in FeGe

In a skyrmion lattice in FeGe, the detailed skyrmion shape changes with applied field but not with temperature

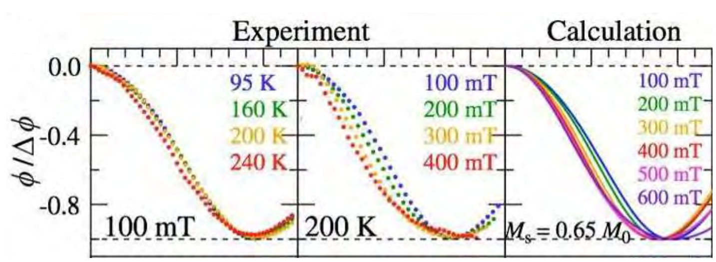

Measurements and calculations of normalized phase distribution across a skyrmion at different temperatures and magnetic fields *vs* distance from its centre.

Kiyou Shibata, Yoshinori Tokura

Magnetic skyrmions in FeGe

TEM sample preparation by FIB milling

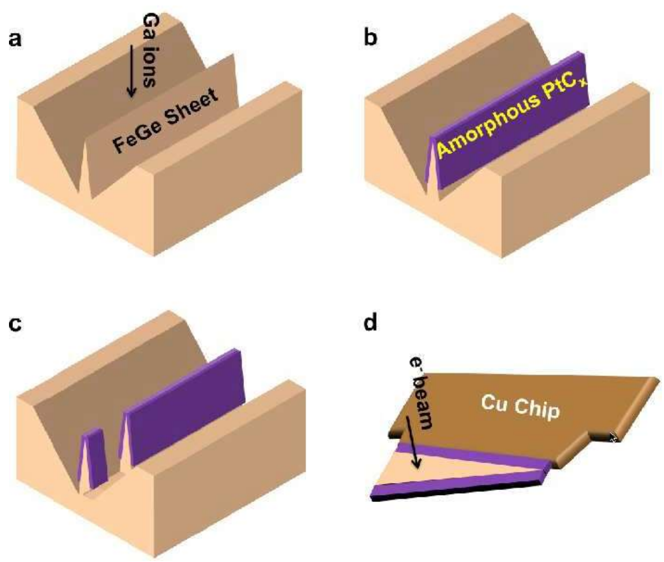

Hai-Feng Du

Skyrmions in FeGe

Magnetic field dependence at 220 K after zero field cooling

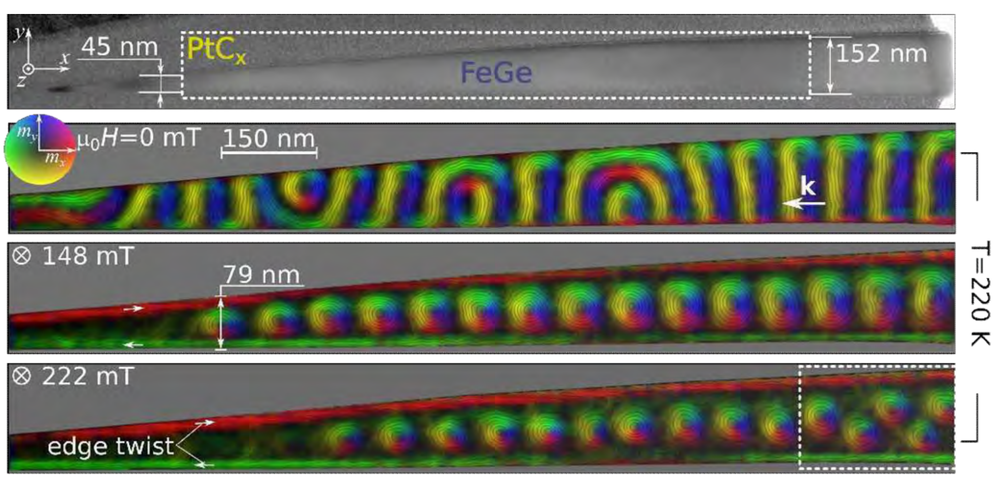

Hai-Feng Du

Magnetic skyrmions in FeGe

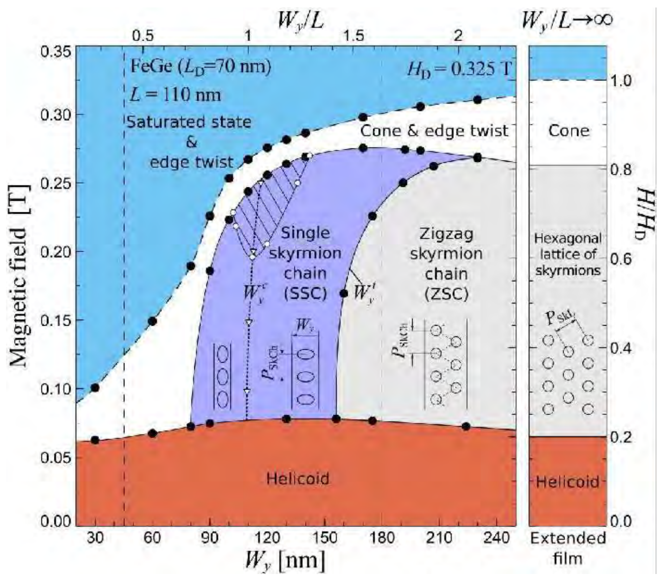

Phase diagram of skyrmions in a nanotripe of B20-FeGe determined from both experimental results and simulations. W_y is the width of the sample and L is its thickness.

Target skyrmion

- Target skyrmion in FeGe

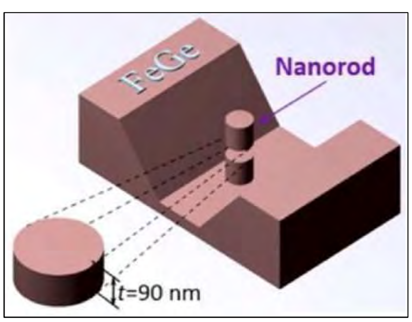

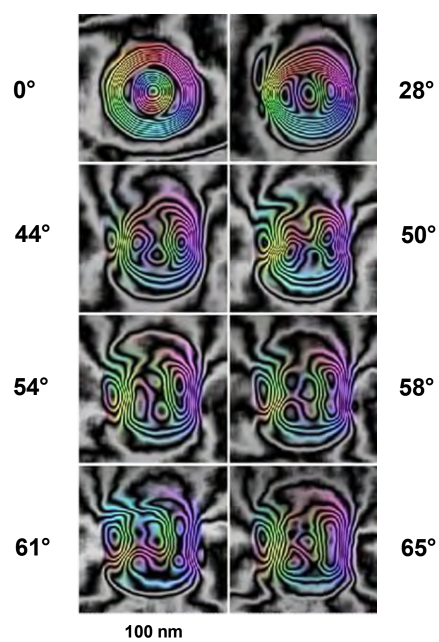

Collaboration with Haifeng Du, Jiadong Zang and colleagues.

Hierarchical phase separation in magnetic HEAs

Magnetic high entroy alloys

Hierarchical phase separation in $AlCo_{0.5}Cr_{0.5}FeNi$ high entropy alloys

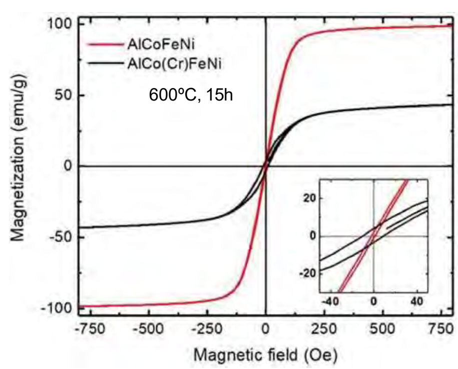

Q. Lan, A. Kovács, J. Caron, H. Du, D. Song, S. Dasari, B. Gwalani, V. Chaudhary, R. V. Ramanujan, R. Banerjee, R. E. Dunin-Borkowski iScience 25 (2022), 104047

Magnetic high entroy alloys

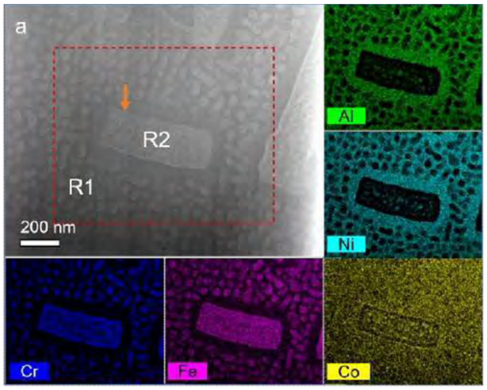

HAADF STEM image and Al, Cr, Fe, Co and Ni EDXS elemental maps of B2 (AlNiCo-rich; CsCl structure) and A2 (FeCrCo-rich; disordered BCC) phases.

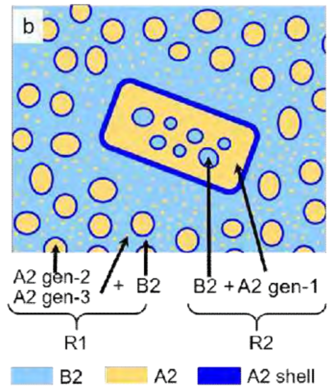

R1: fine and medium A2 precipitates in a B2 matrix.
R2: B2 precipitates in an A2 matrix.

Q. Lan, A. Kovács, J. Caron, H. Du, D. Song, S. Dasari, B. Gwalani, V. Chaudhary, R. V. Ramanujan, R. Banerjee, R. E. Dunin-Borkowski, iScience 25 (2022), 104047

Magnetic high entroy alloys

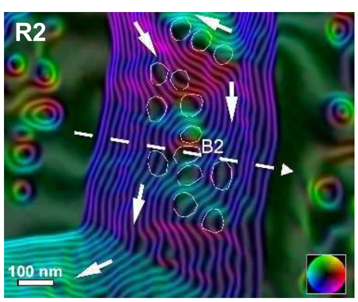

R2: Weakly magnetic B2 precipitates in large magnetic domains of the A2 phase.

R1: Magnetic vortex states in individual A2 precipitates in a weakly magnetic B2 matrix.

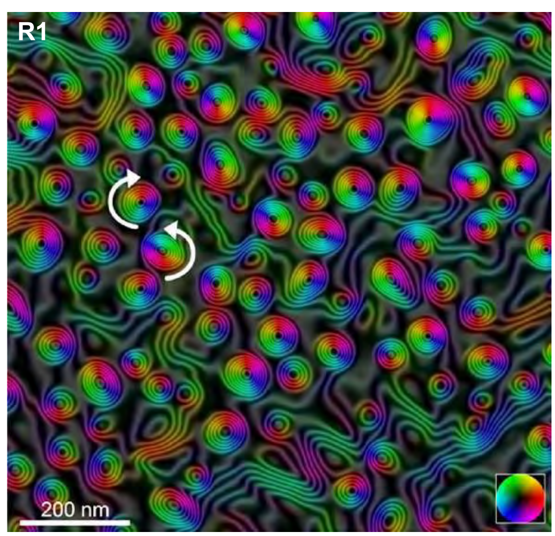

Q. Lan, A. Kovács, J. Caron, H. Du, D. Song, S. Dasari, B. Gwalani, V. Chaudhary, R. V. Ramanujan, R. Banerjee, R. E. Dunin-Borkowski, iScience 25 (2022), 104047

3D magnetic vector field holographic tomography

SKYRMIONS IN 3D IN AN APPLIED FIELD

Two tilt axes, applied field and low temperature.
Cryo holographic vector-field electron tomography of skyrmion tubes in FeGe.

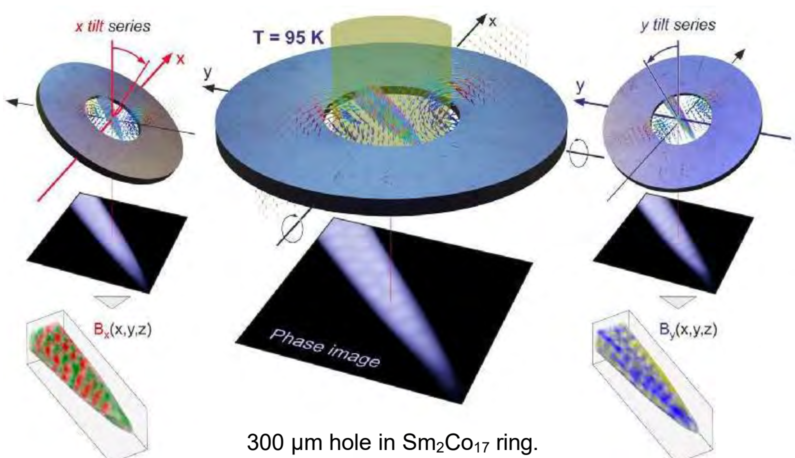

300 µm hole in Sm_2Co_{17} ring.
170 mT out-of-plane field

D. Wolf, S. Schneider, U. K. Rößler, A. Kovács, M. Schmidt, R. E. Dunin-Borkowski, B. Büchner, B. Rellinghaus, A. Lubk, arXiv:2101.12630v1

SKYRMIONS IN 3D

- Local deviations from Bloch character.
- Collapse of skyrmion texture at surfaces.
- Tilts of elongated SkTs at the tip.
- Correlated modulations of SkTs along their axes.

- D. Wolf *et al.*, arXiv:2101.12630v1

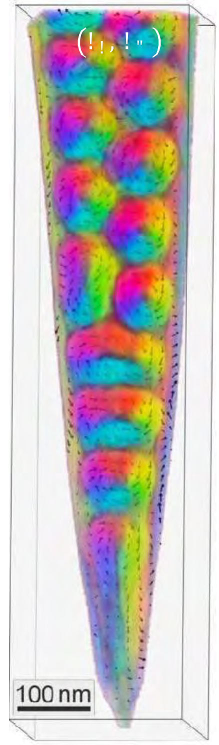

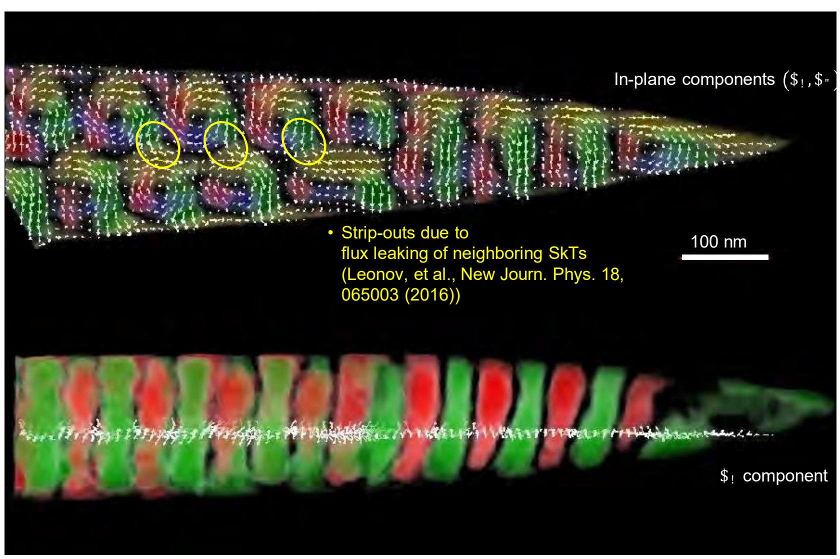

Model-independent measurement of magnetic moment

Model-independent measurement of magnetic moment

$$\mathbf{m} = \iiint \mathbf{M}(\mathbf{r}) \mathrm{d}^3\mathbf{r} \qquad \mathbf{m_B} = \frac{1}{\mu_0} \iiint \mathbf{B}(\mathbf{r}) \mathrm{d}^3\mathbf{r} \qquad \mathbf{m_B} = \left[\frac{1}{2}m_x, \frac{1}{2}m_y, m_z\right]$$

$$\Delta \mathbf{m}_{\mathbf{B}}^{\mathrm{tot}} = \frac{1}{\mu_0} \left\{ \frac{\hbar}{e}[1 - \beta \sin(\gamma)](\hat{\mathbf{z}} \times \mathbf{k}) - \mathbf{B}_{\mathrm{p}}(\mathbf{d}) + \sum_{i=1}^{N} \mathbf{B}_{\mathrm{p}}^{(i)}(\boldsymbol{\rho}_i) \right\} \pi R_c^2$$

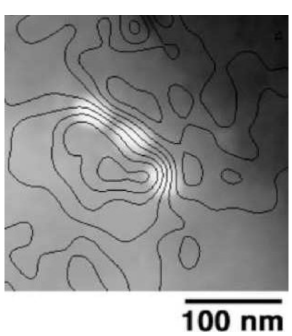

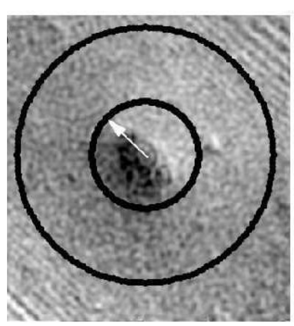

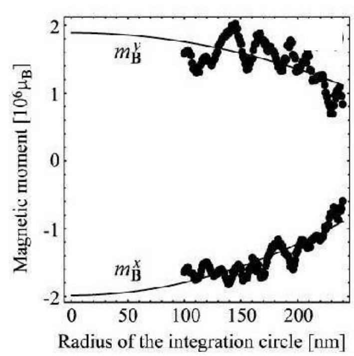

$(2.74 \pm 0.18)\, 10^6\ \mu_B$ oriented at $(136 \pm 4)°$

Acknowledgment: Marco Beleggia

Magnetization as an inverse problem

Retrieval of M and the inverse problem

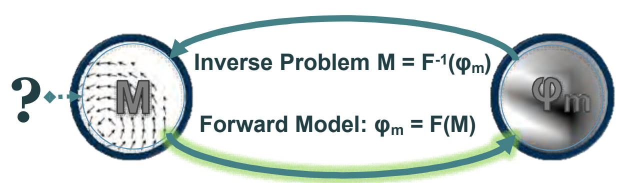

J. Caron, J. Ungermann, M. Riese

Cubic magnetite nanoparticles with truncated corners

Magnetic induction map

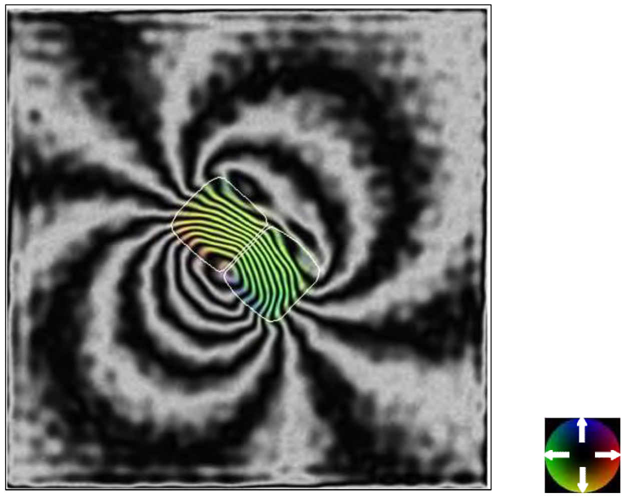

Retrieval of M and the inverse problem

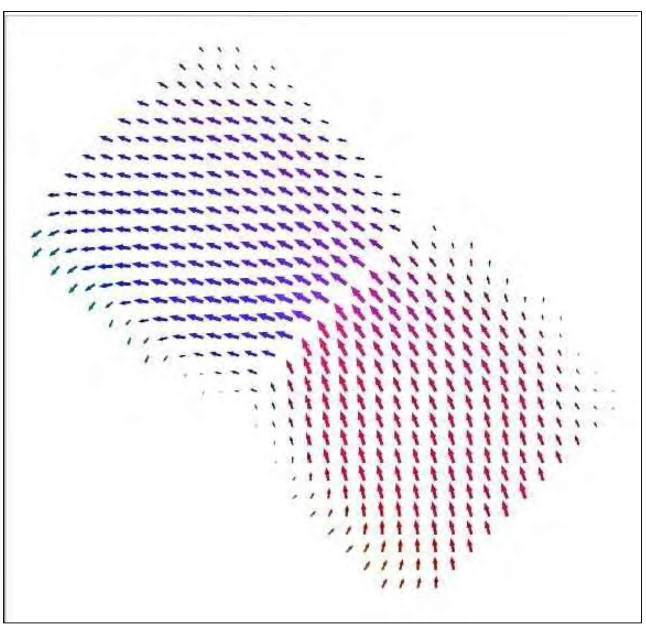

Retrieved projection of M using regularization and boundary moments for two 68 nm magnetite (Fe_3O_4) cuboctahedra.

Retrieval of M and the inverse problem

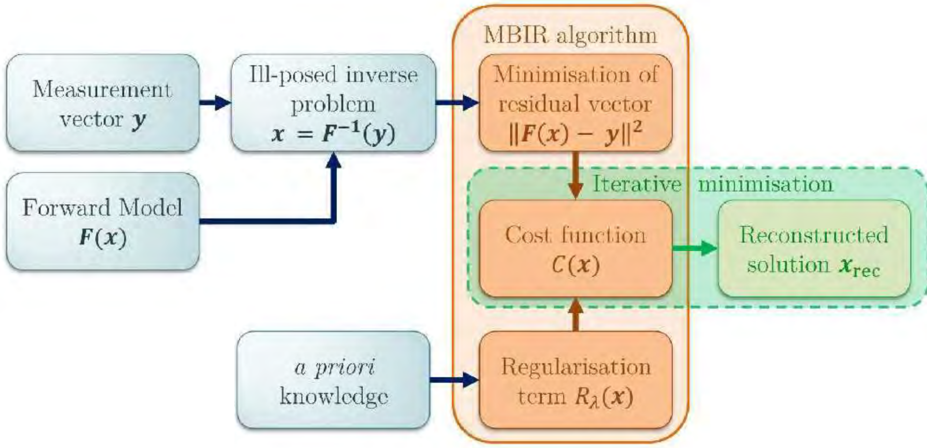

A forward model F(x) maps a physical quantity x onto data described by a measurement vector y. The ill-posed inverse problem is substituted by a minimisation problem. Together with a regularisation term $R_\lambda(x)$, which can be based on *a priori* knowledge, a cost function C(x) is constructed and minimised using a model-based iterative algorithm to find the best-fitting solution x_{rec}.

Retrieval of M and the inverse problem

L-curve analysis

Costfunction:

$$C(x) = \|\mathbf{F}x - y\|^2_{S_\epsilon^{-1}} + \lambda \cdot \|x\|^2_{S_a^{-1}}$$

The regularisation parameter λ balances:

- Compliance with the measurements
- Smoothness of the magnetisation

How to find the best value for λ?

→ L-curve analysis

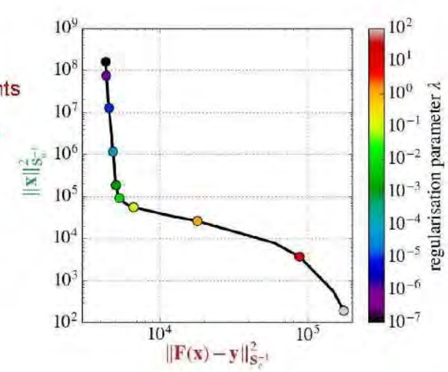

Retrieval of M and the inverse problem

Input:

- Mask that specifies the locations of magnetised objects.
- The direction and distance to the perturbed reference wave.
- Confidence array that specifies other identifiable artefacts.

J. Caron, Ph.D. thesis, RWTH Aachen University.

Retrieval of M and the inverse problem

Considerations:

- Sources of magnetisation outside the field of view can be taken into account by introducing buffer pixels.
- The regularisation strength and the choice of mask significantly influence the resolution of the reconstruction.
- Care required with regularisation to taken into account the null space.

J. Caron, Ph.D. thesis, RWTH Aachen University.

Uniqueness and the null space

Forward model

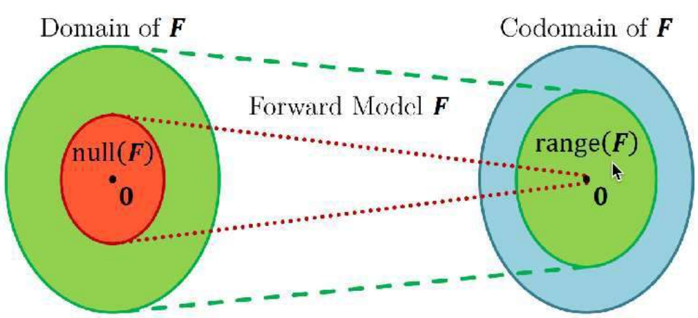

- The null space null (F) is the set of all magnetic states x that are mapped onto the zero vector y = 0, *i.e.*, no phase is produced.
- The range (F) contains all measurement vectors y that can be produced by all magnetisation state vectors x.
- Not all measurements y in the codomain are necessarily attainable by F.
- The measurements y can lie outside of range (F), especially if they are noisy, *i.e.*, no magnetic state x exists that is able to produce the corresponding phase images.

Three-dimensional magnetization reconstruction

3D magnetisation reconstruction

Reconstruction of 3-dimensional magnetisation distributions:

→ Requires fully tomographic approach

→ 2 (optimally) orthogonal tilt series of phase images

Thesis → Simulated tilt series as input for the MBIR algorithm

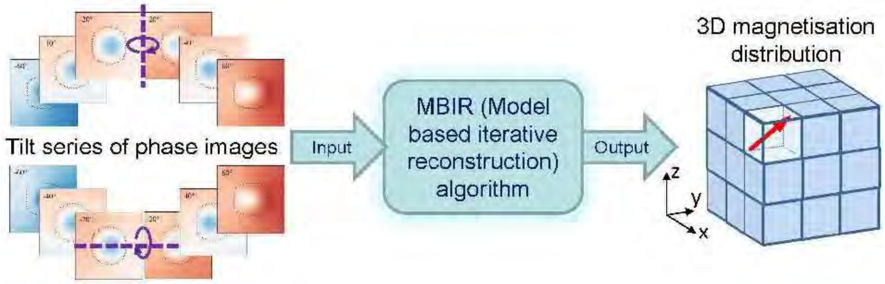

Electron-beam-induced charging

Electron holography at elevated temperature

Electron hologram acquisition during *in situ* heating in vacuum

Problem:

Temperature-dependent electron-beam-induced specimen charging

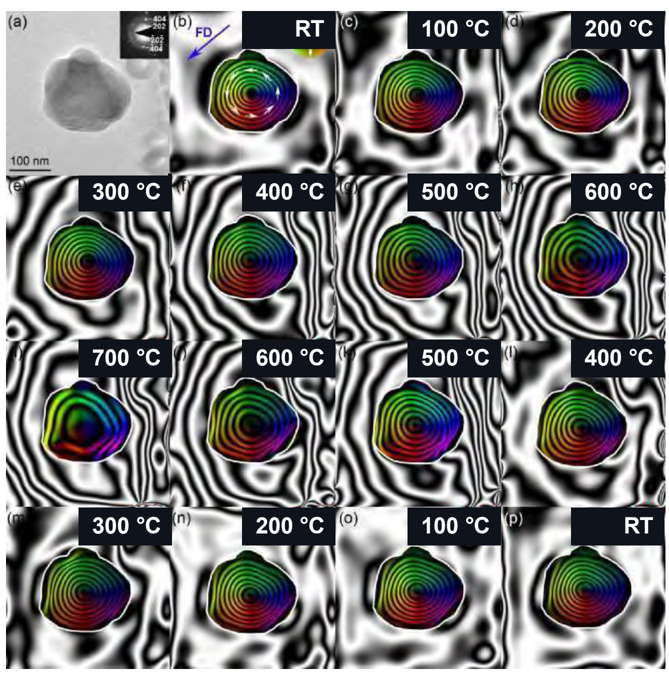

Trevor Almeida

Quantitative and *in situ* mapping of magnetic fields at the nanoscale

Solution:

Calculate and subtract electrostatic (mean inner potential + charging) contribution to phase *at every temperature*

Electron holography at elevated temperature

Fe_3O_4 grain heated to 600 °C and cooled to room temperature

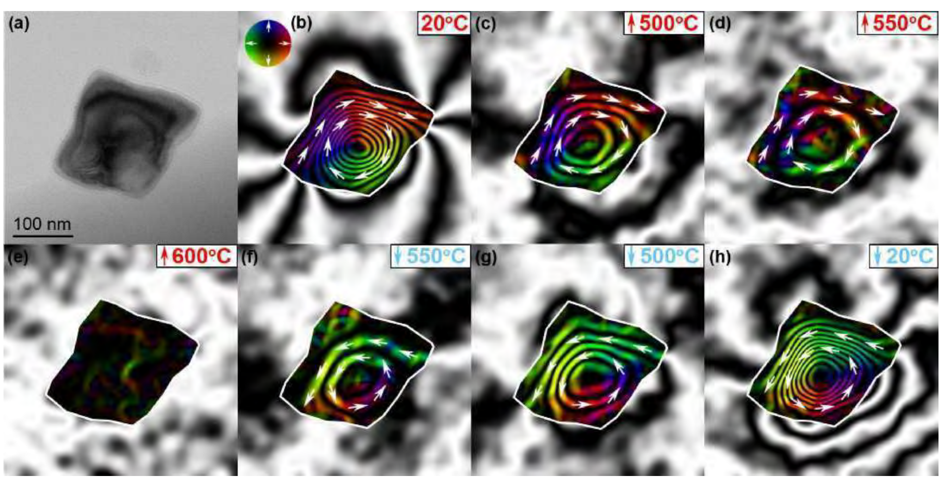

T. Almeida, A. Muxworthy, W. Williams

Oersted magnetic field of a current

Magnetic field of a current-carrying wire

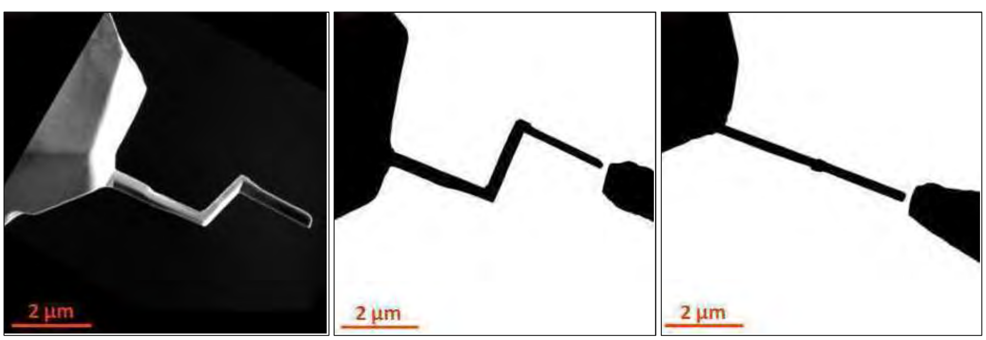

FIB milling and bright-field TEM images of Au needle and hook in a TEM-STM specimen holder with the tilt set first to 70° and then to 0° (with the hook arm parallel to the electron beam direction).

Magnetic field of a current-carrying wire

Experimental 8-times-amplified phase contour maps recorded for currents of 0, 2 and 4 mA through the wire

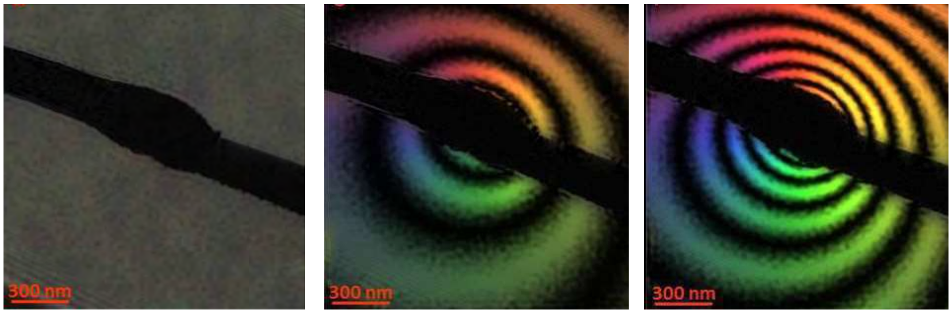

Examples

Specialized devices

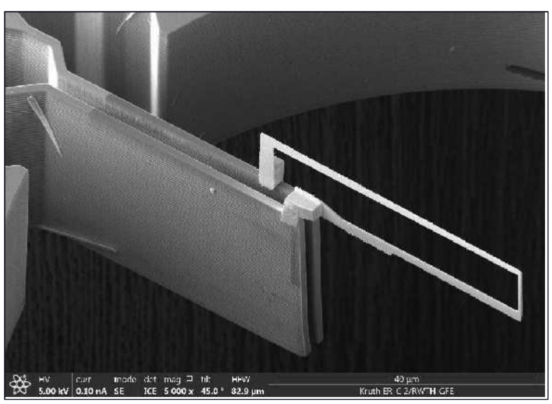

Sample: P. Lu
U-Shape

Acknowledgment: Max Kruth

Summary

- Medium resolution off-axis electron holography allows magnetic and electrostatic fields to be quantified to nm spatial resolution, both inside and outside materials.
- Magnetic and mean inner potential effects must often be separated from each other.
- Digital analysis of holograms is important for the smallest nanostructures.
- High quality experimental data, comparisons with simulations and thin undamaged specimens are essential.

Vision

3D magnetic solitons

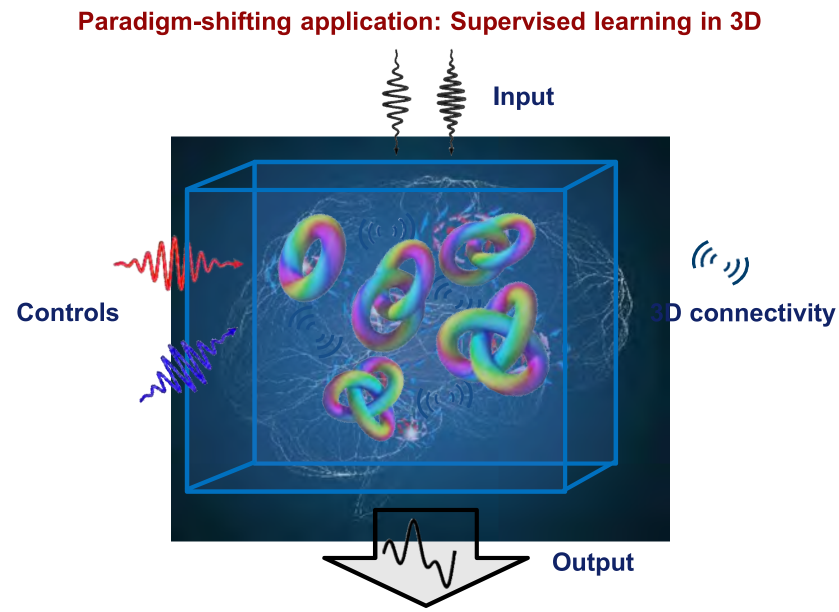

Magnetic imaging in TEM

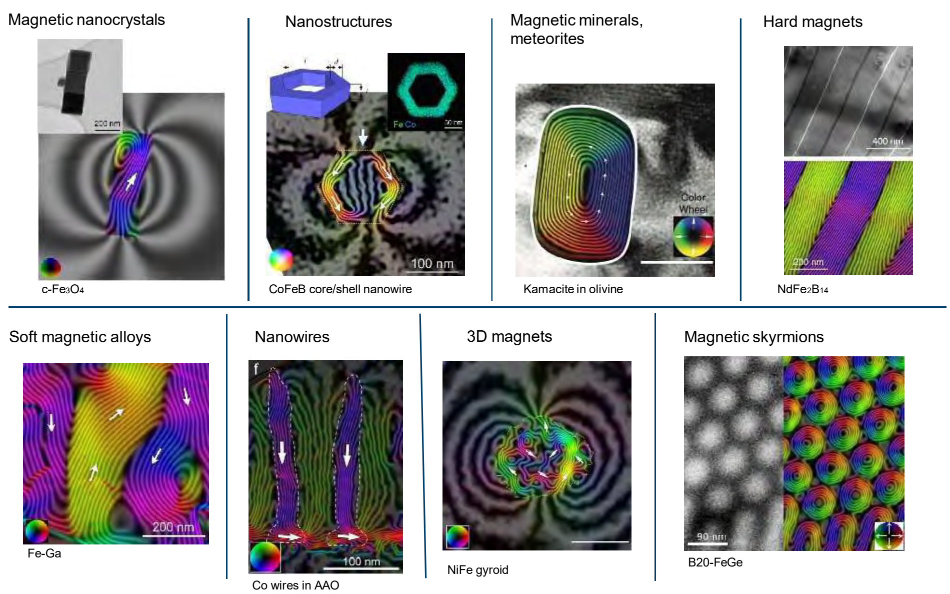

Acknowledgments

- András Kovács, Fengshan Zheng, Thibaud Denneulin, Marco Beleggia
- Michalis Charilaou, Jörg Löffler, Jordi Arbiol, Josep Nogués, Luyan Yang
- Dongsheng Song, Teresa Wessels, Benjamin Zingsem, Michael Farle
- Jan Caron, Patrick Diehle, Jörn Ungermann, Martin Riese, Ulrich Poppe
- Nikolai Kiselev, Andrii Savchenko, Stefan Blügel, Filipp Rybakov
- Haifeng Du, Jiadong Zang, Zi-An Li, Kiyou Shibata, Yoshinori Tokura
- Daniel Wolf, Sebastian Schneider, Bernd Rellinghaus, Axel Lubk
- Qianqian Lan, Rajarshi Banerjee, Raju Ramanujan, Penghan Lu
- Vadim Migunov, Janghyun Jo, Giulio Pozzi, Amir Tavabi, Max Kruth
- Martin Salinga, Xuan Thang Vu, Sebastian Walfort, Benedikt Kersting
- Karina Ruzaeva, Alexander Clausen, Dieter Weber, Lei Jin, Knut Urban

Funding

- European Union's Horizon 2020 Research and Innovation Programme:
  - Grant No. 856538, project “3D MAGiC”
  - Grant No. 823717, project “ESTEEM3”
  - Grant No. 766970, project “Q-SORT”
  - Grant No. 606988, project “SIMDALEE2”
- Deutsche Forschungsgemeinschaft:
  - Project-ID 405553726 – TRR 270 “HoMMage”
- DARPA TEE program through grant MIPR# HR0011831554
- SFB 917 NanoSwitches Collaborative Research Centre

MSE 670: Advanced Microscopy techniques for characterizing the magnetic properties of materials

Characterizing magnetic materials using inelastic Brillouin light scattering (BLS) technique

PING CHE

UNITÉ MIXTE DE PHYSIQUE CNRS, THALES, UNIVERSITÉ PARIS-SACLAY, PALAISEAU 91767, FRANCE

16th – 18th Novembre, EPFL

Contents

I. The basic principle of BLS technique: 1. General aspects of Brillouin scattering

Brillouin scattering:

- Inelastic scattering: the kinetic energy of an incident particle is not conserved. Part of the energy get lost or gained from the scattering process with another quasi-particles, e.g. phonon, magnon.
- Energy and moment conservation: $\hbar\omega_q = \hbar\omega_i \pm \hbar\omega_s$, $\hbar\boldsymbol{k}_q = \hbar\boldsymbol{k}_i \pm \hbar\boldsymbol{k}_s$.
- Stokes (absorption) and anti-Stokes (emission) process.

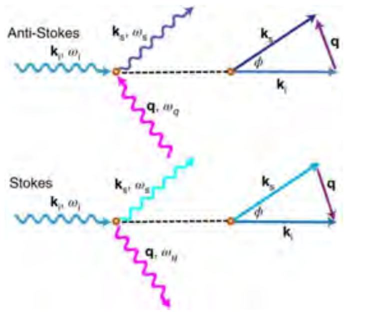

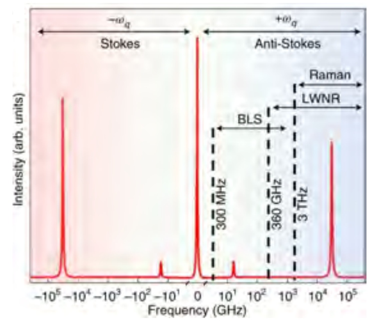

- M. Cardona and G. Guntherodt, Light Scattering in Solids II: Basic concepts and Instrumentation, Volume 50, Springer-Verlag, 1982.
- F. Kargar, and A. A. Balandin, *Nat. Photon.*, **15**, 720–731 (2021).

I-1. General aspects of Brillouin scattering: broad application

Observation of phonon confinement in nanostructured materials

- F. Kargar, et al. *Nat. Commun.*, **7**, 13400 (2016)

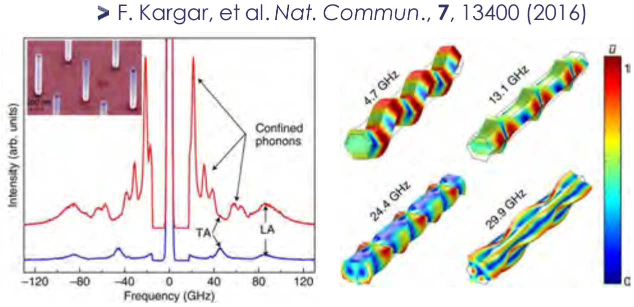

Biomechanical measurement of the crystalline lens in a mouse eye

- G. Scarcelli, and S. H. Yun, *Nat. Photon.*, **2**, 39–43 (2008)

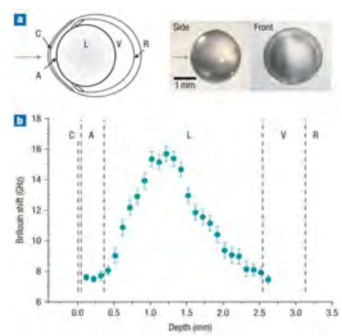

I-1. General aspects of Brillouin scattering: difference with Raman scattering

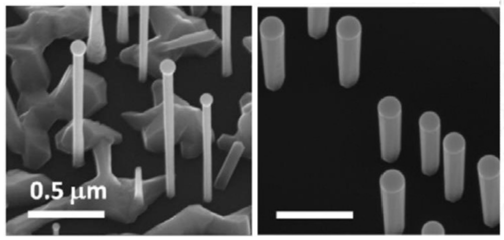

At LMSC

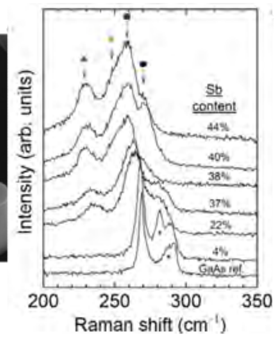

What is the difference between Brillouin scatting and Raman scattering?

E. Alarcón-Lladó, et al., Nanotechnology 24, 405707 (2013).

I-1. General aspects of Brillouin scattering: the Fabry-Perot interferometer

Mirror spacing L

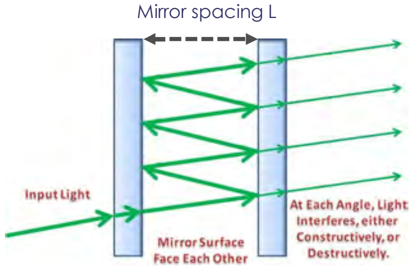

http://www.starkeffects.com/Fabry-Perot-Interferometer.shtml

- **The waves undergo either constructive or destructive interference.**
  - Constructive interference when the resonator length L is equal to an integer multiple of half the wavelength, $q\lambda/2$. q is the mode order of the longitudinal direction.
  - All other wavelengths that do not fit this criteria are not supported by the resonator and destructively interference.

I-1. General aspects of Brillouin scattering: the Fabry-Perot interferometer

Only the frequencies corresponding to the constructive interference can come out of the resonator:

- $\nu_{qmn} = \frac{c}{2L}\left[q + \frac{1}{\pi}(m+n+1)\cos^{-1}\sqrt{g_1 g_2}\right]$
- Here, m and n are the mode numbers of the TEM mode, c is the speed of light, $g_{1,2} = 1 - \frac{L}{R_{1,2}}$ corresponding to the radii of the curvature of the mirrors.

transverse electro-magnetic (TEM) modes

https://perg.phys.ksu.edu/vqm/laserweb/ch-4/F4s3t1p1.htm

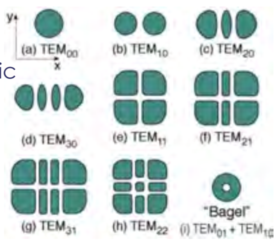

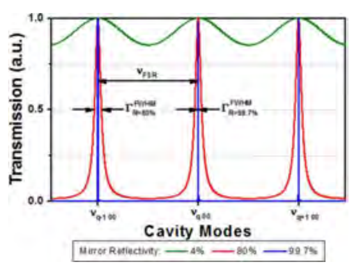

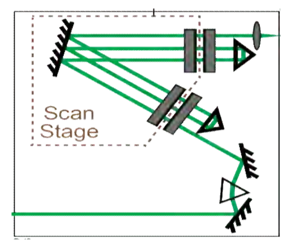

I. The basic principle of BLS technique: 2. Brillouin scattering for magnonics research

Ferromagnetism:

- Magnetization $\boldsymbol{M} = \frac{\sigma_{\Delta V}\mathfrak{M}}{\Delta V}$, $\sigma_{\Delta V}\mathfrak{M}$ is the vector sum of the magnetic moments in the volume ΔV.
- The relation between the magnetization and the applied field is defined as susceptibility tensor $\boldsymbol{M} = \chi \circ \boldsymbol{H}$.
- $\boldsymbol{H}_{\text{eff}} = \boldsymbol{H}_{\text{ext}} + \boldsymbol{H}_{\text{exchange}} + \boldsymbol{H}_{\text{dipole}} + \boldsymbol{H}_{\text{DMI}} + \cdots$
- $\boldsymbol{H}_{\text{eff}} = -\frac{1}{\mu}\frac{\partial \boldsymbol{E}_{tot}}{\partial \boldsymbol{M}}$
- $E_{\text{tot}} = E_{ext} + E_{exchange} + E_{dipole} + E_{DMI} + \cdots$
- The Zeeman interaction, symmetric and asymmetric exchange interactions, dipole interaction, and so on, need to be considered.

F. Kargar, and A. A. Balandin, Nat. Photon., 5, 720–731 (2021).

I-2. Brillouin scattering for magnonics research: spin waves

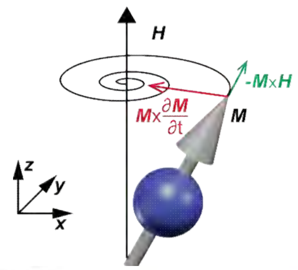

- **Collective motion of magnetic moments**
- **Landau–Lifshitz–Gilbert (LLG) equation**
  - $\frac{\partial \boldsymbol{M}}{\partial t} = -|\gamma|\mu_0 \boldsymbol{M} \times \boldsymbol{H}_{\text{eff}} + \frac{\alpha}{M_s}\boldsymbol{M} \times \frac{\partial \boldsymbol{M}}{\partial t}$
  - $\boldsymbol{H}_{\text{eff}} = \boldsymbol{H}_{\text{ext}} + \boldsymbol{H}_{\text{exchange}} + \boldsymbol{H}_{\text{dipole}} + \boldsymbol{H}_{\text{DMI}} + h_{\text{rf}}$
  - Damping parameter: α

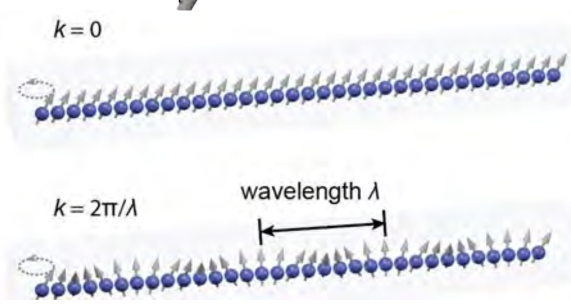

Ferromagnetic resonance (FMR)

- **Kittel formula:**
  - $\omega_0 = \sqrt{[H_{ext} + (N_x - N_z)M_s][H_{ext} + (N_y - N_z)M_s]}$

Spin waves

D. D. Stancil et al. Spin waves, Springer (2009);
B.A. Kalinikos and A.N. Slavin, J. Phys C: Solid State Phys, **19** 7013 (1986).

I-2. Brillouin scattering for magnonics research: spin waves

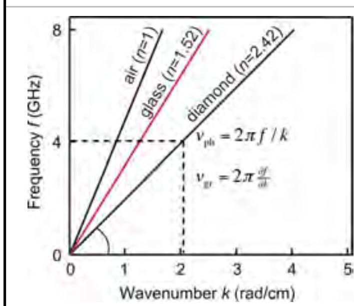

Dispersion of electromagnetic waves, cited from the IEEE Magnetics Society Summer School - Rio de Janeiro, B. Hillebrands

- **The dispersion relations of magnon depends strongly on the relative orientation of spin wavevector *k* and the magnetization *M*.**

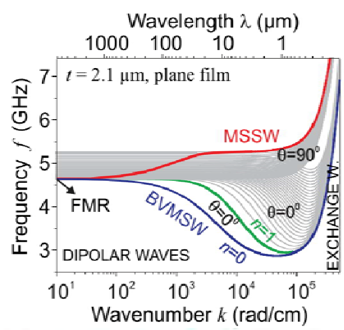

A. V. Chumak *et al.*, *J. Phys. D: Appl. Phys.* **50** 244001 (2017)

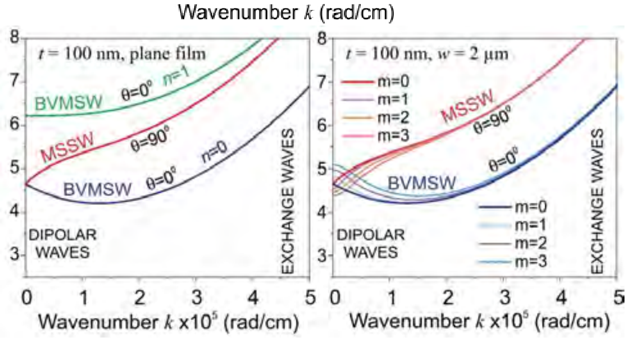

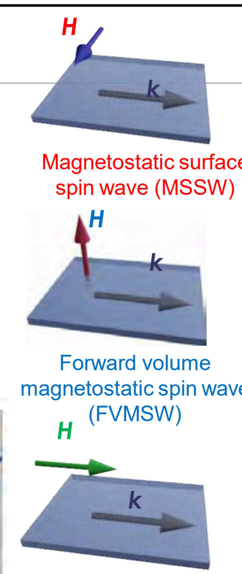

Magnetostatic surface spin wave (MSSW)

Forward volume magnetostatic spin wave (FVMSW)

Backward volume magnetostatic spin wave (BVMSW)

I-2. Brillouin scattering for magnonics research: polarization control

BLS uses linearly polarized light;
- The **E** components decide the polarization.
- For linearly polarized light, when **E** components are in x-y plane, then it is called s-polarization.
- For linearly polarized light, when **E** components are in x-z plane, then it is called p-polarization.

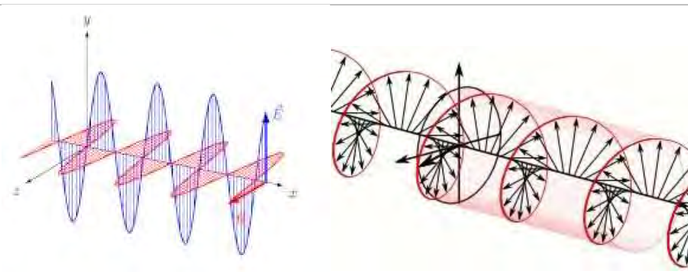

https://en.wikipedia.org/wiki/Plane_of_polarization

Photon-magnon scattering involves a 90 deg polarization rotation;
- Laser source is controlled to emit p-polarized light;
- Polarizers and polarization filters applied to only give p-polarized light to the sample, and leave on s-polarized light to the Fabry-Perot interferometer.
- The Fabry-Perot interferometer only detect s-polarized light.

11 cnrs université PARIS-SACLAY THALES

I-2. Brillouin scattering for magnonics research: back-scattered configuration

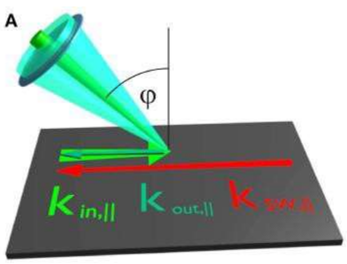

T. Sebastian et al., Front. Phys., **3** 35 (2015).

Magnification = 100x
NA = 0.55
WD = 13.0mm
Focal Length = 2mm
Resolving Power = 0.5µm
Depth of Field = 0.9µm

Wavevector control in back-scattered configuration:
- $k_{SW,||} = 2\frac{2\pi}{\lambda_L} \cdot \sin\varphi$
- φ: the angle of incidence

- For blue laser with $\lambda_L = 460$ nm
- $k_{SW,max} = 27.3$ rad/µm

MitutoyoM Plan Apo SL 100x
So 33 degree of laser angle

The wavevector can be detected are among the range from -27.3 rad/µm to +27.3 rad/µm

12 cnrs université PARIS-SACLAY THALES

I-2. Brillouin scattering for magnonics research: micro-focus BLS setup

Laser source:
- linearly polarized light, normally green (λ = 532 nm) or blue (λ = 473 nm) light;

Polarization control:
- Polarization control to exclude most of the phonon contribution and select the photon scattered with magnon;

Fabry-Perot interferometer:
- To detect tiny energy difference between the scattered photon and incident photon;

Objective lens:
- To focus on the top surface, also possible for the bottom surface focusing for some materials;

CCD camera and white light source:
- To image the structure while data collection and select the region to measure;

Piezostages underneath the sample:
- Spatial scanning function.

Macro BLS has better k_i control without the objective lens close to the sample.

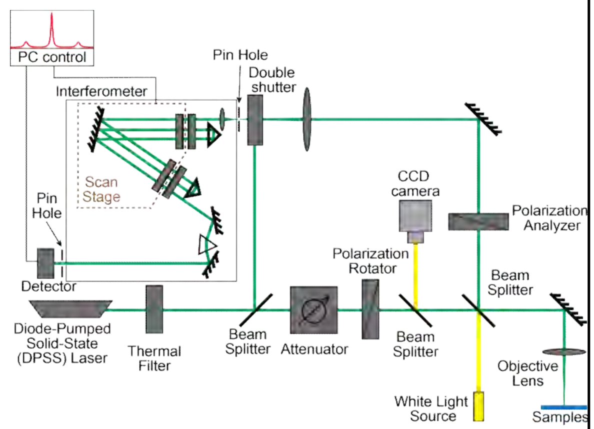

cnrs université PARIS-SACLAY THALES

I-2. Brillouin scattering for magnonics research: difference between micro- and macro-BLS

From the setup construction:
- Micro-BLS has objective lens with high magnification near the sample;

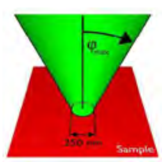

T. Sebastian et al., Front. Phys., **3** 35 (2015).

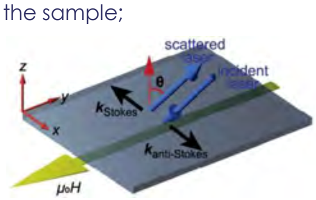

M. Heigl et al., Nat. Commun., **12,** 2611 (2021).

Laser diameter is usually about 40 µm.

- Micro-BLS offers higher spatial resolution.

From the wavevector control:
- In micro-BLS configuration, the laser is focus on the sample with an angle φ_{max}. So the accessible **k** is a range from $-2\frac{2\pi}{\lambda_L}\cdot\sin\varphi_{max}$ to $2\frac{2\pi}{\lambda_L}\cdot\sin\varphi_{max}$.
- In macro-BLS configuration, the laser are aligned to incident with one angle θ. So the accessible **k** is fixed value $-2\frac{2\pi}{\lambda_L}\cdot\sin\varphi_{max}$ and $2\frac{2\pi}{\lambda_L}\cdot\sin\varphi_{max}$.

cnrs université PARIS-SACLAY THALES

I-2. Brillouin scattering for magnonics research: magneto-optical effects

Optical properties of magnetized materials are described by the permittivity tensor

$$\varepsilon_{ij} = \varepsilon_{ij}^{(0)} + \left(\frac{\partial \mathcal{E}_{ij}}{\partial M_k}\right)_{M=0} M_k + \frac{1}{2}\left(\frac{\partial^2 \mathcal{E}_{ij}}{\partial M_k M_l}\right)_{M=0} M_k M_l + \cdots$$

$$\varepsilon_{ij} = \varepsilon_{ij}^{(0)} + K_{ijk} M_k + G_{ijkl} M_k M_l$$

General form of permittivity tensor

$$\varepsilon = \begin{bmatrix} \varepsilon_{xx} & \varepsilon_{xy} & \varepsilon_{xz} \\ \varepsilon_{yx} & \varepsilon_{yy} & \varepsilon_{yz} \\ \varepsilon_{zx} & \varepsilon_{zy} & \varepsilon_{zz} \end{bmatrix}$$

Magneto-optical

Magneto-optical

Optical

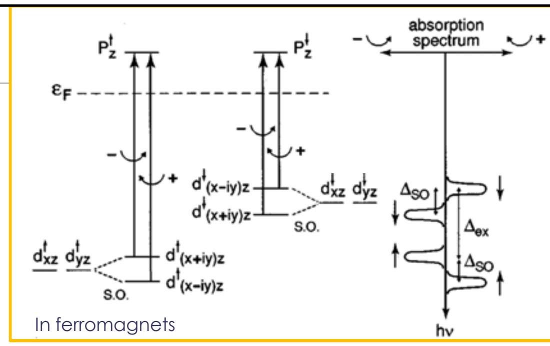

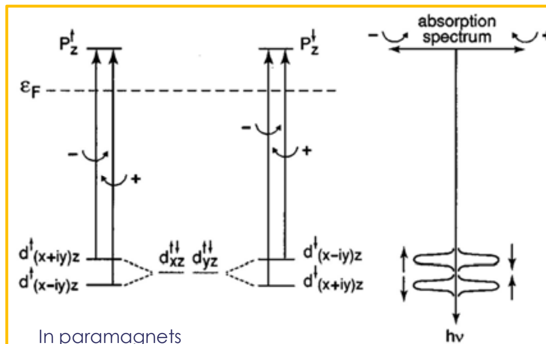

P. Bruno, Y. Suzuki, and C. Chappert, *Phys. Rev. B* **53**, 9214 (1996).

cnrs · université PARIS-SACLAY · THALES

Contents

cnrs · université PARIS-SACLAY · THALES

II. Multiple functions of BLS technique

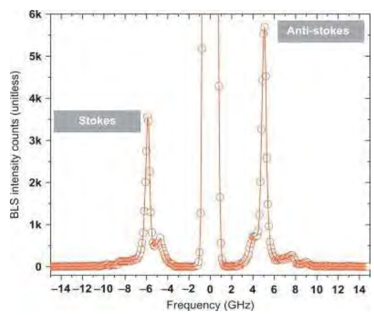

A. O. Adeyeye, and G.Shimon, Handbook of Surface Science, Volume 5, 2015

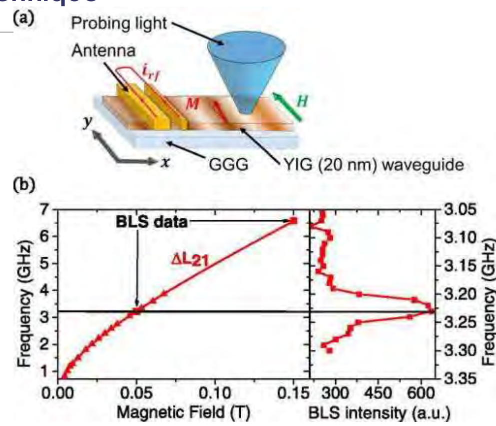

M. Collet, et al., Appl. Phys. Lett. 110, 092408 (2017);

Mostly integrated with micro-BLS.

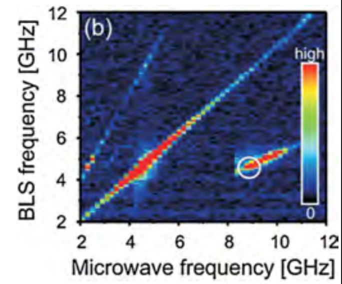

H. Schultheiss, et al., Phys. Rev. Lett., 103, 157202 (2009).

Also possible for nonlinear effects of magnons

Single BLS scan:

- The spectrum offers frequency and intensity information of the magnons in the system, at both the Stokes and anti-Stokes side.

BLS technique offers the function of field scan and rf-assisted excitation.

cnrs université PARIS-SACLAY THALES

II. Multiple functions of BLS technique: 1. Spatial-resolved function

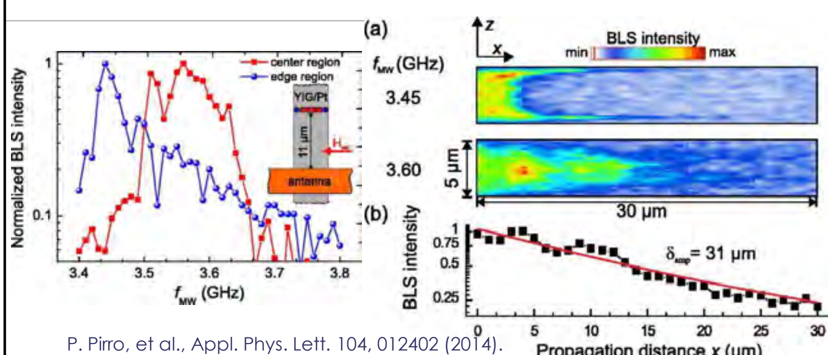

P. Pirro, et al., Appl. Phys. Lett. 104, 012402 (2014).

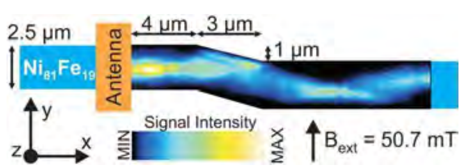

P. Clausen, et al.,Appl. Phys. Lett., 99, 162505 (2011).

Spatial-resolved function

- Achieved by integrating the piezostages underneath the sample.
- BLS intensity has been collected at different locations at each specific frequency;
- Spin waves intensity decay can be observed straightforward and decay length can be extracted.
- In magnon waveguides with unconventional shapes, spatial-resolved BLS offers info on the spin wave channels in the waveguides.
- Reflection of internal field.

cnrs université PARIS-SACLAY THALES

II. Multiple functions of BLS technique: 2. Wavevector-resolved function

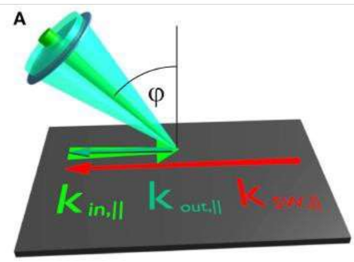

T. Sebastian et al., Front. Phys., **3** 35 (2015).

Wavevector control in back-scattered configuration:

- $k_{SW,||} = 2\frac{2\pi}{\lambda_L} \cdot \sin\varphi$
- φ: the angle of incidence
- By varying the incident angle φ, the in-plane spin wavevector $k_{SW,||}$ varies.
- Convenient tool to explore magnon band structure and relevant physics.

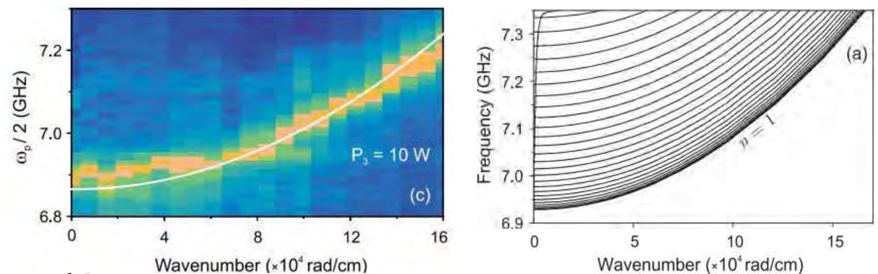

A. A. Serga, et al., Phys. Rev. B, 86,134403 (2012).

II. Multiple functions of BLS technique: 3. Time-resolved function

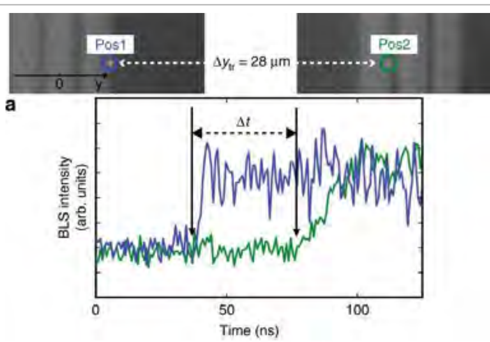

P. Che, K. Baumgaertl, et al., Nat. Commun., 11, 1445 (2020).

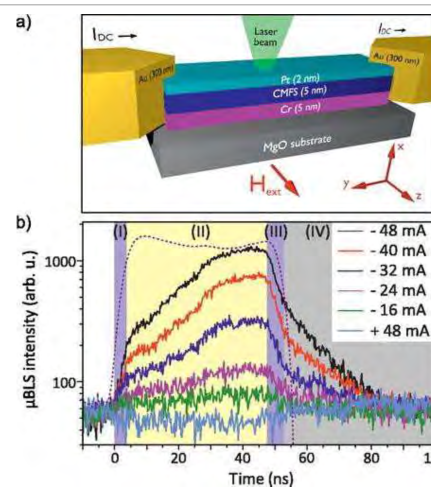

T. Meyer, et al., Appl. Phys. Lett. 112, 022401 (2018).

To measure the group velocity of magnons:

- Time-domain BLS signal collected at different locations;
- $v_g = \frac{\Delta y_{tr}}{\Delta t}$

Time-dependent phenomenon.

- Spin current generated via spin-Hall-effect and the spin-transfer-torque effect.

II. Multiple functions of BLS technique: 4. Phase-resolved function

Phase-resolved BLS configuration:

- Electro-optical modulator (EOM) driven by the same microwave signal used to excite the spin wave;
- Interference between inelastically scattered light created in the process of propagation of the probing laser beam through the sample with reference scattered light provided by the magneto-optic modulation;
- Without phase correlation, the intensities of the sample beam E_s^2 and the reference beam E_r^2 combine to $E_s^2 + E_r^2$;
- With interference conditions, the sample beam and the reference beam combine to $E_s^2 + 2E_sE_r\cos\varphi + E_r^2$, with an additional phase-term.

Phase information of spin waves:

- Wavelength can be extracted;
- Spin wave channels are clearly visualized.

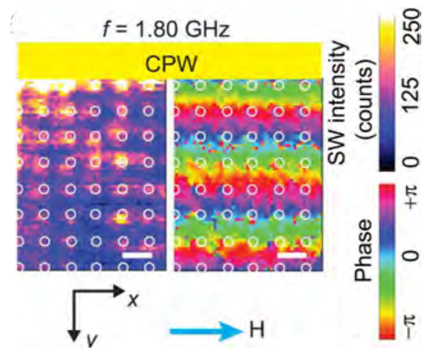

S. Watanabe, et al., Sci. Adv., 7, eabg3771 (2021).

cnrs université PARIS-SACLAY THALES

Contents

cnrs université PARIS-SACLAY THALES

III. Examples of charactering magnetic materials hosting non-collinear spin textures using BLS: 1. Charactering basic magnetic properties of materials

Landau–Lifshitz–Gilbert (LLG) equation

- $\frac{\partial \boldsymbol{M}}{\partial t} = -|\gamma|\mu_0 \boldsymbol{M} \times \boldsymbol{H}_{\text{eff}} + \frac{\alpha}{M_s} \boldsymbol{M} \times \frac{\partial \boldsymbol{M}}{\partial t}$

Kittel formula:

- $\omega_0 = \sqrt{[H_{ext} + (N_x - N_z)M_s][H_{ext} + (N_y - N_z)M_s]}$

E.g. mode dispersion relation:

- $\omega = \sqrt{(H + M_s T4 + Jk^2)(H + M_s T4 + Jk^2) - \frac{e^{-4|k|d} {M_s}^2}{16}(1 + 2e^{2|k|d})}$

Basic magnetic properties of materials:

- Saturation magnetization, in the smaller **k** regime;
- Exchange stiffness, in the higher **k** regime;
- Decay length and damping parameter;
- Dzyaloshinskii-Moriya interaction (DMI) strength.

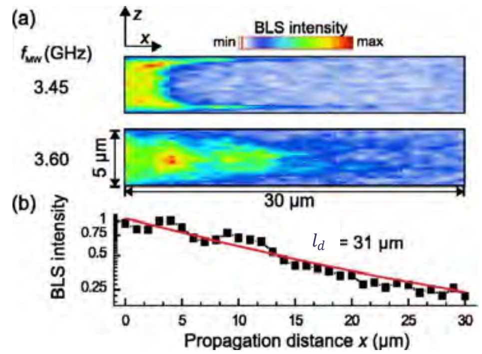

P. Pirro, et al., Appl. Phys. Lett. 104, 012402 (2014).

Decay length $l_d = \frac{v_g}{2\pi\alpha f}$

Relaxation time $\tau = \frac{1}{2\pi\alpha f}$

23

III-1. Charactering basic magnetic properties of materials: DMI

DMI:

- Symmetric exchange interaction: $E_{ex} = -2J_{ij}\boldsymbol{S}_i \cdot \boldsymbol{S}_j$;
- Dzyaloshinskii-Moriya interaction is an asymmetric exchange interaction: $E_{DMI} = D_{ij}\boldsymbol{S}_i \times \boldsymbol{S}_j$.

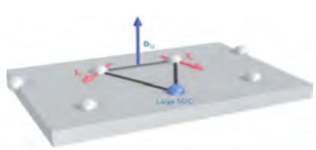

Bulk DMI in non-centrosymmetry chiral magnet

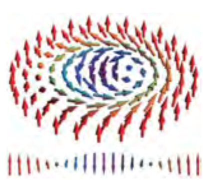

Bloch type skyrmion

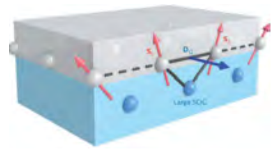

Interfacial DMI in broken inversion symmetry multilayers of normal metal/ferromagnet

Néel type skyrmion

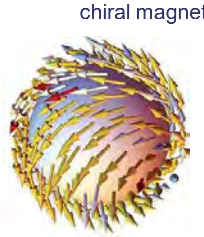

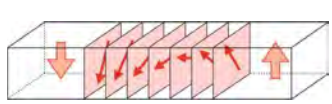

Bloch type domain wall

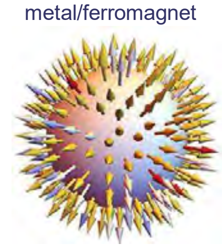

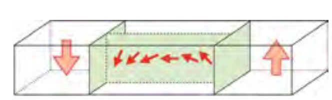

Néel type domain wall

A. Fert et al., Nat. Rev. Materials., **2** 17031 (2017);I. Kezsmarki et al., Nat. Mater., **14** 1116 (2015); S. Seki and M. Mochizuki, Skyrmions in Magnetic Materials, Springer (2016); A. A. Kovalev and S. Sandhoefner, Front. Phys., 27 (2018).

24

III-1. Charactering basic magnetic properties of materials: DMI

DMI type	Bulk DMI	Interfacial DMI
Asymmetric dispersion relations	BV mode, $\vec{k} \parallel \vec{M}$	DE mode, $\vec{k} \perp \vec{M}$

Small-k regime:

$$\frac{\omega}{\gamma\mu_0} = \sqrt{(H + M_s/4 + Jk^2)(H + 3M_s/4 + Jk^2) - \frac{e^{-4|k|d}M_s^2}{16}(1 + 2e^{2|k|d})} + pD^*k$$

Large-k regime:

$$\frac{\omega}{\gamma\mu_0} = \sqrt{(H + Jk^2)(H + M_s + Jk^2)} + pD^*k \qquad D^* = \frac{2D}{\mu_0 M_s}$$

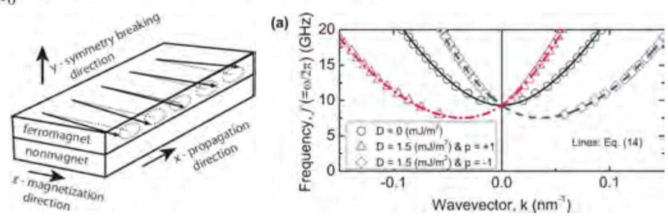

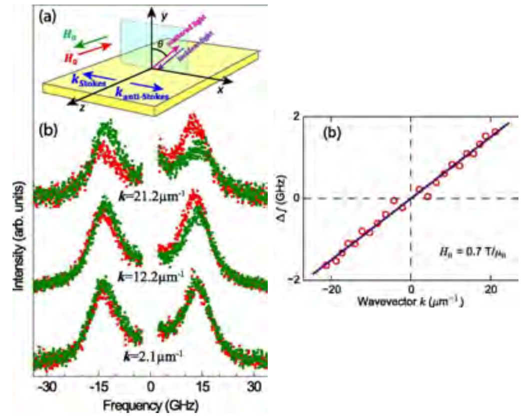

J-H. Moon et al., Phys. Rev. B, 88, 184404 (2013); K. Di et al., Appl. Phys. Lett. 106, 052403 (2015).

cnrs université PARIS-SACLAY THALES

III-1. Charactering basic magnetic properties of materials: DMI

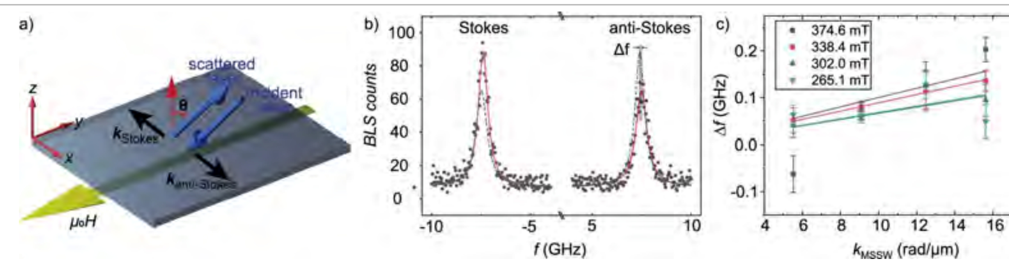

$$\frac{\omega}{\gamma\mu_0} = \sqrt{(H + Jk^2)(H + M_s + Jk^2)} + pD^*k \qquad D^* = \frac{2D}{\mu_0 M_s}$$

Question: The average fitting slot is 0.0105 GHz/ $\frac{rad}{um}$, M_S=230 kA/m, please estimate the DMI strength.

cnrs université PARIS-SACLAY THALES

III-1. Charactering basic magnetic properties of materials: DMI

Possible to measure with BLS but not often seen

DMI type	Bulk DMI	Interfacial DMI
Asymmetric dispersion relations	BV mode, $\vec{k} \parallel \vec{M}$	DE mode, $\vec{k} \perp \vec{M}$

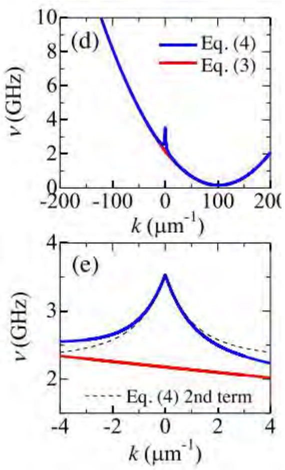

No dipole-dipole interaction

$$\nu = \sigma[\mathrm{sgn}(\vec{k}\cdot\vec{H})]\frac{2DSV_0|k|}{h} + \frac{C_{sym}}{h}$$

and $C_{sym} = JSV_0k^2 + 2KV_0S^3 + \gamma\hbar\mu_0 H$

Considering also dipole-dipole interaction

$$\nu = \sigma[\mathrm{sgn}(\vec{k}\cdot\vec{H})]\frac{2DSV_0|k|}{h} + \frac{C_{sym}}{h}\sqrt{\left(1+\frac{\gamma\hbar\mu_0 M_s}{C_{sym}}\frac{(1-e^{-|k|l})}{|k|l}\right)}$$

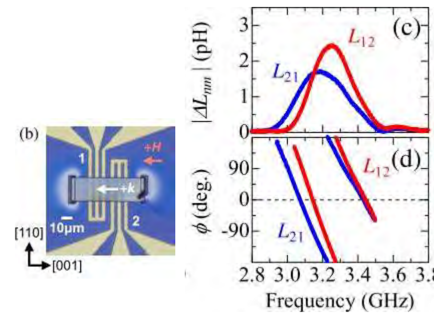

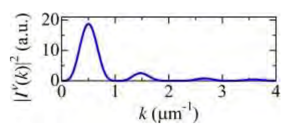

27

S. Seki et al., Phys. Rev. B, 93, 235131 (2016).

III-2. Investigation of Bose–Einstein condensation (BEC) of magnons

Bose-Einstein Condensation induced by spin-orbit torque

S. O. Demokritov, et al., Nature, 443, 430–433 (2006)

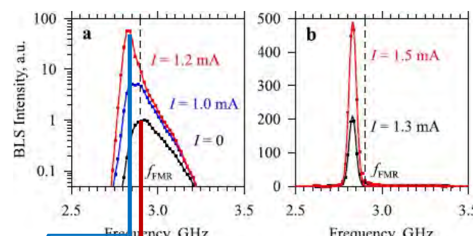

ARTICLE

OPEN

Evidence for spin current driven Bose-Einstein condensation of magnons

B. Divinskiy, H. Merbouche, V. E. Demidov, K. O. Nikolaev, L. Soumah, D. Gouéré, R. Lebrun, V. Cros, Jamal Ben Youssef, P. Bortolotti, A. Anane & S. O. Demokritov

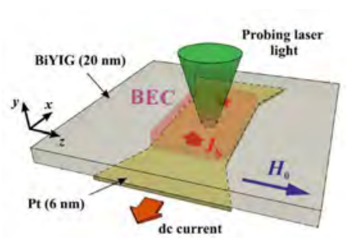

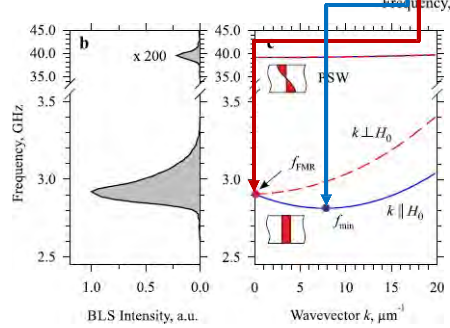

28

III-3. Investigation of magnon band structure with BLS

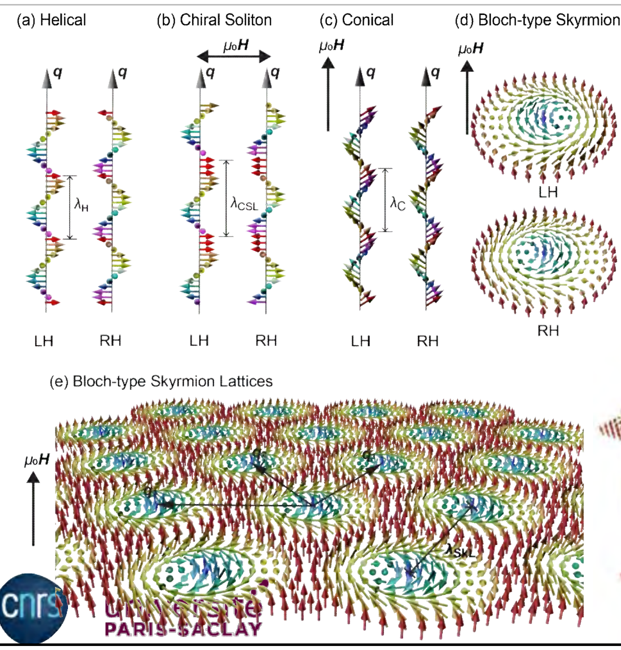

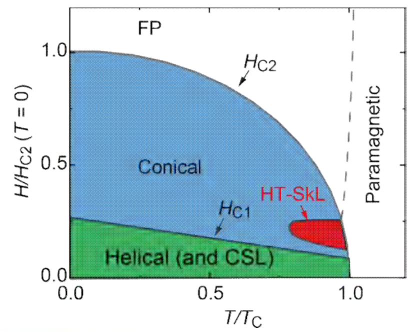

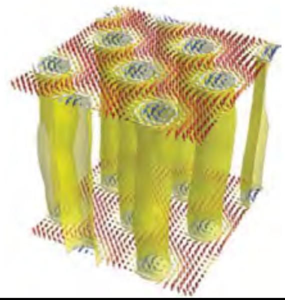

P. Milde et al., Science, **360** 6136 (2013); P. Che, PhD thesis (2021).

III-3. Investigation of magnon band structure with BLS

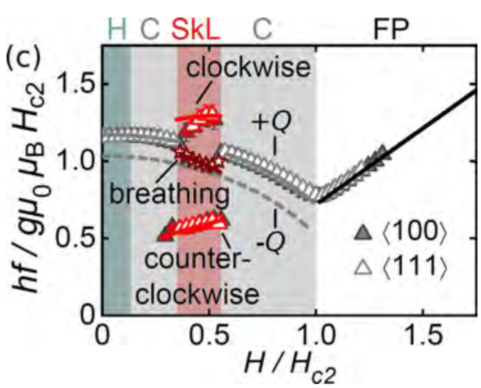

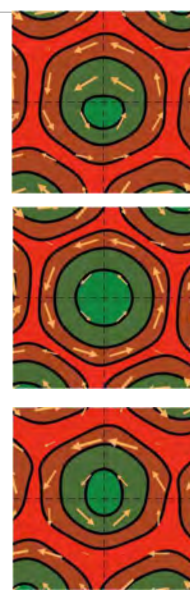

- 2 modes in helical and conical phases.
- 3 modes in skyrmion lattice phase.

T. Schwarze et. al. Nat. Mater. **14,** 478–483 (2015); I. Stasinopoulos et. al. Appl. Phys. Lett. 111, 032408 (2017); M. Weiler et. al. PRL 119, 237204 (2017).

III-3. Investigation of magnon band structure with BLS

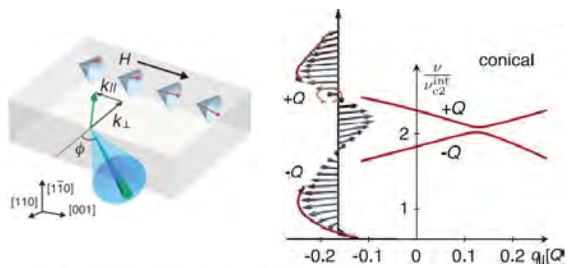

- Spin waves propagate in the conical phases.
- $\vec{k} \perp \vec{H}$
- Spectral weight are asymmetric as well:

$$\frac{\mathcal{Z}_+(\vec{q})}{\mathcal{Z}_-(\vec{q})} \approx \frac{|1 + i2M_sG_{44}/K|^2}{|1 - i2M_sG_{44}/K|^2}$$

$i2M_sG_{44}/K$ = 0.09 of magneto-optical constants

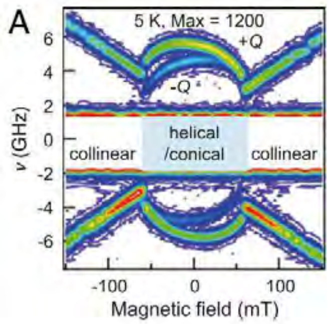

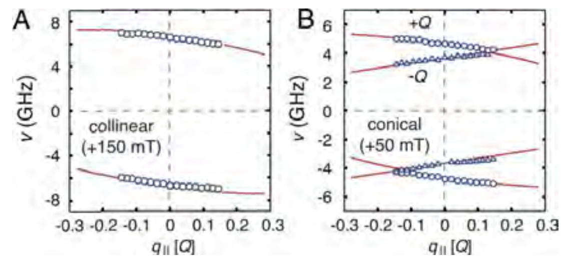

PARIS-SACLAY

N. Ogawa et al., Proc. Natl. Acad. Sci. U.S.A., 118 (8) e2022927118 (2021).

THALES

III-4. Investigation of local phase diagrams of chiral magnets with BLS

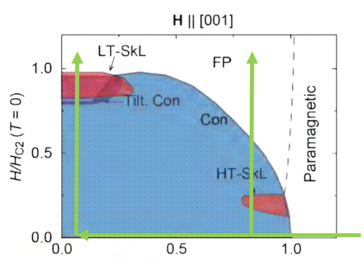

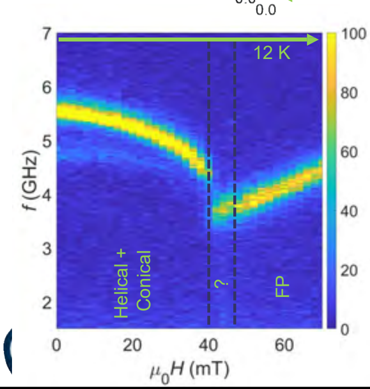

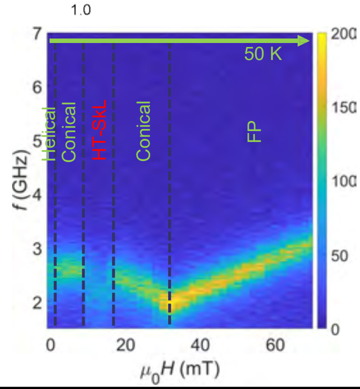

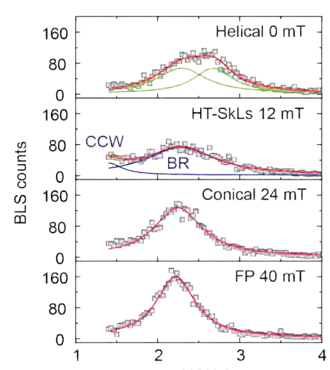

THALES

Magneto-optical Kerr effect (MOKE) and Xray Circular Dichroism (XMCD) - microscopic mechanism and experimental measurement

Instructor: Dr. Phoebe Tengdin
Slide credit: **Jaroslav Hamrle**
(jaroslav.hamrle@vsb.cz)

November 18, 2022

Magneto-optical Kerr effect:

- Change of optical properties (polarization state, reflectivity) by presence/change of magnetization of the sample.

One can separate usage of magneto-optical (MO) effects to:

- MO as a metrology tool to study magnetism:
  - MO magnetometry (study of magnetization reversal).
  - MO microscopy (study of domain wall and its propagation).
  - Magnetization dynamic studies (precession etc.)
  - MO as a tool for ultrafast magnetization processes.
- MO spectroscopy to study optical properties of the MO effect:
  - Magnetism is understand as a perturbation, reducing symmetry of the solids and hence introducing new optical features.
  - Study of spin-orbit interaction.
  - Interaction between light and magnetism – a very fundamental interaction.

MO effect I: Magneto-optical Kerr effect (MOKE):

- For example: incident s-polarized wave.
- Magnetized sample
  ⇒ hence: also p-polarized wave appears on the reflection.

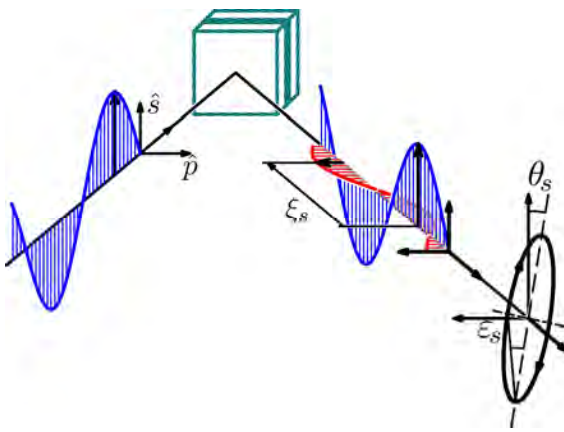

MOKE linear in M

- θ_S: Kerr rotation.
- E_S: Kerr ellipticity.

MO effect I: Kerr and Faraday MO effect:

Due to historical reasons, there are different names for MO effects measured in reflection and transmission.

Kerr effect:
- measured in reflection.
- discovered 1876.

Faraday effect:
- measured in transmission.
- discovered 1845.

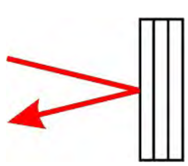

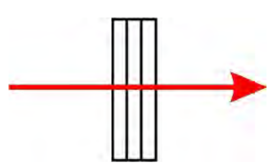

MOKE configurations and permittivity tensor:

Polar MOKE	Longitudinal MOKE	Transversal MOKE
$M \perp$ sample surface	$M \parallel$ plane of incidence	$M \perp$ plane of incidence

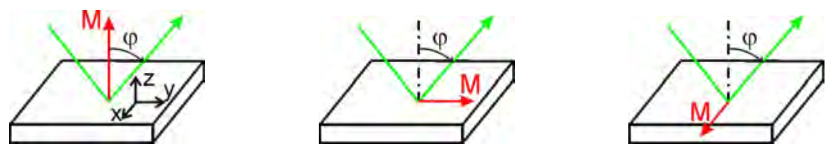

Polarization induced by magnetization: $\Delta P_M = \varepsilon_1 (M \times E)$

$$\begin{pmatrix} \varepsilon_0 & -\varepsilon_1 m_z & 0 \\ \varepsilon_1 m_z & \varepsilon_0 & 0 \\ 0 & 0 & \varepsilon_0 \end{pmatrix} \quad \begin{pmatrix} \varepsilon_0 & 0 & \varepsilon_1 m_y \\ 0 & \varepsilon_0 & 0 \\ -\varepsilon_1 m_y & 0 & \varepsilon_0 \end{pmatrix} \quad \begin{pmatrix} \varepsilon_0 & 0 & 0 \\ 0 & \varepsilon_0 & -\varepsilon_1 m_x \\ 0 & \varepsilon_1 m_x & \varepsilon_0 \end{pmatrix}$$

$\Phi_{s/p}(m_z)$ $\quad$ $\Phi_{s/p}(m_y)$ $\quad$ $\Delta r_{pp}(m_x)$

MO effect II: transversal MOKE:

- Incident p-polarized wave.
- Magnetization in-plane and perpendicular to the incident plane (so-called transversal magnetization direction).
- Change of the reflected p-polarized intensity due to magnetization in the sample (in this particular case, no change in polarization of the reflected light appears).

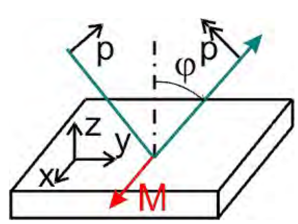

MO effect III: Magnetic dichroism and birefringence:

Dichroism: different damping of both light's eigen-modes.

Birefringence: different propagation speed of both light's eigen-modes.

Magnetic circular dichroism (MCD):

- Different absorption for circularly left and right polarized light.
- MCD linear in M.
- MOKE and MCD has the same microscopic origin, they just manifest in different ways.

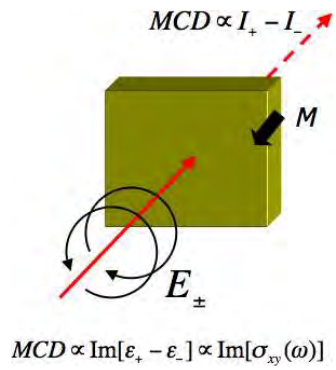

MO effect IV: Voigt effect:

- Discovered 1899.
- Different absorption or phase shift for linear polarization parallel and perpendicular with the magnetization.
- Quadratic in M ($\sim M^2$).
- Also called Cotton-Mouton effect or linear magnetic dichroism/birefringence (LMD/LMB)
- The same microscopic origin as quadratic MOKE (QMOKE) (more precisely, Voigt effect is simplest case of QMOKE).

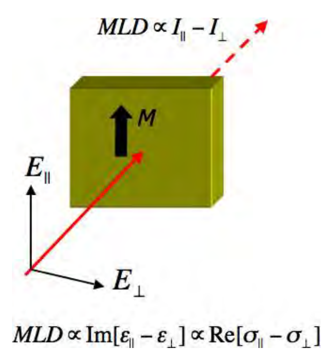

Classification of the MO effects:

- Even / odd effect in magnetization.
- Measured in transmission / reflection.
- Detected change of intensity / polarization.
- Probing light is linearly / circularly polarized.

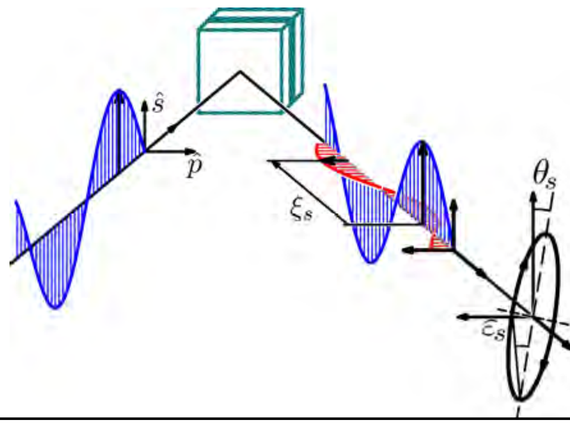

Family of magneto-optical effects:

Linear pol.	Detected: Polariz.	Detected: Intensity
Linear in M	MOKE, (Kerr and Faraday effect) [Hall effect]	Transversal-MOKE
Quadratic in M	QMOKE, Voigt effect, Linear Magnetic Birefringence (LMB)	Linear Magnetic Dichroism (LMD) [AMR]
Circular pol.	Detected: Polariz.	Detected: Intensity
Linear in M	Mag. Circular Birefringence (MCB)	Magnetic Circular Dichroism (MCD)
Quadratic in M	?	quadratic-MCD (?)

[...] denotes nomenclature in research of conductivity.

Origin of MO effect (microscopic):

Electronic structure of the FM material
[microscopic description]
⇓
Permittivity tensor of each layer
[phenomenological description]

$$\varepsilon = \begin{pmatrix} \varepsilon_{xx} & \varepsilon_{xy} & \varepsilon_{xz} \\ \varepsilon_{yx} & \varepsilon_{yy} & \varepsilon_{yz} \\ \varepsilon_{zx} & \varepsilon_{zy} & \varepsilon_{zz} \end{pmatrix}$$

⇓
Reflectivity matrix of whole sample
[maximal accessible optical information]

$$R = \begin{pmatrix} r_{ss} & r_{sp} \\ r_{ps} & r_{pp} \end{pmatrix}$$

⇓
Measured Kerr effect: $\Phi_s = \frac{r_{ps}}{r_{ss}}$
⇓
Signal measured by MO setup

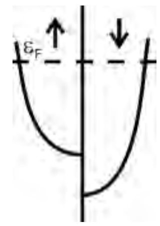

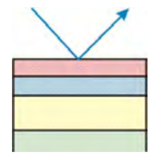

MO effects and permittivity tensors

[Note: tensors on this slide are only illustrative.]

⇒ Linear MOKE: PMOKE, LMOKE, TMOKE, MCD, MCB, [Hall]

$$\begin{pmatrix} \varepsilon_0 & -\varepsilon_1 m_z & \varepsilon_1 m_y \\ \varepsilon_1 m_z & \varepsilon_0 & -\varepsilon_1 m_x \\ -\varepsilon_1 m_y & \varepsilon_1 m_x & \varepsilon_0 \end{pmatrix} \quad \text{MO signal} \sim \varepsilon_1(m_i)$$

⇒ Quadratic MOKE:

$$\begin{pmatrix} \varepsilon_0 & \varepsilon_1(m_i m_j) & 0 \\ \varepsilon_1(m_i m_j) & \varepsilon_0 & 0 \\ 0 & 0 & \varepsilon_0 \end{pmatrix} \quad \text{MO signal} \sim \varepsilon_1(m_i m_j)$$

⇒ Voigt effect: MLD, MLD, [AMR]

$$\begin{pmatrix} \varepsilon_{xx}(m_i m_j) & 0 & 0 \\ 0 & \varepsilon_{yy}(m_i m_j) & 0 \\ 0 & 0 & \varepsilon_{zz}(m_i m_j) \end{pmatrix} \quad \text{MO signal} \sim \varepsilon_{zz}(m_i m_j) - \varepsilon_{yy}(m_i m_j)$$

Photon absorption: electric-dipole approximation:

- The largest contribution to the absorption is given by so-called electric-dipole approximation (valid for $\lambda \gg a$), providing so-called electric-dipole transitions.
- Hence, whole vast energy range can be described by so-called Kubo formula, determining conductivity (absorption) for a given photon energy (shown later).

Selection rules of electric-dipole transitions:

Electric dipole transition is allowed when following conditions are fulfilled:

Energy: $E_f - E_i = \hbar\omega$ (absorbed photon energy is difference between energies of the final and initial electron states)

Momentum: $\hbar\omega/c \approx 0$ (photon has negligible momentum compared to one of the electron. I.e. the momentum of the electron is kept between initial and final state (vertical transitions)).

Electron spin : $\Delta s = 0$ (as photon has no spin, spin of electron is preserved for electric dipole transitions)

Orbital momentum: $\Delta l = \pm 1$ (photon has angular momentum $1\hbar$). Therefore only $s \leftrightarrow p$, $p \leftrightarrow d$ etc. transitions are allowed.

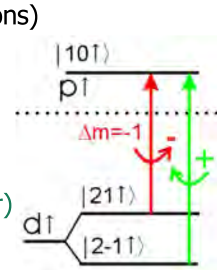

Orbital momentum along z-axis (magnetic number) $\Delta m = \pm 1$ (determines if photon is circularly right or left polarized).

Ab-initio calculation of permittivity tensor

Kubo formula: conductivity determination.

$$S[\varepsilon_{xx}] \sim \sum_{i,f} (f(E_i)-f(E_f))\times[|(i|p_+|f)|^2+|(i|p_-|f)|^2]\times\delta(E_f-E_i-n\omega)$$

$$!R[\varepsilon_{xy}] \sim \sum_{i,f} (f(E_i)-f(E_f))\times[|(i|p_+|f)|^2-|(i|p_-|f)|^2]\times\delta(E_f-E_i-n\omega)$$

where

- $(i|$, $|f)$: initial and final states, respectively.
- $p_\pm = p_x \pm ip_y$, $p_x = in\partial/\partial x$, momentum operator
- terms in the Kubo formula means:
  - summation over all initial and final states, $(i|$ and $|f)$.
  - $f(E_f)$, $f(E_i)$: electron occupancy of initial and final states.
  - $|(i|p_\pm|f)|^2$: probability of the photon to be absorbed between $(i|$ and $|f)$ states for circularly left/right polarized light (non-zero only when electric-dipole selection rules are fulfilled).
  - $\delta(E_f - E_i - n\omega)$ assures energy conservation.

Magneto-optical spectroscopy microscopic picture

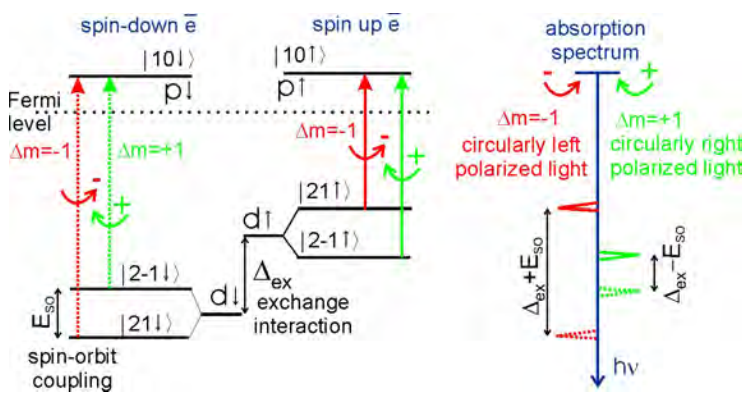

Simplified electronic structure for one point of the k-space.

No spin-orbit coupling assumed:

⇒ no MOKE effect

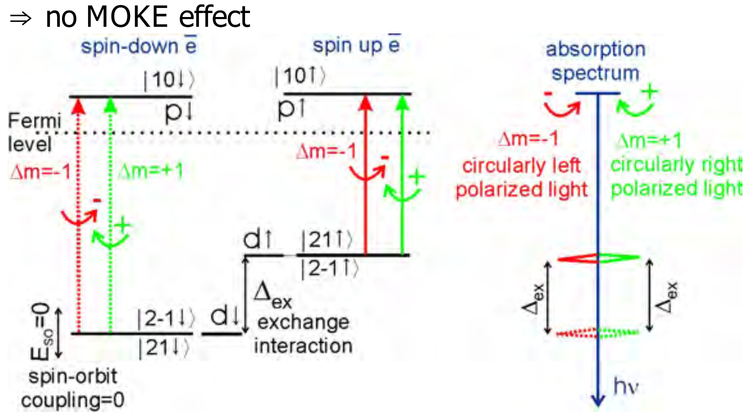

No exchange assumed:

⇒ no MOKE effect

⇒ both SO coupling and exchange must be present to have MOKE.

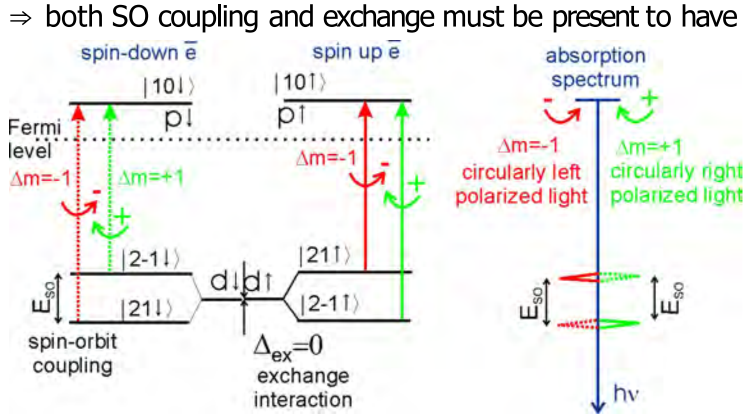

Quadratic Magneto-optical Kerr effect (QMOKE):

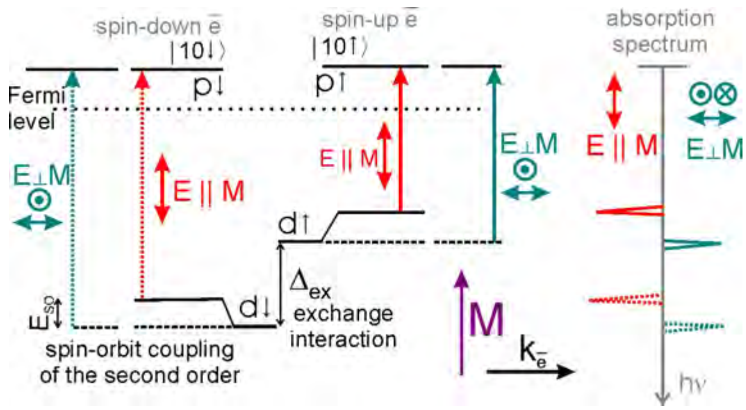

QMOKE arises from different absorptions for $E \perp M$ and $E||M$.

Quadratic Magneto-optical Kerr effect (QMOKE):

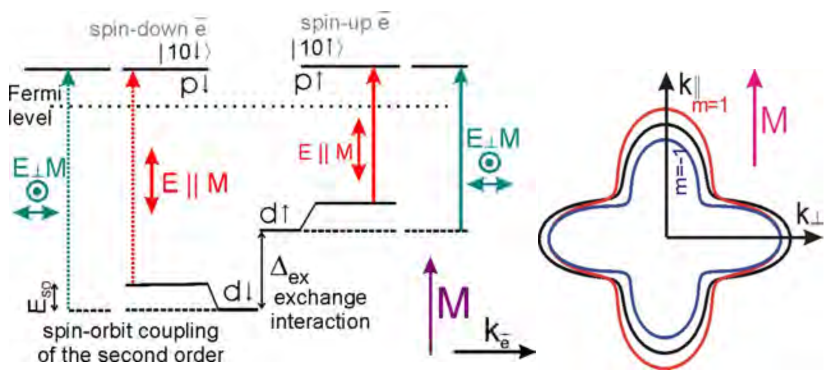

QMOKE arises from different absorptions for $E \perp M$ and $E||M$.
⇒ arrises from different electronic structure in $k_e \perp M$ and $k_e||M$.

Phenomenological description of MOKE

Inputs are permittivity tensors and layer thicknesses
Phenomenological description based on 4×4 matrix formalism.
(light propagation through layer & continuity of lateral E and H field)
calculated reflectivity matrix
calculated MO Kerr effect

Visible MOKE advantages and disadvantages:

- spatial resolution limited by wavelength limit (~300nm for visible light) → but sub-wavelength resolution demonstrated.
- investigation 'on distance', light can be transported nearby sample by a fibre.
- no need of vacuum or special sample preparation.
- depth resolution about 30nm.
- measurements do not influence sample magnetization.
- high time resolution (down to 20 fs).
- depth selectivity.
- vectorial resolution (possible to determine all magnetization components).
- robust, cheap technique.

BUT:

- spatial resolution limited by wavelength limit.
- easy to overcome Kerr signal by spurious noise (S/N ratio problem).
- not direct information about the electronic structure or magnetic moments etc.

Extensions of MOKE:

- XMCD, XMLD for high photon energy.

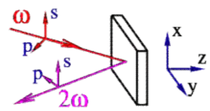

- Non-linear magneto-optics
  ⇒ MO second harmonic generation.
- Inverse Faraday effect (ultrafast optical switching).

(Stanciu et al, PRL 99, 047601 (2007))

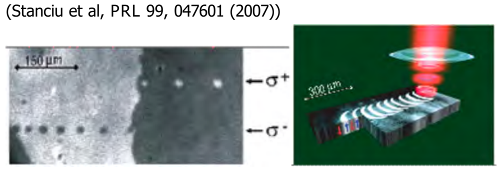

- Observation of spin accumulation in GaAs (spin Hall effect).

(Kato et al, Science, 2004)

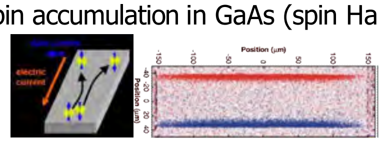

X-ray absorption spectroscopy (XAS):

XAS is extremely sensitive to the chemical state each element, as each element have its own characteristic binding energies. XAS measurements can distinguish the form in which the element crystallizes (for example one can distinguish diamond and graphite, which both entirely consist of C), and can also distinguish between different sites of the same element.

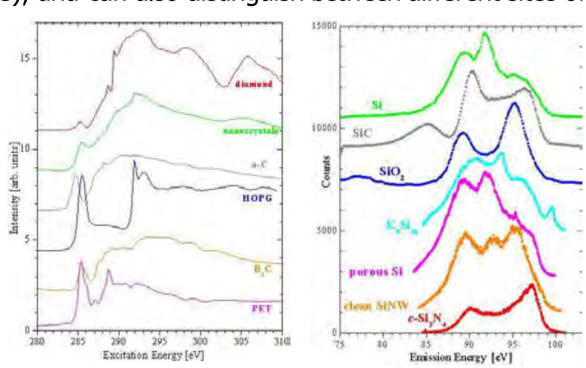

http://beamteam.usask.ca/

XAS on Fe:

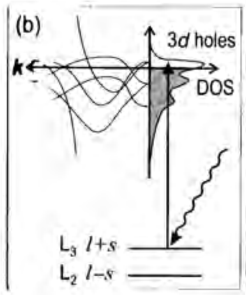

St¨ohr, Siegmann, Magnetism: From fundamentals to nanoscale dynamics

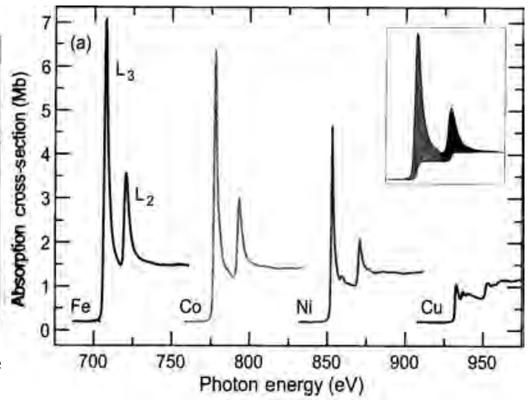

Starting L2, L3 edge (i.e. $2p^{1/2}$, $2p^{3/2}$, respectively):

$$I_{XAS,\ p\to d} \sim N_h$$

N_h: number of free d-states. $p \to s$ has small contribution.

XMCD: X-ray Magnetic circular dichroism:

Circular Dichroism: different absorption for circularly left and right light polarization.

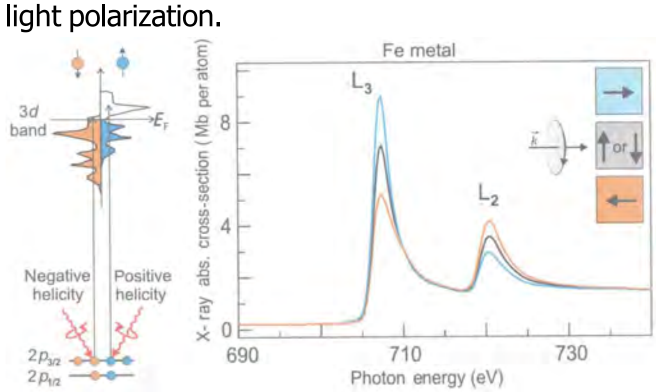

Different absorbed intensity for opposite magnetization orientations.

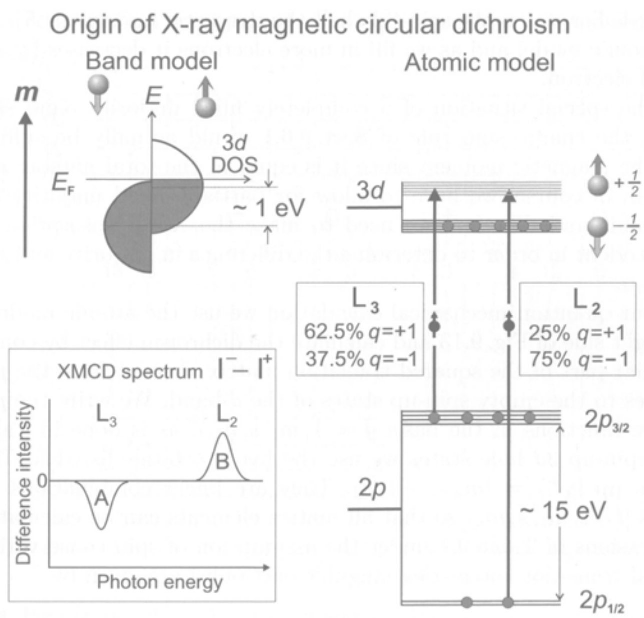

XMCD: Detailes p → d transition

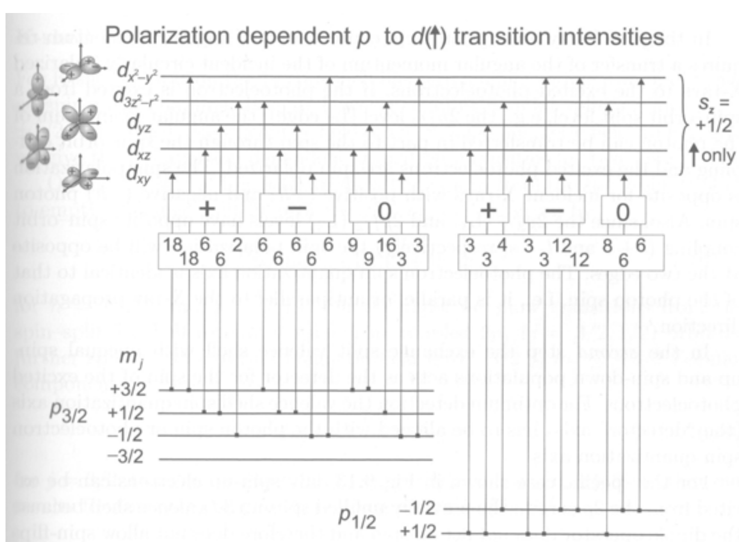

XMCD: sum rules:

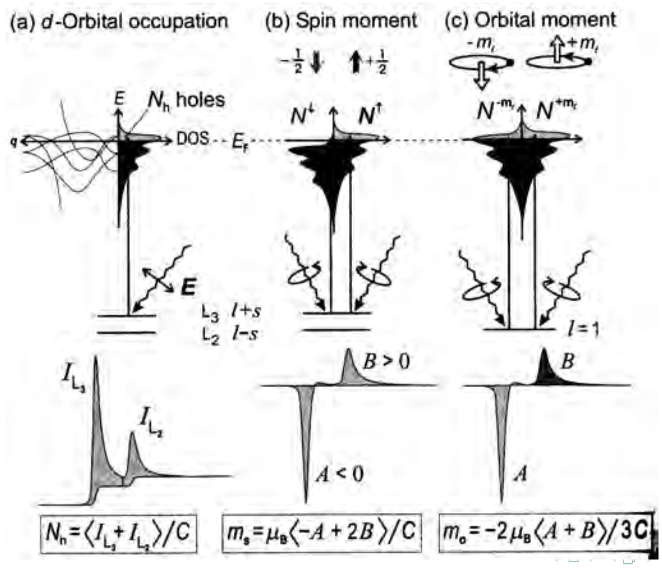

Magneto-optical Kerr effect (MOKE)
└Magneto-optical effect
└Use of magneto-optical effects

Advantages of X-ray spectroscopies:

- element selective.
- quantitative determination of material characterization (e.g. magnetic moment, orbital moment).
- can be both interface or bulk sensitive.
- can provide excellent lateral resolution ($\sim$ 15 nm).
- can provide excellent time resolution ($\sim$ 100 fs).

Disadvantages:

- due to width of the initial (core) line, the energy resolution is limited to $\sim$1 eV.
- synchrotron needed (or high harmonics, see next slides)

DC conductivity:

DC conductivity can be understand as a limit of absorption spectroscopy for $\omega \to 0$.
Due to different history and different available experimental techniques, different names are used in each area:

Transport (dc)	Optics	X-ray
conductivity	absorption	∼ X-ray absorption (XAS)
Hall effect	MOKE effect	XMCD
quadratic-Hall effect	quadratic MOKE (QMOKE)	∼ X-ray linear magnetic dichroism
Anisotropy magneto-resistance (AMR)	Cotton-Mouton, Voigt effect	X-ray linear magnetic dichroism

Unique Tabletop Experimental setup: EUV MOKE

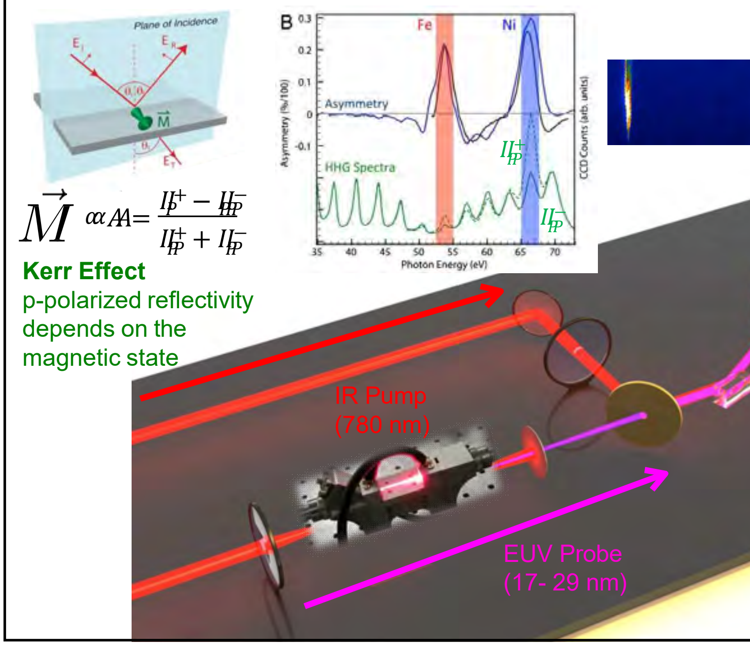

PRL **103**, 257402 (2009)
PRX **2**, 011005 (2012)
PNAS **109**, 4792 (2012)
Nat. Commun. **3**, 1037 (2012)
PRL **110**, 197201 (2013)
PRB **94**, 220408(R) (2016)
PRB **97**, 024433 (2018)
Sci Adv **4**:eaap9744 (2018)
PRL **121**, 077204 (2018)

M-edge Spectroscopy: a unique tool

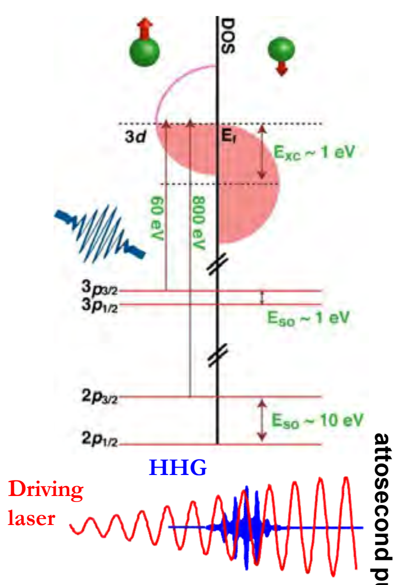

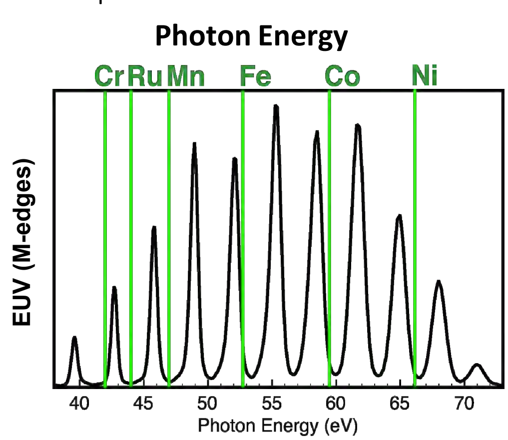

UNIQUE ADVANTAGES
- Element selective
- Multiple elements simultaneously
- <<10fs time resolution, no jitter
- Span entire M edges, L edges

Rundquist et al, *Science* ***280****, 1412 (1998)*
Chen et al., PRL **105**, 173901 (2010)
Popmintchev et al, *Science* ***336****, 1287 (2012)*

10

PHYSICAL REVIEW B VOLUME 12, NUMBER 11 1 DECEMBER 1975

Calculation of the M_{23} magneto-optical absorption spectrum of ferromagnetic nickel

J. L. Erskine*
Department of Physics, University of Illinois, Urbana, Illinois 61801
E. A. Stern†
Department of Physics, University of Washington, Seattle, Washington 98195
(Received 28 April 1975)

The M_{23} magneto-optical absorption spectrum of ferromagnetic nickel is calculated using an approach similar to the component state-density method that has been successfully used in obtaining valence-band emission and absorption x-ray spectra of metals. The M_{23} magneto-optical effects result predominantly from spin-orbit splitting of the $3p$ core state in conjunction with the final d-state spin polarization. The calculated spectrum exhibits features that are directly related to electronic structure parameters including the $3p$ core spin-orbit splitting, and the unfilled d-band spin polarization. Temperature variations in the magneto-optical structure can be used to determine separately the exchange-splitting variation and spin-wave excitation contributions to the decrease in the magnetization. Experimental verification of these predictions should provide insight into the applicability of the Stoner model to ferromagnetic nickel and may be helpful in resolving some of the apparently conflicting results of other experimental probes of the spin polarization near the Fermi level in nickel.

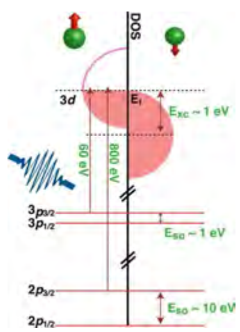

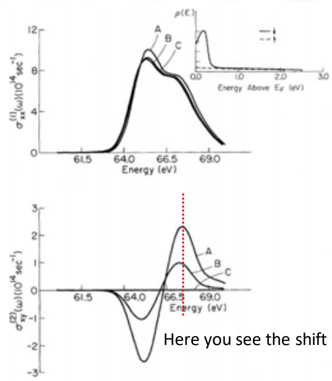

The spin-wave excitation mechanism by itself, if no consequent decrease in exchange splitting occurs, will simply decrease the magnitude of magneto-optical absorption without changing its shape. A decrease in the Stoner exchange splitting will change the shape of the magneto-optical absorption spectrum. Changes in the ordinary optical spectrum are much weaker, and consequently are that much more difficult to detect and interpret.

Time- resolved experiments: we attempted to answer this question: Stoner vs. Heisenberg via reduction of magnetic contrast at the M-edge

PHYSICAL REVIEW B 94, 220408(R) (2016)

Stoner versus Heisenberg: Ultrafast exchange reduction and magnon generation during laser-induced demagnetization

Emrah Turgut,[1] Dmitriy Zusin,[1] Dominik Legut,[2,3] Karel Carva,[3,4] Ronny Knut,[1] Justin M. Shaw,[5] Cong Chen,[1] Zhensheng Tao,[1] Hans T. Nembach,[5] Thomas J. Silva,[5] Stefan Mathias,[6] Martin Aeschlimann,[7] Peter M. Oppeneer,[4] Henry C. Kapteyn,[1] Margaret M. Murnane,[1] and Patrik Grychtol[1]
[1]Department of Physics and JILA, University of Colorado, Boulder, Colorado 80309, USA
[2]IT4Innovations Center, VSB Technical University of Ostrava, CZ-70833 Ostrava, Czech Republic
[3]Department of Condensed Matter Physics, Charles University, CZ-12116 Prague 2, Czech Republic
[4]Department of Physics and Astronomy, Uppsala University, P.O. Box 516, S-75120 Uppsala, Sweden
[5]Electromagnetics Division, National Institute of Standards and Technology, Boulder, Colorado 80305, USA
[6]I. Physikalisches Institut, Georg-August-Universität Göttingen, D-37077 Göttingen, Germany
[7]University of Kaiserslautern and Research Center OPTIMAS, D-67663 Kaiserslautern, Germany
(Received 6 May 2016; revised manuscript received 18 November 2016; published 28 December 2016)

PHYSICAL REVIEW B 97, 024433 (2018)
Editors' Suggestion

Direct measurement of the static and transient magneto-optical permittivity of cobalt across the entire M-edge in reflection geometry by use of polarization scanning

Dmitriy Zusin,[1,*] Phoebe M. Tengdin,[1] Maithreyi Gopalakrishnan,[1] Christian Gentry,[1] Adam Blonsky,[1] Michael Gerrity,[1] Dominik Legut,[2] Justin M. Shaw,[3] Hans T. Nembach,[3] T. J. Silva,[3] Peter M. Oppeneer,[4] Henry C. Kapteyn,[1] and Margaret M. Murnane[1]
[1]Department of Physics and JILA, University of Colorado, Boulder, Colorado 80309, USA
[2]Nanotechnology & IT4Innovations Center, VSB Technical University Ostrava, CZ-708 33 Ostrava-Poruba, Czech Republic
[3]Quantum Electromagnetics Division, National Institute of Standards and Technology, Boulder, Colorado 80305, USA
[4]Department of Physics and Astronomy, Uppsala University, S-75120 Uppsala, Sweden

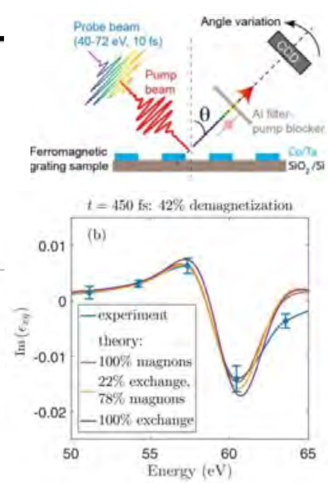

Second paper: we showed that you cannot exclude magnons even in the reduction of the moment in Cobalt (which has the strongest Weiss field)

Here we directly compared magneto-optical results to photoemission data

Band structure in Ni

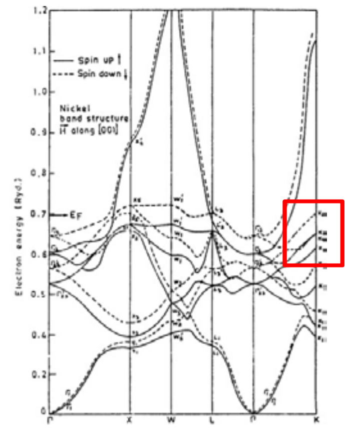

Fig. 1. The band structure of ferromagnetic nickel

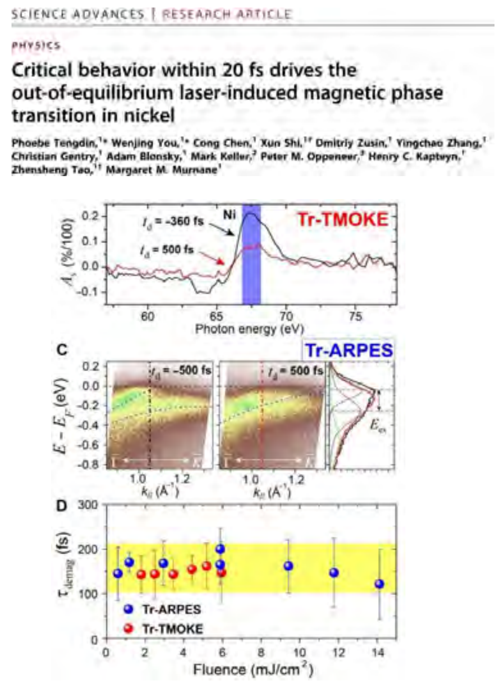

Light induced spin transfer: Half metallic System

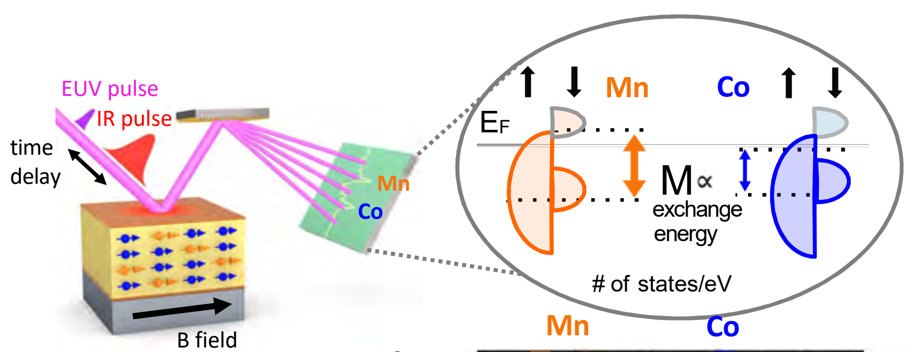

- Half metallic: one spin state condu
- Half-metal gap in Mn is bigger thar
- Expect to see slower dynamics due

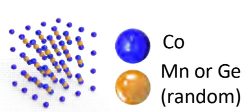

Half-metal Phase

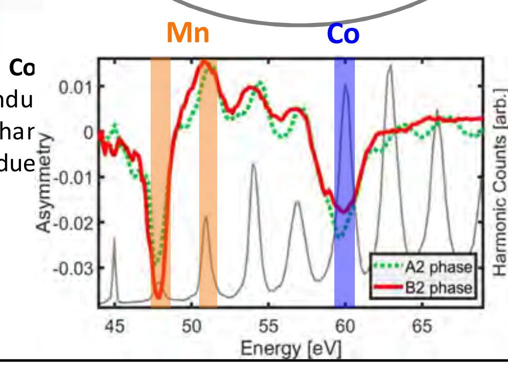

Ultrafast transfer of magnetization between different elements

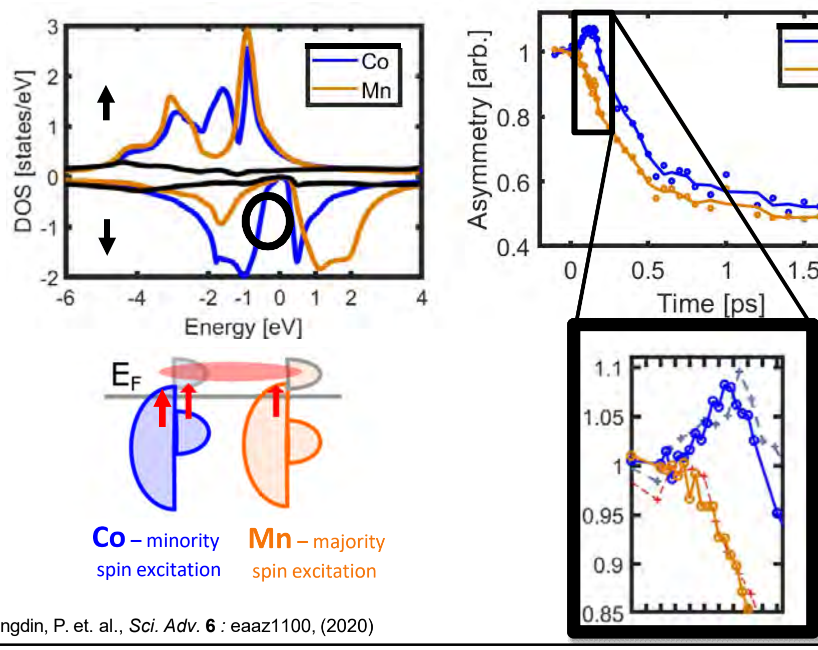

Tengdin, P. et. al., *Sci. Adv.* **6** : eaaz1100, (2020)